Neutron diffraction studies of crystal structures in nickel-titanium alloys

by

Scott Thomas Carey

A Thesis Submitted to the

Graduate Faculty in Partial Fulfillment of the

Requirements for the Degree of

MASTER OF SCIENCE

Department: Mechanical Engineering
Major: Nuclear Engineering

Iowa State University
Ames, Iowa
1990

TABLE OF CONTENTS

LIST OF ABBREVIATIONS

A:	austenite
esd:	estimated standard deviation
GSAS:	Generalized Structure Analysis System
HIPD:	High Intensity Powder Diffractometer
HP:	Hewlett-Packard
LAMPF:	Los Alamos Meson Physics Facility
LANL:	Los Alamos National Laboratory
LANSCE:	Manuel Lujan, Jr. Neutron Scattering Center
L-S:	least squares
M:	martensite
NiTi:	nickel-titanium
NPD:	Neutron Powder Diffractometer
PSR:	Proton Storage Ring
SMA:	shape memory alloy
SME:	shape memory effect
TOF:	time of flight
V-Nb:	vanadium-niobium

PARTIAL LIST OF GSAS PROGRAMS

EXPEDT: interactive editor which handles all input of structural data, program controls and other non-diffraction data

FSTBUSBIN: program which places raw diffraction data in appropriate TOF channels and changes the raw data to a format recognized by GSAS

GENLES: batch oriented generalized least squares program

POWPLOT: powder profile plotting routine which displays intensity versus d-spacing histograms for each detector bank

POWPREF: powder data preparation program which prepares powder diffraction data to be run by GENLES

ABSTRACT

Nickel-titanium (NiTi) of near equiatomic composition exhibits a phenomenon known as shape memory whereby it "remembers" a predetermined shape after being deformed below a particular temperature. A thermoelastic martensitic transformation is thought to be responsible for this behavior. Neutron diffraction studies were performed at the Manuel Lujan, Jr. Neutron Scattering Center, and Rietveld refinements were performed on the diffraction data to determine the crystal structures present in several samples under a variety of conditions. NiTi wires were tested at the High Intensity Powder Diffractometer (HIPD), and NiTi rods and powders (lathe turnings) were tested at the Neutron Powder Diffractometer (NPD).

The apparatus at the HIPD was designed so that temperature and electrical resistance could be measured while the NiTi wires were mounted in the diffractometer. In addition, the axial tensile stress on the wires could be varied. No difference in the diffraction results was detected, however, for the two stress levels applied (1.9 and 4.5 MPa). At 100°C, in the high-temperature austenite phase, the crystal structure was determined to belong to the $Pm3m$ space group (B2 or CsCl structure) in agreement with previous investigators, with lattice parameter $a = 3.023(3)$Å. The wires were also found to have a large amount of preferred orientation with the $< 111 >$ direction along the wire axis. Upon cooling to the high temperature side of the resistivity peak

(about 29°C), the 110 Bragg reflection of austenite was considerably broadened. Further cooling to the low-temperature side of the resistivity peak (about 18°C) showed what is considered to be the early stages of splitting of the 110 austenite reflection into two peaks. This is believed to indicate the distorting of the austenite unit cell into a rhombohedral one.

Curves of nominal resistivity versus temperature for various tensile stresses up to 56 MPa obtained by a previous investigator on NiTi wires from the same heat were corrected for changes in form factor due to transformation strain. The anomalous resistivity peak becomes narrower and the resistivity in the martensite increases with increasing tensile stress.

An yttrium-doped NiTi rod was used on the NPD to determine the crystallographic characteristics of the low temperature phase, martensite. Its unit cell was found to belong to the monoclinic $P2_1/m$ space group with lattice parameters $a = 2.9036(8)$Å, $b = 4.116(1)$Å, $c = 4.663(1)$Å and $\beta = 97.836(2)^\circ$. Anisotropic thermal parameters were used to account for the thermal motion of the atoms.

1. INTRODUCTION

Nickel-titanium of near-equiatomic composition has been studied considerably because of its unusual properties. By undergoing a kind of thermoelastic martensitic transformation, it exhibits a phenomenon known as shape memory which allows it to "remember" a predetermined configuration. The characteristics of martensitic transformations and shape memory alloys in general and of nickel-titanium alloys in particular will be discussed. Emphasis will be placed on the crystal structures present.

1.1 Martensitic Transformations

1.1.1 General characteristics

The interstitial solid solution of iron and carbon known as the γ phase is also termed *austenite* after Sir W. C. Roberts-Austen, an English metallurgist who did research in steels in the late nineteenth century [1]. Austenite consists of iron atoms at the face-centered cubic locations with carbon occupying interstitial sites [2]. If austenite with 0.8 weight percent carbon is cooled slowly below the eutectoid temperature (723°C), the steel will transform into α ferrite and cementite (Fe_3C). The α ferrite phase has iron atoms at the body-centered cubic sites with carbon at the interstitial positions while cementite has an orthorhombic unit cell. This two-phase

structure is known as pearlite. However, if this same composition of steel is rapidly cooled, a new phase known as *martensite* forms below about 220°C [3]. Martensite is a supersaturated solid solution of carbon in α iron (because of the increased carbon content, the unit cell elongates into a body-centered tetragonal structure [2]) and gets its name from A. Martens, a German metallurgist [1]. Since the steel transforms from austenite to martensite, the latter phase change is known as a *martensitic transformation.*

Originally, martensitic transformations were thought to occur only in the iron-carbon system, but, after similar characteristics were discovered in other materials, this terminology was generalized to other systems. Shimizu and Tadaki [4] define a martensitic transformation as "a lattice transformation involving shearing deformation and resulting from cooperative atomic movement." Characteristics of a martensitic transformation can now be summarized:

1) The high temperature structure is a single phase referred to as austenite or the parent phase and is denoted by A, and the low temperature structure is a single phase called martensite and is indicated by M.

2) Unlike most solid-solid phase transitions, there is no atomic diffusion associated with the transformation. In fact, the reaction takes place so fast that the speed of the boundary between the austenitic and martensitic phases may approach the speed of sound in the transforming material [3]. Also, the atoms generally move less than one interatomic spacing. For this reason, atomic concentrations before and after the phase transition remain unchanged, and each atom tends to preserve its own original neighbors.

3) Because the martensitic transformation involves shearing deformation, shape

changes, including the formation of surface relief and the bending of scribed lines, occur in the sample. For example, consider a line scratched on the surface of a polished austenitic sample. If the sample is cooled such that a small region of martensite is formed around part of the line, bends will form in the scribed line at the boundaries between the austenite and martensite. Furthermore, these bends will have a definite orientation which depend on the crystal orientation of the austenitic phase. This gives evidence that the movement of atoms during the transformation is coordinated and ordered.

4) The interface between austenite and martensite, known as the *habit plane*, has specific Miller indices (although they are often irrational). Habit planes are usually specified by the indices of planes in the austenitic phase. As discussed above, the habit plane can travel at high speeds. Also, the macroscopic distortion along the habit plane is zero, i.e., the habit plane exhibits *invariant plane strain*.

5) A definite relationship exists between the crystal lattices of austenite and martensite. In carbon steels, this can be described by the Kurdjumov-Sachs orientation relationship as discussed below.

6) Lattice deformations such as slip shear and twinning shear play a major role in the transformation because they allow invariant plane strain to exist. The transformation can be thought of as a change in the unit cell followed by a shear to relieve the internal stresses induced by this shape change. In reality, the two deformations occur simultaneously [2].

7) The martensitic transformation does not usually begin until the temperature drops below the martensite start temperature (M_S). As the temperature is lowered below M_S, more and more martensite is formed until the martensite finish temper-

ature (M_f) is reached. Generally, the amount of martensite formed depends on the amount of subcooling below M_s, i.e., the transformation is usually athermal. Similarly, on heating, a specimen of martensite will not begin to transform to austenite until the austenite start temperature (A_s) is reached. The phase change is complete at the austenite finish temperature (A_f).

In order for the martensitic phase to form, it must have a lower chemical free energy than the austenitic phase. If the temperature at which A and M have the same chemical free energy is called T_0, it may appear that T_0 should also coincide with M_s when the sample is cooled and with A_s when the sample is heated. This, however, is not the case due to the presence of nonchemical free energies such as interfacial energy between M and the parent phase, transformation elastic strain energy and plastic deformation energy. To initiate the transformation requires the difference in chemical free energies of A and M to be slightly greater than the nonchemical free energies. This means that M_s must be lower than T_0 to achieve the necessary driving force to counteract the nonchemical free energy. Similarly, A_s is higher than T_0.

1.1.2 Thermoelasticity

Martensitic transformations may be classified as either thermoelastic or non-thermoelastic. In some cases, when martensite is formed in the parent phase, the M crystals grow very quickly to their final size, and they do not grow further with decreased temperature or increased time. If the specimen is then heated to transform it back to the parent phase, the A crystals nucleate within the existing martensite. This is a *non-thermoelastic transformation.* On the other hand, in *thermoelastic transformations*, the velocity at which the M crystals grow within the parent phase

is dependent upon the rate at which the sample is cooled. In addition, upon heating, the last M crystals formed at M_f are the first to revert back to A crystals at A_s.

Thermoelasticity is observed because a balance exists between the chemical driving force and the nonchemical free energy needed for transformation. More specifically, if interfacial and plastic deformation energies are assumed negligible, the balance exists between thermal and elastic energies (hence the name, thermoelasticity). The assumption of very small interfacial and plastic deformation energies is valid for 1) small lattice deformations (and consequently, small volume changes), 2) M and A crystals which are ordered so as to achieve coherency between the two phases, and 3) M crystals containing internal twins which can be easily detwinned. Anything which changes this balance in energy, such as a change in temperature or a change in an external force, results in the growth or shrinkage of the M crystals to regain the balance. This indicates that a thermoelastic martensitic transformation is reversible. Also, it can be seen that systems which do not fall under the assumptions mentioned above will generally exhibit non-thermoelasticity.

This equivalence between temperature and stress in the thermoelastic reaction leads to the possibility of *stress-assisted martensite*. If a stress is applied to a sample that is above M_s, stress-assisted martensite may form provided the temperature is below M_d which is the maximum temperature at which stress-assisted martensite will form. If $A_f < T < M_d$, the stress-assisted martensite will be unstable and will return to the parent phase when the stress is removed [5] [6].

1.1.3 Martensite variants

As discussed above, a definite relationship exists between the two lattices of A and M. As an example, in carbon steels the Kurdjumov-Sachs relations may be used to explain this correspondence:

$$\{111\}_A \parallel \{011\}_M, \quad <\bar{1}01>_A \parallel <\bar{1}\bar{1}1>_M \tag{1.1}$$

where A and M represent the austenitic and martensitic phases, respectively. Notice that the $\{111\}$ planes in the austenite could be any one of four different planes: (111), $(\bar{1}11)$, $(1\bar{1}1)$ and $(11\bar{1})$. In addition, for each of these planes, three different pairs of shear directions may be chosen: for example, for (111), $[10\bar{1}]$ and $[\bar{1}01]$, $[0\bar{1}1]$ and $[01\bar{1}]$, and $[1\bar{1}0]$ and $[\bar{1}10]$. This gives a total of 24 crystallographically equivalent martensite lattices known as *variants*; each variant will have different (although crystallographically equivalent) habit plane indices. Note that two variants formed by one shear direction pair, say the $[10\bar{1}]$ and the $[\bar{1}01]$ directions, are twin related. If a single crystal of austenite were to undergo a martensitic transformation, all 24 variants would form in the martensite (assuming there are no external or residual stresses present).

While all 24 martensite variants may be found in the transformed sample, the process is not entirely random. When the martensitic transformation begins in a stress-free sample, there is an equal probability of each variant forming. However, as the transformation continues, the martensite induces stresses in the surrounding austenite which increases the amount of free-energy present. The next variants that form will be orientated such that the free energy is decreased; as the phase change continues, the orientation of the subsequent variants becomes less random [7]. This

process is known as *self-accommodation.*

In a specimen which transforms from an austenitic composition to a martensitic one, the overall change in shape is reduced due to self-accommodation. However, if an external force is applied, the additional elastic energy will require martensite variants to grow which will regain the thermoelastic energy balance. In this case the force will induce a change in shape in the sample.

1.1.4 Invariant plane strain

As discussed above, a martensitic transformation is characterized by surface relief and by the bending of fiducial marks, giving evidence that the A and M phases are highly coherent. Generally, the M unit cell is lower in symmetry than the A unit cell. Since the A and M crystals have rather different structures there is a mismatch between the two phases so as the M crystals grow, the strain energy in the sample begins to increase–sometimes dramatically. In a nucleation and growth reaction, this energy increase would usually lead to a loss of coherency since the two unit cells cannot physically match each other. But in a martensitic transformation, the extra strain energy is tolerated because alternative reactions progress at much slower rates making the martensitic reaction kinetically favorable [8]. Also, in a martensitic transformation, the overall strain energy is decreased by introducing lattice deformations such as twins.

Figure 1.1 shows a sample undergoing a martensitic transformation. The top portion of the sample is still in the austenitic phase while the bottom has transformed to martensite. To maintain coherency between the two phases, the interface between the two phases (the habit plane) is characterized by *invariant plane strain.* Notice

that two twin-related crystals (indicated by 1 and 2) are shown in the martensite. The change in shape of the martensitic portion of the sample is due primarily to the change in the unit cell which describes it. In an actual stress-free sample more than two martensite variants would likely form, and self-accommodation would decrease the overall change in shape of the specimen.

The macroscopic shape of the martensite differs from its microscopic features. Consider Figure 1.2 which shows an enlarged portion of several twin-related martensite variants. It can now be seen how the martensitic transformation maintains coherence between the A and M phases while allowing the free energy of the sample to remain at a minimum. As twin 1 forms, the strain energy of the sample increases due to the mismatch between the A and M crystals. To compensate for this increase in energy, twin 1 ceases to grow, and twin 2 begins to form. The orientation of twin 2 is such that it offsets the increase in strain energy caused by twin 1. This interplay between the two twins results in the habit plane being a plane of zero macroscopic distortion even though there is some distortion on the microscopic scale. In this example, the macroscopic distortion reduces to zero after only two twin bands have been formed. In a real crystal where many martensite variants may exist, several variants must be produced before the net distortion is zero.

A phenomenological theory, developed by Wechsler, Lieberman and Read (the WLR theory) [9], [10], predicts the relationship between the crystallographic orientations of A and M. It also predicts the relative amounts of twins 1 and 2 which will lead to a minimum in the free energy. Moreover, the WLR theory shows that there is a unique habit plane of zero macroscopic distortion.

1.2 The Shape Memory Effect

A sample is formed into a particular shape (say that of a straight wire) and annealed so it is entirely austenitic. The straight wire is then cooled below M_f and plastically deformed. If the sample is now heated to A_s, it will begin to straighten, and the wire will be back to its original shape at A_f. This process is shown schematically in Figure 1.3 and is known as *the shape memory effect* (SME). More specifically, this is an example of *one-way shape memory.*

If the *shape memory alloy* (SMA) is cycled several times and always bent into the same shape when its temperature is below M_f, it may be "trained" to remember the low-temperature shape as well. In other words, the sample may show *two-way shape memory.* In two-way shape memory alloys, the sample assumes one shape when heated and a second shape when cooled [11].

1.2.1 Applications

When a SMA transforms, it can exert an external force and do work on its surroundings. This it true whether the effect is one-way or two-way. For this reason, SMAs have found applications in several areas. The Grumman F-14 jet fighter uses SMA hydraulic-tube couplings [12]. The coupling, when held below M_s (below -120°C), has an inside diameter just large enough to slip over the hydraulic tube. When the temperature of the coupling is allowed to rise, the coupling contracts to make a very tight seal. Other applications include solid state heat engines [13], [14], heat-activated switches, temperature-sensitive valves and other actuators [15], robotic applications, pen recorders, medical and dental uses [16], and energy beam position detectors [17]. It has also been proposed to use SMA heat engines to convert

the waste heat rejected by electrical power plants into mechanical energy [18].

1.2.2 The SME mechanism

In order for an alloy to exhibit the SME, the material must have three properties: 1) it must exhibit a thermoelastic martensitic transformation, 2) the austenitic and martensitic phases must be ordered, and 3) the martensite must be internally twinned [19]. First consider a stress-free sample which has been cooled below M_f so that it is made up of a mixture of 24 variants. If a stress is now applied to the sample, some variants will first change their orientation to that of their twin in order to decrease the applied stress, i.e., detwinning will decrease the number of variants from 24 to 12. As additional stress is applied, the 12 remaining variants will coalesce to further reduce the applied stress. Evidence of this coalescence can be seen in the decrease in internal friction in nickel-titanium alloys [20]. Since there are fewer variants, there are fewer interfaces; this causes a decrease in internal friction. This conversion will continue until the sample consists of a single martensite variant. That single variant will be the one which gives the largest strain in response to the applied stress [21]. If the material is now heated above A_f, the atomic structure will revert back to a structure whose unit cell and orientation are identical to the parent phase before it was cooled below M_s. This is the basis of the shape memory effect.

The three prerequisites of the SME can now be explained. First, in a non-thermoelastic transformation, when the sample is heated to transform M to A, the A crystals form in various orientations within the M crystals. This piecemeal transformation cannot reproduce the original austenite orientation, and the sample cannot completely regain its original shape (although a partial shape memory may be ob-

served). Second, if the alloy is not ordered, there is a loss of coherence between the M and A phases. This prevents the M from growing and shrinking reversibly, and the transformation is not thermoelastic. Third, the necessity of a plane of invariant strain has already been discussed. In order to achieve a plane of zero macroscopic distortion between two different unit cells, lattice dislocations must be introduced. To allow the reaction to be reversible (thermoelastic) requires that these lattice dislocations not be mobile, and this precludes the introduction of slip. However, if twin bands exist such that when a stress is applied, one twin may easily grow at the expense of the other, the process will be reversible. The presence of martensite twins has been unambiguously identified in nickel-titanium alloys [22]. After the sample has been cooled, deformed and heated once, a pattern of residual stresses exists in the parent phase [7]. These stresses tend to dictate which variants are formed when the sample is again cooled below M_S. The formation of these select variants brings the specimen back to its deformed shape, and a two-way memory effect is observed. The more this procedure is repeated, the more prominent is the memory effect when the sample is cooled.

If the sample is thermally cycled while under an applied stress, the material will actually be trained in a single run. This is because the stress will cause those martensite variants to form which best alleviate the stress and decrease the free energy. Since a variant formed during the first run is more likely to form in subsequent cycles, and since the applied load has caused a select set of variants to form during the first thermal cycle, the two-way memory is coded into the material. This code may be erased during thermal cycling either by reversing the direction of the applied stress or by employing alternating stresses.

1.3 Nickel-Titanium Alloys

While the SME has been observed to some extent in a variety of alloys since the 1930s [12], one of the most-studied SMAs is nickel-titanium (NiTi) of near equiatomic composition [23]. This SMA is also known as Nitinol. (The name is derived from the **ni**ckel and **ti**tanium constituents and the U. S. Naval **O**rdnance **L**aboratory where its shape memory properties were first observed.) Figure 1.4 shows the nickel-titanium phase diagram between 600°C and 1800°C.

1.3.1 Crystal structures

1.3.1.1 Austenite The crystal structure of nearly equiatomic NiTi has been studied for over 40 years using a variety of diffraction techniques. As early as 1950, Duwez and Taylor [24] indexed the high temperature phase as having the "body-centered CsCl type cubic structure" with a lattice parameter, a, of 2.980Å. Purdy and Parr [23] found the lattice parameter to range from 3.010Å to 3.050Å depending on temperature and composition. Wang *et al.* [25] suggested a two-phase mixture for austenite using the $Pm3m$ space group (the Hermann-Mauguin symbol for the CsCl structure) and the $P\bar{3}m1$ space group, although they conceded the diffraction patterns of the two structures are so similar they are nearly indistinguishable.

Presently, nearly all researchers are in agreement that the austenitic phase of NiTi is the CsCl or B2 structure whose space group is $Pm3m$ [20] [22] [26]–[31]. Although the lattice parameter may have some temperature and composition dependence, most studies have found a to be very close to 3.015Å. Bührer *et al.* [20], using NiTi wires from the same heat as this study, determined the austenite to have a high degree of preferred orientation, with the [111] direction being aligned with the wire

axis.

1.3.1.2 Martensite While the atomic structure of austenite seems to be well understood, a great deal of disagreement has ensued over the crystal structure of martensite. It is generally agreed that the structure is of lower symmetry than austenite and that its lattice parameters depend on the ratio of nickel to titanium [29]. Dautovich and Purdy [27] indexed an x-ray diffraction pattern using a triclinic unit cell with $a = 4.60\text{Å}$, $b = 2.86\text{Å}$, $c = 4.11\text{Å}$, $\alpha = 90.1^\circ$, $\beta = 90.9^\circ$ and $\gamma = 96.7^\circ$. Wang *et al.* [25] suggested using three different structures: $P\bar{1}$, $P1$ and $P6/m$. However, the majority of the evidence points to martensite having a monoclinic unit cell (specifically, a monoclinic distortion of the AuCd or B19 structure).

Table 1.1: Summary of crystal structures used for NiTi martensite

Researchers	OSS[a]	HS[b]	MS[c]	B−[d]	K−[e]
Space Group	$P12/c1$	$P2_1/m$[f]	$P2_1/m$[f]	$P2_1/m$	$P2_1/m$
a(Å)	2.889	2.883	2.885	2.884	2.898
b(Å)	4.120	4.117	4.120	4.110	4.108
c(Å)	4.622	4.623	4.622	4.665	4.646
β(°)	96.8	96.8	96.8	98.10	97.78
Atom Positions					
Ni	$\frac{1}{2}y\frac{1}{4}, \frac{1}{2}\bar{y}\frac{3}{4}$	$x\frac{1}{4}z, \bar{x}\frac{3}{4}\bar{z}$	$x\frac{1}{4}z, \bar{x}\frac{3}{4}\bar{z}$	$x\frac{1}{4}z, \bar{x}\frac{3}{4}\bar{z}$	$x\frac{1}{4}z, \bar{x}\frac{3}{4}\bar{z}$
x		0.0	0.0525	-0.034	0.0372
y	0.167				
z		0.1875	0.693	0.830	0.6752
Ti	$0y\frac{1}{4}, 0\bar{y}\frac{3}{4}$	$x\frac{1}{4}z, \bar{x}\frac{3}{4}\bar{z}$	$x\frac{1}{4}z, \bar{x}\frac{3}{4}\bar{z}$	$x\frac{1}{4}z, \bar{x}\frac{3}{4}\bar{z}$	$x\frac{1}{4}z, \bar{x}\frac{3}{4}\bar{z}$
x		0.5	0.4726	0.561	0.4176
y	0.333				
z		0.3125	0.221	0.267	0.2164

[a] Otsuka, Sawamura and Shimizu [22].

[b] Hehemann and Sandrock [32].

[c] Michal and Sinclair [33].

[d] Bührer, Gotthardt, Kulik, Mercier, and Staub [34].

[e] Kudoh, Tokonami, Miyazaki and Otsuka [35].

[f] The original $\vec{b}$ and $\vec{c}$ axes and y and z coordinates have been interchanged as was done by Kudoh *et al.*[35].

Table 1.1 summarizes some of the monoclinic crystal structures used over the past 20 years to describe martensite. It should be noted that the space group originally cited by Michal and Sinclair (MS) [33] and by Hehemann and Sandrock (HS) [32] was $P112_1/m$. This is identical to the $P2_1/m$ space group used by Bührer *et al.* (B+) [20] [34] [36] and by Kudoh *et al.* (K+) [35] if the $\vec{b}$ and $\vec{c}$ axes and the y and z atomic coordinates are interchanged; this also changes the unique angle from γ to β. The space group used by Otsuka *et al.* (OSS) [22] also has the $\vec{b}$ axis as the unique axis, but the atom positions differ from the other structures listed.

Comparisons between the crystal structures have been done [35]. In the OSS work, the 001, $10\bar{1}$ and 101 reflections are forbidden by the crystal structure used, but they are observed in the diffraction patterns [22]. Similarly, the HS study observed the 010 and 110 reflections which should not have been seen with their crystal structure. Kudoh *et al.* used a least-square refinement to compare the MS, B+ and K+ studies. By applying the MS model to the K+ x-ray diffraction data (the MS sample was Ti-50.0 ± 0.1 atomic % Ni, and the K+ sample was Ti-49.2 atomic % Ni), an R-factor of 38.6% was found[1] where Kudoh *et al.* defined R using observed and calculated structure factors,

$$R = \frac{\Sigma||F_O| - |F_C||}{\Sigma|F_O|}. \tag{1.2}$$

The major difference between MS and K+ is the use of anisotropic temperature factors in the K+ model. This gave a final R-factor of 4.5% for K+. Anisotropic

[1] MS listed their R-factor as 17% for their data because they used an alternate definition for R replacing observed and calculated stucture factors with observed and calculated intensities. In addition, MS used only 14 low angle reflections while K+ used 307 reflections including high angle ones.

Table 1.2: Anisotropic and equivalent isotropic temperature factors ($\times 10^4$) for NiTi martensite [35]

Atom	β_{11}	β_{22}	β_{33}	β_{12}	β_{13}	β_{23}	B_{iso} (Å^2)
Ni	391	47	144	0.0	-66	0.0	0.99
Ti	226	90	131	0.0	-12	0.0	0.84

temperature factors, β_{ij}, are dimensionless quantities and are expressed as

$$T = \exp[-(\beta_{11}h^2 + \beta_{22}k^2 + \beta_{33}l^2 + 2\beta_{12}hk + 2\beta_{13}hl + 2\beta_{23}kl)] \tag{1.3}$$

where the structure factor for each reflection is multiplied by T to correct for changes in observed intensity due to the thermal motion of the atoms. To obtain an equivalent isotropic temperature factor, the following relationship may be used

$$B_{iso} = \frac{4}{3}\sum_{i=1}^{3}\sum_{j=1}^{3}\beta_{ij}(\vec{a_i}\cdot\vec{a_j}) \tag{1.4}$$

where the a's represent the lattice vectors of the unit cell [37]. For isotropic temperature factors, the correction is expressed as

$$T = \exp[-B_{iso}(\sin^2\theta/\lambda^2)]. \tag{1.5}$$

Chapter 3 discusses how temperature factors were handled in this work. Table 1.2 shows the values of the anisotropic temperature factors (β_{ij}) and the equivalent isotropic temperature factors (B_{iso}) obtained by Kudoh *et al.* [35].

In addition, Kudoh *et al.* [35] applied their K+ model to neutron diffraction data obtained by Bührer *et al.* [34] on NiTi wires (Ti-49.93 atomic % Ni). This yielded an R-factor of 25% and is attributed to possible preferred orientation in the B− bulk sample and "rather poor accuracy in neutron diffraction." It is interesting to note

that Saburi [38] feels that the dispute over the crystal structure of NiTi martensite has been settled, and he cites the space group and lattice parameters of Kudoh *et al.* as the structure of choice for Ti-49.2 atomic % Ni alloys.

Golestaneh and Carpenter [39] suggested using two unit cells to describe NiTi martensite: $P112_1/m$, as used by MS [33]; and $P12/c1$, as used by OSS [22]. The lattice parameters were found to vary throughout the sample, but their mean values were very close to those listed in Table 1.1. The atomic coordinates of the $P112_1/m$ space group are identical to those used by Michal and Sinclair [33], and the coordinates of the $P12/c1$ space group differed slightly from those used by Otsuka *et al.* [22].

1.3.1.3 Intermediate phase A special feature of Nitinol is that it does not undergo the usual martensitic transformation from austenite to martensite upon cooling. Purdy and Parr [23] were the first to observe another phase at temperatures intermediate to that of the austenite and martensite phases, commonly known as the *R phase*, which they indexed as hexagonal with $a = 4.572$Å and $c = 4.660$Å. Dautovich and Purdy [27] used a rhombohedral unit cell with $a = 6.02$Å and $\alpha = 90.1^\circ$. Chandra and Purdy [26] also used a rhombohedral space group, but with $a = 9.03$Å and $\alpha = 89.3^\circ$. Goo and Sinclair [31] found the R phase to be hexagonal with space group $P\bar{3}1m$ and lattice parameters $a = 7.38$Å and $c = 5.32$Å. They further found the orientation relationship between A and R to be

$$(111)_A \parallel (0001)_R, < \bar{2}11 >_A \parallel < 2\bar{1}\bar{1}0 >_R . \tag{1.6}$$

There has also been a report [40] of the R phase being a distorted CsCl structure of monoclinic symmetry ($P2/m$).

Ling and Kaplow [41]–[44] did a great deal of investigation into the R phase of NiTi. Their observations indicate that the 110 austenite reflection splits into two reflections as the austenite unit cell distorts into a rhombohedral unit cell. Wang *et al.* [25] also reported this splitting.

Although the presence of the R phase has been well established, there are cases where investigators have not observed its attributes in x-ray and neutron diffraction work [36] [45]. This may be due to the weakness in intensity of the R reflections or to the lack of adequate resolution to observe the splitting of the 110 reflection.

1.3.2 Electrical resistivity versus temperature behavior

One of the first physical indications that NiTi transformed in a way that was different from many other martensitic transformations was found in its electrical resistivity. Upon cooling, an anomalous peak appears around room temperature [27] [29] [43] [44], and the summit of this peak is often considered to correspond to M_S. A peak is sometimes observed upon heating as well [46]. The amount of hysteresis, the shape of the curves and the characteristic temperatures, e.g., M_S, are dependent upon the thermomechanical history as well as the exact composition of the specimen.

1.3.2.1 Effects of stress Hsu [47] studied the effects of increasing levels of applied stress to NiTi wires. Figure 1.5 shows how stress affects resistivity and strain as the samples are thermally cycled. As the stress was increased, the transformation strain also increased. This is explained by the preferred activation of those martensite variants which give the largest strain in the stress direction. In addition, the nominal resistivity shows stress dependence in the low temperature regime, with the nominal

resistivity increasing with increasing stress. Hsu explained this stress dependence by some R phase being retained in the martensite when the sample was cooled below M_S.

Ling and Kaplow [43] used x-ray diffraction to study the change in crystal structure as the sample was cycled through the resistivity peak. They found that as tensile stress was increased on the NiTi sample, the intensity of the R phase reflections shifted from hkl to $\bar{h}kl$.

1.3.2.2 Reaction mechanism The presence of the R phase is not always seen as a precursory event leading to the formation of martensite. By adding alloying elements, such as iron, M_S may be lowered while the temperature at which R forms remains near room temperature [48]. Also, a large number of transformation cycles has been found to decrease M_S and A_S, thus causing the transformation to occur in several stages since T_R, the temperature at which the R phase begins to form, seems to be unaffected [47]. In other alloys, the formation of R and M appears to occur simultaneously. This has lead to some confusion over whether the transformation from austenite to martensite is first or second order. (First order reactions display a discontinuous change in physical properties, while second order reactions show more gradual changes.) Otsuka *et al.* [45] explain that diffraction experiments are superior to specific heat measurements in determining the reaction order. This is because a martensitic transformation takes place over a range of temperatures (unlike freezing, for example). As the specimen is cooled, any latent heat released from a first order reaction will be incorporated into the change in specific heat. The result is a peak in the specific heat versus temperature curve which is not sharply defined, and the first

order reaction is misinterperted. By observing the changes in lattice reflections with changes in temperature, this mistake may be avoided.

While there are almost as many conclusions that the reaction in NiTi is a first order reaction [29] [31] [45] as there are that the reaction is a second reaction [25] [26] [49], Miyazaki and Wayman [46] [50] conclude that it is both. They suggest the transition from austenite to martensite occurs in several steps.

Figure 1.6 summarizes the steps in the NiTi transformation upon heating and cooling as described by Miyazaki and Wayman [46]. With the sample in the parent phase, the sample is cooled. At T_R' extra, diffuse reflections of the type $\frac{1}{3}(110)$ and $\frac{1}{3}(111)$ appear in the austenite diffraction pattern [26]. This is an indication of the presence of a charge-density wave with a density modulation that does not quite match the periodicity of the metal ions. It is said that the electronic density is *incommensurate* with the underlying lattice [51]. This is a second order transition. As the sample is cooled to T_R, the parent phase transforms to a rhombohedral unit cell, and the incommensurate reflections "lock in" to commensurate positions. This is a first order transformation. Due to the presence of surface relief and invariant plane strain along the $\{111\}$ directions, the B2 — I — R sequence has been classified as a very simple martensitic transformation which is electronic in origin [50]. It was also observed that the R phase consisted of four distinct variants [50].

As mentioned above, true martensite is often considered to begin to form from the R phase at the peak of the resistivity curve. According to Wayman [50], the two phases coexist until M_f is reached. He considers this transformation to be a first order reaction. Upon heating the steps occur in reverse order. As mentioned above, M_s may be depressed by adding alloying elements without affecting the R

phase formation. In fact, Ling and Kaplow found that several reactions are possible: A=R, A=M and R=M [41] [44]. This indicates that the R phase transformation is independent of the austenite-to-martensite transformation, so to call the R phase "premartensitic", as has been frequently done in the literature, is not entirely correct.

Just as certain martensite variants can be preferentially formed with the application of stress, the R variants also experience a rearrangement when stresses are present in the specimen [48]. In addition, just as stress-assisted martensite may be formed [5] [42], the R phase may be induced in austenite by stresses. Goldstein [52] indicated that as the R phase forms, it induces stresses in the surrounding austenite which causes more R phase to form. Since R phase resistivity is higher than the austenite resistivity, a peak is observed in the resistivity curve. As the R transforms to M, the stresses are relieved, the amount of R decreases and the resistivity decreases to the linear behavior seen in the martensitic phase. In a strain-free sample of NiTi, it is proposed that the sample transforms directly from A to M since no peak is observed in the resistivity [49].

1.4 Purpose of the Study

The present work used neutron diffraction to determine the crystal structures present in NiTi wires at different temperatures and under different tensile stresses. In several experiments, electrical resistance was observed while the samples were mounted in the diffractometer to monitor the transformation. Rietveld refinements were then performed on the diffraction data. Major areas of investigation which support this purpose are:

1. Determine the crystallographic parameters of NiTi austenite.

2. Determine the crystallographic parameters of NiTi martensite.

3. Investigate the transition from austenite to martensite by a possible intermediate phase, and determine its attributes (correlation with the resistivity peak).

4. Observe how a change in tensile stress affects the characteristics of the martensitic and intermediate phases.

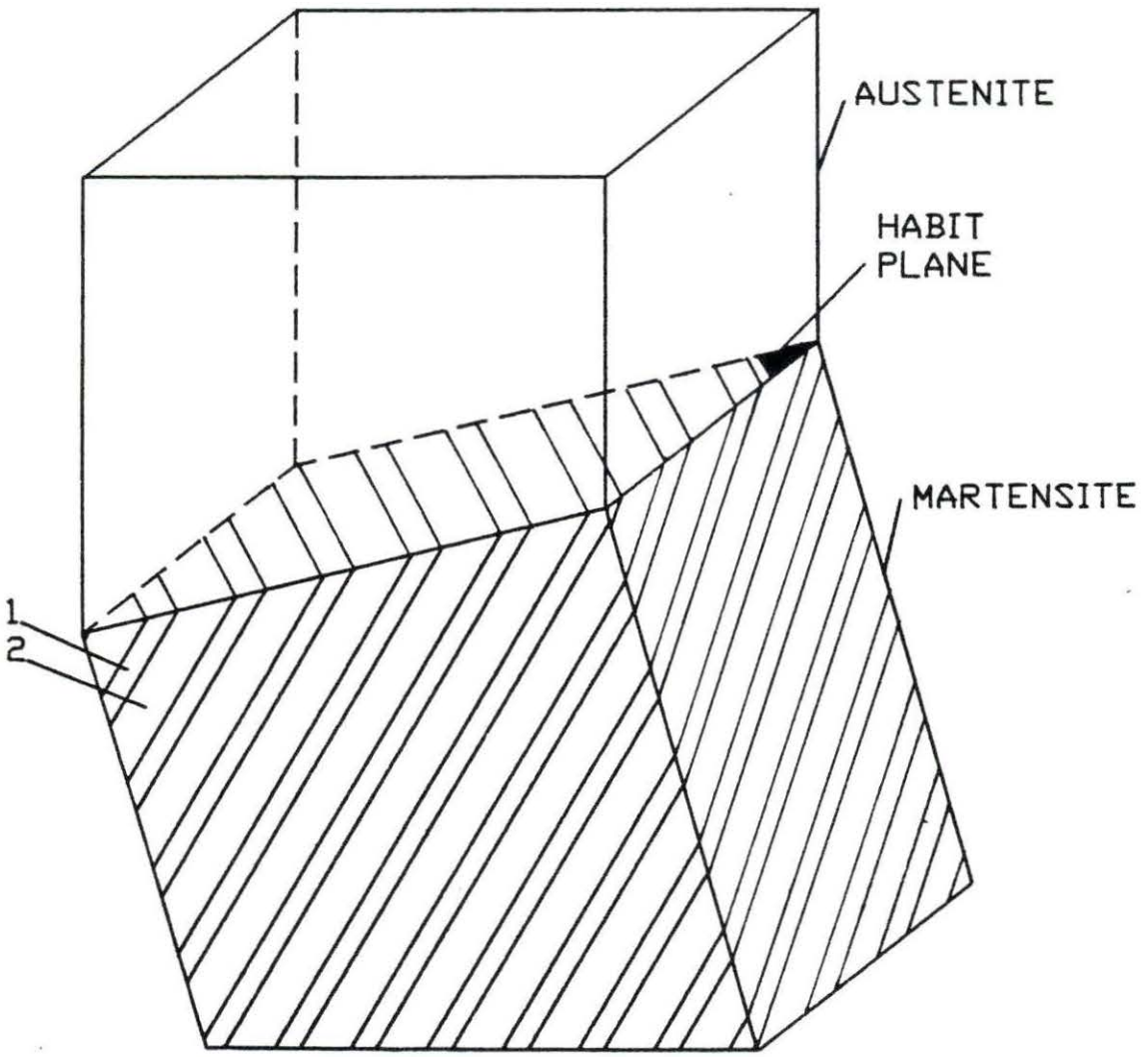

Figure 1.1: A sample undergoing a martensitic transformation showing the habit plane and internal twinning in the martensite [53]

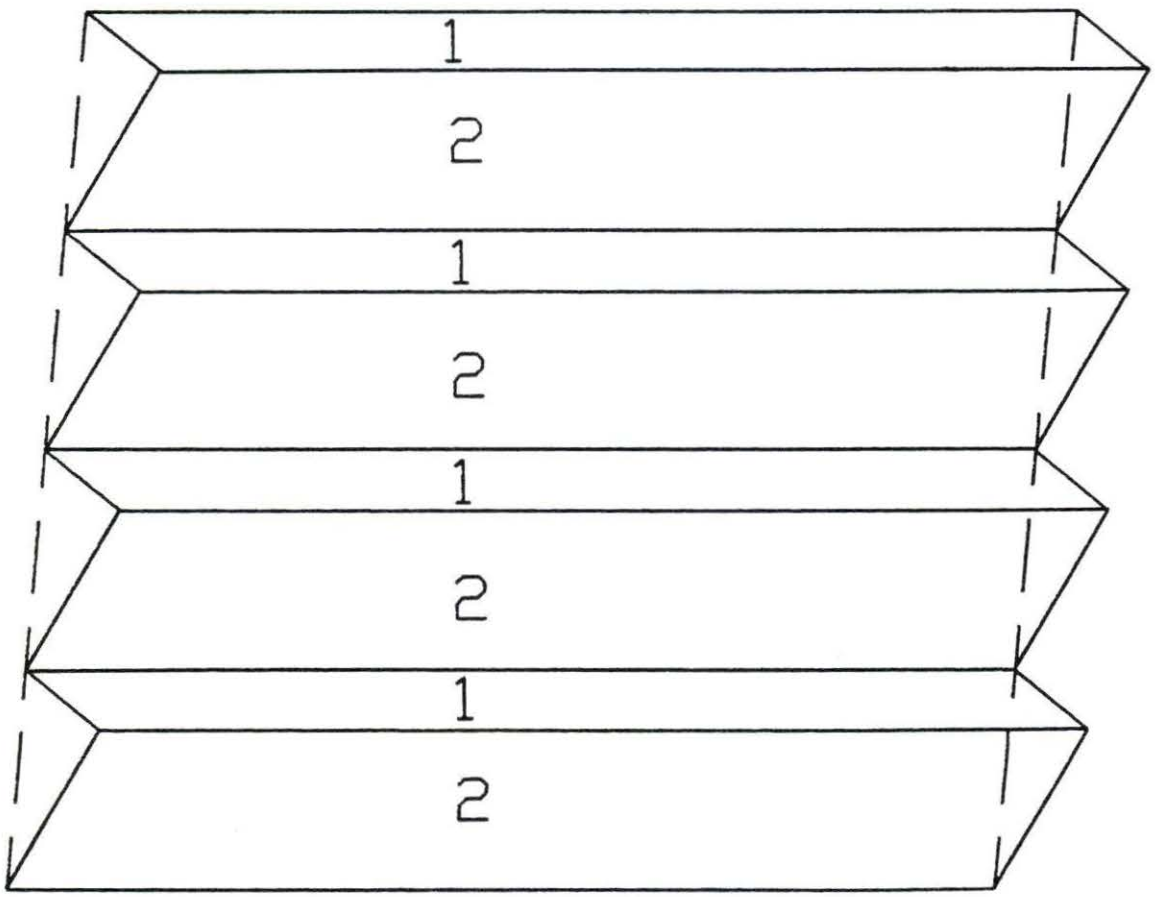

Figure 1.2: Production of invariant plane strain by twinning (After [2])

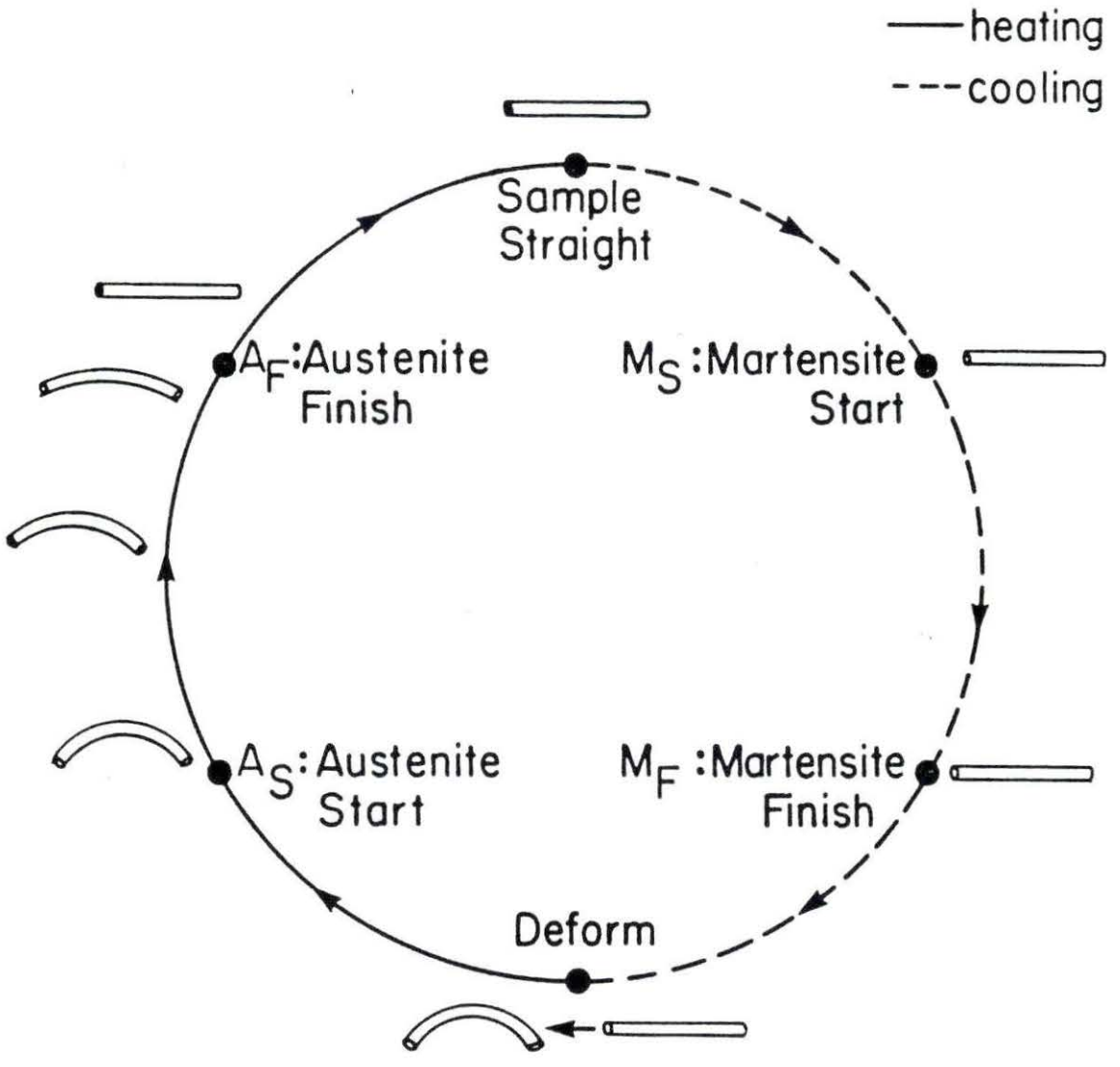

Figure 1.3: Schematic representation of the shape memory effect [54]

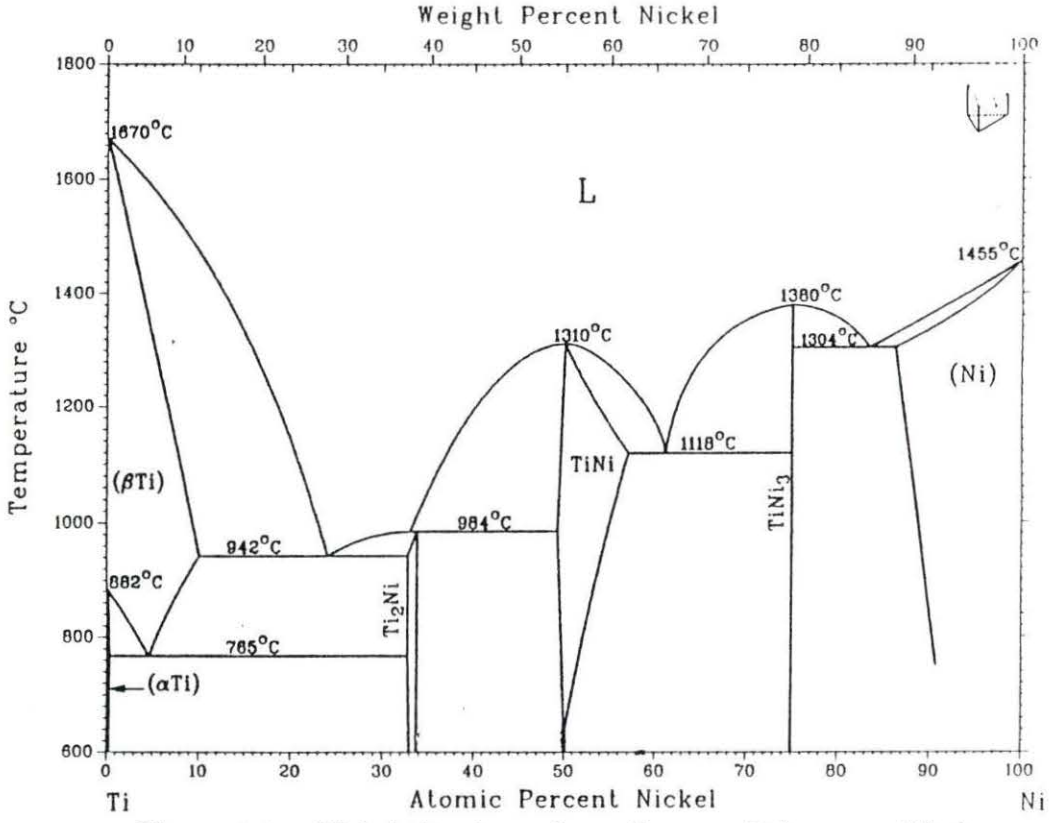

Figure 1.4: Nickel-titanium phase diagram [55], as modified

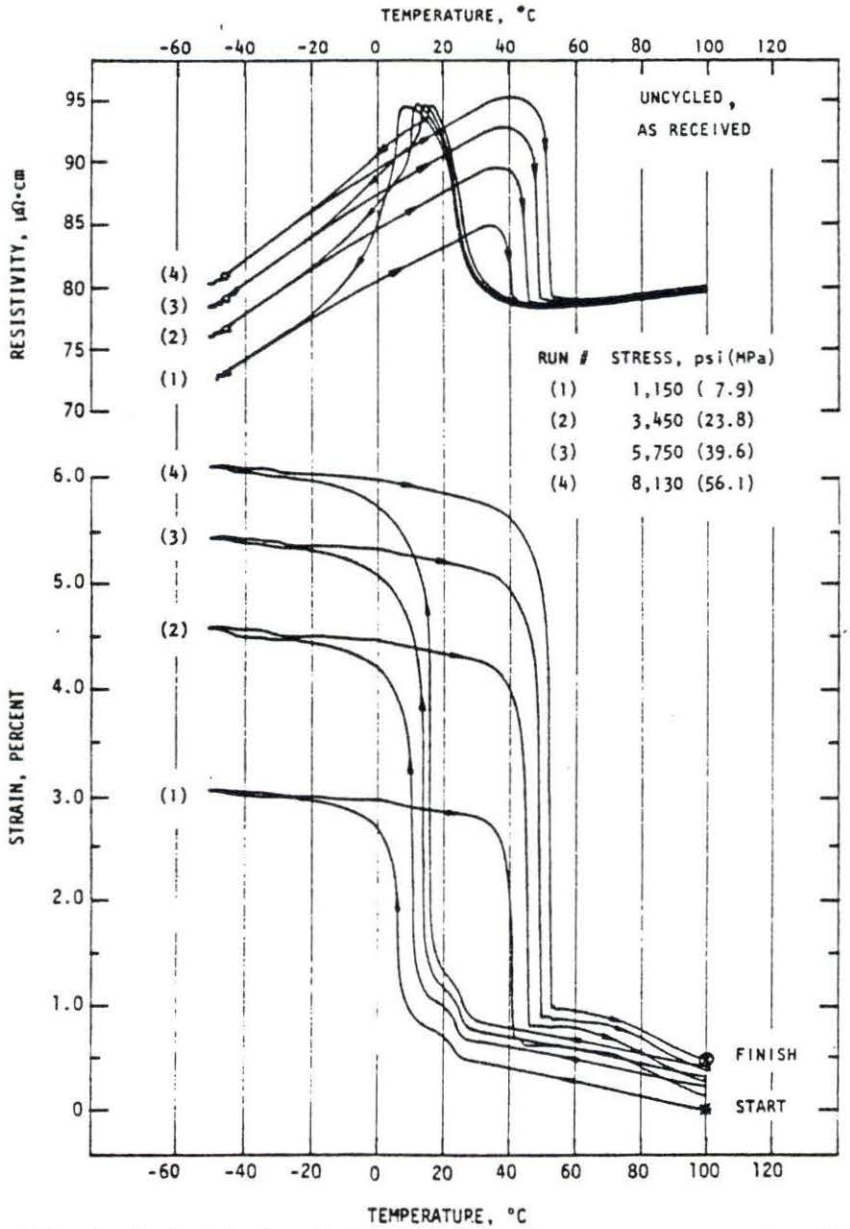

Figure 1.5: Nominal electrical resistivity and strain versus temperature for uncycled, as-received, NiTi wires [47]

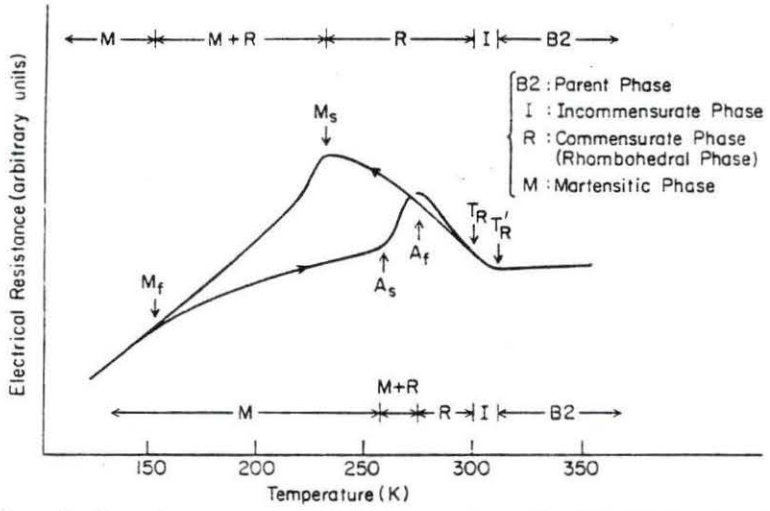

Figure 1.6: Electrical resistance versus temperature for Ti-50.5 atomic % Ni single crystal [46]

2. EXPERIMENTAL SETUP AND PROCEDURES

During the summers of 1988 and 1989 nickel-titanium (NiTi) specimens with compositions near 50 atomic percent were used in neutron diffraction experiments. For some of these samples, the martensitic transformation was monitored by observing the electrical resistance as a function of temperature while the samples were installed in the neutron diffractometer. Also, two values of tensile stress were applied to observe the stress-dependence of transformation characteristics.

2.1 Neutron Diffraction Facilities

Neutron diffraction experiments were carried out at the Manuel Lujan, Jr. Neutron Scattering Center (LANSCE) at the Los Alamos National Laboratory (LANL). As explained in [56], spallation neutrons are generated at LANSCE by 800 MeV protons directed at a tungsten target. The proton beam is provided by the half-mile long linear accelerator at the Los Alamos Meson Physics Facility (LAMPF) and an associated Proton Storage Ring (PSR). The PSR compresses the pulse width of the proton beam provided by LAMPF from 750 microseconds to 270 nanoseconds which is more suitable to produce short intense bursts of thermal neutrons. The PSR can also change the pulse intensity and repetition rates. Presently the rate of the proton beam striking the target is 12 Hz. After their production at the target, the neutrons

are then slowed to thermal energies by means of water and liquid hydrogen moderators. The chilled water moderators provide peak neutron intensities in the 5 to 10 meV range. The moderated neutrons finally pass down several flight paths to various experimental instruments.

Since LANSCE is a pulsed neutron source, time of flight (TOF) of each detected neutron can be determined by measuring the time elapsed since the impact of the proton beam with the target. From TOF data, the wavelengths of the neutrons can be easily calculated if the length of the flight path is known. These wavelengths can be transformed to the distances between adjacent atomic planes (d-spacings) in the following manner. Let 2θ be the angle between the incident and diffracted beams so that θ is the angle between either the incident or diffracted beams and the plane of atoms whose d-spacing is represented by d'. If λ is the de Broglie wavelength of the incident neutrons, Bragg's law may be written as

$$n\lambda = 2d' \sin\theta \tag{2.1}$$

were n is the order of the reflection. If Equation 2.1 is divided by n, we have

$$\lambda = 2d \sin\theta \tag{2.2}$$

where $d = d'/n$. In Equation 2.2, the reflections may all be considered first-order reflections with $\frac{1}{n}$ the d-spacings of those in Equation 2.1 [57]. Data acquisition is accomplished by storing TOF information in a memory module controlled by a computer system. After the experiment has been completed, a single set of programs makes appropriate calculations to convert the TOF information into diffraction histograms of intensity versus d-spacings for each detector bank.

The High Intensity Powder Diffractometer (HIPD) has a sample-to-moderator distance of 9 meters and has detector banks at 2θ angles of $\pm 153^{\circ}$, $\pm 90^{\circ}$, $\pm 40^{\circ}$, $\pm 14^{\circ}$ and $\pm 5^{\circ}$ to the incident beam. Its close proximity to the 10°C water moderator renders it capable of high data rates; this makes it ideally suited for samples of small mass. The sample chamber can be operated under pressures as low as 5×10^{-6} torr and contains a two-stage, closed cycle refrigerator (Displex) capable of operating between 13 K and room temperature.

The Neutron Powder Diffractometer (NPD) is located 32 meters from the 10°C water moderator, and at the time these experiments were performed, used detectors at angles of $\pm 148^{\circ}$ and $\pm 90^{\circ}$. Provisions have been made to install additional detectors at $\pm 45^{\circ}$ and $\pm 20^{\circ}$. While its greater distance from the moderator sacrifices beam intensity, the resolution, in units of $\Delta d/d$, in the $\pm 90^{\circ}$ and $\pm 148^{\circ}$ banks are 0.25% and 0.15%, respectively. The NPD sample chamber also contains a Displex with a controller capable of producing temperatures ranging from 10 K to 380 K.

Figure 2.1 shows a typical cross section of a diffractometer (in this case, the NPD). The neutron beam enters from the left and impinges on the sample in the center of the circular area shown. The scattered neutrons move down argon-filled flight paths to the detectors, or are absorbed in borated wax shielding. The unscattered neutrons are absorbed in the beam dump at the right. The cross section of the HIPD has similar features.

Table 2.1: A summary of NiTi sample codes used for neutron diffraction

Code	Composition (weight percent)	Form	Was sample annealed?
A	54.9 Ni, 44.9 Ti, 0.15 impurities	6 wires	No
B	{99.9 [55 Ni - 45 Ti] - 0.1 Y}	machined rod	Yes
C	same as B	lathe turnings from B	No
D	same as B	lathe turnings from B	Yes
E	55 Ni, 45 Ti	electropolished rod	Yes

2.2 Samples and Procedures

2.2.1 The High Intensity Powder Diffractometer

Five different sample preparations were used during the two summers in which experiments were performed at LANSCE. A letter code was assigned to each to aid in their identification in later work, and a summary of these codes can be seen in Table 2.1. Sample A consisted of six NiTi wires, 20 mils in diameter and approximately 3.5 inches in length. The samples originated from TIMET heat V4609, and Hsu and Wechsler [58] and Wechsler *et al.* [59] discovered the composition of the wires to be 54.9 weight percent nickel, 44.9 weight percent titanium and 0.15 weight percent trace impurities, as determined by wet chemistry. Considering only Ni and Ti atoms, this gives a concentration of 49.9 atomic percent Ni, 50.1 atomic percent Ti. The wires were used in their as-received condition. Figure 2.2 shows the resistance versus temperature behavior of sample A upon cooling from 100°C to −20°C and upon heating back up to 100°C under low stress conditions. The arrows indicate the cooling and heating curves (compare Figure 2.2 to the nominal resistivity versus temperature curves in Figure 1.5 on page 29).

2.2.1.1 The HIPD sample holder Figures 2.3 and 2.4 along with Table 2.6 show the sample holder used for sample A during the 1989 experiments. Each of six NiTi wires (only two are shown at G in Figures 2.3 and 2.4) was passed through one of six small holes drilled in a hexagonal array in a Macor[1] disk (B), and endcaps (E) were laser-welded on both ends of each wire. The Macor disk was fastened with three sets of bolts (K) and nuts (J) to a Ledloy[2] weight (A) with a countersunk hole to accommodate the six endcaps; this provided the necessary weight to put the wires under tension during the diffraction experiments. Tables 2.2 and 2.3 show the masses producing the tensile stresses on the NiTi wires for the two stress levels used. Springs (D) attached to the endcaps on the top ends of the wires hooked into holes drilled in six brass screws (C) which were threaded into a second (upper) Macor disk. This second disk was suspended from an aluminum cap (P) by three threaded rods (L) and appropriately placed nuts. The aluminum cap fit on top of a quarter-inch-thick aluminum can (H), and two set screws (O) assured correct azimuthal alignment of the entire assembly within the can.

Four windows (I) were cut in the can to allow the incident, diffracted and unscattered beams to enter and exit the sample holder. A thin sheet of aluminized Mylar[3] was glued over these windows for the 1988 experiments and remained in place during the 1989 experiments. Also, some fiberglass pipe-wrap insulation was placed around the outside of the aluminum can for the 1989 runs. Next, an aluminum transition piece (Q) was fabricated to allow the can to mate to an existing mushroom-shaped

[1] Macor is the trade name for a machinable glass ceramic material.

[2] Ledloy is the trade name for a leaded steel alloy.

[3] Mylar is a trademark for a polyester produced in very thin, transparent sheets [1].

Table 2.2: Masses used to apply tensile stress to NiTi wires (low stress)

Object	Mass (grams)
lower endcaps	1.700
lower Macor disk	16.10
Ledloy weight	203.875
3 screws, 3 flat washers, 3 lock washers and 3 nuts	9.6214
Total mass	231.30
Stress = 1.87 MPa	

Table 2.3: Masses used to apply tensile stress to NiTi wires (high stress)

Object	Mass (grams)
initial mass from low stress case	231.30
attaching screw	2.734
lead weight	321.538
Total mass	555.57
Stress = 4.48 MPa	

attachment, which was secured to the warmer stage of the Displex on the HIPD. A locating slot (S) was cut in the fabricated piece to coincide with a pin on the "mushroom" to preserve correct sample alignment. The warmer stage of the Displex was kept at a constant temperature approximately equal to the boiling point of liquid nitrogen (77 K). A heater coil wrapped around the colder stage of the Displex (R) allowed its temperature to be set between about 13 K and room temperature.

In addition to placing the NiTi sample wires under tensile stress, provisions were also made to monitor their electrical resistance and temperature. Small lengths of nickel wire (F) were spot-welded between two ends of adjacent NiTi wires. By connecting the bottom of the first NiTi wire to the bottom of the second, connecting the top of the second to the top of the third and so on, the six wires were linked in electrical series. Additional leads at the ends of the first and sixth wires allowed the passing of an electrical current through the six NiTi wires. Two more similarly placed leads were used to monitor the voltage drop across the sample so its electrical resistance could be calculated. (The two current leads and two voltage leads are shown at M in Figures 2.3 and 2.4.) Two chromel-alumel (type K) thermocouples (the four thermocouple leads are shown at N in Figures 2.3 and 2.4) were also spot-welded on the upper and lower ends of one of the sample wires; it was assumed that the temperatures registered by these two thermocouples were representative of the temperatures of the other five samples.

All electrical leads passed through a hole in the aluminum cap (T) and then through a Lucite[4] lid on top of the sample chamber via a vacuum feedthrough connection. Of course the total resistance observed included not only that of the six

[4]Lucite is an acrylic plastic which may be molded into transparent sheets [1].

NiTi wires, but also that of the nickel wire connectors and their spot-welded joints. A small bead of epoxy cement was placed on each of the thermocouple joints and on the four current and voltage connections to improve their life-expectancy. While both thermocouples worked for the 1988 experiments, a mishap just before the 1989 runs rendered the bottom thermocouple inoperative for the subsequent runs.

2.2.1.2 Temperature and resistance data acquisition A data acquisition system was used to monitor the temperature and the resistance of the sample as a function of time. A DC power supply was connected in series with the NiTi sample wires and a one ohm standard resistor. The voltage drops across the sample wires and across the standard resistor and the voltages from the two thermocouples were sampled by a Hewlett-Packard (HP) Data Acquisition Controller, which was operated by a HP-85 Personal Computer. A computer program, written by R. D. Brown of the Los Alamos National Laboratory, controlled the sampling time of the data acquisition unit, calculated the resistance of the NiTi wires and temperatures of the upper and lower thermocouples, and stored these data on a floppy disk. After the run was completed, these data could then be printed out. A copy of this program may be found in Appendix A.

2.2.1.3 Temperature control To change the temperature of the samples two methods were used. First, to raise the temperature of the samples above the ambient temperature, the electrical current was increased, and the Displex was turned off. Second, for those experimental runs operating below room temperature the current was turned down to a minimal value and the Displex was turned on. The aluminum can, being in intimate contact with the warmer stage of the Displex and

being very near the colder stage, transferred heat away from the NiTi wires by conduction through the threaded rods and by radiation to the walls of the can. Since this was a very inefficient method of transferring heat, temperatures changed rather slowly. Adjusting the electrical current through the sample regulated the steady state temperature once it was reached.

While most data taken on the HIPD used the setup described above, four runs done during the summer of 1988 used a slightly different method to alter the temperature of sample A. In this configuration the three threaded rods, after passing through the aluminum cap, went through the Lucite lid resting over the opening of the sample chamber on the HIPD. These threaded rods were held in place by nuts above and below the Lucite lid so the aluminum can and its contents hung suspended from the lid. The aluminum transition piece did not exist at this time so no connections were made to the Displex below.

To provide the additional cooling required to bring the temperature of the NiTi samples slightly below the rather warm ambient temperature of the experimental hall, a quarter-inch-diameter copper tube, with somewhat of an L-shaped bend at the bottom, was brazed vertically to the outside of the aluminum can. The bend at the bottom brought the end of the copper tube just inside the bottom of the aluminum can which was then covered with aluminized Mylar, while the top of the copper tube protruded above the Lucite lid.

Dry helium gas, supplied by a pressurized tank and regulator, was allowed to pass through a coil of copper tubing immersed in a Dewar filled with liquid nitrogen. The cooled helium gas then flowed down through the copper tube attached to the aluminum can, up past the NiTi samples and out several small openings in the Lucite

lid. Since the HIPD sample chamber was not vacuum-tight, the diffraction data were taken at atmospheric pressure.

2.2.1.4 HIPD experiment summaries Beam time allowed four diffraction runs on the HIPD during the summer of 1988, and Table 2.4 summarizes the conditions and run numbers for the experiments done on the HIPD. The first run (number 526) was designed to see the high temperature phase of the NiTi wires. By using ohmic heating within the wires, their temperature was increased so the top thermocouple (T_{top}) read between 96.8°C and 101.3°C during diffraction data acquisition while the bottom thermocouple (T_{bottom}) ranged from 77.1°C to 81.1°C. Figures 2.5 and 2.6 show the variations of sample resistance and temperature during the diffraction experiment. It should be noted that the following graphs in which time is the abscissa, do not begin at zero seconds. This is because the temperature and resistance data acquisition system was started up before neutron data were started. These graphs show the information taken only while diffraction data were obtained.

Upon completion of this run, cooled helium gas as described above, cooled the wires to temperatures ranging from 26.3°C to 28.0°C for T_{top} and 30.9°C to 33.2°C for T_{bottom}. This put the sample on the high-temperature side of the anomalous resistivity peak. See Figures 2.7, 2.8 and 2.9 for the resistance and temperature data taken during this run (number 527). Notice that in Figure 2.8 T_{bottom} is higher than T_{top} which is opposite to the behavior seen in Figure 2.5. This may be due to the cooled helium gas passing more directly past the top of the wires while being somewhat blocked from the bottom portion by the Ledloy weight. Before the experiment could be completed, however, there was an interruption in neutron beam

Table 2.4: Experiments performed on the HIPD (Sample A used for all runs)

Date	Run Number	Stress Level	Approximate Temperature in $^{\circ}C(K)$
16Jul88	526	Low	99 (372)
16-17 & 23-24Jul88	527 & 530	Low	29 (302)
24Jul88	531	Low	27 (300)
7Aug89	704	Low	104 (377)
7-8Aug89	705 & 706	Low	16.8 (290)
8-9Aug89	707 & 708	High	19.9 (293)
17-18Aug89	709	High	33.7 (307)[a]
18-19Aug89	710	Low	33.2 (306)[a]

[a] Following heating from -34°C.

production. Therefore, after the diffraction data were saved, the sample was allowed to heat back up to room temperature. The experiment was continued one week later (run number 530). Before diffraction data acquisition was resumed, the sample was heated to approximately 100°C and cooled to about the same point on the resistivity curve as had previously been obtained. During this time, T_{top} ranged from 27.0°C to 33.0°C while T_{bottom} ranged from 29.8°C to 34.5°C. Since both runs 527 and 530 were taken at approximately the same position on the resistance curve, the diffraction data from these two runs were combined into a single data set and analyzed as such.

When data acquisition was completed for run 530, the current through the wires was decreased to allow the temperature to reach the low-temperature side of the resistivity peak. A relatively brief set of data was obtained under these conditions. For this run (number 531) T_{top} varied between 25.8°C and 27.8°C while T_{bottom} varied between 25.7°C and 28.0°C. Figures 2.10, 2.11, 2.12 and 2.13 show the resistance and temperature information for both diffraction runs 530 and 531. Again, notice

that $T_{bottom} > T_{top}$.

During the summer of 1989 seven more diffraction runs were done on the HIPD using sample A and the experimental setup described above. The first set of data (run number 704) was again taken in the sample's austenitic region to see if any differences between the 1988 and the 1989 experiments could be ascertained. Refer to Figures 2.14 and 2.15 for temperature and resistance information during this run. They show T_{top} ranged from 103.8°C to 106.1°C. (For all 1989 runs, T_{top} was the only thermocouple available.) Next, the Displex was used to cool the wires below room temperature to the low side of the resistivity peak, and the electrical current through the sample was used to hold the temperature at its desired value. Since the wires cooled rather slowly, the current had to be continuously monitored and adjusted to maintain a constant temperature. Diffraction run number 705 was taken under these conditions.

After it appeared the sample had reached thermal equilibrium, the equipment was allowed to operate without additional adjustments made to the current. With the power supply operating unsupervised, it was decided to end run 705 and immediately begin a new diffraction data run, 706. This would insure that at least part of the diffraction data would have been acquired under the desired experimental conditions in the event the temperature of the wires changed considerably during this unsupervised period. However, at the end of run 706 it appeared the temperature had not changed significantly. For this reason, the diffraction data from runs 705 and 706 were combined into a single data set, and refinements were performed on this combined set. T_{top} ranged between 14.6°C to 17.6°C during this combined data set. Figures 2.16, 2.17 and 2.18 show the conditions for both runs 705 and 706.

Similar experimental conditions existed for runs 707 and 708 except the lead weight was attached to the Ledloy weight, and the vertical position of the wires had to be raised to account for the additional stretching of the springs at the tops of the wires. Again, the wires were heated into their austenitic region (about 100°C), cooled with the Displex to the low-temperature side of the resistivity peak, and held at the desired temperature by adjusting the current through the wires. The temperature of the samples was adjusted by changing the current as required during run 707; run 708 ran unsupervised. Since the temperature appeared fairly constant over both runs (see Figures 2.19, 2.20 and 2.21), the diffraction data were again merged into a single data set. In this combined data set, T_{top} ranged from 18.5°C to 20.2°C.

The last two diffraction experiments done on the HIPD were designed to observe the martensitic phase alone. At first it was thought that the temperature of the samples would have to remain well below M_f to assure the existence of a single phase sample during the diffraction work. However, due to hysteresis effects, NiTi remains in the martensitic phase at higher temperatures once it has been cooled below M_f (see Figure 1.5, page 29). To be sure A_s was indeed above room temperature, the wires were heated from room temperature to about 100°C. This showed the transformation on heating to begin around 36°C according to the resistance versus temperature graph (Figure 2.22). Since this was done just prior to the run 709, it is believed that Figure 2.22 gives a relatively good indication of the value of A_s during the last two diffraction runs. The wires were then cooled to about −34°C in a vacuum chamber external to the HIPD, using a Displex apparatus in the laboratory similar to the one in the HIPD. When the samples returned to room temperature, they were assumed to be single phase martensite. The wires were replaced in the

HIPD sample chamber, and diffraction runs 709 and 710 were done under high and low stress levels, respectively. Since the Displex temperature read 33.6°C and 33.2°C for runs 709 and 710, respectively, the assumption that the samples remained below A_S seems reasonable.

2.2.2 The Neutron Powder Diffractometer

2.2.2.1 Samples Because of the relatively low incident neutron intensity at NPD, the NiTi wires used on the HIPD would have resulted in prohibitively long exposure times due to their small mass. For this reason, and since the holding device for sample A was tailored to the HIPD sample chamber, different samples were used on the NPD (see Table 2.5). These samples were placed in a thin-walled vanadium can with a stainless steel lid held in place by four screws. The outside of the lid contained a threaded hole which screwed onto the colder stage of the Displex in the NPD sample chamber. By turning the refrigerator compressor off and increasing the current through the heater windings on the Displex head, the sample could be brought to a maximum temperature of 380 K.

Table 2.5: Experiments performed on the NPD

Date	Run Number	Sample Code	Approximate Temperature in °C (K)
28Jun89	266	B	~ 27 (~ 300)
29Jun89	267	B	-263 (10)
	268	B	~ 27 (~ 300)
1Jul89	269	C	107 (380)
	270	C	97 (370)
	271	C	87 (360)
	272	C	77 (350)
	273	C	67 (340)
	274	C	57 (330)
	275	C	47 (320)
	276	C	47 (320)
	277	C	37 (310)
13Jul89	282	D	67 (340)
	283	D	107 (380)
	284	E	107 (380)
	285	E	87 (360)
	286	E	67 (340)
	287	E	47 (320)
	288	E	27 (300)
	289	E	7 (280)
	290	E	-33 (240)
	291	E	-73 (200)
	292	E	107 (380)
	293	E	97 (370)
	294	E	87 (360)
	295	E	77 (350)
	296	E	67 (340)
	297	E	57 (330)

The composition of sample B was {0.999 [0.55 Ni - 0.45 Ti] - 0.001 Y} where all values are weight fractions. The form of the sample was a cast rod which was machined to a smaller diameter on a lathe, cleaned with a reagent of 18% H_2O_2, 4.8% HF and 77.2% H_2O (volume percent) and annealed for 24 hours at 700°C at 10^{-6} torr. When the rod was machined, the lathe turnings were saved, washed in an ultrasonic cleaner, and rinsed first in water then in acetone. The turnings were used in their unannealed, cold-worked condition and coded sample C. These same turnings, after being used for neutron diffraction work, were annealed for 24 hours at 700°C at 10^{-6} torr and coded sample D. The fifth sample-code E-was in the form of a rod which had been annealed and electropolished. Table 2.1 summarizes the samples used.

2.2.2.2 NPD experiment summaries Diffraction data were taken on sample B at room temperature, 10 K and again at room temperature. Upon completion of the second room temperature run, it was decided to track the martensitic transformation in the sample as it cooled. To accomplish this, the rod had to first be heated into its austenitic phase. By using the heater coils on the Displex, the sample was warmed to 380 K, which should have put it in the high temperature, austenitic phase. After some preliminary diffraction patterns were taken (which were not saved), it was found that the rod was still in the martensitic phase.

One explanation for this may be the fact that the thermocouple was not attached to the sample itself but to the Displex head above the sample. Therefore, the indicated temperature of 380 K may not have been the actual temperature of the sample. However, it still seems unlikely that its temperature was considerably cooler than 380

K, given the fact that the Displex head was held at 380 K for at least one hour, and the vanadium can was quite hot to the touch when the specimen was removed from the NPD sample chamber. In addition, the rod rested on some vanadium foil, which put it in direct contact with the stainless steel lid connected, in turn, to the Displex head. Nevertheless, the observed diffraction pattern was the monoclinic structure of martensite. Since 380 K was the maximum temperature allowed on the Displex, it was decided to use the remaining beam time on another sample.

The unannealed lathe turnings (sample C) were put into the vanadium can, placed on the NPD Displex and heated to 380 K. The diffraction pattern for this sample surprisingly revealed the CsCl pattern of austenite. The pattern was surprising; because the residual stresses, no doubt present from cold working during machining, should have produced some stress-induced martensite. The data acquisition system was then programmed to take diffraction data for approximately 1.5 hours, halt data acquisition and save the data set, cool the sample 10 K, wait 30 minutes for the sample to equilibrate, and begin the next run.

When the sample reached 320 K some martensite peaks began to appear in the diffraction pattern so the sample was reheated, held at 380 K for approximately 15 minutes and cooled back to 320 K with the Displex. The data acquisition system was programmed to run overnight and continue to take data in 10 K steps to about 280 K. Unfortunately, the LAMPF proton beam was intermittent throughout the night so only runs at 320 K and 310 K were completed (two runs were inadvertently done at 320 K). At this point another user was scheduled to use the NPD so no more runs were started. Also, since none of these data sets lasted for more than about 1.5 hours, the amount of significant information contained in them did not warrant

a detailed analysis.

Two diffraction data sets were collected on sample D (annealed lathe turnings). The first data at 340 K revealed the martensite pattern. The annealed lathe turnings were heated to 380 K in hopes that they would transform into the high temperature phase. Although some cubic reflections were seen in addition to the monoclinic pattern, the sample had obviously not transformed completely. Again, the relatively short exposure time on these two runs made them of limited use.

In a final effort to monitor the progress of the martensitic transition in NiTi, diffraction experiments were done on a fifth specimen (sample E). First, the Displex heated the electropolished rod to 380 K and a 1.5 hour data set was taken. Similar data were taken after the temperature controller decreased the sample temperature in 20 K increments down to 280 K and then in 40 K increments to 200 K. At each temperature, 30 minutes elapsed before the diffraction data acquisition started to assure temperature equilibrium. All eight runs showed the martensitic pattern.

Since the Displex head's maximum temperature was apparently not high enough to heat sample E into the austenitic phase, a different approach was used. The vanadium can, with the sample inside it, was taken off the Displex head and held on a steady surface. A heat gun then blew hot air past the can while its temperature was measured with a digital thermometer. The maximum temperature recorded was 220°C (493 K). While the sample can was still hot, it was put back on the Displex head (which was being held at 380 K) and placed back in the NPD. The usual automatic mode was then implemented in 10 K increments down to 330 K. At 380 K the sample was nearly all austenite with some small martensite peaks. As the sample cooled, the austenite peaks decreased, and the martensite peaks increased in

intensity. It is believed that if the heat gun would have been held in place longer, all of the sample material would have transformed to austenite. The martensitic transformation could then have been followed more carefully and in smaller temperature increments.

2.3 Summary

Several neutron diffraction experiments were performed at LANSCE during 1988 and 1989. While the experiments performed on the HIPD were of primary concern, information derived from work done on the NPD contributed additional information about the crystal structures present in nearly equiatomic nickel-titanium. The wire specimens used on the HIPD were thermally cycled under two different tensile stresses, and their resistance, as a function of temperature, was used to monitor the martensitic transformation. Also several other experiments were performed on the NPD to observe the martensitic phase in a cast, yttrium-doped NiTi rod and to attempt to track the martensitic transformation upon cooling in other NiTi samples.

Table 2.6: Legend for Figures 2.3 and 2.4

A	Ledloy weight
B	2 circular Macor disks
C	6 brass screws (only 2 shown)
D	6 springs (only 2 shown)
E	12 endcaps (only 4 shown)
F	5 Ni wire connections (only 1 shown)
G	6 NiTi wires (only 2 shown)
H	cylindrical aluminum can
I	4 neutron beam windows (only 2 shown)
J	13 nuts (only 5 shown)
K	bolt
L	3 threaded rods (only 1 shown)
M	2 current and 2 voltage leads
N	4 leads for 2 thermocouples
O	2 set screws (only 1 shown)
P	aluminum cap
Q	aluminum transition piece
R	colder stage of Displex head
S	locating slot
T	hole for current, voltage and thermocouple leads

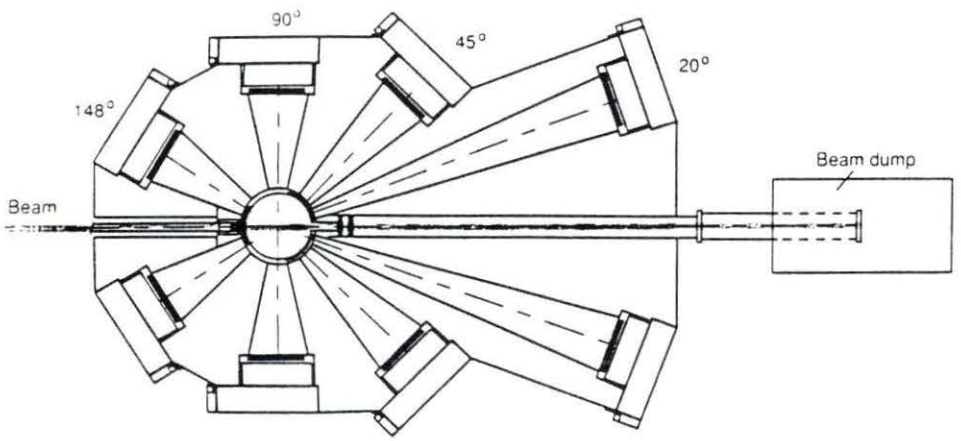

Figure 2.1: Beam-level cross section of the NPD showing the incident neutron beam entering from the left [56]

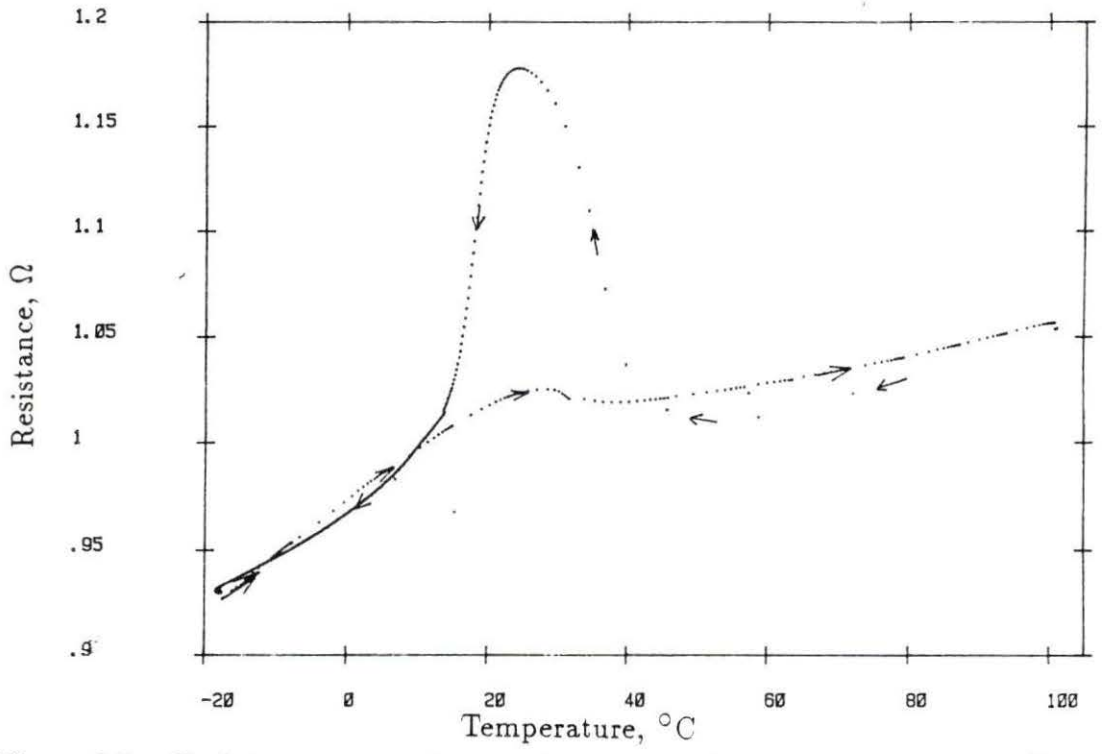

Figure 2.2: Resistance versus temperature curves for sample A upon cooling and upon heating (see arrows)

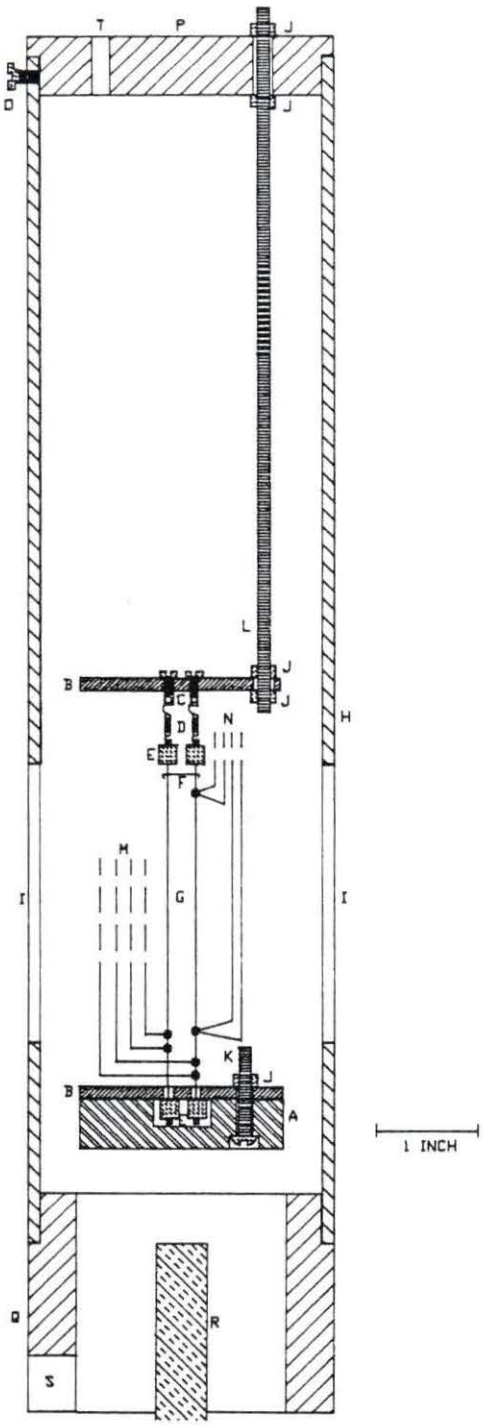

Figure 2.3: Sample holder used during 1989 experiments on the HIPD (See Table 2.2 for legend)

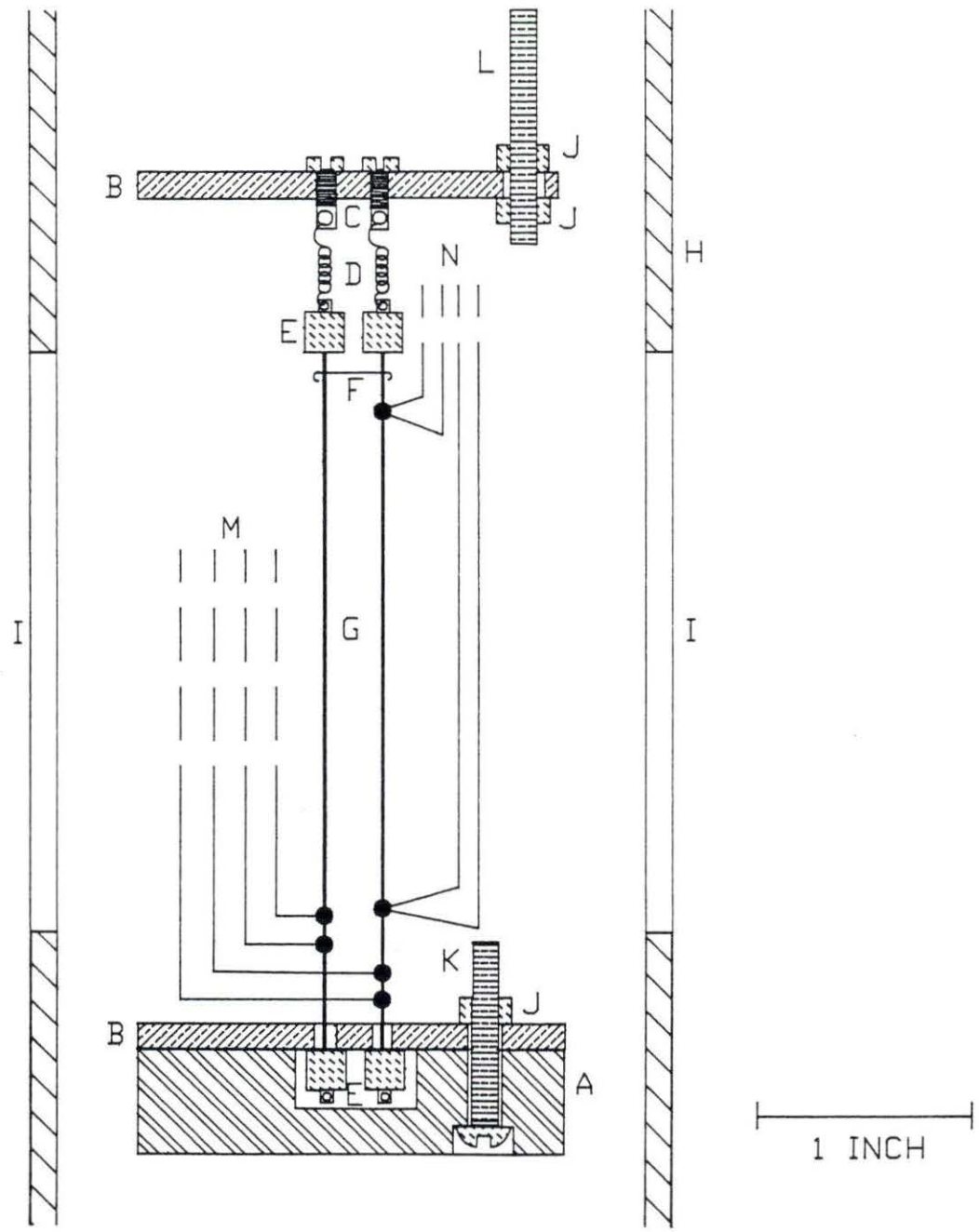

Figure 2.4: Enlarged view of the central portion of Figure 2.3 (See Table 2.2 for legend)

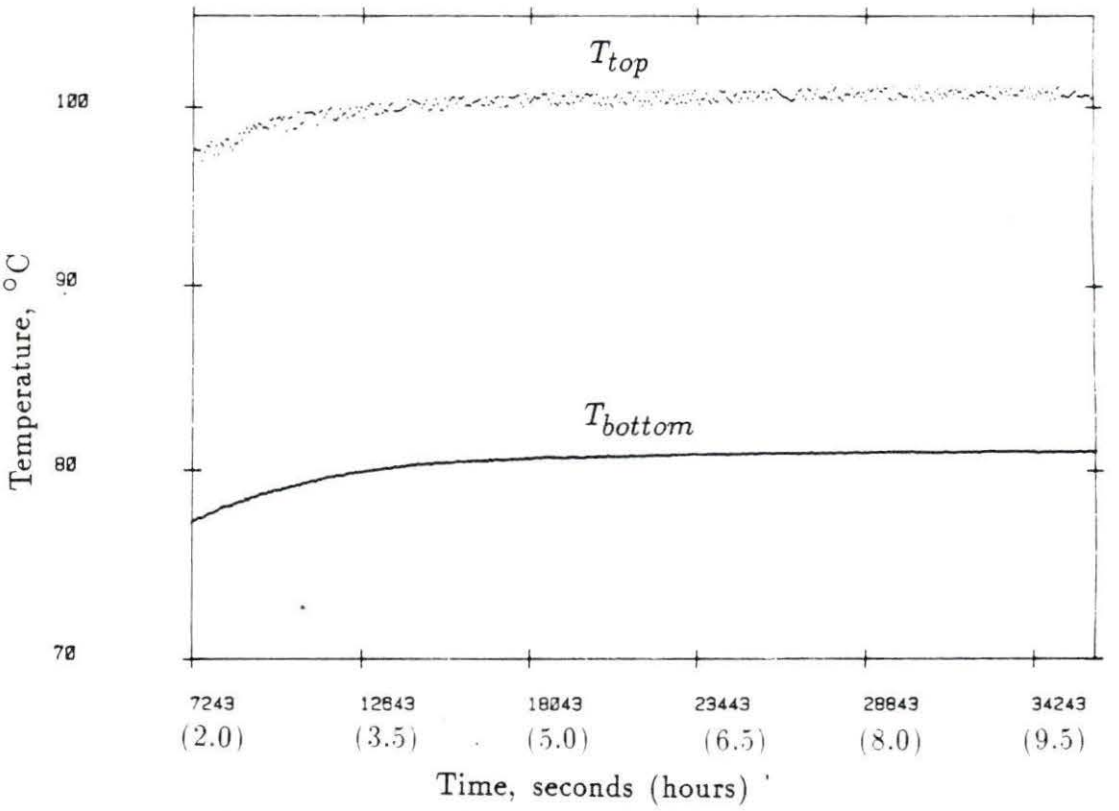

Figure 2.5: T_{top} (upper curve) and T_{bottom} (lower curve) versus time for run 526

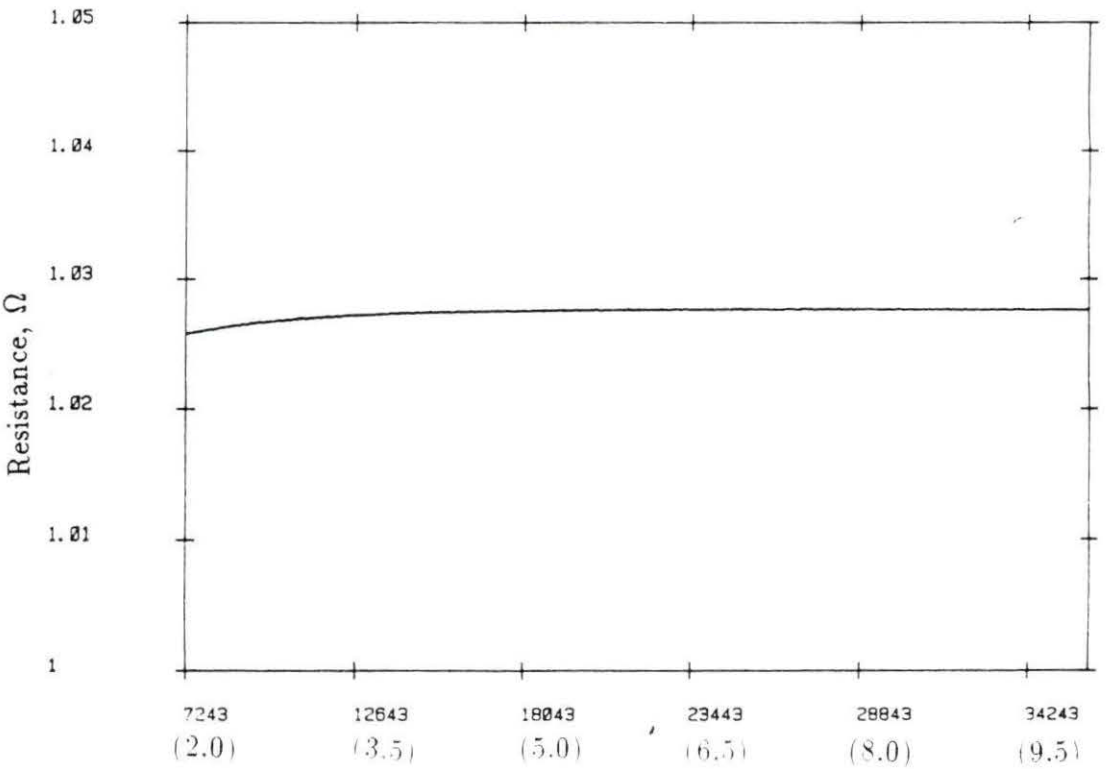

Figure 2.6: Resistance versus time for run 526

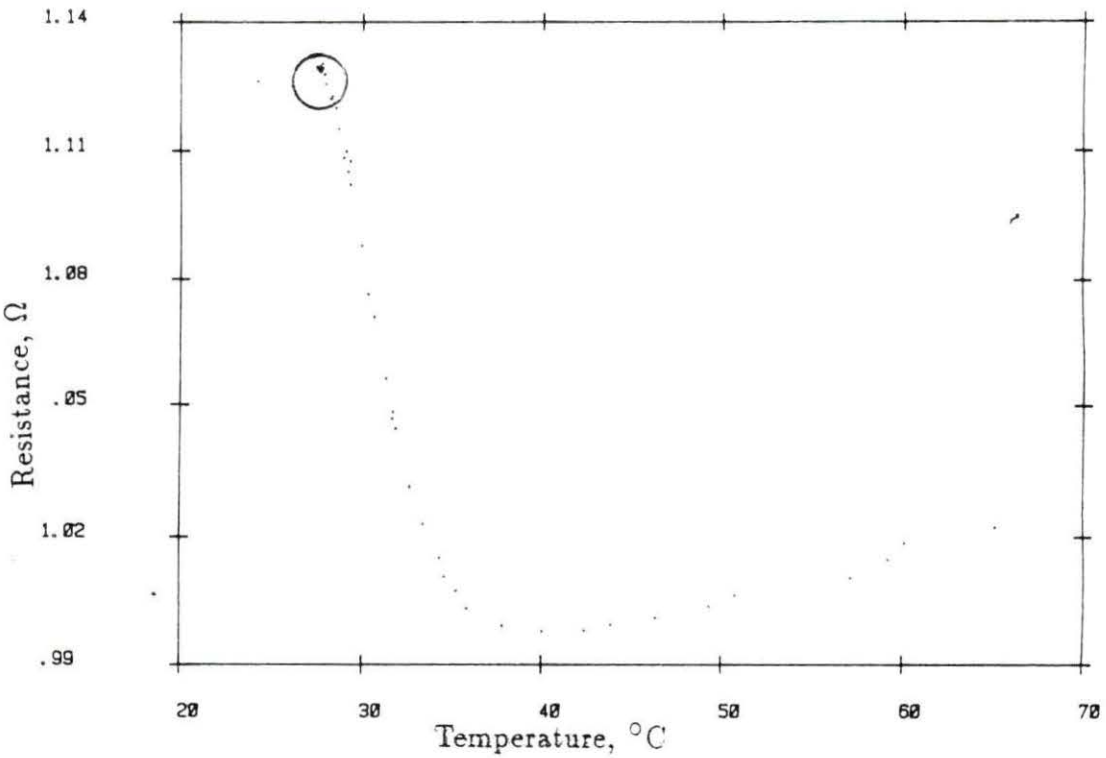

Figure 2.7: Location (circle) of run 527 on the graph of resistance versus temperature

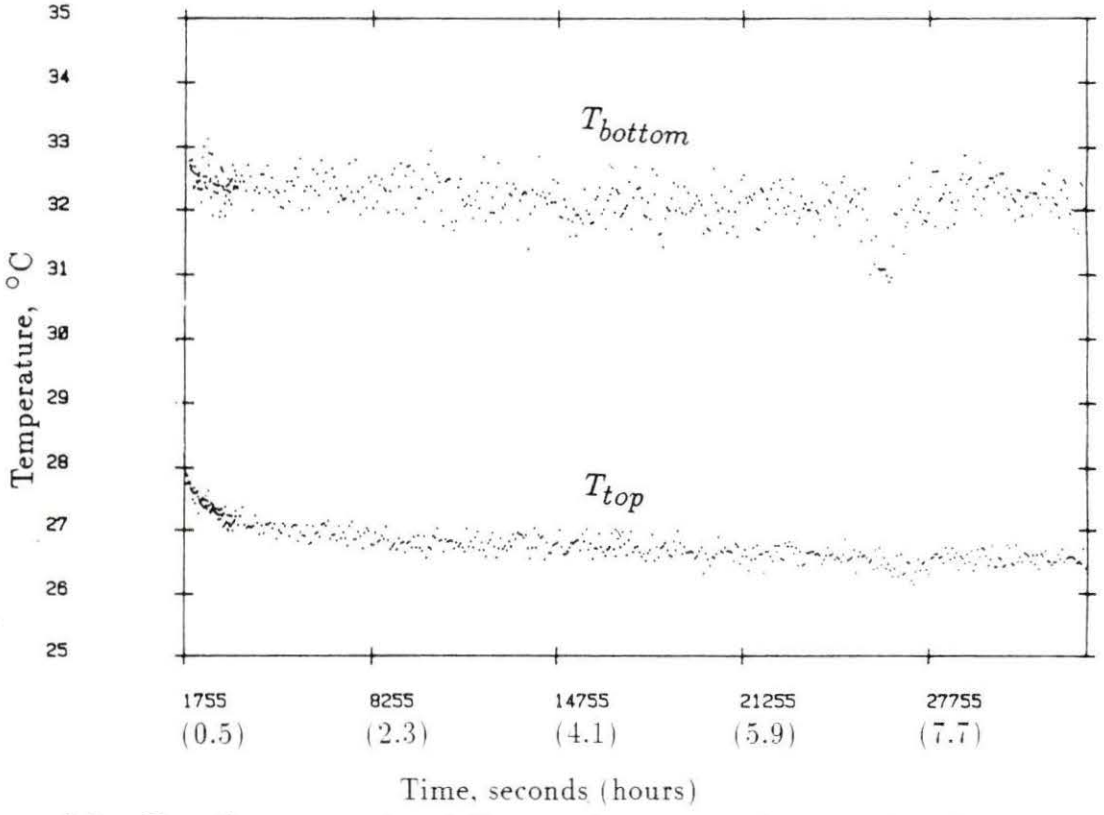

Figure 2.8: T_{top} (lower curve) and T_{bottom} (upper curve) versus time for run 527

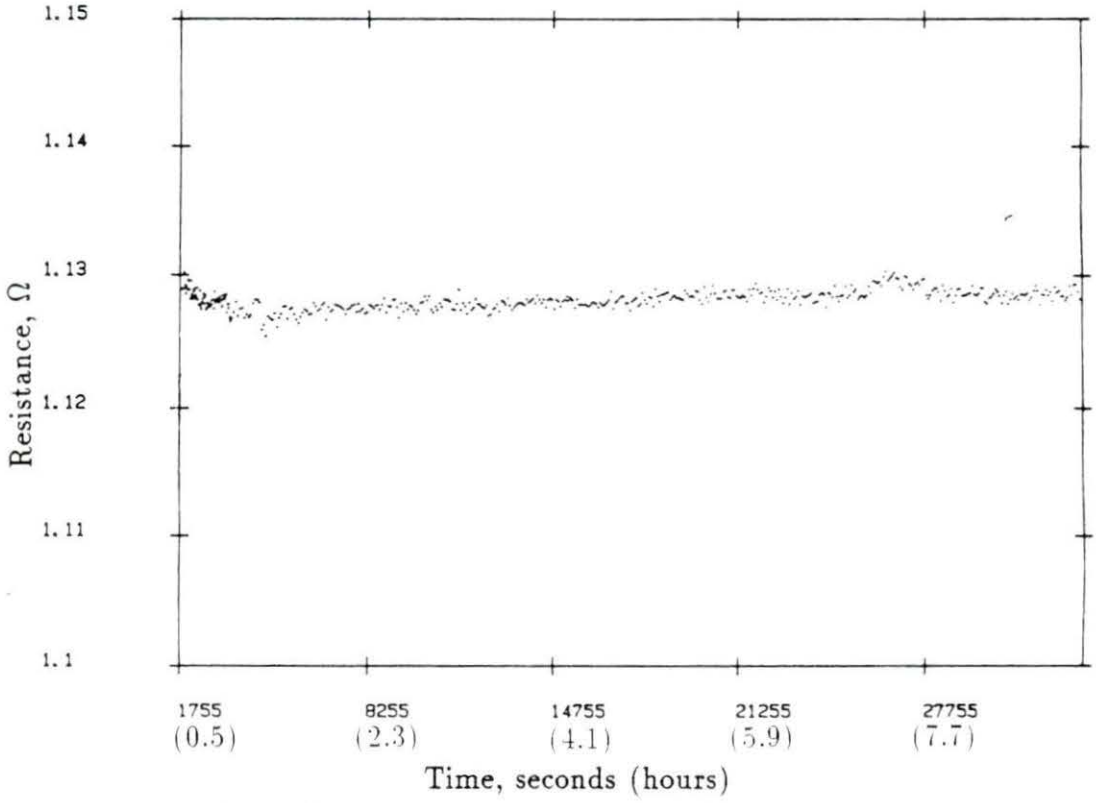

Figure 2.9: Resistance versus time for run 527

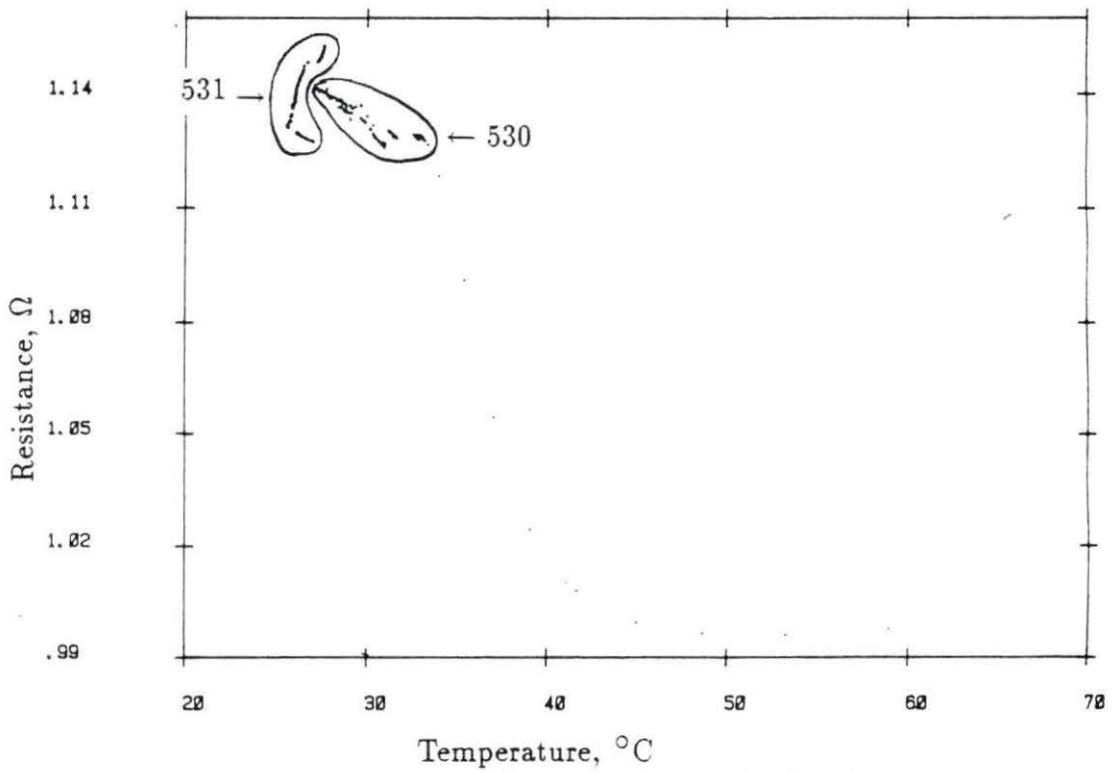

Figure 2.10: Location of runs 530 and 531 on the graph of resistance versus temperature on cooling

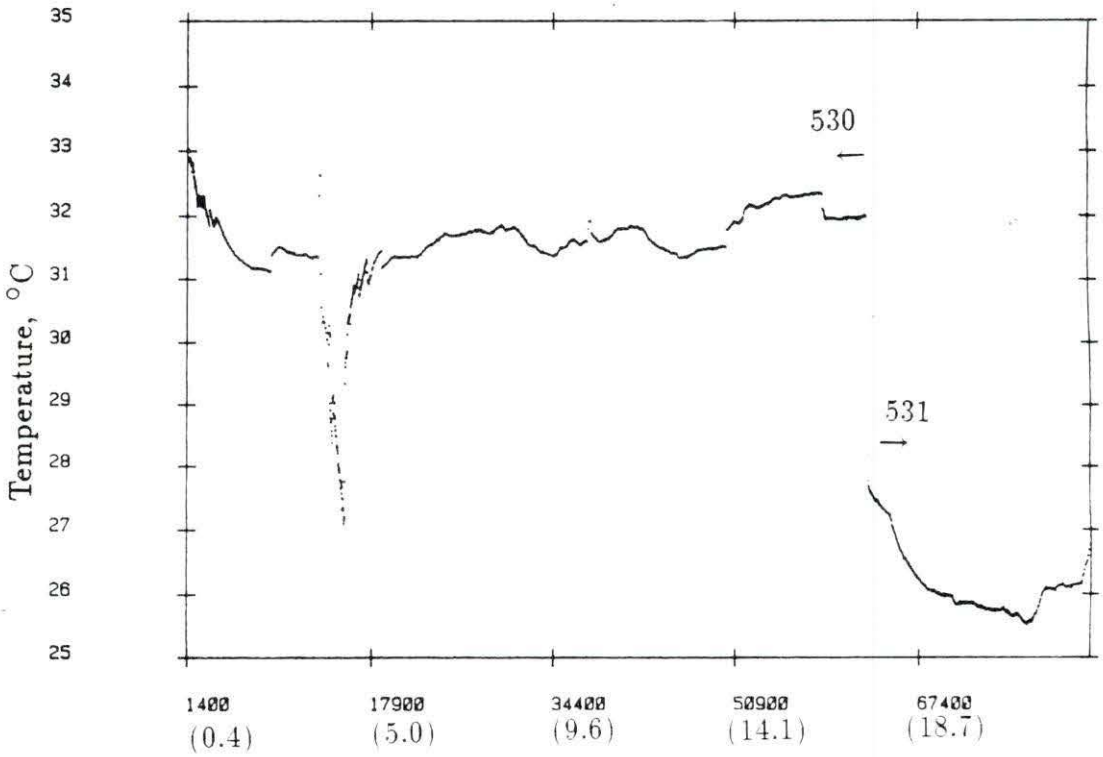

Figure 2.11: T_{top} versus time for runs 530 and 531

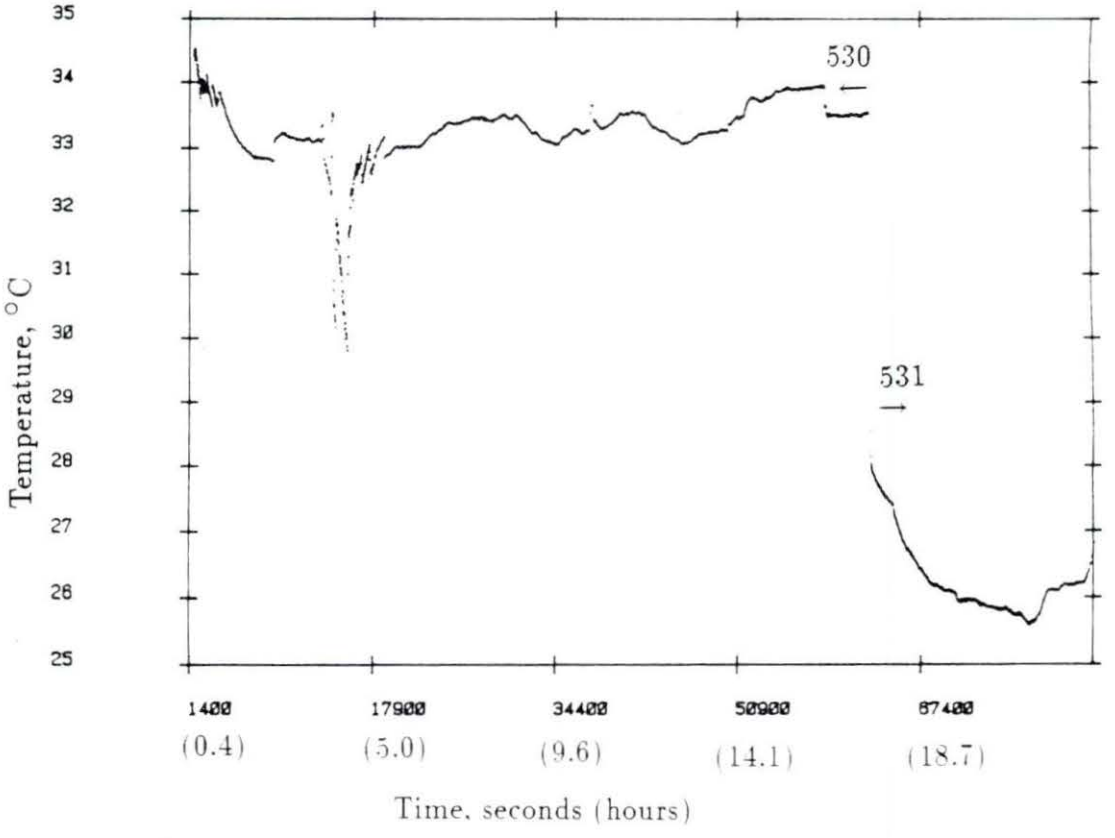

Figure 2.12: T_{bottom} versus time for runs 530 and 531

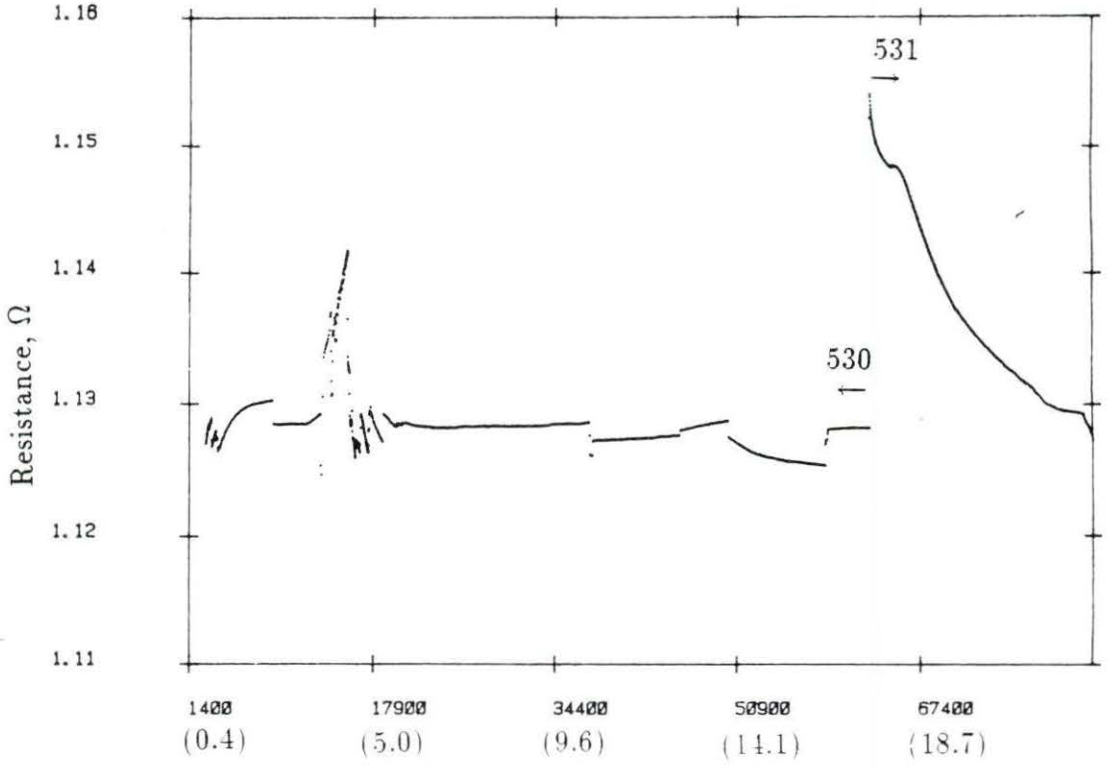

Figure 2.13: Resistance versus time for runs 530 and 531

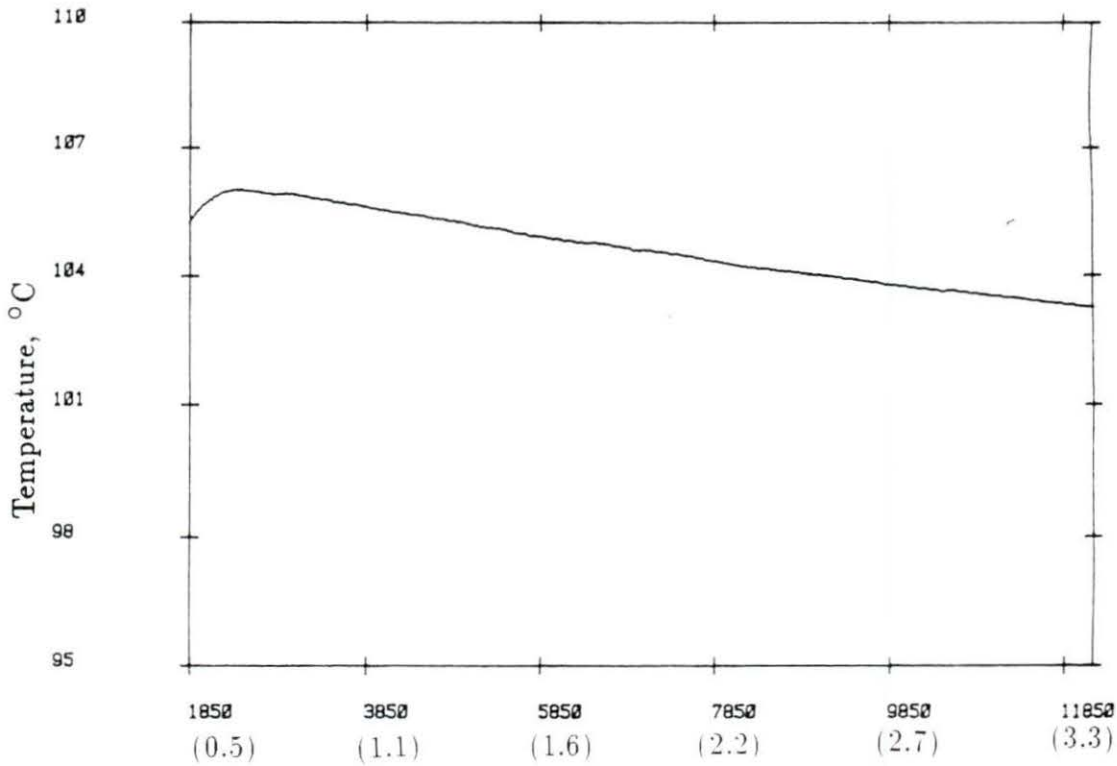

Figure 2.14: T_{top} versus time for run 704

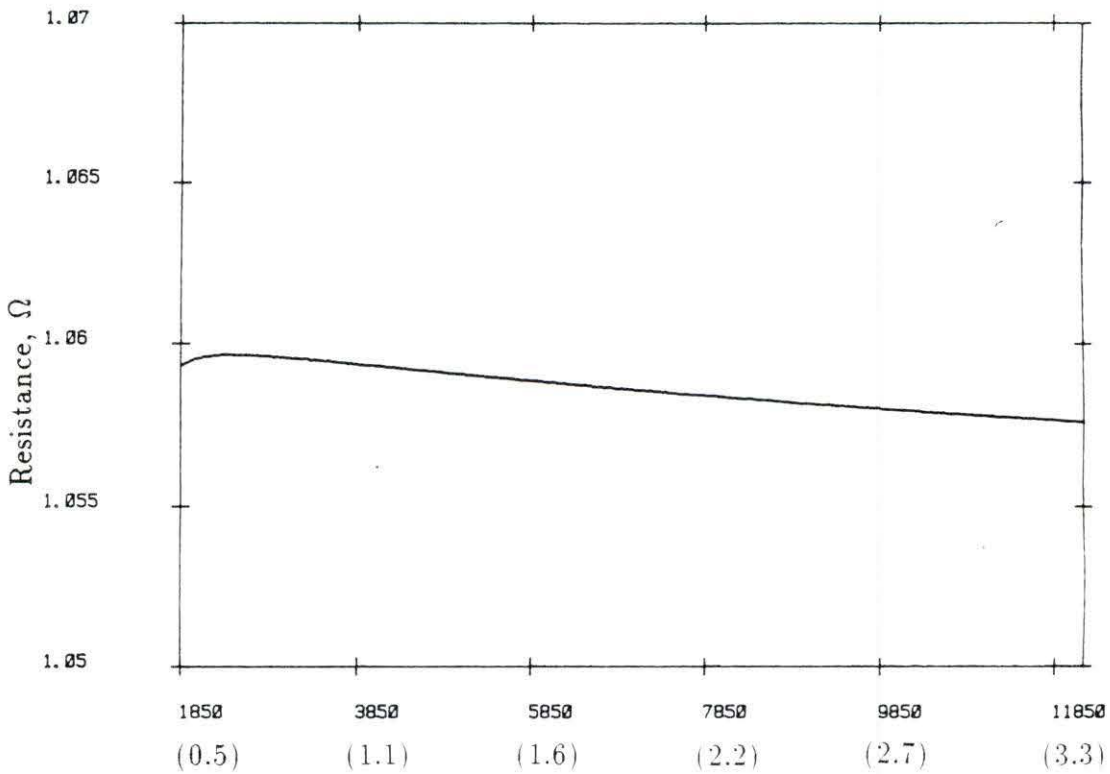

Figure 2.15: Resistance versus time for run 704

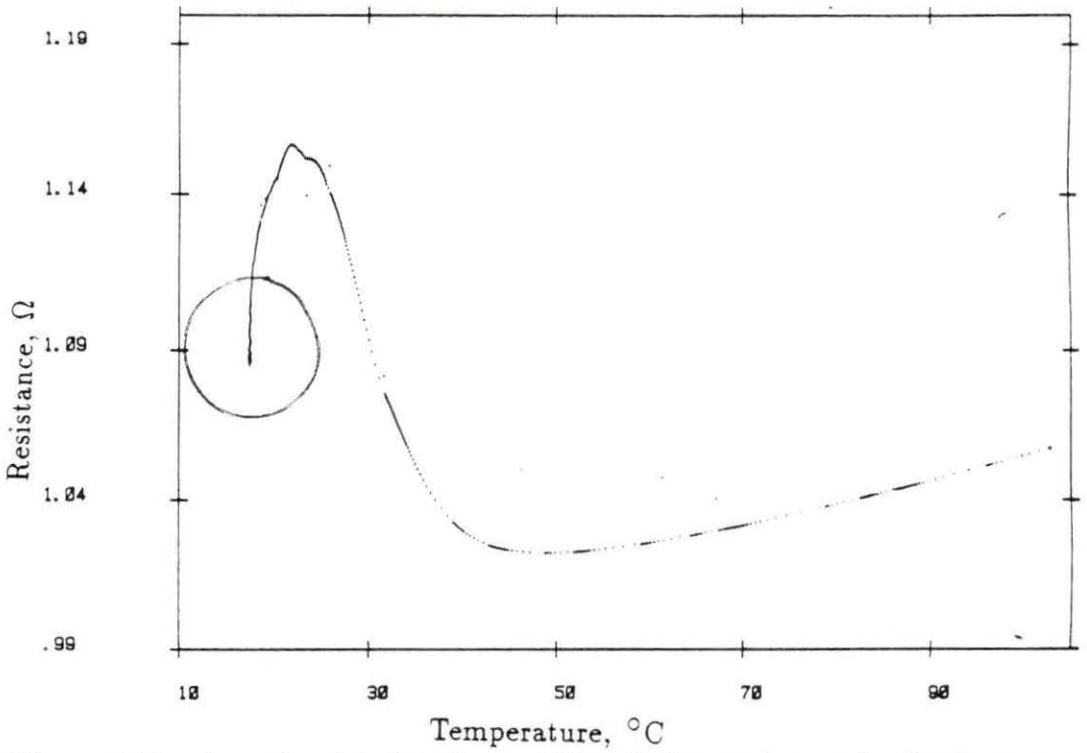

Figure 2.16: Location (circle) of runs 705 and 706 on the graph of resistance versus temperature

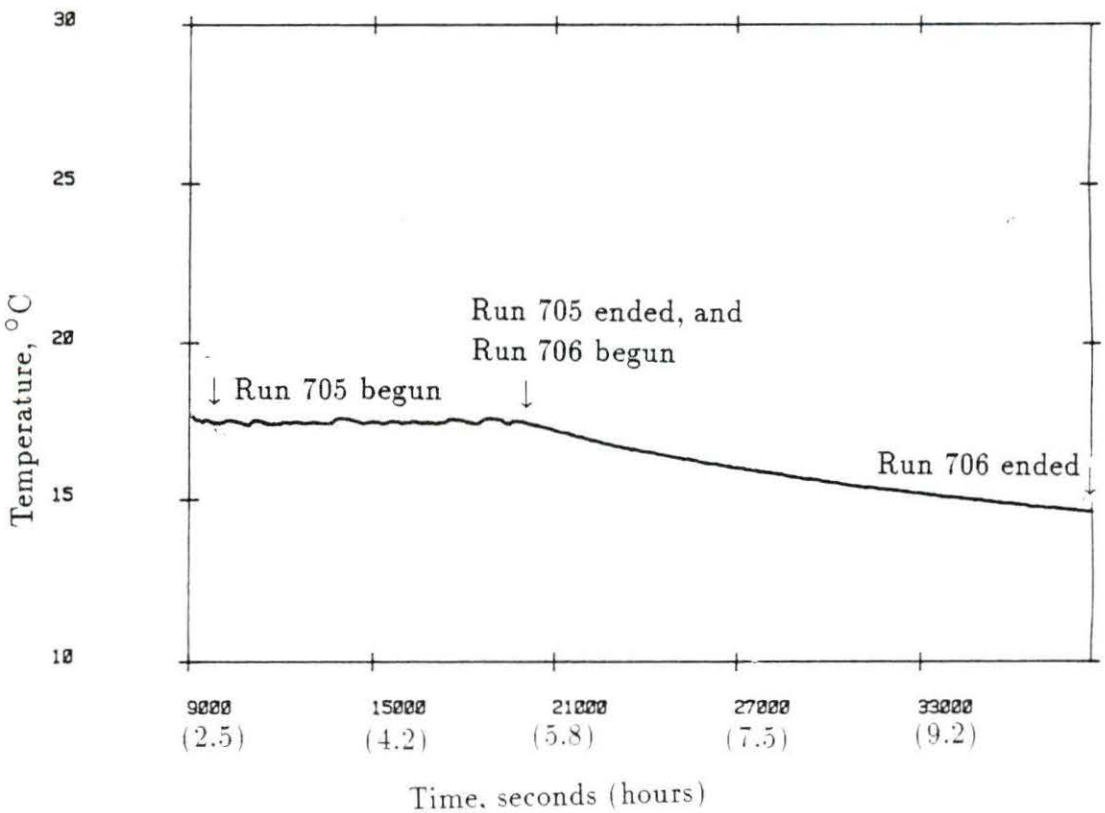

Figure 2.17: T_{top} versus time for runs 705 and 706

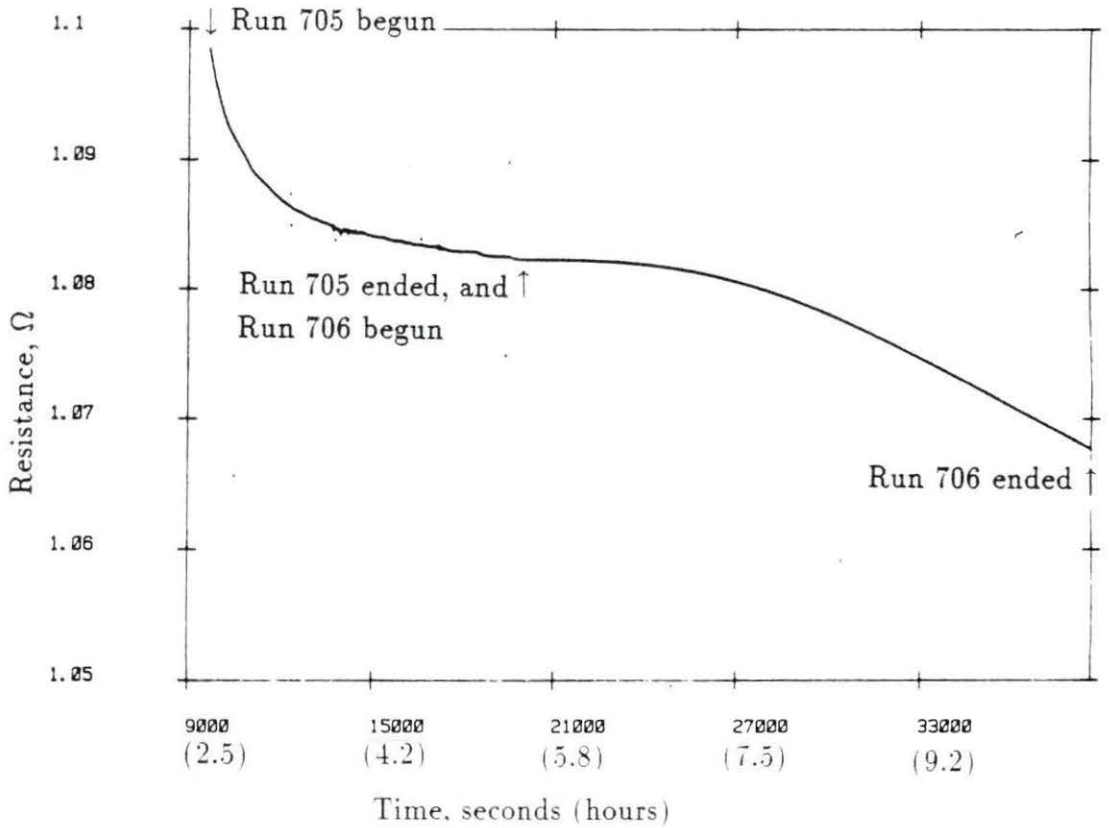

Figure 2.18: Resistance versus time for runs 705 and 706

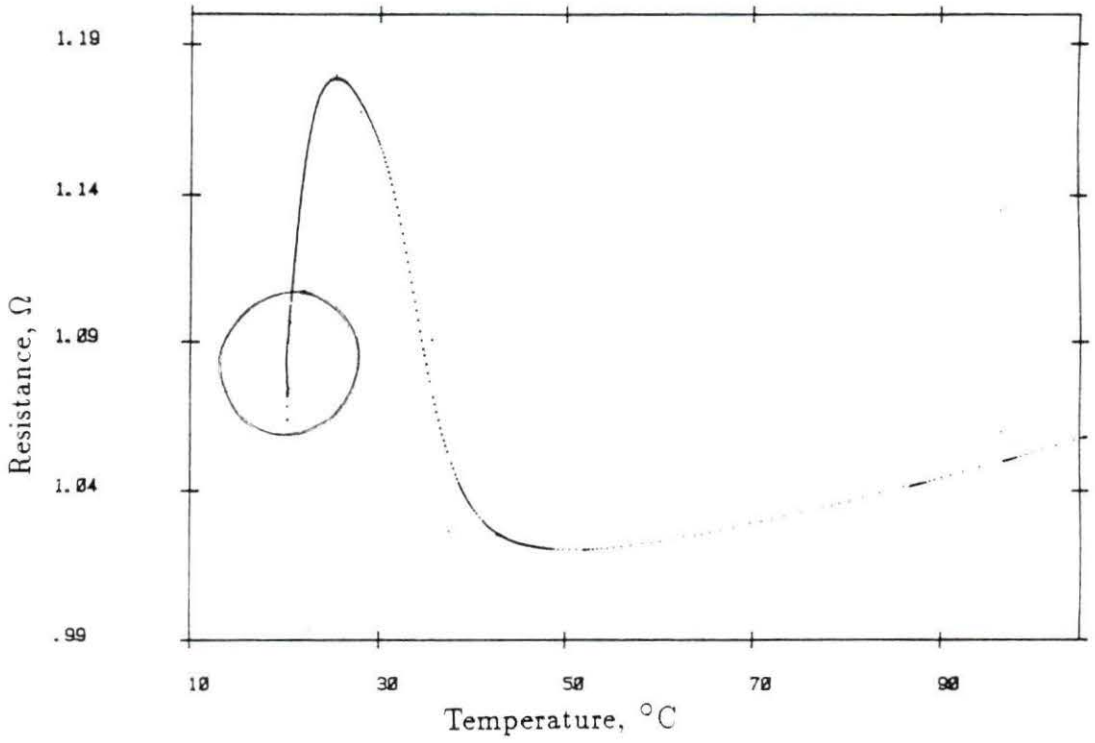

Figure 2.19: Location (circle) of runs 707 and 708 on the graph of resistance versus temperature

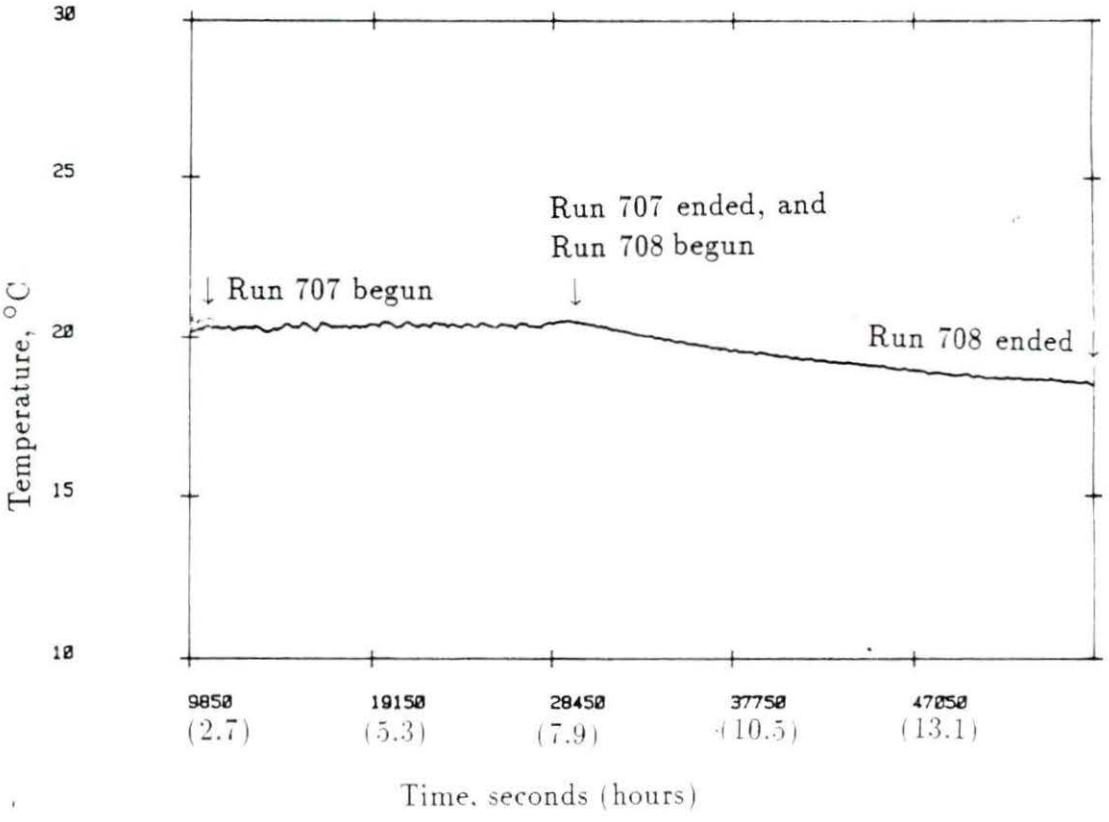

Figure 2.20: T_{top} versus time for runs 707 and 708

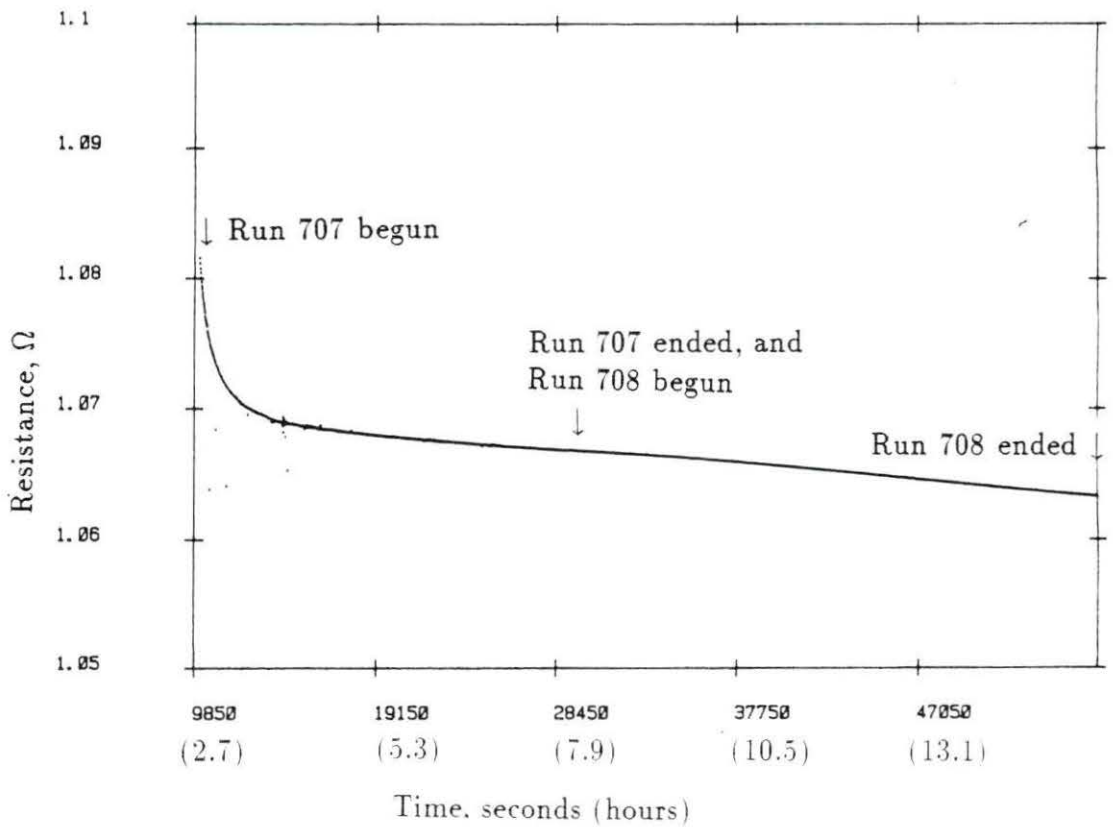

Figure 2.21: Resistance versus time for runs 707 and 708

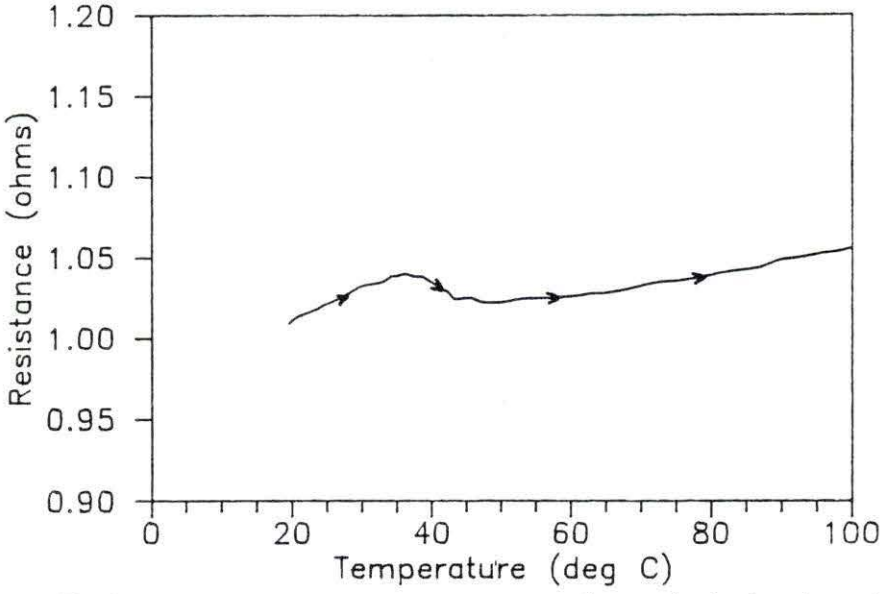

Figure 2.22: Resistance versus temperature curve of sample A showing A_s equal to about 36°C

3. GENERALIZED STRUCTURE ANALYSIS SYSTEM

The Generalized Structure Analysis System (GSAS) is a suit of programs designed to process and analyze neutron and x-ray diffraction data obtained from powder or single crystal samples and was written by A. C. Larson and R. B. Von Dreele at the Los Alamos National Laboratory [60]. In this study, GSAS was used to do Rietveld refinements [61] [62] on the TOF neutron diffraction data from the experiments described in Chapter 2. A Rietveld refinement uses a least squares fitting of a calculated profile to an observed diffraction profile without the use of integrated intensities [63]. It is superior to methods using total integrated intensities because it allows the maximum amount of information to be extracted from profiles where adjacent reflections overlap by taking advantage of the fact that a Bragg reflection may be very well described by a Gaussian function. GSAS uses a nested series of menus that allows the user to enter the crystallographic information known about the sample. Once GSAS has been given the necessary preliminary information, a set of batch jobs is run to calculate appropriate d-spacings for Bragg reflections, and a model spectrum is fit to the observed data by least squares refinement techniques. Finally, graphs of the observed and calculated spectra in each detector bank as well as the values of the refinement parameters are obtained. GSAS has the capability to fit multiple data sets (i.e., several detector bank histograms) on the same sample

and multiple phases within a sample.

3.1 Overview

After the completion of a diffraction experiment at LANSCE, the data from each detector bank are stored in an archiving system. By using a GSAS program, FSTBUSBIN, these data can then be retrieved and put into a format that can be read by other GSAS refinement and plotting routines. EXPEDT is an interactive editor, which allows the user to set program controls and structural and nonstructural data. With EXPEDT, the Hermann-Mauguin symbol for the space group must be entered for each phase assumed to be present in the sample. In addition, the lattice parameters of the unit cell, the types of atoms present and their positions within the unit cell, the fractional occupancy of each atom site and the value of the isotropic or anisotropic temperature factors for each atom are entered by the user. By using the interactive characteristic of EXPEDT, the analyst also decides which physical parameters (such as those due to extinction, absorption and preferred orientation) will be allowed to vary in the next least squares refinement. In addition, the default values of these parameters provided by GSAS may be used as initial guesses, or better estimates may be entered by the user.

After all known crystallographic information about the sample as listed above has been entered using EXPEDT, the batch oriented program, POWPREF, can be run. POWPREF generates the allowed reflections and their d-spacings according to the lattice parameters and space group of each phase. Also, the channel position and width, incident intensity, refinement weight and intensities contributed from nearby reflections are calculated for each channel.

When the data in each histogram have been used by POWPREF, the next GSAS program, GENLES, is usually run. GENLES is also batch oriented and computes the calculated diffraction profile by a least squares routine. POWPREF and GENLES are the primary tools used in determining the values of the physical parameters of the samples discussed below.

Once POWPREF and GENLES have been used, the observed and calculated diffraction profiles may be plotted using the graphics program, POWPLOT. This plotting routine is also capable of displaying reflection markers and difference curves. GSAS contains many other programs, which will not be discussed here. The reader may refer to Larson and Von Dreele [60] for explanations of these additional routines, as well as further explanations of EXPEDT, POWPREF, GENLES and POWPLOT.

3.2 The Rietveld Method of Analyzing Powder Diffraction Data

As can be seen in Figure 3.1, the observed intensity at a particular TOF channel will contain contributions from two components: 1) nearby Bragg reflections and 2) background scattering. Therefore, the number of counts observed, I'_O, in a channel of width W yields an observed normalized profile intensity of

$$I_O = \frac{I'_O}{WI_i} \tag{3.1}$$

where I_i is the incident intensity. The form of I_i for a particular diffractometer is usually found by using a vanadium-niobium (V-Nb) sample. The scattering lengths, b, for V and Nb are -0.3824 fm and 7.054 fm, respectively [64]. An alloy whose composition is 95 atomic percent V and 5 atomic percent Nb yields an average total scattering length of approximately zero. This means that practically no coherent

scattering takes place in the sample since the structure factor is proportional to the average scattering length, $\bar{b}$ [65]. Instead, the incident spectrum is scattered by the V-Nb alloy into the several detector banks of the diffractometer. The spectrum is next fit with one of five different functions available within GSAS. The function used in this study was of the form

$$I_i = P_1 + P_2 e^{-(P_3 T)} - P_4 e^{-(P_5 T^2)} - \ldots \tag{3.2}$$

where the P_i's are constants and T is TOF, typically in milliseconds. There is a maximum of 11 constants. This function is usually fit for a particular diffractometer at the beginning of a LANSCE run cycle, and its parameters are stored in the diffractometer's instrument parameter file. The coefficients are not usually refined for individual diffraction experiments.

The profile intensity calculated by GSAS, I_c, is found by adding those counts due to scattering by nondiffraction interactions (referred to as background) to the contributions from nearby Bragg reflections. (see Figure 3.1)

$$I_c = I_b + \Sigma Y_{p,h}. \tag{3.3}$$

Here I_b is the background value and $Y_{p,h}$ is the contribution from the h-th reflection of the p-th phase; the summation is only over those Bragg reflections close enough to the channel of interest to make a significant contribution in intensity. The program, GENLES, then minimizes the function

$$M = \Sigma[w(I_o - I_c)^2] \tag{3.4}$$

where the weight, w, is a function of the variances in I_o' and I_i.

As an indication of the "goodness of fit" between the observed and calculated profiles, the profile residual value, R_p, and the weighted profile residual value, R_{wp}, are calculated for each histogram, where

$$R_p = \frac{\Sigma \mid I_O - I_C \mid}{\Sigma I_O} \tag{3.5}$$

and

$$R_{wp} = \sqrt{\frac{M}{\Sigma[wI_O^2]}} = \sqrt{\frac{\Sigma[w(I_O - I_C)^2]}{\Sigma[wI_O^2]}}. \tag{3.6}$$

In addition, the reduced chi-square parameter, χ^2, is defined as

$$\chi^2 = \frac{\Sigma w(I_O - I_C)^2}{N - P} \tag{3.7}$$

where N is the number of observations and P is the number of variables in the refinement. It can be used to calculate the "expected R_{wp}" by

$$\text{expected } R_{wp} = \frac{R_{wp}}{\sqrt{\chi^2}}. \tag{3.8}$$

. Of course, the "best" value of χ^2 is 1 since R_{wp} then equals its expected value.

3.3 Fitted Parameters

3.3.1 Background

During the course of a Rietveld refinement using GSAS, different parameters are allowed to vary. Once the convergence criteria have been met for a particular set of parameters, others may be added. The basic mathematical treatment of the variables refined in this study will be discussed; the first of which is background, I_b. The user chooses between three different background functions; the one chosen for

these refinements is a cosine Fourier series with up to 12 refinable parameters,

$$I_b = B_1 - \sum_{i=2}^{12} B_i \cos(P_{i-1}) \tag{3.9}$$

Generally, a maximum of only six coefficients were used in this work to adequately fit the background. If constant wavelength neutrons were used, P_j would be the detector position in 2θ. However, with TOF data, the times are scaled by

$$P_j = \left(\frac{T_j}{T_{max}}\right) 180^\circ \tag{3.10}$$

where T_j is the TOF for the j-th channel (or TOF bin in which diffracted intensity counts are accumulated; see, abscissa, Figure 3.1) and T_{max} is the maximum allowed TOF in the incident spectrum or some maximum termination time selected by the user.

3.3.2 Calculated Bragg peak intensity

The second term in the calculated spectrum (Equation 3.3), the sum of the Bragg peaks contributing significant intensity to a particular detector channel, contains the other refinable parameters

$$Y_{p,h} = S_{p,h} F_p^2 K_{p,h} H(T - T_{p,h}). \tag{3.11}$$

In this equation, $S_{p,h}$ is the scale factor of the p-th phase and the h-th histogram and is a constant of proportionality [63]. F_p^2 is the square of the structure factor for a particular reflection, $K_{p,h}$ is the product of several intensity correction factors, and $H(T - T_{p,h})$ is the profile peak shape function for a reflection at TOF position T displaced from the expected position $T_{p,h}$, of the reflection.

Several factors–sample dependent and geometry dependent–affect the diffracted intensity. $K_{p,h}$ is the product of these parameters which, in turn, contain variables refinable by GSAS.

$$K_{p,h} = \frac{E_{p,h} A_h O_{p,h} M_p L}{V_p}. \tag{3.12}$$

The correction factors are due to: extinction, $E_{p,h}$; absorption, A_h; preferred orientation, $O_{p,h}$; reflection multiplicity, M_p; scattering angle dependence (also called the Lorentz factor), L; and the volume of the unit cell, V_p. Each of these parameters will also be discussed.

3.3.2.1 Scale factor The purpose of the scale factor, $S_{p,h}$, is to bring the scale of the calculated profile in line with that of the observed profile. It can be constrained so that all histograms will have the same scaling value, i.e., one variable may used for the scale factor regardless of the number of detector banks. The scale factor is proportional to the number of unit cells of each phase present within the sample.

3.3.2.2 Structure and temperature factors The structure factors, F_p, are calculated using the coordinates of atoms within the unit cell, form factors for the atomic species present and temperature factors. The temperature factors are root-mean-square thermal vibration displacements; they may be either isotropic (U_{iso}) or anisotropic (U_{ij}) depending on the symmetry at each atom site. The temperature correction to the structure factor is either, for the isotropic case,

$$T = \exp -(8\pi^2 U_{iso} \sin^2 \theta / \lambda^2), \tag{3.13}$$

where θ and λ are the Bragg angle and de Broglie wavelength, respectively, or for the anisotropic case,

$$T = \exp -[2\pi^2(U_{11}h^2a^{*2} - \ldots - 2U_{12}hka^*b^* - \ldots)], \tag{3.14}$$

where h, k and l are the Miller indices of the reflection and a^*, b^* and c^* are the lattice parameters in reciprocal space. To relate the U's here to the β's used in Chapter 1, the following relations are used:

$$B_{iso} = 8\pi^2 U_{iso},$$

$$\beta_{ij} = 2\pi^2 a_i^* a_j^* U_{ij}. \tag{3.15}$$

3.3.2.3 Extinction correction The extinction correction, $E_{p,h}$, is given by

$$E_{p,h} = E_b \sin^2\theta + E_l \cos^2\theta \tag{3.16}$$

where the Bragg component is

$$E_b = \frac{1}{\sqrt{1+x}} \tag{3.17}$$

and the Laue component

$$E_l = \begin{cases} 1 - \frac{x}{2} + \frac{x^2}{4} - \frac{5x^3}{48} + \frac{7x^4}{192} \ldots & \text{for } x \leq 1 \\ \sqrt{\frac{2}{\pi x}}\left(1 - \frac{1}{8x} - \frac{3}{128x^2} - \frac{15}{1024x^3} - \ldots\right) & \text{for } x > 1 \end{cases} \tag{3.18}$$

where

$$x = E_x\left(\frac{\lambda F_h}{V_p}\right)^2. \tag{3.19}$$

Here λ is the wavelength of the incident radiation, F_h is the calculated structure factor for a particular reflection, V_p is the volume of the unit cell, and E_x is the block size of the powder sample and is the parameter refined by GSAS [66].

3.3.2.4 Absorption correction The correction term due to absorption, A_h, is taken into account by an empirical formula, and it is indistinguishable from multiple scattering within the sample. It is assumed that the sample is cylindrical and that the absorption cross sections of all atomic species present vary as 1/velocity. The refinable absorption coefficient, A_B, is used to calculate A_h by

$$A_h = \epsilon^{-(T_1 A_B \lambda - T_2 A_B^2 \lambda^2)} \tag{3.20}$$

where the empirical relations

$$T_1 = 1.7133 - 0.0368 \sin^2 \theta$$

$$T_2 = -0.0927 - 0.3750 \sin^2 \theta \tag{3.21}$$

are used. A_B is further defined as

$$A_B = \frac{\mu r}{\lambda} = \frac{N \sigma_a r}{\lambda} \tag{3.22}$$

where μ is the mean linear absorption coefficient, N is the number density of the sample material, σ_a is the microscopic absorption cross section and r is the radius of the cylindrical specimen [67] [68]. The assumption of 1/velocity dependence for σ_a gives

$$A_B = \frac{N r \frac{\sigma_O}{v}}{\frac{h}{mv}} = \frac{N r \sigma_O}{h/m} \tag{3.23}$$

where h is Planck's constant, m is the mass of the neutron, σ_O is the 2200 meter-per-second absorption cross section and v is the velocity of the incident neutrons. This makes A_B depend on the sample size (r), the sample material ($N\sigma_O$) and a constant (h/m).

When the incident spectrum is fit using the V-Nb sample, absorption is not taken into account. Therefore, it is possible for a sample to exhibit negative absorption values if it has a smaller absorption cross section than the V-Nb standard.

3.3.2.5 Preferred orientation correction Some specimens may exhibit a certain amount of preferred orientation, which also affects the magnitude of the intensities of each reflection. The expression for the preferred orientation correction factor, $O_{p,h}$, contains the refinable parameter R_O.

$$O_{p,h} = \frac{1}{M_p} \sum_{j=1}^{n} \left(R_O^2 \cos^2 \phi_j + \frac{\sin^2 \phi_j}{R_O} \right)^{-3/2} \tag{3.24}$$

where M_p is the multiplicity of the reflection, ϕ_j is the angle between the preferred orientation axis and the reflection vector, $\vec{h_p}$, and the summation is over all reflections crystallographically equivalent to $\vec{h_p}$.

R_O indicates the amount of preferred orientation in the sample. It can be thought of as the effective amount of compression or extension of the sample. If the crystals are plate-shaped,

$$R_O = \frac{d}{d_0} \tag{3.25}$$

where d_0 is the thickness of a specimen showing uniform pole density on a stereographic projection (no preferred orientation) and d is its thickness after axial extension or compression. If the crystals are needle-shaped,

$$R_O = \frac{d_0}{d}. \tag{3.26}$$

Naturally, if R_O is exactly unity, there is no preferred orientation. The model assumes the texture axis is either perpendicular to the diffraction plane or parallel to the scattering vector [69].

3.3.2.6 Other intensity corrections The last three intensity correction factors are multiplicity, unit cell volume and the Lorentz factor. The multiplicity, M_p, is computed by POWPREF from the space group information entered by the user. The unit cell volume, V_p, is calculated from the lattice parameters for each phase. The Lorentz factor, L, corrects for variations in intensity due to diffraction angle and neutron wavelength,

$$L = d^4 \sin\theta \tag{3.27}$$

where d is the d-spacing of a particular reflection and θ is the diffraction angle.

3.3.2.7 Profile peak shape function The last set of parameters discussed involves the calculation of the profile peak shape function, $H(T - T_{p,h})$. First, to transform TOF data into d-spacings, the total distance from the moderator to the detector must be known. If L_1 is the length of the flight path, L_2 is the distance from the sample position to the detector bank, L_3 is the detector tube height and θ is the diffraction angle, it can be shown that

$$\text{DIFC} = (252.816)(2\sin\theta)\left(L_1 + \sqrt{L_2^2 + \frac{L_3^2}{16}}\right) \tag{3.28}$$

where L_i is in meters. This value can then be used in the relationship between TOF and d-spacing by

$$\text{TOF} = \text{DIFC}(d_p) + \text{DIFA}(d_p^2) + \text{ZERO}; \tag{3.29}$$

DIFA and ZERO are correction parameters and have no physical significance. The nominal values of DIFC, DIFA and ZERO are found by observing the diffraction pattern from a calibration sample of known lattice parameter at a given temperature, e.g., CaF_2 at 302 K. However, since subsequent experiments will not have the

placement of their samples in exactly the same location as the calibration sample, refinement of DIFC, DIFA and ZERO may also be done by GSAS.

In a pulsed neutron source, the method of producing and moderating neutrons yields an asymmetric pulse which cannot be described by a simple Gaussian function. For this reason, a more complex profile function must be used to describe the pulse since its shape also affects the diffracted profiles. While there are three different profile functions from which to choose, this study used the convolution function (for example, see [70])

$$H(T - T_{p,h}) = H(\Delta T) = N[e^{u}\mathrm{erfc}(y) + e^{v}\mathrm{erfc}(z)] \tag{3.30}$$

where N, u, v, y and z are calculated from the profile coefficients described below, and erfc is the complementary error function which is defined as

$$\mathrm{erfc}(x) = \frac{2}{\sqrt{\pi}} \int_{x}^{\infty} e^{-y^2} dy. \tag{3.31}$$

Equation 3.30 results from the convolution of growing and decaying exponentials with a Gaussian function

$$H(\Delta T) = \int_{-\infty}^{\infty} G(\Delta T - \tau)P(\tau)d\tau \tag{3.32}$$

where the growing exponential is given by

$$P(\tau) = 2Ne^{\alpha\tau} \text{ for } \tau \leq 0, \tag{3.33}$$

the decaying exponential is

$$P(\tau) = 2Ne^{-\beta\tau} \text{ for } \tau \geq 0, \tag{3.34}$$

and the Gaussian function is defined as

$$G(\Delta T - \tau) = \frac{1}{\sqrt{2\pi\sigma^2}} \exp - \left(\frac{(\Delta T - \tau)^2}{2\sigma^2} \right). \tag{3.35}$$

The normalization factor, N is given by

$$N = \frac{\alpha\beta}{2(\alpha + \beta)}, \tag{3.36}$$

while the coefficients u, v, y and z are

$$u = \frac{\alpha(\alpha\sigma^2 + 2\Delta T)}{2} \tag{3.37}$$

$$v = \frac{\beta(\beta\sigma^2 - 2\Delta T)}{2} \tag{3.38}$$

$$y = \frac{(\alpha\sigma^2 + \Delta T)}{\sqrt{2\sigma^2}} \tag{3.39}$$

$$z = \frac{(\beta\sigma^2 - \Delta T)}{\sqrt{2\sigma^2}}. \tag{3.40}$$

Finally, α, β and σ^2, are defined in terms of other parameters refined by GSAS

$$\alpha = \alpha_0 + \frac{\alpha_1}{d} \tag{3.41}$$

$$\beta = \beta_0 + \frac{\beta_1}{d^4} \tag{3.42}$$

$$\sigma^2 = \sigma_0^2 - \sigma_1^2 d^2 + \sigma_2^2 d^4 + (\sigma_{0e}^2 + \sigma_{1e}^2 d^2 - \sigma_{2e}^2 d^4)\cos^2\phi \tag{3.43}$$

where ϕ is the angle between the reflection vector and an anisotropic broadening axis, if one exists. Notice there are ten parameters that GENLES may be allowed to vary: α_0, α_1, β_0, β_1, σ_0^2, σ_1^2, σ_2^2, σ_{0e}^2, σ_{1e}^2 and σ_{2e}^2.

Consider the d-spacings of a strain-free sample, i.e., all unit cells have the same lattice parameters. If the sample undergoes uniform strain, the positions of the Bragg peaks will change due to the change in d-spacings of the reflecting planes. However, if the strain is nonuniform, a range of d-spacings will result. Since diffraction may occur from all of these planes, the spread in d-spacing leads to a distribution of Bragg

peaks which are observed as a single broad peak near the d-spacing of the original unstrained reflection. In addition, this nonuniform strain may be anisotropic. It can be shown that σ_1^2, the value of which determines the width of the profile peaks, is related to the amount of strain present in the sample

$$strain = \frac{100\%}{\mathrm{DIFC}} \sqrt{(8 \ln 2)(\sigma_1^2 - \sigma_{1i}^2)} \tag{3.44}$$

where σ_{1i}^2 is the initial value of σ_1^2 as determined by fitting Equation 3.2 to the incident spectrum. If anisotropic strain exists, the parallel component is found by

$$strain_{\parallel} = \frac{100\%}{\mathrm{DIFC}} \sqrt{(8 \ln 2)(\sigma_1^2 + \sigma_{1e}^2 - \sigma_{1i}^2)}, \tag{3.45}$$

and the perpendicular component is given by

$$strain_{\perp} = \frac{100\%}{\mathrm{DIFC}} \sqrt{(8 \ln 2)(\sigma_1^2 - \sigma_{1i}^2)}. \tag{3.46}$$

Notice that if σ_{1e}^2 is zero, the parallel and perpendicular components are equal to the isotropic strain. Isotropic strain is assumed throughout this study.

In addition to strain broadening, particle size also affects the peak profile shape and can be computed from σ_2^2. The size of the particle, p, is found by

$$p = 2\mathrm{DIFC} \sqrt{\frac{8 \ln 2}{\sigma_2^2}} \tag{3.47}$$

If there exists anisotropy in particle size, then

$$p_{\parallel} = 2\mathrm{DIFC} \sqrt{\frac{8 \ln 2}{\sigma_2^2 + \sigma_{2e}^2}}. \tag{3.48}$$

and

$$p_{\perp} = 2\mathrm{DIFC} \sqrt{\frac{8 \ln 2}{\sigma_2^2}}. \tag{3.49}$$

All ten profile coefficients are not always refined. In fact, other parameters described here may also be omitted in the analysis if it is thought that they contribute little additional information about the sample.

3.4 Summary

The Generalized Structure Analysis System performs Rietveld refinements on the TOF neutron diffraction data obtained at LANSCE. Generally the following parameters are refined for each histogram using GSAS: scale factors, lattice parameters, background coefficients, preferred orientation parameters for a particular texture axis, atomic positions within the unit cell (as long as the atoms are not at high symmetry positions), σ_1^2 and σ_2^2 of the profile function, absorption coefficients, extinction coefficients, thermal parameters (either isotropic or anisotropic), DIFC, DIFA, and ZERO. In addition, constraints may be entered so that one variable will be used for a parameter regardless of the number of histograms present: some parameters may also be constrained over different phases. Since the following variables are properties of the sample and should have little angle dependence, they are usually constrained across all histograms for each phase in the sample: scale factors, preferred orientation, absorption and extinction parameters. Finally, as an indication of how well the calculated spectrum fits the observed data three values are computed by GSAS: χ^2, R_p and R_{wp}.

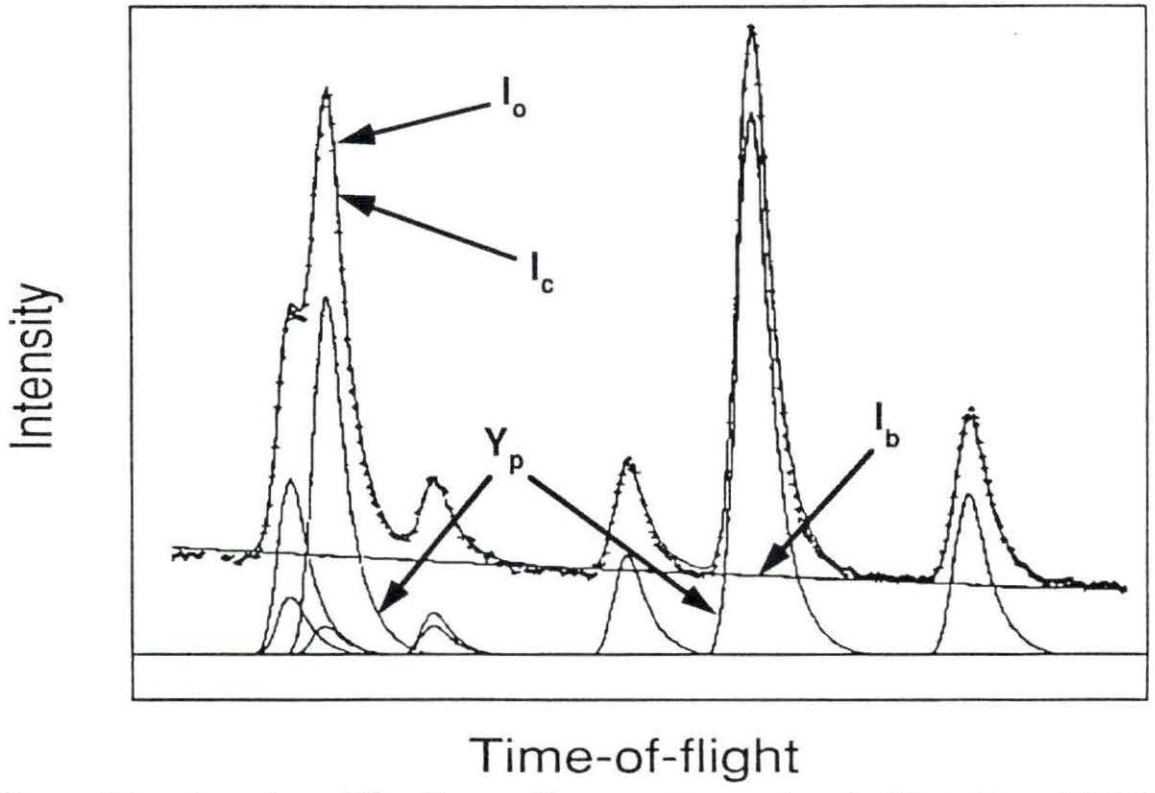

Figure 3.1: A neutron diffraction profile or spectrum using the Rietveld model [64]

4. RESULTS AND DISCUSSION

The nominal resistivity curves obtained by Hsu [47] were corrected for a change in form factor and were further investigated to see if the stress dependence seen at lower temperatures was a real effect. Also, several neutron diffraction runs described in Chapter 2 were refined using GSAS. The crystallographic characteristics of austenite, martensite and the R phase were investigated using seven experiments done on the HIPD and three experiments done on the NPD. Where appropriate, graphs of some of the highest resolution detector banks are plotted to show the observed and calculated diffraction profiles, and summaries of the converged values of refined parameters are listed.

4.1 Corrected Resistivity Curves

The resistivity curves shown in Figure 1.5 (page 29) are termed "nominal" since they were not corrected for the change in form factor which results when the NiTi wire transformed from austenite to martensite (the form factor at 100°C was used for all temperatures). To correct for this change, the resistivity and strain data in Figure 1.5 were digitized, and a program was written to correct the resistivity for changes in cross-sectional area, assuming constant volume of the sample. The results of this correction can be seen in Figure 4.1, and details on this correction process are

found in Appendix B.

Also, the data in Figure 1.5 were further investigated to see if the stress dependence seen in the resistivity curves at low temperatures was a real effect, or whether this could be explained by an error in measurement of the strain values. (This error in strain measurement would then lead to erroneous corrections in the form factor and the corrected resistivity.) To get the low-temperature, linear portions of the four resistivity curves to coincide, it was found that the strain values would have to be increased by 191%. Figure 4.2 shows how the corrected resistivity versus temperature curves would look if the strain values were increased by this factor. Notice that while the plots on heating nearly coincide, the cooling curves still show a stress dependence on the lower side of the anomalous resistivity peak. Also, since it seems unlikely that the calibration of the instruments was off such that the actual strain values were nearly twice their measured values, the stress dependence seen in the corrected resistivity curves at lower temperatures seems to be a real effect.

4.2 GSAS Results

The HIPD has detector banks at $\pm 153^\circ$, $\pm 90^\circ$, $\pm 40^\circ$, $\pm 14^\circ$ and $\pm 5^\circ$ to the incident beam. Resolution is best at detectors located at large angles (like the 153° banks), but the detectors located at small scattering angles (like the 5° banks) are capable of observing reflections from planes of larger d-spacings. This is attributed to the characteristics of a "white" pulse of neutrons. Consider a single pulse of neutrons containing a range of TOFs and corresponding wavelengths. For a given detector bank, Bragg's law will allow reflections to be observed from planes whose d-spacings satisfy Equation 2.1 (page 32) for each wavelength incident on the sample. Now,

if a different detector bank at a larger diffraction angle is used, and if the range of wavelengths is the same, the maximum d-spacing from which reflections will occur will be less than that seen in the lower angle bank. In addition, the Bragg peaks will be more widely distributed in the diffraction profile so resolution is enhanced in the higher angle detectors. A similar situation exists for the $\pm 148^{\circ}$ and the $\pm 90^{\circ}$ banks on the NPD. In all refinements, only four of the highest resolution detector banks were used for analysis.

4.2.1 Austenite

As described in Chapter 2 (Table 2.4, page 41), two experiments were done on the HIPD to observe the characteristics of the austenitic phase of NiTi: runs 526 and 704. Both runs were done under low stress conditions.

4.2.1.1 Run 526 GSAS performed Rietveld refinements on the data from run 526. Figures 4.3 through 4.6 are shown here to compare the data collected in the four banks with the highest diffraction angles. In addition Figures 4.7 through 4.14 show enlarged portions of these graphs. For these and all subsequent GSAS plots, the ordinate (normalized intensity) has units of inverse microseconds, and the abscissa (d-spacing) has units of angstroms. The plus symbols represent the observed intensity in a particular TOF channel, the solid line represents the calculated intensity profile generated by GENLES, and the line at the bottom displays the difference between the observed and calculated profiles. The "tick" marks beneath the observed and calculated curves appear at the d-spacings of allowed Bragg reflections as calculated by POWPREF. The heading of each plot indicates the detector bank number and

its angular position in 2θ, the number of least squares (L-S) cycles completed by GENLES and the fact that observed and calculated profiles are plotted.

To aid in the indexing of the Bragg peaks in the austenite profiles, Table 4.2 shows the d-spacings of the first fifteen reflections. Since this is a cubic structure with lattic parameter, a, the following equation is used to calculated the d-spacing of a reflection with Miller indices hkl:

$$\frac{1}{d^2} = \frac{h^2 + k^2 + l^2}{a^2}. \tag{4.1}$$

Tables 4.3 and 4.4 summarize the converged values for run 526. The values are divided into two tables with the first showing values which do not depend on the diffraction angle, and the second table summarizing angle dependent values. Note that constraints were placed on the scale, preferred orientation, absorption and extinction parameters. This was done to give the variables a more physical significance. That is, since the six NiTi wires were seen as a single sample by the incident neutrons (neutrons diffracted from a single wire may be diffracted to any of the detector banks), there is really only one value for each sample-specific parameter. Also, several parameters were not refined. The atom positions were not refined since they were high symmetry locations. The DIFC, DIFA and ZERO parameters were used to calculate the d-spacings from TOF information which determined the d-spacings of the observed Bragg peaks. Since this determined the lattice parameters calculated by GSAS, the DIFC, DIFA, ZERO and lattice parameters were not independent, and one of them had to be fixed at some default value. In all cases, this was chosen as the DIFC parameter in one of the highest resolution detector banks (in this study, the $+153^\circ$ bank on the HIPD and the $+148^\circ$ bank on the NPD).

The initial values of σ_1^2 are listed (σ_{1i}^2) in Table 4.1 so the amount of strain could

be calculated using Equation 3.44 (page 86). These were fit when the V-Nb standard was used and are not typically refined. For all diffraction runs, σ_2^2 was refined, but the results were negative which are nonphysical according the Equation 3.47 (page 86). For this reason, they were reset to their default value (zero for all detector banks) and are not listed in the summary tables.

The number of significant figures used in each parameter differs and is determined by the estimated standard deviation (esd) of each value as calculated by GENLES. The rightmost digit of a value is the least significant, and the number in parentheses is the esd of the rightmost digit. For example, the lattice parameter is listed as $a = 3.023(3)$Å. This means that the "3" is the least significant digit; its esd is 3 so the esd of the lattice parameter is 0.003Å.

The results of the refinements on run 526 show a number of things. The lattice parameter agrees fairly well with the commonly quoted value of 3.015Å (see Chapter 1). Also the NiTi wires show a great deal of preferred orientation, having the [111] direction aligned with the wire axis. By using Equation 3.44, the strain calculated for the $+153^\circ$, -153°, $+90^\circ$ and -90° banks are 0.544%, 0.548%, 0.646% and 0.602%, respectively. This gives an average strain of 0.584% for run 526. The value of χ^2, 1.01, indicates a very good fit.

4.2.1.2 Run 704 Figure 4.15 shows the full diffraction profiles for the $+153^\circ$ bank for run 704 while Figures 4.16 and 4.17 show more detail. For this and all subsequent runs, additional plots may be found in Appendix C. The results from run 704 should have been very similar to the results from run 526 since the experiments were performed under similar conditions. The difference was that approximately one

year elapsed between the two runs. In addition, the wires experienced a number of thermal cycles during this time.

Tables 4.5 and 4.6 show the converged values of run 704. It should be noted that GSAS will not refine atom positions located at high symmetry locations. Also notice that only four background parameters were used, as opposed to six for run 526. It can be seen in the diffraction profiles that the background has a slight curvature while the background in run 526 was quite "flat". This may indicate that something other than NiTi may have been in the incident beam (such as an electrical lead wire). Since no extra diffraction peaks are seen, this may indicate the presence of either an amorphous or hydrogen-rich substance. The plastic insulation on the electrical lead wires seems to be a reasonable candidate. This curvature is seen to a certain extent in all 1989 experiments done on the HIPD.

The average strain calculated for run 704 (0.62%) is about 6% larger than the average strain for run 526. Also, the preferred orientation parameter, R_O, and the absorption coefficient, A_B, were found to have increased by about 8% and 5%, respectively. However, the extinction coefficient, E_x, decreased by 78%. The isotropic thermal parameters also changed, with U_{iso} decreasing by 9% for nickel and decreasing by 71% for titanium. The values of DIFC, DIFA, ZERO and scale also changed, but this is not unusual since they depend on the specific conditions of each experiment.

The differences between the results from runs 704 and 526 are all less than 10% with the exception of the extinction coefficient and the isotropic thermal parameter for titanium. This could be attributed to the problems in fitting the background. The larger value of χ^2 equal to 2.35% for run 704 (Table 4.5) as compared to χ^2

Table 4.1: Values of $\sigma^2_{1/}$ on the HIPD and the NPD (all units in $\mu sec^2/\AA^2$)

	DETECTOR POSITION in 2θ			
INSTRUMENT	-153°	-153°	$+90^\circ$	-90°
HIPD	38.1	80.6	64.6	162
NPD	54.0	51.0	228	238

equal to 1.01% for run 526 (Table 4.3) indicates that some additional refinements could lead to a better fit, and this may bring the converged values closer to those found in run 526.

Table 4.2: D-spacings for the first fifteen Bragg reflections for the $Pm3m$ space group ($a = 3.023$Å)

Reflection Number	h	k	l	d-spacing (Å)
1	1	0	0	3.023
2	1	1	0	2.138
3	1	1	1	1.745
4	2	0	0	1.512
5	2	1	0	1.352
6	2	1	1	1.234
7	2	2	0	1.069
8	2	2	1	1.008
9	3	0	0	1.008
10	3	1	0	0.956
11	3	1	1	0.911
12	2	2	2	0.873
13	3	2	0	0.838
14	3	2	1	0.808
15	4	0	0	0.756

Table 4.3: Summary of parameter values which are independent of the scattering angle for run 526 on the HIPD: numbers in parentheses are estimated standard deviations (esds) calculated by GSAS (Sample A, NiTi wires, low stress, $T_{top} \approx 100^{\circ}$C)

Space group: $Pm3m$			
Lattice parameter: $a = 3.023(3)$Å			
Atom positions[a]	x	y	z
Ni:	0	0	0
Ti:	$\frac{1}{2}$	$\frac{1}{2}$	$\frac{1}{2}$
Isotropic thermal parameters, $U_{iso} \times 10^2$ (Å^2)			
Ni:	4.66(9)		
Ti:	1.24(6)		
Total R_p (%):	5.2		
Total R_{wp} (%):	7.1		
χ^2:	1.01		

[a] Unrefined parameters.

Table 4.4: Summary of parameter values which depend on the scattering angle for run 526 on the HIPD; numbers in parentheses are esds calculated by GSAS (Sample A, NiTi wires, low stress, $T_{top} \approx 100^{\circ}$C)

PARAMETER	DETECTOR POSITION in 2θ			
	$+153^{\circ}$	-153°	$+90^{\circ}$	-90°
Background, B_i $\times 10^3$ (sec^{-1})				
B_1	10.52(6)	7.90(4)	13.1(6)	14.7(7)
B_2	-3.0(1)	-0.83(8)	-11(1)	-12(1)
B_3	0.10(8)	0.03(7)	7.7(9)	7(1)
B_4	0.20(9)	0.61(7)	-5.2(6)	-5.2(7)
B_5	-0.45(6)	-0.55(5)	2.7(3)	2.7(3)
B_6	0.21(5)	0.33(4)	-1.1(1)	-1.3(1)
$\sigma_1^2 \times 10^{-2}$ ($\mu sec^2/Å^2$)	1.74(8)	2.18(9)	1.63(4)	2.48(6)
DIFC (μsec/Å)	5036[a]	5028(8)	3619(5)	3626(6)
DIFA ($\mu sec/Å^2$)	-6(2)	-5(2)	-6(1)	-6(2)
ZERO (μsec)	-8(4)	-5(4)	-9(2)	-11(3)
R_p (%)	5.0	5.7	5.3	4.9
R_{wp} (%)	7.0	8.2	6.9	6.5
Scale[b], $S_{p,h}$ ($Å^{-3}$)	5.5(3)	5.5(3)	5.5(3)	5.5(3)
Preferred Orientation[b], R_o ([111] along wire axis)	4.86(2)	4.86(2)	4.86(2)	4.86(2)
Absorption[b], A_B ($Å^{-1}$)	0.443(6)	0.443(6)	0.443(6)	0.443(6)
Extinction[b], E_x $\times 10^{-2}$ (μm^2)	1.5(2)	1.5(2)	1.5(2)	1.5(2)

[a] Unrefined parameter.

[b] Constrained parameter (one variable used for all histograms).

Table 4.5: Summary of parameter values which are independent of the scattering angle for run 704 on the HIPD: numbers in parentheses are esds calculated by GSAS (Sample A, NiTi wires, low stress, $T_{top} \approx 100^{\circ}C$)

Space group: $Pm3m$			
Lattice parameter: $a = 3.023(6)$Å			
Atom positions[a]	x	y	z
Ni:	0	0	0
Ti:	$\frac{1}{2}$	$\frac{1}{2}$	$\frac{1}{2}$
Isotropic thermal parameters, $U_{iso} \times 10^2$ (Å^2)			
Ni:	4.26(6)		
Ti:	0.36(4)		
Total R_p (%):	6.8		
Total R_{wp} (%):	9.3		
χ^2:	2.35		

[a] Unrefined parameters.

Table 4.6: Summary of parameter values which depend on the scattering angle for run 704 on the HIPD; numbers in parentheses are esds calculated by GSAS (Sample A, NiTi wires, low stress, $T_{top} \approx 100^{\circ}$C)

PARAMETER	DETECTOR POSITION in 2θ			
	-153°	-153°	$+90^{\circ}$	-90°
Background, $B_i \times 10^3$ (sec^{-1})				
B_1	80.(2)	34(1)	-111(2)	-31(4)
B_2	-74(4)	-24(2)	196(4)	72(7)
B_3	29(2)	10.(1)	-102(2)	-39(3)
B_4	-17.5(8)	-5.7(5)	30.8(5)	12.7(9)
$\sigma_1^2 \times 10^{-2}$ (μsec^2/Å^2)	1.9(2)	2.4(1)	1.7(4)	2.6(6)
DIFC (μsec/Å)	5033[a]	5032(9)	3599(7)	3632(8)
DIFA (μsec/Å^2)	-5(3)	-6(3)	-7.2(8)	-8(1)
ZERO (μsec)	-5(6)	-8(4)	-9(2)	-13(2)
R_p (%)	4.9	6.0	9.8	5.7
R_{wp} (%)	6.7	8.4	13	7.3
Scale[b], $S_{p,h}$ (Å^{-3})	9.9(4)	9.9(4)	9.9(4)	9.9(4)
Preferred Orientation[b], R_o ([111] along wire axis)	5.24(2)	5.24(2)	5.24(2)	5.24(2)
Absorption[b], A_B (Å^{-1})	0.463(8)	0.463(8)	0.463(8)	0.463(8)
Extinction[b], $E_x \times 10^{-2}$ (μm^2)	0.33(9)	0.33(9)	0.33(9)	0.33(9)

[a] Unrefined parameter.

[b] Constrained parameter (one variable used for all histograms).

4.2.2 Martensite

Five experiments were done in order to ascertain the crystallographic characteristics of NiTi martensite: runs 266, 267 and 268 on sample B in the NPD, and runs 709 and 710 on sample A in the HIPD. Experimental conditions for these runs are summarized in Tables 2.4 (page 41) and 2.5 (page 45). Even though the sample used on the NPD (sample B) contained 0.1 weight percent yttrium, it is thought that its crystallographic characteristics were not significantly different from the NiTi wires (sample A) since the yttrium represents a small fraction of the entire sample.

4.2.2.1 Run 266 Figures 4.18 through 4.20 show some of the diffraction profiles obtained on the NPD that were plotted by POWPLOT. The d-spacings of the first twenty Bragg reflections for the $P2_1/m$ space group are found in Table 4.7. They were calculated using the following equation for the monoclinic structure:

$$\frac{1}{d^2} = \frac{1}{\sin^2\beta}\left(\frac{h^2}{a^2} + \frac{k^2\sin^2\beta}{b^2} + \frac{l^2}{c^2} - \frac{2hl\cos\beta}{ac}\right) \tag{4.2}$$

There is good agreement between the observed and predicted positions of Bragg peaks (indicated by the small "tick" marks beneath the observed and calculated profiles). However, upon closer examination, it appears there is some discrepancy in the calculated and observed intensities, for example, in Figure 4.19 for the two most intense reflections. This may be due to preferred orientation in the sample.

Tables 4.8 and 4.9 show the converged values for run 266 on the NPD. Six background parameters were used, and the scale and absorption parameters were constrained. Also, anisotropic thermal parameters were found to be appropriate because of the lower symmetry of the monoclinic unit cell.

As mentioned above, the presence of preferred orientation in the sample may account for the discrepancies seen between the observed and calculated intensities. Several preferred orientation directions were tried, but R_O changed little from unity, indicating little preferred orientation in those directions. Directions that were tried include $[11\bar{1}]$ and $[10\bar{2}]$. In addition, the extinction coefficient could not be varied without the equations diverging. The amount of strain in the sample using the data from the -148°, -148°, -90° and -90° banks is 0.306%, 0.256%, 0.314% and 0.330%, respectively. This gave an average strain of 0.302%.

The lattice parameters and atom positions found by refining the data from run 266 may be compared to those found in the literature. Table 4.10 compares the values of these parameters to researchers who have used the $P2_1/m$ space group to describe NiTi martensite. There is fair agreement between the present study and the results found by other researchers. In addition, the anisotropic thermal parameters may be compared to those found using the K+ model. Since Table 1.2 (page 18) lists these using a slightly different definition then that used by GSAS, they have been recalculated by applying the Equation 3.15 (page 80). The results are found in Table 4.11. The anisotropic thermal parameters obtained for run 266 are, in some instances, an order of magnitude larger than those found by Kudoh *et al.* [35], although a value of 1.32 for χ^2 shows a relatively good fit.

4.2.2.2 Run 267 As described in Chapter 2, the NiTi-Y rod was cooled to -263°C for run 267. The diffraction plots for the -90° bank for this experiment can be found in Figures 4.21 through 4.23.

Few differences are seen between the diffraction profiles of runs 266 and 267.

There are still some problems with the calculated intensities, but preferred orientation may again account for this. The values of refined parameters are found in Tables 4.12 and 4.13.

As with run 266, preferred orientation and extinction were not allowed to vary. The average strain for run 267 was 0.32%. All atom positions changed by less than 1% with the exception of the x coordinate for nickel which increased (negatively) by 3.9%. Also, the anisotropic thermal parameters decreased considerably, as would be expected at a lower temperature. There was also a change in the lattice parameters with a and b decreasing and c and β increasing. This led to a decrease in the volume of the unit cell from 55.21Å^3 to 55.08Å^3. A curious point is the decrease in the absorption coefficient by nearly a factor of ten; in fact, its value is almost zero. According to Equation 3.22 (page 81), the only temperature dependent values in the definition of A_B are the number density, N, and the radius of the sample, r. As the sample is cooled, N will increase and r will decrease due to thermal contraction. Since the increase in N should outweigh the decrease in r, it is expected that the absorption should have actually increased as the temperature of the sample was lowered. With a χ^2 value of 2.56 and total R_{wp} value of 7.6, the expected R_{wp} value is 4.75 which indicates that more refinements may be possible on this diffraction data set.

4.2.2.3 Run 268 The last experiment done on the NPD that was refined was run 268. It followed directly after run 267 and was done at room temperature. The diffraction profiles obtained for the -90° bank for this run are found in Figures 4.24 through 4.26.

Tables 4.14 and 4.15 summarize the values of the parameters refined for run

268. The average strain was 0.337%, and the preferred orientation and extinction parameters were not varied. The anisotropic thermal parameters, while larger than those found in run 267, were not as large as those found in run 266. Also, the lattice parameters and atom positions were actually closer to the values obtained in run 267 than to those found in run 266. Another interesting point is the negative absorption coefficient. This is possible only if the sample has a smaller macroscopic absorption cross section than the V-Nb standard used to obtain the incident spectrum. With the esd as large as the value itself, it could be argued that the value is not significantly different from the 0.006 value found in run 267. The absorption parameters for runs 266 and 268 should have been nearly equal, but they were not. The reason for this is not clear.

The crystallographic characteristics found in runs 266, 267 and 268 were not as self-consistent as would be expected. The sample had just been annealed before run 266 was performed, so it had not been thermally cycled through the martensitic transformation before the diffraction data were taken. Since the martensitic transformation did not take place prior to runs 267 and 268, this change in temperature should not have changed the characteristics of the sample (except for temperature sensitive parameters). The fact still remains that the only variable changed for the three runs was the sample temperature so it is not clear how this affected the sample. Consequently, the refinement done on run 266 should be the most reliable since it was done directly after annealing, and the lattice parameters for this run will be used below.

4.2.2.4 Runs 709 and 710 The other two experiments designed to observe

the martensitic phase of NiTi were runs 709 and 710 on the HIPD which were done under high and low stress conditions, respectively. Diffraction profiles for run 709 are found in Figures 4.27 through 4.29, and diffraction profiles for run 710 are seen in Figures 4.30 through 4.32.

Some problems were encountered in trying to fit the $P2_1/m$ space group to the data in runs 709 and 710 due to the apparent presence of a considerable amount of preferred orientation. Since only scale, background, lattice parameter and preferred orientation were varied, summary tables were not made for these runs. Refinements on runs 526 and 704 showed the austenitic phase in the NiTi wires had a [111] texture axis along the axis of the wires. As discussed in Chapter 1, when austenite transforms to martensite there is a definite relationship between the crystallographic axes of the two phases. However, a powder diffractometer where the sample is fixed does not easily lend itself to determining the preferred orientation axis because a trial-and-error approach is required. (A diffractometer with a multi-axis goniometer would make this type of approach unnecessary.) Also, in a specimen with such a large amount of preferred orientation it is imperative to vary this parameter early in the refinement since some strong reflections may actually be absent from the diffraction profile. In this case, refining other parameters before the preferred orientation parameter has been refined usually leads to diverging equations.

The trial-and-error approach was used on the data obtained in runs 709 and 710. Several directions were tried but with little success: [001], [101], [011], [100] and $[\bar{1}00]$, to name a few. However, when the [110] direction was used, χ^2 decreased and R_O took on a value significantly different from unity. The angle, ϕ measured from the $\vec{a}$ axis to a particular direction in the a-b plane was varied, and the values of R_O

and χ^2 were noted. Table 4.16 along with Figures 4.33 and 4.34 show the results of this work. For comparison, χ^2 was equal to 19.06 and 30.34 for runs 709 and 710, respectively, when no preferred orientation was used in the model.

Although the value of R_O was as high as 5.02, there was still a great discrepancy between the observed and calculated profiles in runs 709 and 710. This is seen in the large χ^2 values and in the profiles themselves. A possible explanation may be that the specimen may not have been single phase martensite, but it may have started to transform to either the R or A phases. Even though the resistance versus temperature curve indicated that the sample should not have transformed at the ambient temperature of the experimental hall, A_S is quite dependent on the thermomechanical history of the sample so this remains a possibility.

Table 4.7: D-spacings for the first twenty Bragg reflections for the $P2_1/m$ space group ($a = 2.9036$Å, $b = 4.116$Å, $c = 4.663$Å, $\beta = 97.836^\circ$)

Reflection Number	h	k	l	d-spacing (Å)
1	0	0	1	4.619
2	0	1	1	3.073
3	1	0	0	2.876
4	1	0	-1	2.606
5	1	1	0	2.358
6	0	0	2	2.310
7	1	0	1	2.305
8	1	1	-1	2.202
9	0	2	0	2.058
10	0	1	2	2.014
11	1	1	1	2.011
12	1	0	-2	1.934
13	0	2	1	1.880
14	1	1	-2	1.751
15	1	0	2	1.692
16	1	2	0	1.674
17	1	2	-1	1.615
18	1	1	2	1.565
19	0	0	3	1.540
20	0	2	2	1.537

Table 4.8: Summary of parameter values which are independent of the scattering angle for run 266 on the NPD; numbers in parentheses are esds calculated by GSAS (Sample B, NiTi-Y rod, $T \approx 25^{\circ}$C)

Space group: $P2_1/m$						
Lattice parameters:						
$a = 2.9036(8)$Å						
$b = 4.116(1)$Å						
$c = 4.663(1)$Å						
$\beta = 97.836(2)^{\circ}$						
Atom positions		x	y	z		
Ni:		-0.0388(3)	$\frac{1}{4}^a$	0.8250(2)		
Ti:		0.5774(7)	$\frac{1}{4}^a$	0.2830(4)		
Anisotropic thermal parameters, $U_{ij} \times 10^2$ (Å^2)						
	U_{11}	U_{22}	U_{33}	U_{12}	U_{13}	U_{23}
Ni:	1.29(4)	0.36(2)	0.73(3)	0.0^a	-0.26(2)	0.0^a
Ti:	0.80(9)	0.41(6)	0.4(1)	0.0^a	0.06(6)	0.0^a
Total R_p (%):			5.9			
Total R_{wp} (%):			8.7			
χ^2:			1.32			

[a] Unrefined parameter.

Table 4.9: Summary of parameter values which depend on the scattering angle for run 266 on the NPD: numbers in parentheses are esds calculated by GSAS (Sample B, NiTi-Y rod, $T \approx 25^{\circ}$C)

PARAMETER	DETECTOR POSITION in 2θ			
	-153°	-153°	$+90^{\circ}$	-90°
Background, B_i $\times 10^3$ ($\sec^{-1}$)				
B_1	55.2(3)	55.5(3)	54.2(2)	52.5(2)
B_2	10.7(5)	11.4(5)	8.8(4)	9.4(4)
B_3	6.0(4)	5.3(4)	4.8(3)	3.2(4)
B_4	1.3(4)	3.2(4)	3.8(3)	2.5(4)
B_5	2.9(3)	1.8(3)	0.0(3)	2.3(3)
B_6	0.3(3)	1.3(3)	3.2(2)	1.3(2)
$\sigma_1^2 \times 10^{-3}$ (μsec^2/Å^2)	1.90(3)	1.80(3)	1.34(1)	1.47(2)
DIFC (μsec/Å)	16514[a]	16518(6)	12505(4)	12518(4)
DIFA (μsec/Å^2)	-3(2)	0(2)	-1.7(7)	-1.4(7)
ZERO (μsec)	-6(3)	1(3)	-6(2)	-3(2)
R_p (%)	6.2	5.7	5.8	5.9
R_{wp} (%)	9.1	8.6	8.5	8.6
Scale[b], $S_{p,h}$ (Å^{-3})	18.4(3)	18.4(3)	18.4(3)	18.4(3)
Preferred Orientation[b], R_o	1.0	1.0	1.0	1.0
Absorption[b], A_B (Å^{-1})	0.048(3)	0.048(3)	0.048(3)	0.048(3)
Extinction[b], E_x $\times 10^{-2}$ (μm^2)	0	0	0	0

[a] Unrefined parameter.

[b] Constrained parameter (one variable used for all histograms).

Table 4.10: Summary of crystal structures using the $P2_1/m$ spacegroup for NiTi martensite

Researchers	HS[a]	MS[b]	B−[c]	K−[d]	Present work
Space Group	$P2_1/m$[e]	$P2_1/m$[e]	$P2_1/m$	$P2_1/m$	$P2_1/m$
a(Å)	2.883	2.885	2.884	2.898	2.9036(8)
b(Å)	4.117	4.120	4.110	4.108	4.116(1)
c(Å)	4.623	4.622	4.665	4.646	4.663(1)
β(°)	96.8	96.8	98.10	97.78	97.836(2)
Atom Positions					
Ni	$x\frac{1}{4}z, \bar{x}\frac{3}{4}\bar{z}$	$x\frac{1}{4}z, \bar{x}\frac{3}{4}\bar{z}$	$x\frac{1}{4}z, \bar{x}\frac{3}{4}\bar{z}$	$x\frac{1}{4}z, \bar{x}\frac{3}{4}\bar{z}$	$x\frac{1}{4}z, \bar{x}\frac{3}{4}\bar{z}$
x	0.0	0.0525	-0.034	0.0372	-0.0388(3)
z	0.1875	0.693	0.830	0.6752	0.8250(2)
Ti	$x\frac{1}{4}z, \bar{x}\frac{3}{4}\bar{z}$	$x\frac{1}{4}z, \bar{x}\frac{3}{4}\bar{z}$	$x\frac{1}{4}z, \bar{x}\frac{3}{4}\bar{z}$	$x\frac{1}{4}z, \bar{x}\frac{3}{4}\bar{z}$	$x\frac{1}{4}z, \bar{x}\frac{3}{4}\bar{z}$
x	0.5	0.4726	0.561	0.4176	0.5774(7)
z	0.3125	0.221	0.267	0.2164	0.2830(4)

[a] Hehemann and Sandrock [32].

[b] Michal and Sinclair [33].

[c] Bührer, Gotthardt, Kulik, Mercier, and Staub [34].

[d] Kudoh, Tokonami, Miyazaki and Otsuka [35].

[e] The original $\vec{b}$ and $\vec{c}$ axes and y and z coordinates have been interchanged as was done by Kudoh *et al.* [35].

Table 4.11: Anisotropic thermal parameters ($\times 10^2$) for NiTi martensite using the results obtained by K+ [35] and the relationship between β_{ij} and U_{ij} (Equation 3.15); also shown are the converged values from run 266 (shown in parentheses), all units in $\AA^2$

Atom	U_{11}	U_{22}	U_{33}	U_{12}	U_{13}	U_{23}
Ni	5.15	1.3	4.89	0.0	-1.4	0.0
	(1.29)	(0.36)	(0.73)	(0.0)	(-0.26)	(0.0)
Ti	2.98	2.4	4.45	0.0	-0.25	0.0
	(0.80)	(0.41)	(0.4)	(0.0)	(0.06)	(0.0)

Table 4.12: Summary of parameter values which are independent of the scattering angle for run 267 on the NPD; numbers in parentheses are esds calculated by GSAS (Sample B, NiTi-Y rod, $T = -263^{\circ}C$)

Space group: $P2_1/m$						
Lattice parameters:						
$a = 2.8979(6)$Å						
$b = 4.1018(8)$Å						
$c = 4.6840(9)$Å						
$\beta = 98.393(2)^{\circ}$						
Atom positions		x	y	z		
Ni:		-0.0403(2)	$\frac{1}{4}^a$	0.8263(1)		
Ti:		0.5811(5)	$\frac{1}{4}^a$	0.2844(3)		
Anisotropic thermal parameters, $U_{ij} \times 10^2$ (Å^2)						
	U_{11}	U_{22}	U_{33}	U_{12}	U_{13}	U_{23}
Ni:	0.52(2)	0.01(2)	0.20(2)	0.0^a	-0.25(1)	0.0^a
Ti:	0.05(5)	0.33(5)	0.21(6)	0.0^a	0.18(4)	0.0^a
Total R_p (%):			5.2			
Total R_{wp} (%):			7.6			
χ^2:			2.56			

[a] Unrefined parameter.

Table 4.13: Summary of parameter values which depend on the scattering angle for run 267 on the NPD: numbers in parentheses are esds calculated by GSAS (Sample B, NiTi-Y rod, $T = -263^{\circ}C$)

	DETECTOR POSITION in 2θ			
PARAMETER	$+153^{\circ}$	-153°	$+90^{\circ}$	-90°
Background, $B_i \times 10^3$ (sec^{-1})				
B_1	130.4(6)	128.3(6)	131.4(5)	130.2(6)
B_2	10.(1)	15(1)	7.0(9)	3(1)
B_3	12(1)	8.4(9)	8.4(7)	10.3(8)
B_4	-1(1)	2.0(9)	5.8(8)	7.2(8)
B_5	5.3(7)	4.3(7)	-3.5(6)	-6.1(7)
B_6	0.0(7)	0.9(7)	7.2(5)	8.6(5)
$\sigma_1^2 \times 10^{-3}$ ($\mu sec^2/\AA^2$)	2.00(2)	1.97(2)	1.40(1)	1.53(1)
DIFC ($\mu sec/\AA$)	16509[a]	16519(4)	12504(3)	12521(3)
DIFA ($\mu sec/\AA^2$)	-5(1)	-5(1)	-4.2(5)	-5.0(6)
ZERO (μsec)	-8(2)	-6(2)	-10.(1)	-10.(1)
R_p (%)	5.2	4.2	5.0	6.1
R_{wp} (%)	7.6	6.3	7.3	8.8
Scale[b], $S_{p,h}$ ($\AA^{-3}$)	40.4(4)	40.4(4)	40.4(4)	40.4(4)
Preferred Orientation[b], R_O	1.0	1.0	1.0	1.0
Absorption[b], A_B ($\AA^{-1}$)	0.006(2)	0.006(2)	0.006(2)	0.006(2)
Extinction[b], $E_x \times 10^{-2}$ (μm^2)	0	0	0	0

[a] Unrefined parameter.

[b] Constrained parameter (one variable used for all histograms).

Table 4.14: Summary of parameter values which are independent of the scattering angle for run 268 on the NPD: numbers in parentheses are esds calculated by GSAS (Sample B, NiTi-Y rod, $T \approx 25^{\circ}$C)

Space group: $P2_1/m$						
Lattice parameters:						
$a = 2.9004(7)$Å						
$b = 4.106(1)$Å						
$c = 4.681(1)$Å						
$\beta = 97.292(2)^{\circ}$						
Atom positions			x	y	z	
Ni:			-0.0401(3)	$\frac{1}{4}^a$	0.8258(1)	
Ti:			0.5818(6)	$\frac{1}{4}^a$	0.2845(3)	
Anisotropic thermal parameters, $U_{ij} \times 10^2$ (Å^2)						
	U_{11}	U_{22}	U_{33}	U_{12}	U_{13}	U_{23}
Ni:	0.65(3)	0.05(2)	0.24(2)	0.0^a	-0.26(2)	0.0^a
Ti:	0.24(7)	0.26(6)	0.16(7)	0.0^a	0.21(5)	0.0^a
Total R_p (%):			6.3			
Total R_{wp} (%):			9.1			
χ^2:			1.62			

[a] Unrefined parameter.

Table 4.15: Summary of parameter values which depend on the scattering angle for run 268 on the NPD; numbers in parentheses are esds calculated by GSAS (Sample B, NiTi-Y rod, $T \approx 25^{\circ}$C)

PARAMETER	DETECTOR POSITION in 2θ			
	$+153^{\circ}$	-153°	$+90^{\circ}$	-90°
Background, $B_i \times 10^3$ ($\sec^{-1}$)				
B_1	57.4(2)	56.5(3)	60.9(3)	56.6(3)
B_2	7.8(6)	10.3(6)	0.7(5)	4.6(5)
B_3	4.8(5)	3.2(5)	6.6(4)	3.7(4)
B_4	0.3(5)	2.7(5)	1.5(4)	3.9(4)
B_5	2.4(4)	1.5(4)	-1.0(3)	-2.7(3)
B_6	0.2(3)	1.0(3)	3.0(3)	4.1(3)
$\sigma_1^2 \times 10^{-3}$ ($\mu\sec^2/\text{Å}^2$)	2.12(3)	2.03(3)	1.42(2)	1.56(2)
DIFC (μsec/Å)	16511[a]	16521(5)	12502(4)	12517(4)
DIFA ($\mu\sec/\text{Å}^2$)	-8(2)	-6(1)	-4.1(7)	-4.0(7)
ZERO (μsec)	-12(2)	-8(2)	-10.(2)	-10.(2)
R_p (%)	6.0	5.5	6.2	7.2
R_{wp} (%)	8.8	8.3	8.8	10.
Scale[b], $S_{p,h}$ (Å^{-3})	17.0(2)	17.0(2)	17.0(2)	17.0(2)
Preferred Orientation[b], R_o	1.0	1.0	1.0	1.0
Absorption[b], $A_B \times 10^3$ (Å^{-1})	-2(2)	-2(2)	-2(2)	-2(2)
Extinction[b], $E_x \times 10^{-2}$ (μm^2)	0	0	0	0

[a] Unrefined parameter.

[b] Constrained parameter (one variable used for all histograms).

Table 4.16: The change in R_O and χ^2 as the preferred orientation axis is varied in the a-b plane for runs 709 and 710 (ϕ is measured from the $\vec{a}$ axis to the indicated direction)

				Run 709		Run 710	
h	k	l	$\phi(^\circ)$	R_O	χ^2	R_O	χ^2
1	1	0	60.1	2.32	18.26	2.36	28.98
2	3	0	71.4	3.26	15.72	3.25	24.74
1	2	0	77.7	3.44	14.62	3.48	22.89
23	48	0	78.5	4.08	14.50	4.42	22.67
11	24	0	79.3	5.02	14.35	5.00	22.40
21	48	0	80.1	4.55	14.44	4.57	22.54
5	12	0	81.0	4.33	14.64	4.37	22.88
9	24	0	82.6	4.09	15.34	4.17	24.06
1	3	0	84.3	3.68	16.43	3.78	25.93
1	4	0	87.7	2.89	18.23	2.84	29.17
1	5	0	89.7	1.42	18.98	1.40	30.22
0	1	0	97.8	1.12	19.05	1.12	30.32

4.2.3 Intermediate temperature phases

Six diffraction runs were performed on the HIPD: runs 527 and 530 on the high-temperature side of the anomalous resistivity peak (under low stress), runs 705 and 706 (under low stress) and runs 707 and 708 (under high stress) on the low-temperature side of the resistance peak. As discussed in Chapter 2, these six data sets were merged into three data sets which will be referred to in the following way: run 527530, run 705706 and run 707708.

4.2.3.1 Run 527530 As a first approximation, the $Pm3m$ space group that describes austenite was used to fit run527530. Figures 4.35 through 4.37 show the results of the refinements on this merged data set.

It is quite obvious that the $Pm3m$ space group does not fit this pattern very well. First, the 110 reflection at 2.1Å appears to broaden considerably and may even show the early stages of splitting. This is in agreement with work done by Ling and Kaplow [41]-[44]. Also, there are four new reflections between 1.3Å and 1.8Å. Tables 4.17 and 4.18 show the fitted values of the usual parameters. The rather large values of σ_1^2 are most likely due to the apparent broadening of the 110 reflection. Since GSAS has only calculated a single reflection for this peak, it must try to fit it with a single broad peak.

The next approach used a rhombohedral space group to fit the data. The $R\bar{3}mr$ space group was used (where the r indicates the rhombohedral rather than the hexagonal setting), and the results of this space group are summarized in Tables 4.19 and 4.20 (only those parameters which were refined are included in Table 4.20). The refinement was not entirely successful since the equations diverged when the isotropic

thermal parameters were allowed to vary. The calculated profiles can be seen in Figure 4.38 through 4.40. Other detector banks were not included in Appendix C since they did not add any additional information. Although there was an additional reflection predicted near the 2.1Å peak, its calculated intensity was essentially zero so it did not account for the broadening of the 110 peak. The first twenty Bragg reflections for the $R\bar{3}mr$ space group were calculated using the following equation:

$$\frac{1}{d^2} = \frac{(h^2 + k^2 - l^2)\sin^2\alpha + 2(hk + kl + hl)(\cos^2\alpha - \cos\alpha)}{a^2(1 - 3\cos^2\alpha + 2\cos^3\alpha)}. \qquad (4.3)$$

The results of this calculation are found in Table 4.21.

4.2.3.2 Runs 705706 and 707708 Two experiments were run to see if any change in crystal structure could be seen as the applied stress was changed while the samples were at approximately the same point on the low-temperature side of the resistivity peak. Since it is often thought that M_s coincides with the summit of the peak, it was expected that a two-phase mixture would be observed. This does seem to have been the case as explained below. Figures 4.41 through 4.44 show the profiles for run 705706 using the $P2_1/m$ martensite space group and lattice parameters obtained from run 266. It is apparent that this does fit a number of the observed reflections including the intense peak at 4.7Å. The next set of plots, Figures 4.45 through 4.47, show the same data set using the $R\bar{3}mr$ rhombohedral space group. As with run 527530, this explains some of the Bragg peaks, but it still does not account for the apparent splitting of the 110 austenite peak at 2.1Å. The splitting was even more pronounced in runs 705706 and 707708 than it was in run 527530. This can be seen best in Figure 4.44 for run 705706 and in Figure 4.51 for run 707708. Both phases were used together to try to fit run 705706, but the equations diverged when the

lattice parameters were varied so no plots or parameter summaries were included. For comparison, run 707708 profiles are shown in Figures 4.48 through 4.51.

The splitting of the peak at 2.1Å (the 110 austenite reflection) that was seen in these two experiments gives evidence the R phase was probably present. Also, the rather large peak seen at 4.7Å coincides with the 001 martensite reflection so martensite was probably also present.

Refinements were not successful on either of these data sets. This is attributed to the same problems found in runs 709 and 710 as well as run 527530. First, if martensite is present, it will most likely have a great deal of preferred orientation. Until the correct texture axis can be found, these results cannot be applied to runs 705706 and 707708. Also, until the correct space group is found for the R phase and a refinement is completed on this crystal structure, any two-phase mixture which contains the R phase will be very difficult to refine.

Since converged values were not obtained for runs 705706 or 707708, little can be concluded about how stress affected these two data sets. Judging only from the plots themselves, there does not seem to be a difference between the two stress levels.

Table 4.17: Summary of parameter values which are independent of the scattering angle for run 527530 on the HIPD ($Pm3m$ space group); numbers in parentheses are esds calculated by GSAS (Sample A, NiTi wires, low stress, $T_{top} \approx 29^{\circ}$C)

Space group: $Pm3m$			
Lattice parameter:			
$a = 3.011(4)$Å			
Atom positions[a]	x	y	z
Ni:	0	0	0
Ti:	$\frac{1}{2}$	$\frac{1}{2}$	$\frac{1}{2}$
Isotropic thermal parameters, $U_{iso} \times 10^2$ (Å^2)			
Ni:	5.78(7)		
Ti:	1.59(5)		
Total R_p (%):	7.0		
Total R_{wp} (%):	9.4		
χ^2:	3.64		

[a] Unrefined parameters.

Table 4.18: Summary of parameter values which depend on the scattering angle for run 527530 on the HIPD ($Pm3m$ space group); numbers in parentheses are esds calculated by GSAS (Sample A, NiTi wires, low stress, $T_{top} \approx 29^{\circ}$C)

PARAMETER	DETECTOR POSITION in 2θ			
	$+153^{\circ}$	-153°	$+90^{\circ}$	-90°
Background, B_i $\times 10^3$ ($\sec^{-1}$)				
B_1	16.6(1)	17.1(1)	14.3(1)	16.2(1)
B_2	2.9(2)	2.4(2)	0.7(2)	0.9(2)
B_3	1.6(2)	1.7(2)	3.0(2)	3.1(2)
B_4	2.4(2)	2.2(2)	0.9(2)	1.3(2)
B_5	-0.7(1)	-0.7(1)	0.5(1)	0.5(1)
B_6	0.6(1)	0.5(1)	0.22(9)	0.41(9)
$\sigma_1^2 \times 10^{-2}$ (μsec^2/Å^2)	5.8(2)	6.0(2)	3.7(6)	4.3(8)
DIFC (μsec/Å)	5030[a]	5014(9)	3627(6)	3626(6)
DIFA (μsec/Å^2)	0.(2)	4(2)	-3(1)	-3(1)
ZERO (μsec)	-1(4)	6(4)	-8(2)	-7(3)
R_p (%)	6.3	6.3	7.6	7.6
R_{wp} (%)	8.7	8.6	10.	9.7
Scale[b], $S_{p,h}$ (Å^{-3})	44(2)	44(2)	44(2)	44(2)
Preferred Orientation[b], R_o ([111] along wire axis)	4.79(1)	4.79(1)	4.79(1)	4.79(1)
Absorption[b], A_B (Å^{-1})	0.475(4)	0.475(4)	0.475(4)	0.475(4)
Extinction[b], E_x $\times 10^{-2}$ (μm^2)	6.2(5)	6.2(5)	6.2(5)	6.2(5)

[a] Unrefined parameter.

[b] Constrained parameter (one variable used for all histograms).

Table 4.19: Summary of parameter values which are independent of the scattering angle for runs 527 and 530 on the HIPD ($R\bar{3}mr$ space group); numbers in parentheses are esds calculated by GSAS (Sample A, NiTi wires, low stress, $T_{top} \approx 29^{\circ}$C)

Space group: $R\bar{3}mr$			
Lattice parameters:			
$a = 5.983(3)$Å			
$\alpha = 90.57(7)^{\circ}$			
Atom positions[a]	x	y	z
Ni:	0	0	0
Ni:	$\frac{1}{2}$	0	0
Ni:	$\frac{1}{2}$	$\frac{1}{2}$	0
Ni:	$\frac{1}{2}$	$\frac{1}{2}$	$\frac{1}{2}$
Ti:	$\frac{1}{4}$	$\frac{1}{4}$	$\frac{1}{4}$
Ti:	$\frac{3}{4}$	$\frac{1}{4}$	$\frac{1}{4}$
Isotropic thermal parameters[a], $U_{iso} \times 10^2$ (Å^2)			
Ni:	2.5		
Ti:	2.5		
Total R_p (%):	6.5		
Total R_{wp} (%):	10.		
χ^2:	18.6		

[a] Unrefined parameters.

Table 4.20: Summary of refined parameter values which depend on the scattering angle for run 527530 on the HIPD ($R\bar{3}mr$ space group); numbers in parentheses are esds calculated by GSAS (Sample A, NiTi wires, low stress, $T_{top} \approx 29^{\circ}$C)

PARAMETER	DETECTOR POSITION in 2θ			
	$+153^{\circ}$	-153°	$+90^{\circ}$	-90°
Background, B_i $\times 10^2$ (sec^{-1})				
B_1	55(2)	34(2)	7.2(3)	29.1(5)
B_2	-61(4)	-35(3)	6.9(5)	-23.0(9)
B_3	26(2)	15(2)	-2.3(3)	9.9(5)
B_4 ,	-11.6(7)	-6.3(5)	2.2(1)	-4.4(2)
R_p (%)	3.8	4.7	11	4.8
R_{wp} (%)	5.5	6.8	15	7.2
Scale[a], $S_{p,h}$ (Å^{-3})	0.25(4)	0.25(4)	0.25(4)	0.25(4)
Preferred Orientation[a], R_O ([111] along wire axis)	4.22(4)	4.22(4)	4.22(4)	4.22(4)

[a]Constrained parameter (one variable used for all histograms).

Table 4.21: D-spacings for the first twenty Bragg reflections for the $R\bar{3}mr$ space group ($a = 5.983$Å, $\alpha = 90.57^{\circ}$)

Reflection Number	h	k	l	d-spacing (Å)
1	1	0	0	5.984
2	1	0	-1	4.251
3	0	-1	-1	4.212
4	1	-1	-1	3.466
5	1	1	1	3.423
6	2	0	0	2.992
7	2	0	-1	2.686
8	2	1	0	2.665
9	2	-1	-1	2.454
10	1	-1	-2	2.446
11	2	1	1	2.422
12	2	0	-2	2.126
13	0	-2	-2	2.105
14	2	-1	-2	2.003
15	3	0	0	1.994
16	1	-2	-2	1.994
17	1	2	2	1.977
18	3	0	-1	1.897
19	3	1	0	1.886
20	3	-1	-1	1.812

4.3 Suggestions for Further Work

Several things may be done in the future to provide more information on the martensitic transformation of NiTi. First, a true powdered sample in which preferred orientation is of very little concern could be used on the NPD to better determine the crystallographic parameters of martensite and the R phase. Other peak-fitting techniques could be used to analyze these data, since Rietveld refinements are not very efficient in determining unknown crystal structures. Once this is done, the preferred orientation axis of the martensitic phase in the wires could be discovered by standard methods (for example, using orientation distribution functions to interpret pole figures [72]) using an x-ray diffractometer with a multi-axis goniometer. This information could then be used to obtain better refinements on runs 709, 710, 705706 and 707708. In addition, GSAS is capable of simultaneously refining neutron and x-ray diffraction data. When this is done, the uncertainty in the refinements is greatly reduced due to the complementary qualities of neutron and x-ray diffraction. Finally, larger weights could be applied to the NiTi wires so that a greater stress dependence on the low-temperature side of the resistivity peak could be seen and investigated.

4.4 Summary

Two runs were done on the HIPD to observe the austenite phase of NiTi. They both showed a large amount of preferred orientation with the [111] direction along the wire axis. Five runs were done to determine the characteristics of the martensite phase, three on the NPD and two on the HIPD. While the NPD experiments were refined, the HIPD runs were inconclusive, probably because the correct preferred

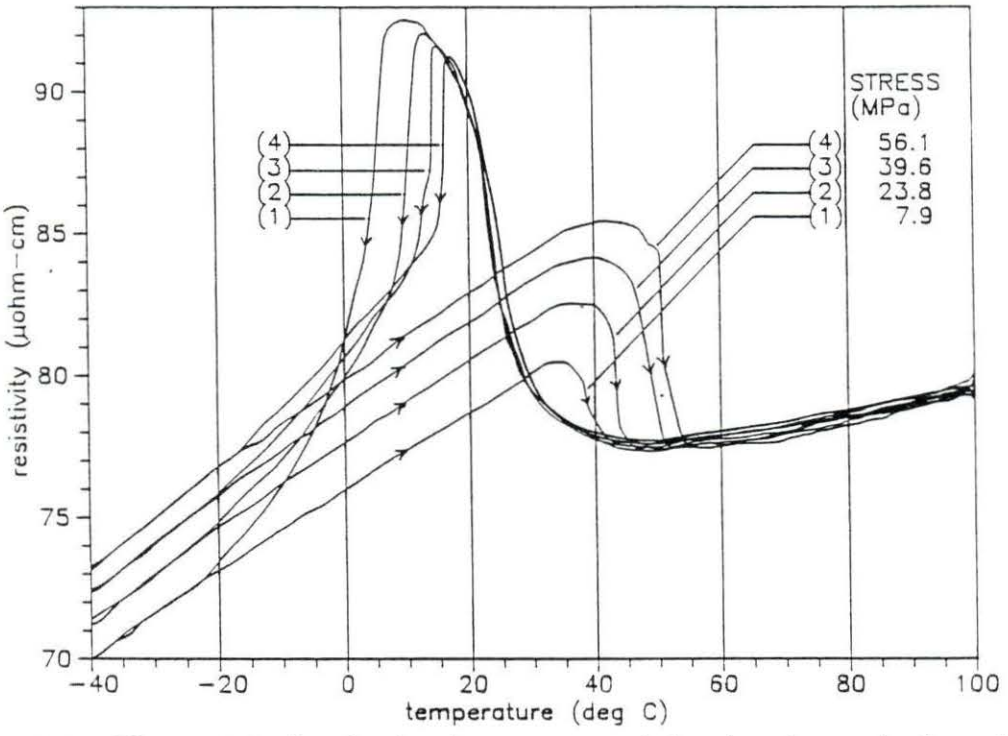

Figure 4.1: Figure 1.5 after having been corrected for the change in form factor, assuming constant volume (See Appendix B)

orientation axis was not known. Finally, three experiments were performed on the HIPD to investigate the presence of the R phase and determine how different stress levels affected the sample. These refinements were also inconclusive because of the problems encountered with the martensite experiments mentioned above and because the correct rhombohedral space group was apparently not known.

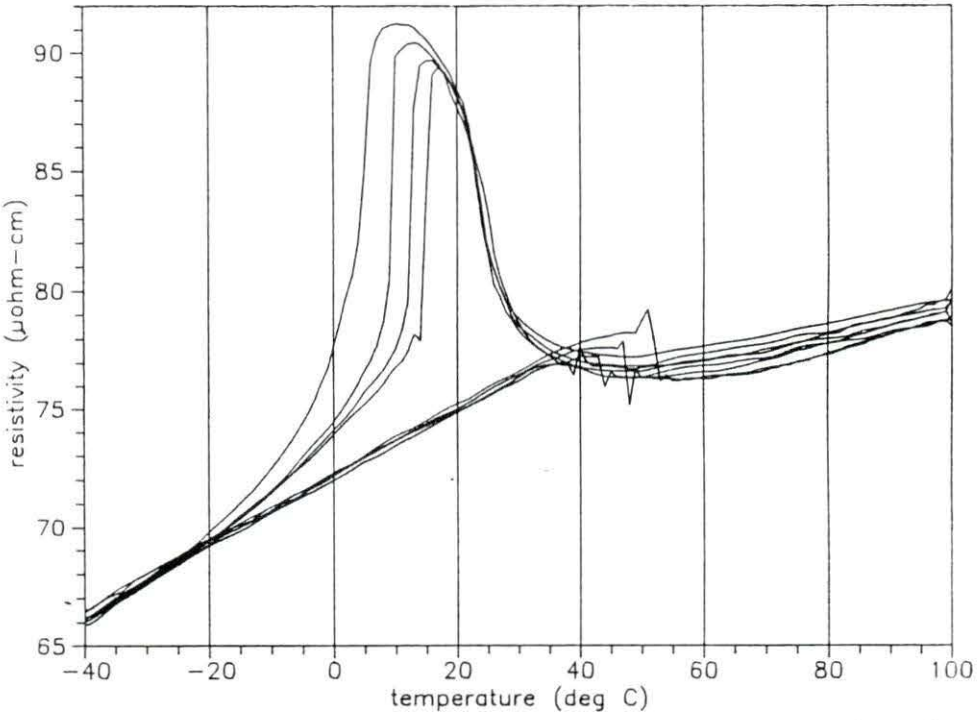

Figure 4.2: Figure 1.5 which has been corrected for the change in form factor, assuming a 191 % increase in the strain values (See Appendix B)

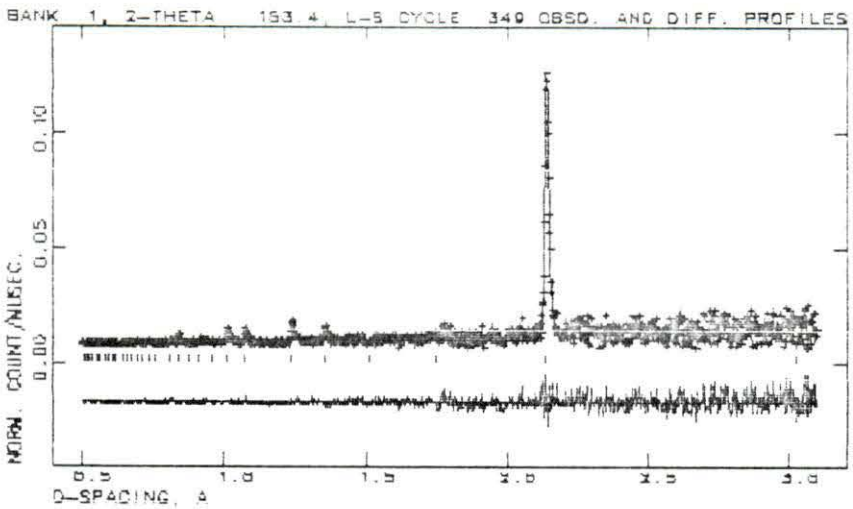

Figure 4.3: Diffraction profile for run 526 on the HIPD showing the 0.5Å to 3.1Å region from the $+153^{\circ}$ detector bank

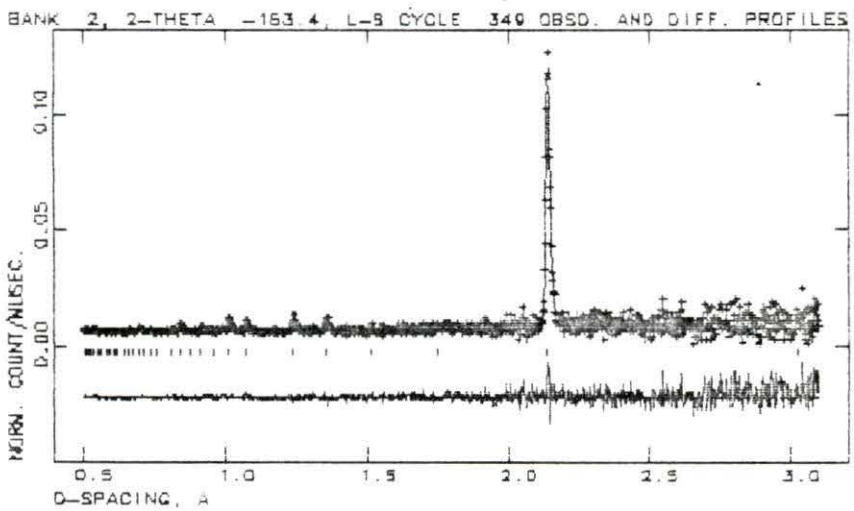

Figure 4.4: Diffraction profile for run 526 on the HIPD showing the 0.5Å to 3.1Å region from the -153° detector bank

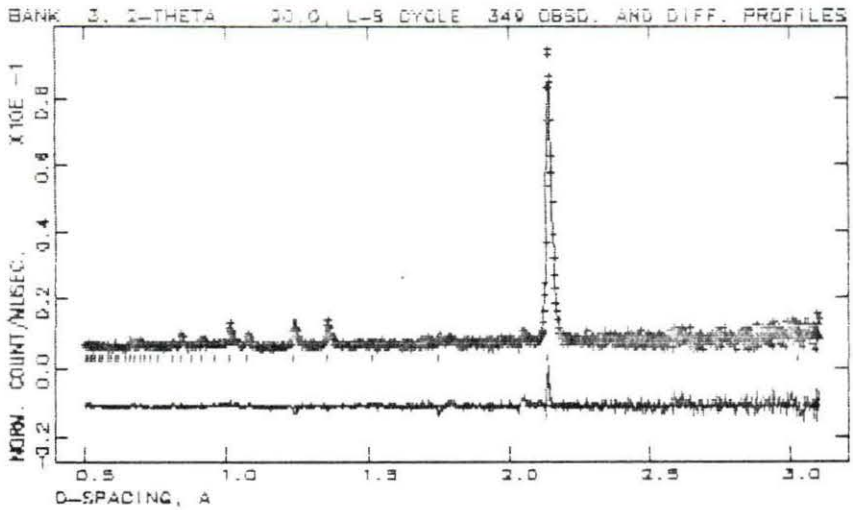

Figure 4.5: Diffraction profile for run 526 on the HIPD showing the 0.5Å to 3.1Å region from the $+90^{\circ}$ detector bank

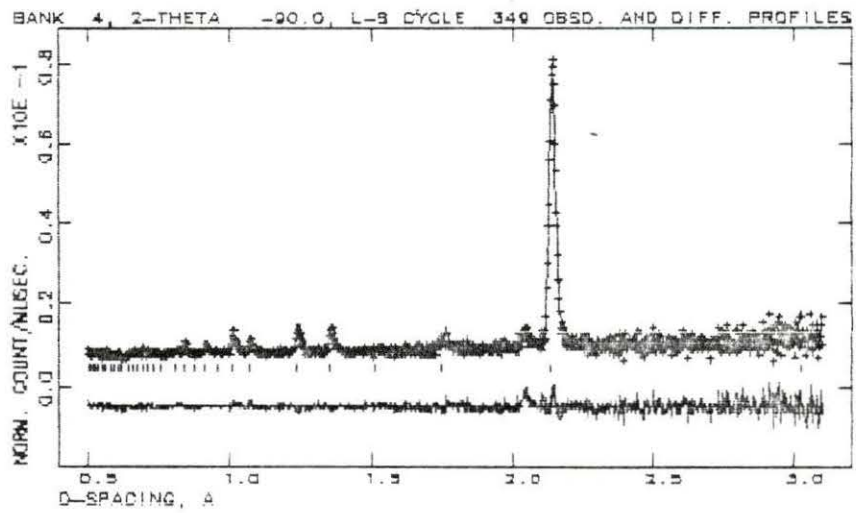

Figure 4.6: Diffraction profile for run 526 on the HIPD showing the 0.5Å to 3.1Å region from the -90° detector bank

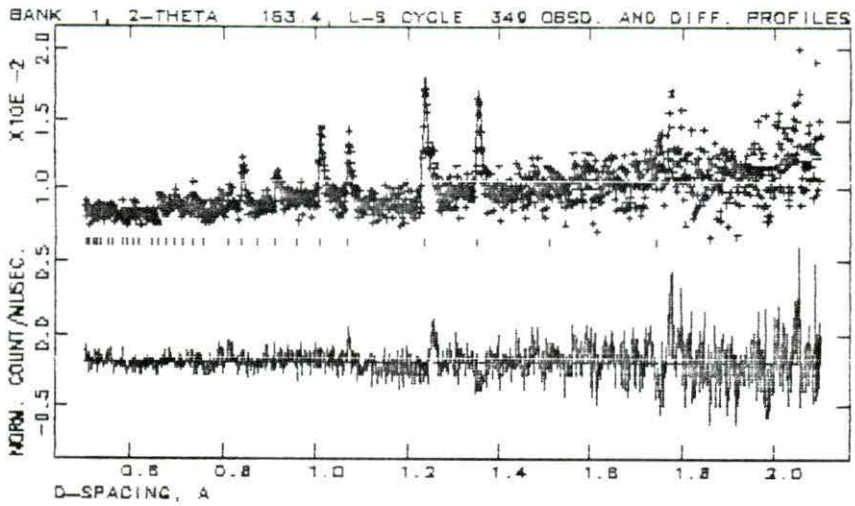

Figure 4.7: Diffraction profile for run 526 on the HIPD showing the 0.5Å to 2.1Å region from the $+153^{\circ}$ detector bank

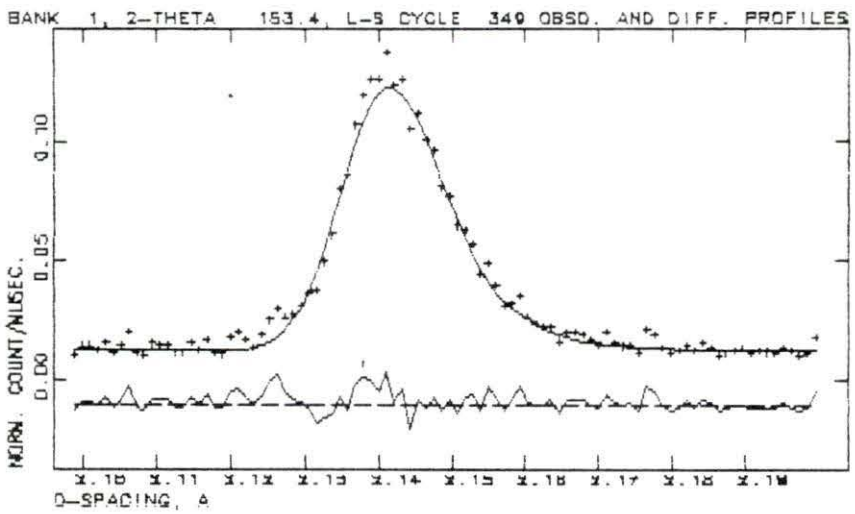

Figure 4.8: Diffraction profile for run 526 on the HIPD showing the 2.1Å to 2.2Å region from the $+153^{\circ}$ detector bank

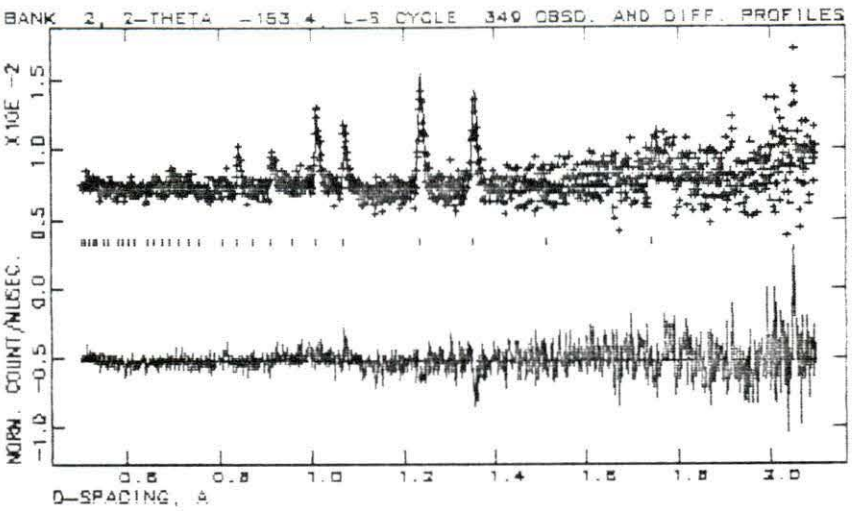

Figure 4.9: Diffraction profile for run 526 on the HIPD showing the 0.5Å to 2.1Å region from the -153° detector bank

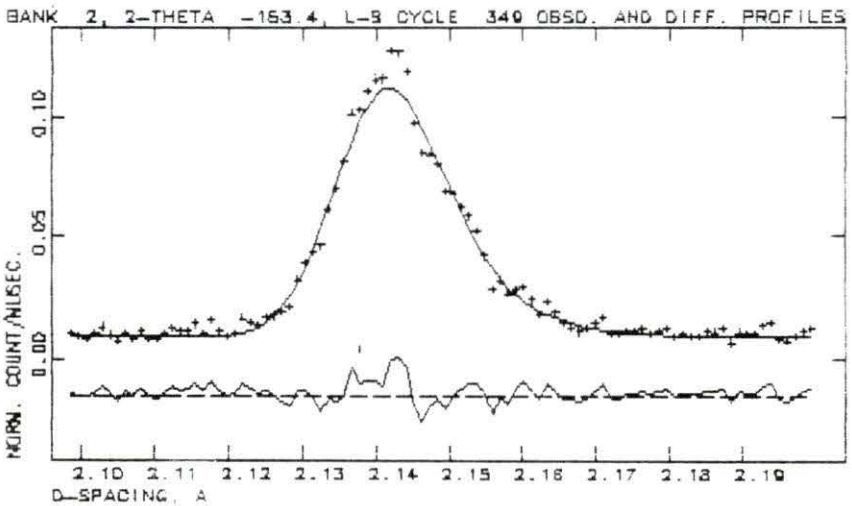

Figure 4.10: Diffraction profile for run 526 on the HIPD showing the 2.1Å to 2.2Å region from the -153° detector bank

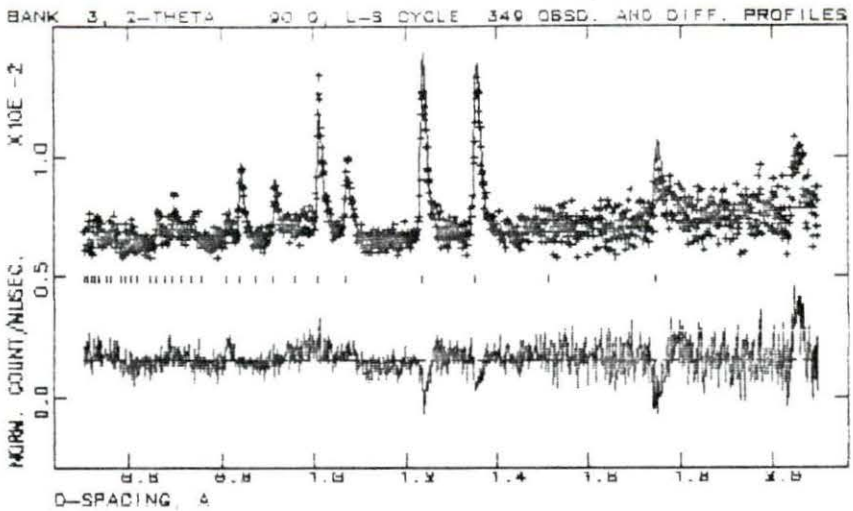

Figure 4.11: Diffraction profile for run 526 on the HIPD showing the 0.5Å to 2.1Å region from the $+90^{\circ}$ detector bank

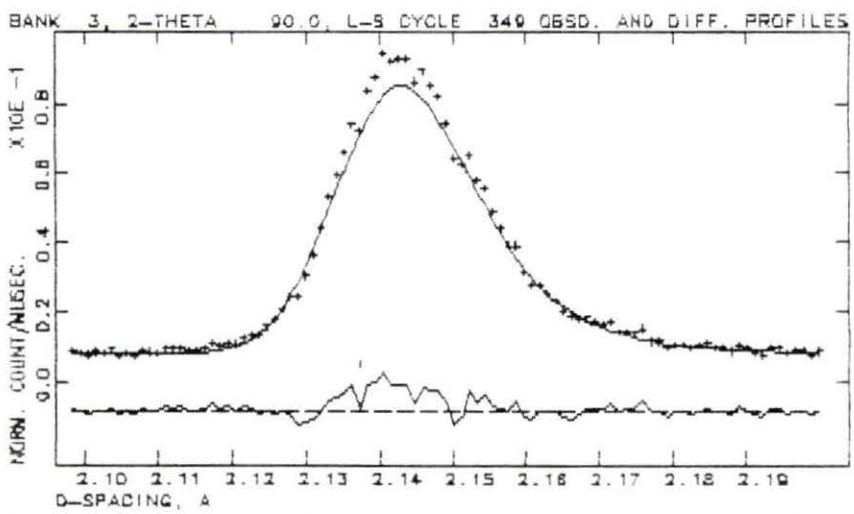

Figure 4.12: Diffraction profile for run 526 on the HIPD showing the 2.1Å to 2.2Å region from the $+90^{\circ}$ detector bank

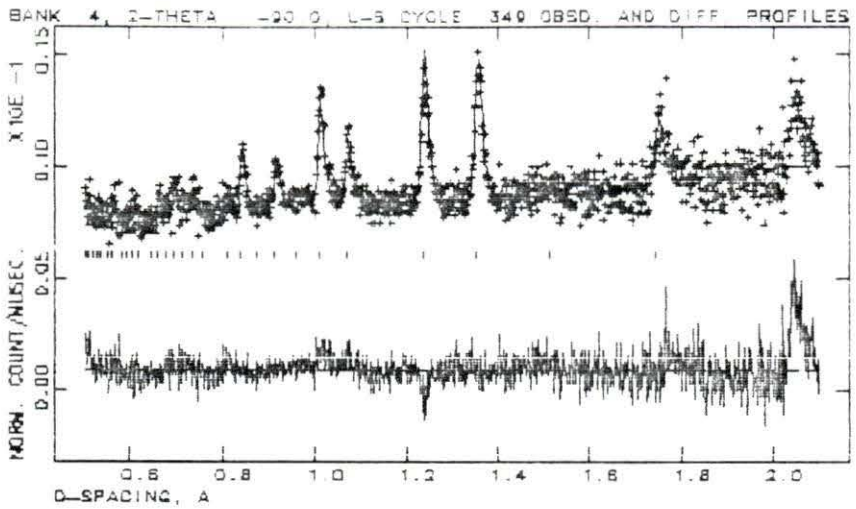

Figure 4.13: Diffraction profile for run 526 on the HIPD showing the 0.5Å to 2.1Å region from the -90° detector bank

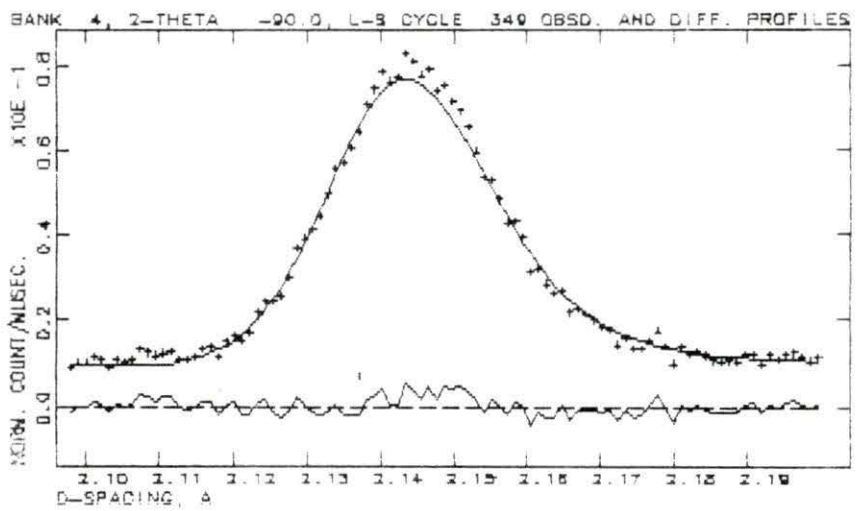

Figure 4.14: Diffraction profile for run 526 on the HIPD showing the 2.1Å to 2.2Å region from the -90° detector bank

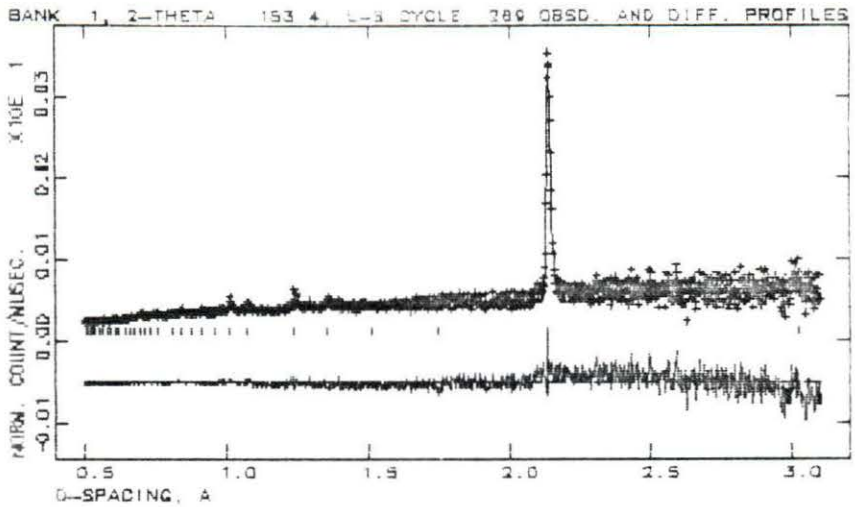

Figure 4.15: Diffraction profile for run 704 on the HIPD showing the 0.5Å to 3.1Å region from the $+153^{\circ}$ detector bank

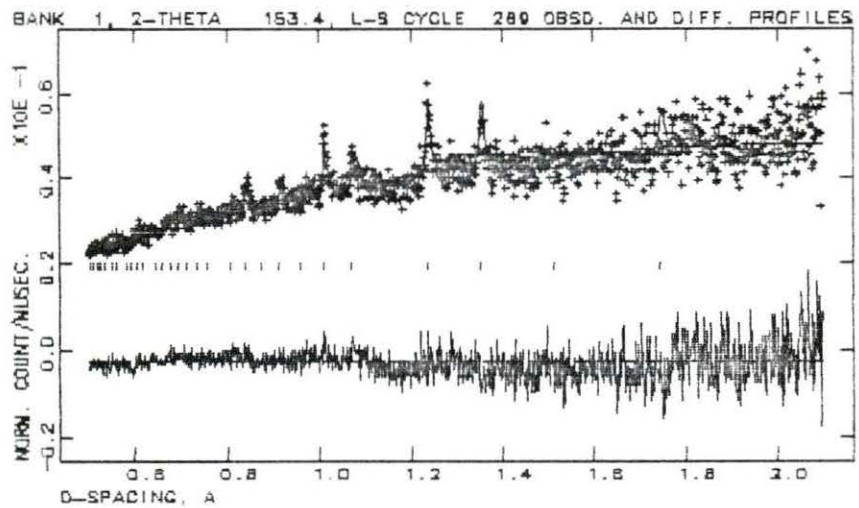

Figure 4.16: Diffraction profile for run 704 on the HIPD showing the 0.5Å to 2.1Å region from the $+153^{\circ}$ detector bank

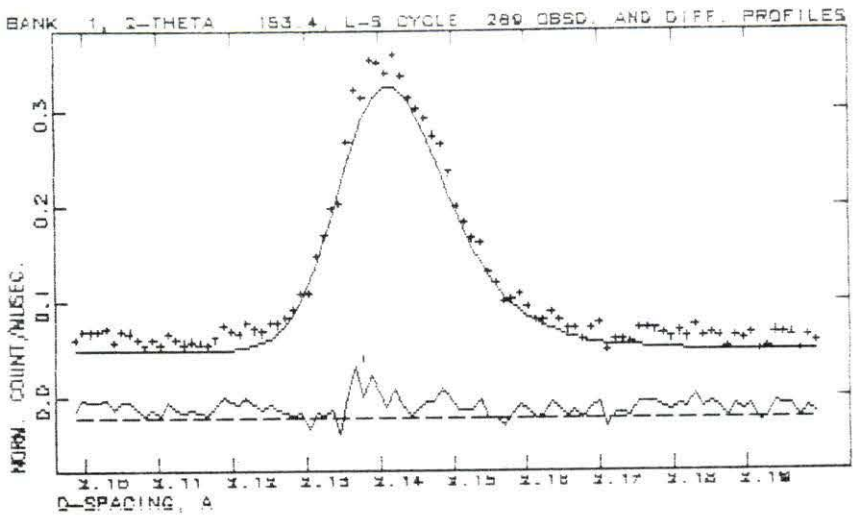

Figure 4.17: Diffraction profile for run 704 on the HIPD showing the 2.1Å to 2.2Å region from the $+153^{\circ}$ detector bank

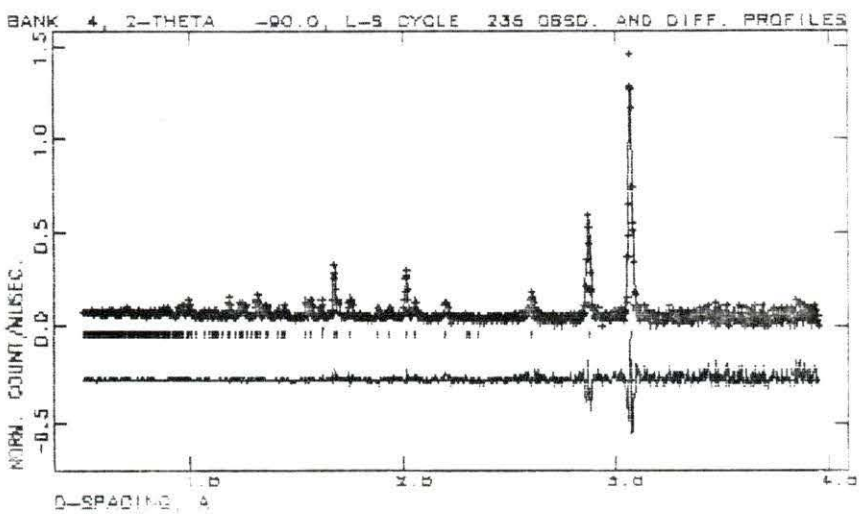

Figure 4.18: Diffraction profile for run 266 on the NPD showing the 0.5Å to 4.0Å region from the -90° detector bank

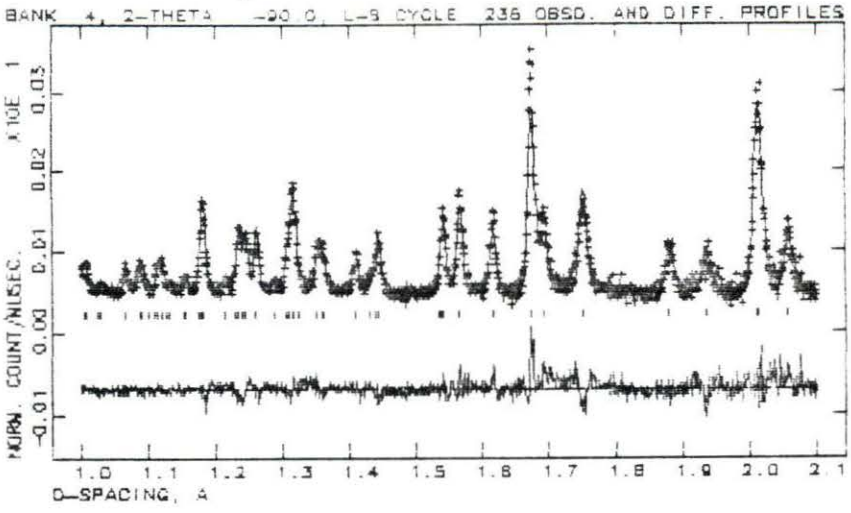

Figure 4.19: Diffraction profile for run 266 on the NPD showing the 1.0Å to 2.1Å region from the -90° detector bank

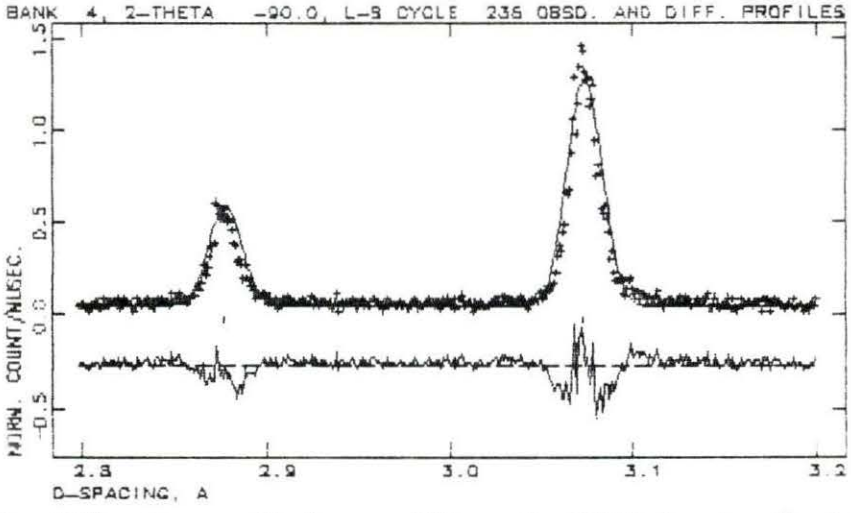

Figure 4.20: Diffraction profile for run 266 on the NPD showing the 2.8Å to 3.2Å region from the -90° detector bank

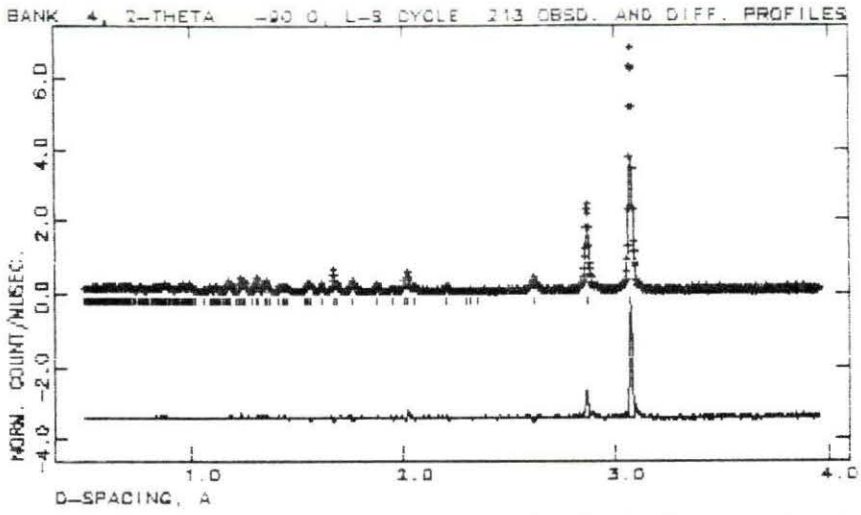

Figure 4.21: Diffraction profile for run 267 on the NPD showing the 0.5Å to 4.0Å region from the -90° detector bank

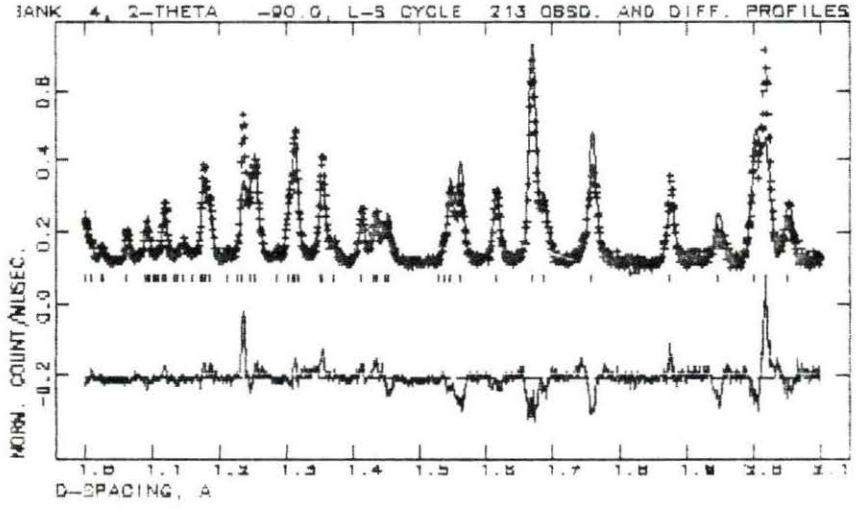

Figure 4.22: Diffraction profile for run 267 on the NPD showing the 1.0Å to 2.1Å region from the -90° detector bank

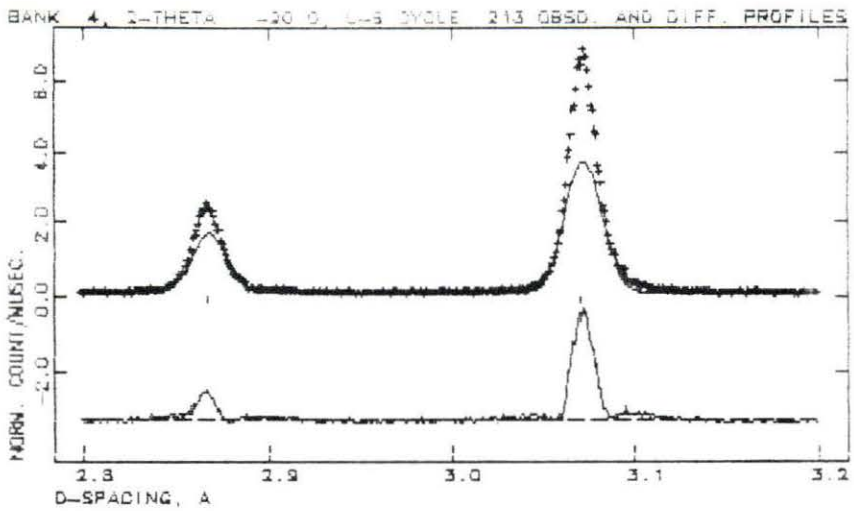

Figure 4.23: Diffraction profile for run 267 on the NPD showing the 2.8Å to 3.2Å region from the -90° detector bank

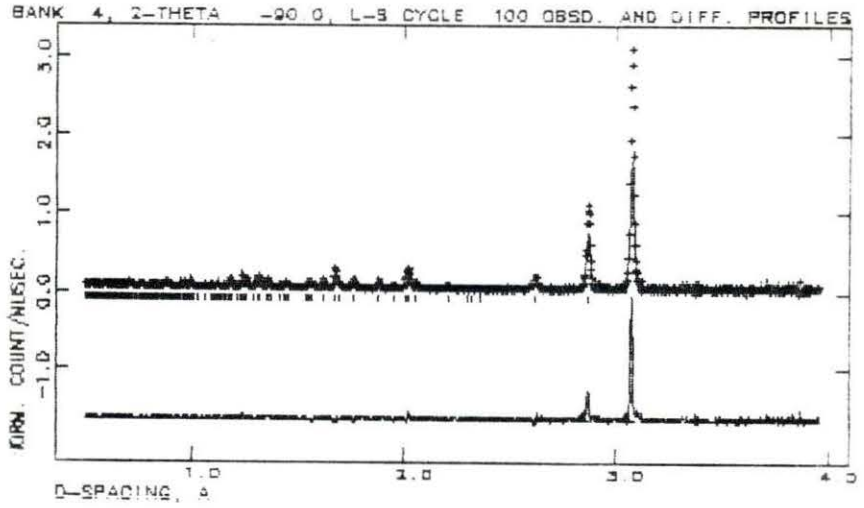

Figure 4.24: Diffraction profile for run 268 on the NPD showing the 0.5Å to 4.0Å region from the -90° detector bank

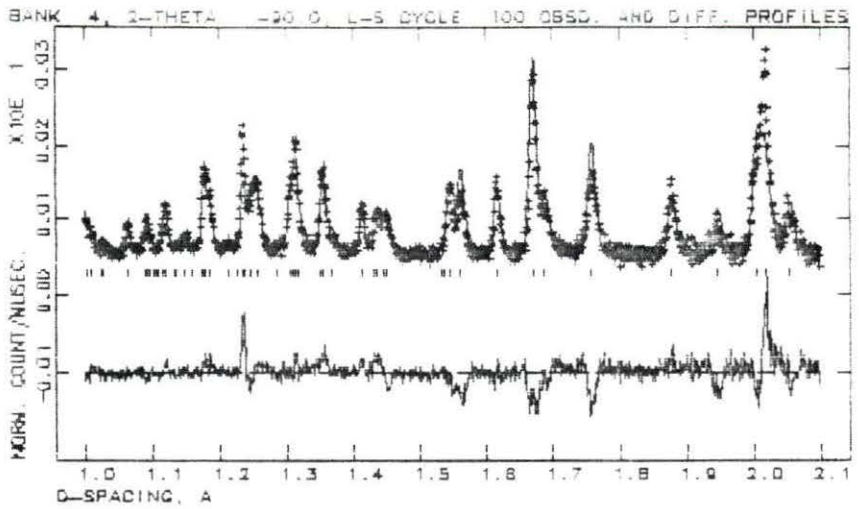

Figure 4.25: Diffraction profile for run 268 on the NPD showing the 1.0Å to 2.1Å region from the -90° detector bank

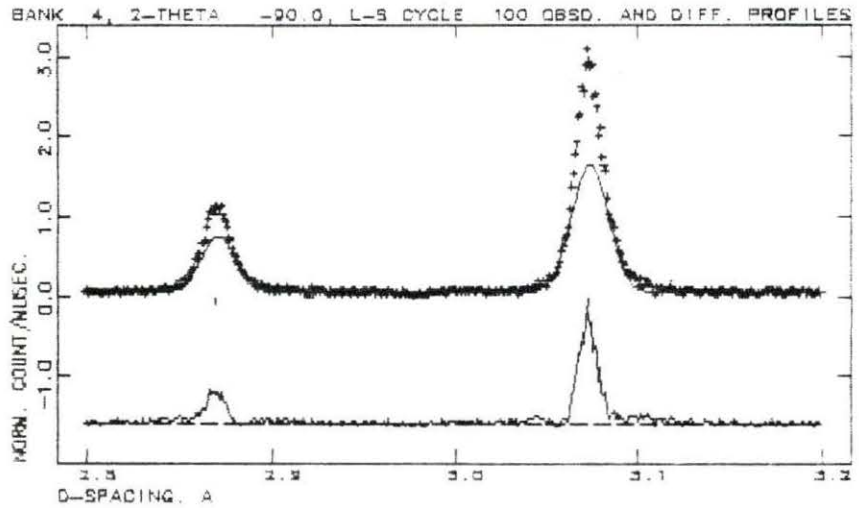

Figure 4.26: Diffraction profile for run 268 on the NPD showing the 2.8Å to 3.2Å region from the -90° detector bank

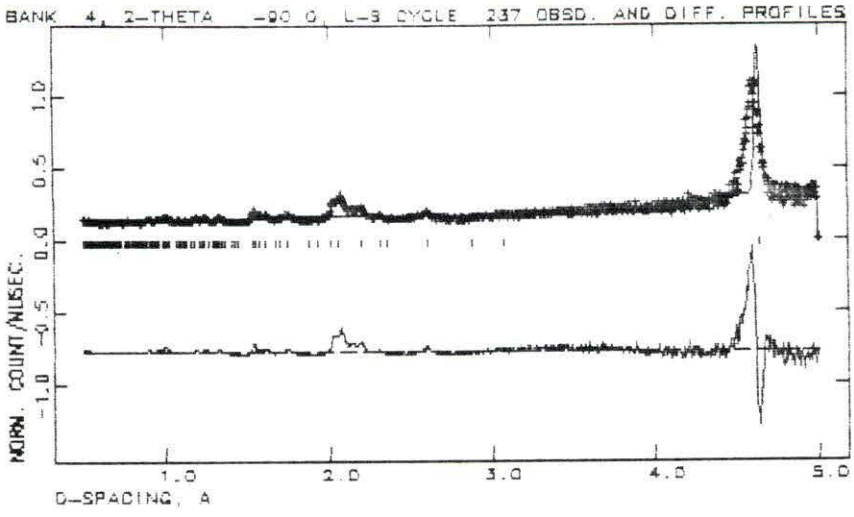

Figure 4.27: Diffraction profile for run 709 on the HIPD showing the 0.5Å to 5.0Å region from the -90° detector bank

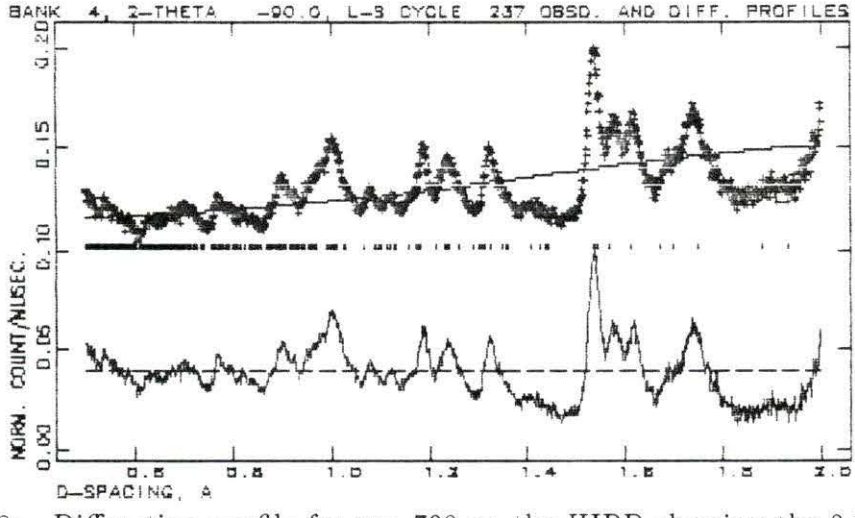

Figure 4.28: Diffraction profile for run 709 on the HIPD showing the 0.5Å to 2.0Å region from the -90° detector bank

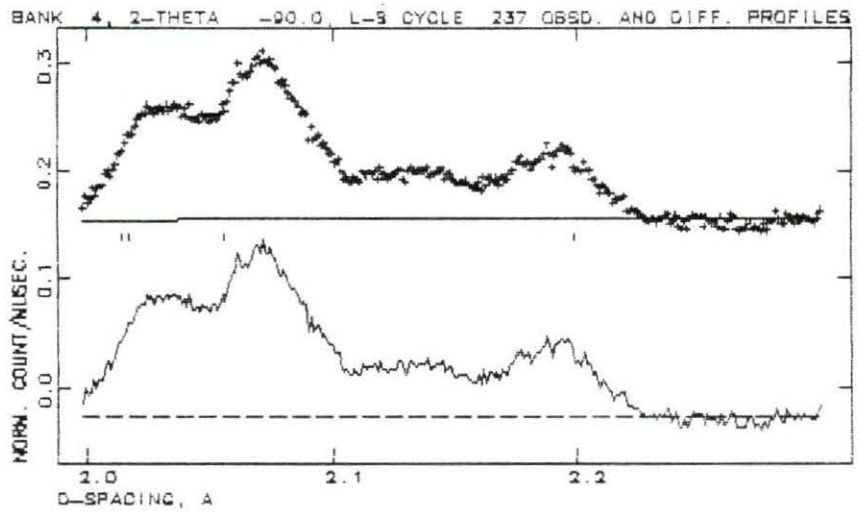

Figure 4.29: Diffraction profile for run 709 on the HIPD showing the 2.0Å to 2.3Å region from the -90° detector bank

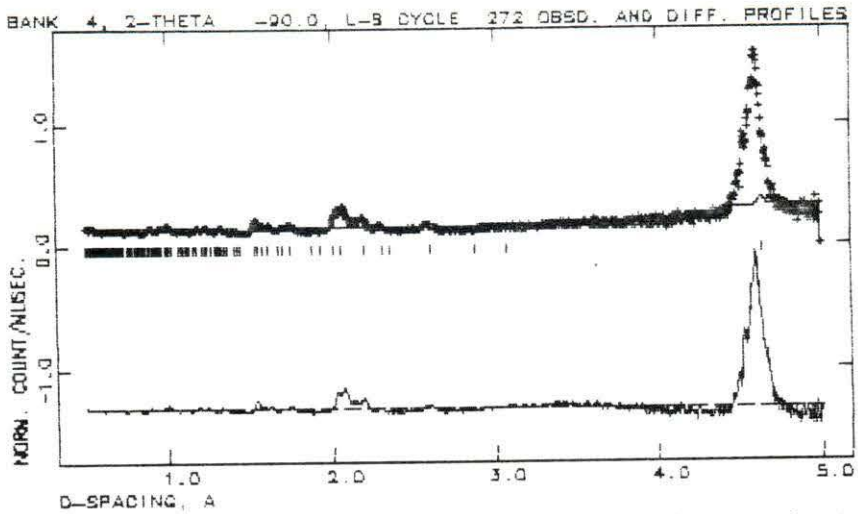

Figure 4.30: Diffraction profile for run 710 on the HIPD showing the 0.5Å to 5.0Å region from the -90° detector bank

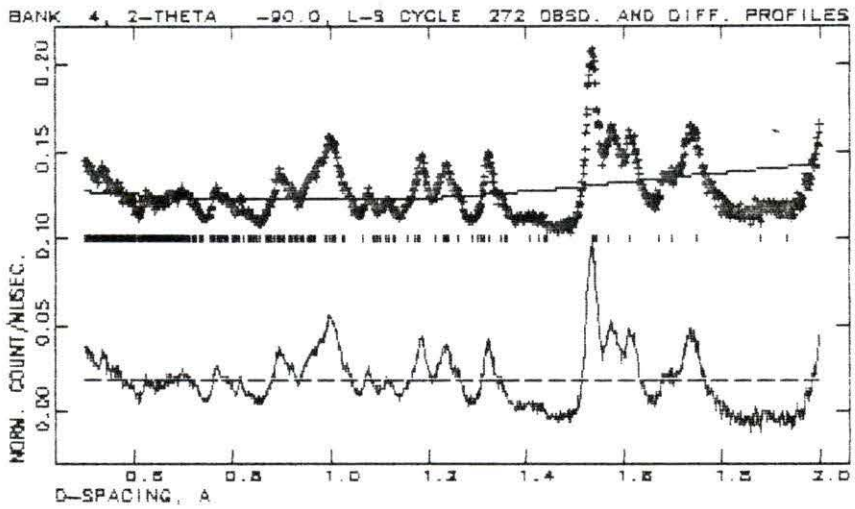

Figure 4.31: Diffraction profile for run 710 on the HIPD showing the 0.5Å to 2.0Å region from the -90° detector bank

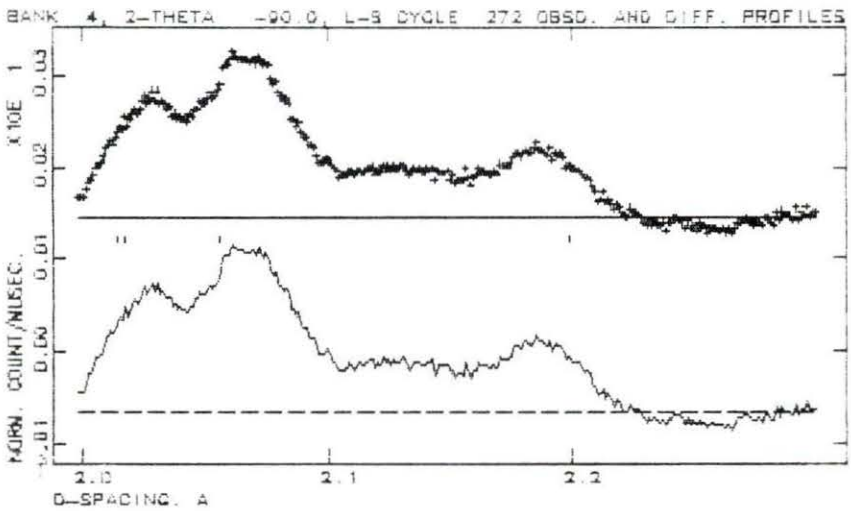

Figure 4.32: Diffraction profile for run 710 on the HIPD showing the 2.0Å to 2.3Å region from the -90° detector bank

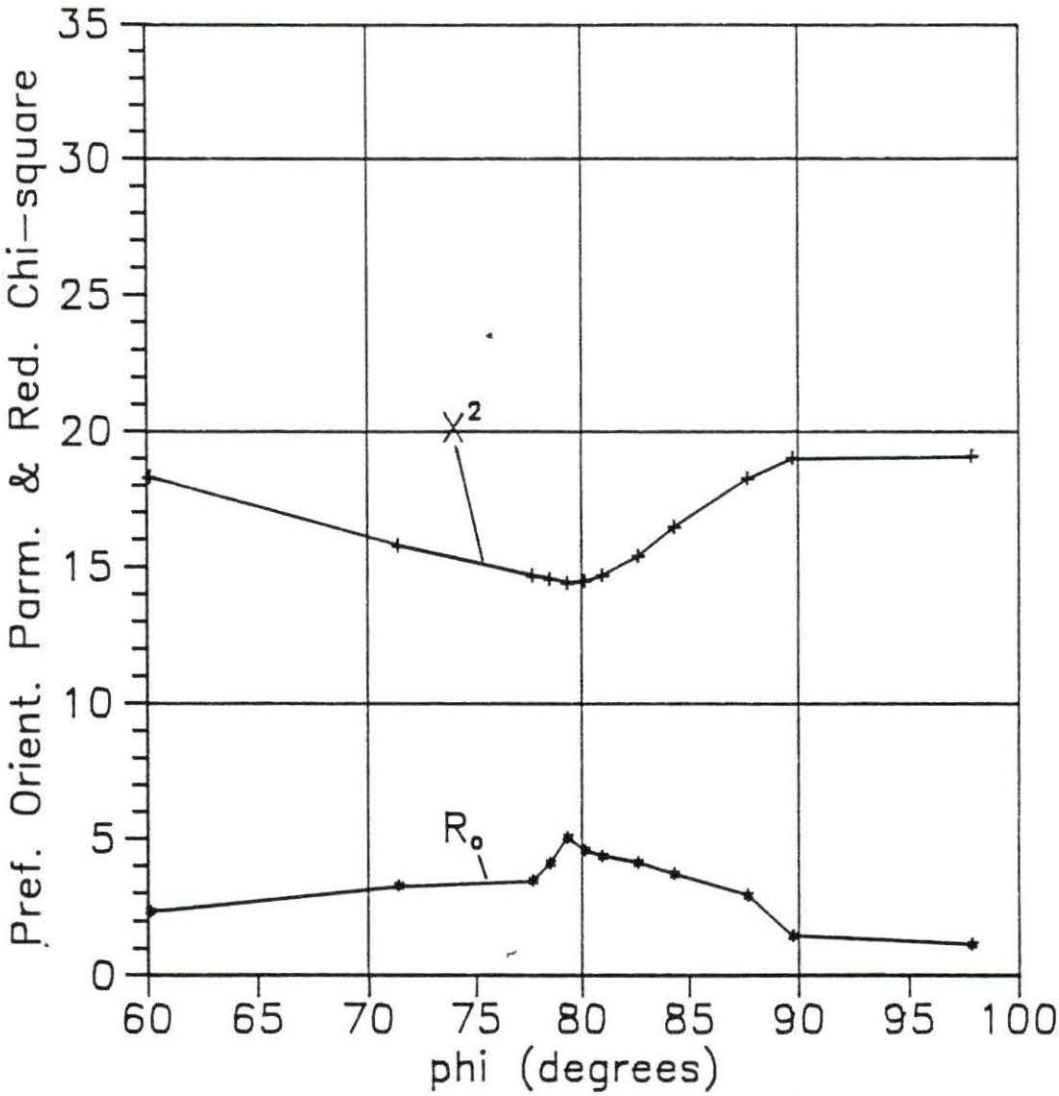

Figure 4.33: Preferred orientation parameter, R_O, and χ^2 as a function of ϕ for run 709

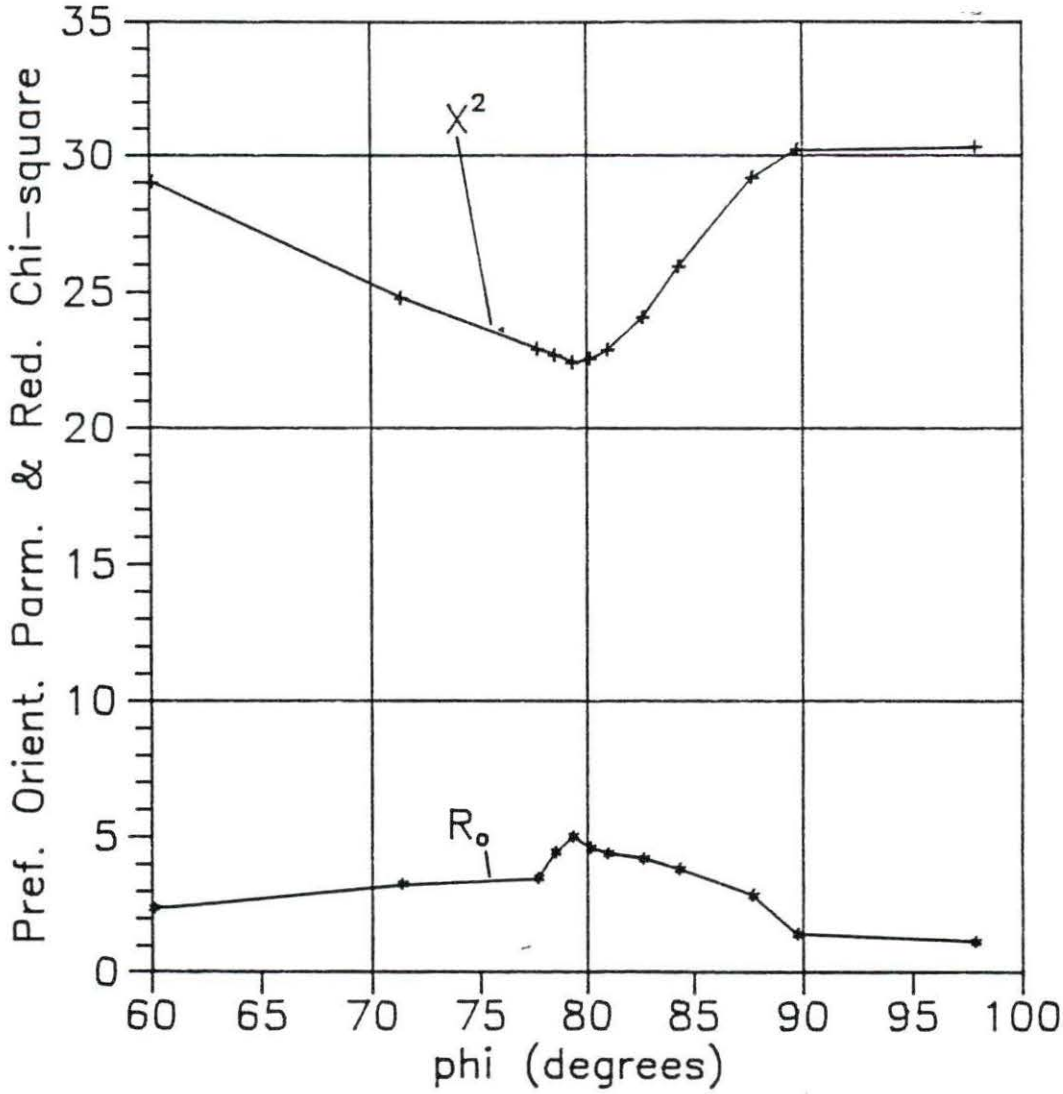

Figure 4.34: Preferred orientation parameter, R_O, and χ^2 as a function of ϕ for run 710

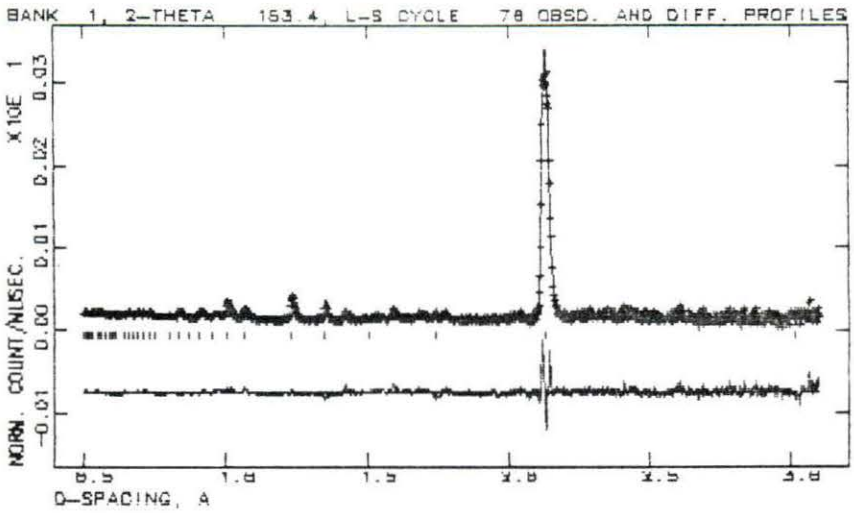

Figure 4.35: Diffraction profile for run 527530 on the HIPD showing the 0.5Å to 3.1Å region from the $+153^{\circ}$ detector bank ($Pm3m$ space group)

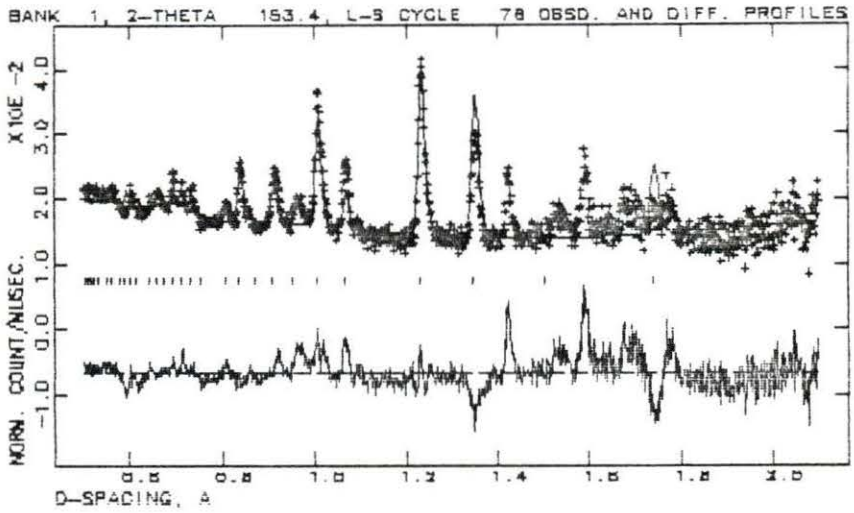

Figure 4.36: Diffraction profile for run 527530 on the HIPD showing the 0.5Å to 2.1Å region from the $+153^{\circ}$ detector bank ($Pm3m$ space group)

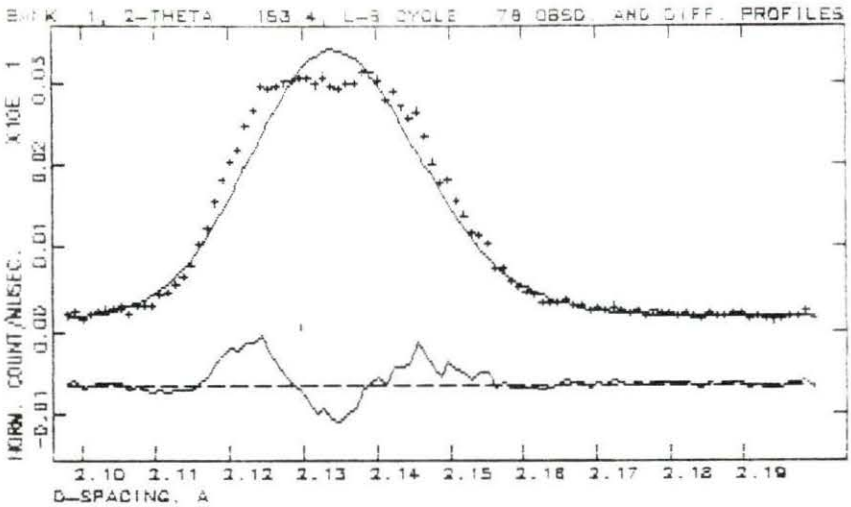

Figure 4.37: Diffraction profile for run 527530 on the HIPD showing the 2.1Å to 2.2Å region from the $+153^{\circ}$ detector bank ($Pm3m$ space group)

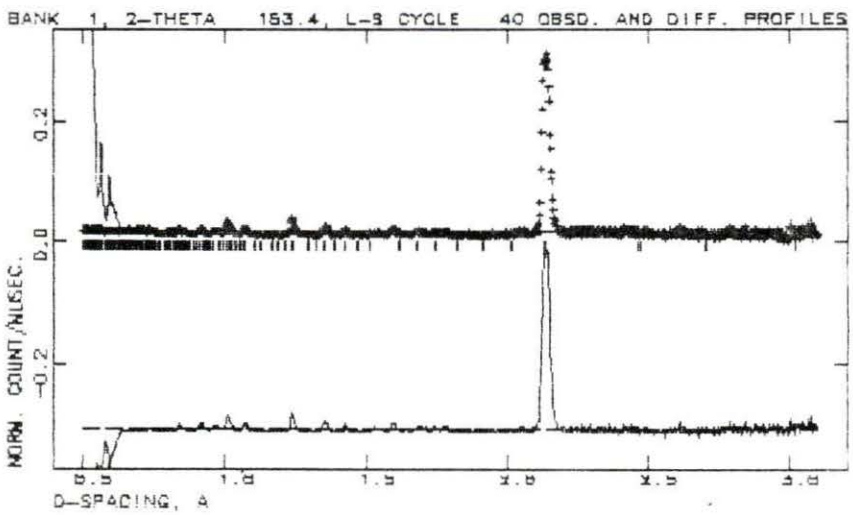

Figure 4.38: Diffraction profile for run 527530 on the HIPD showing the 0.5Å to 3.1Å region from the $+153^{\circ}$ detector bank ($R\bar{3}mr$ space group)

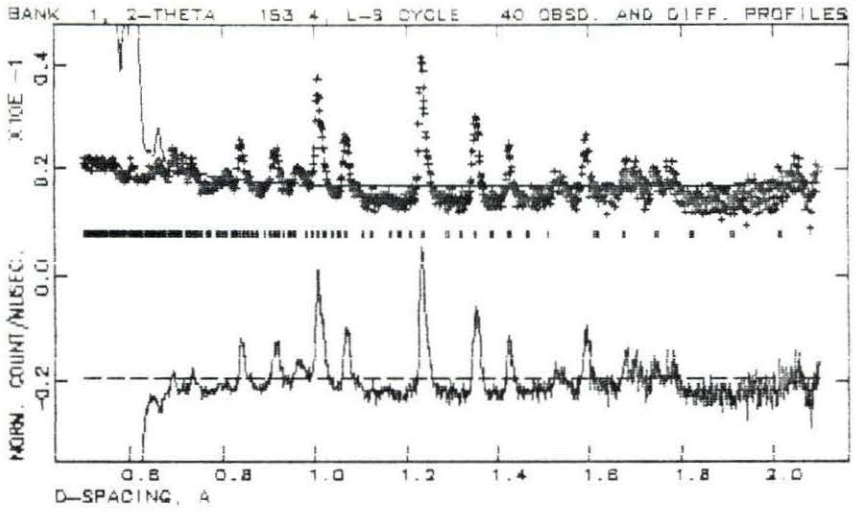

Figure 4.39: Diffraction profile for run 527530 on the HIPD showing the 0.5Å to 2.1Å region from the $+153^{\circ}$ detector bank ($R\bar{3}mr$ space group)

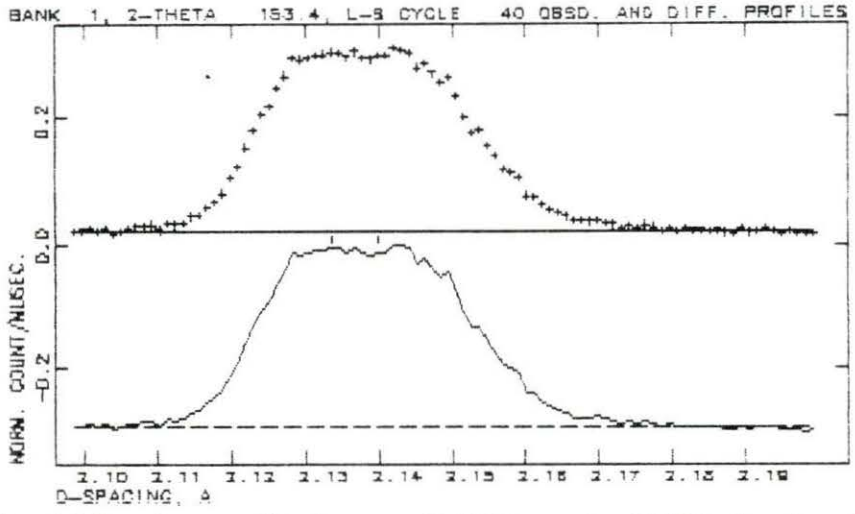

Figure 4.40: Diffraction profile for run 527530 on the HIPD showing the 2.1Å to 2.2Å region from the $+153^{\circ}$ detector bank ($R\bar{3}mr$ space group)

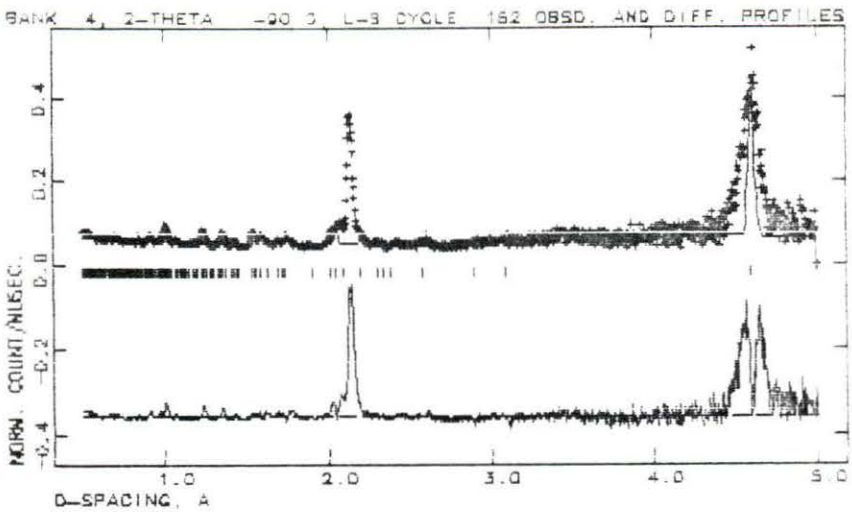

Figure 4.41: Diffraction profile for run 705706 on the HIPD showing the 0.5Å to 5.0Å region from the -90° detector bank ($P2_1/m$ space group)

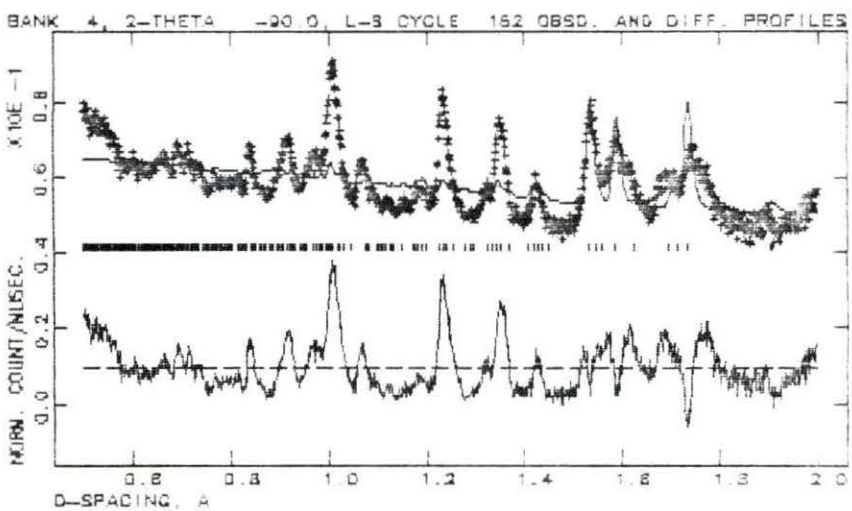

Figure 4.42: Diffraction profile for run 705706 on the HIPD showing the 0.5Å to 2.0Å region from the -90° detector bank ($P2_1/m$ space group)

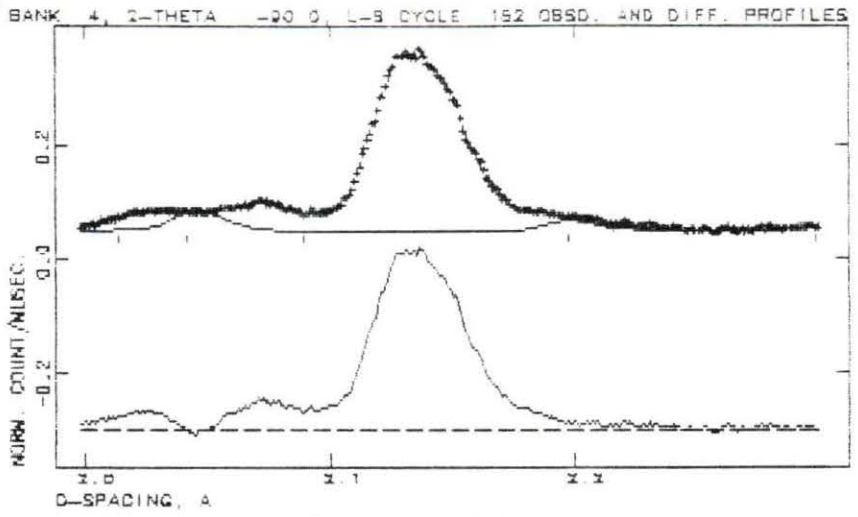

Figure 4.43: Diffraction profile for run 705706 on the HIPD showing the 2.0Å to 2.3Å region from the -90° detector bank ($P2_1/m$ space group)

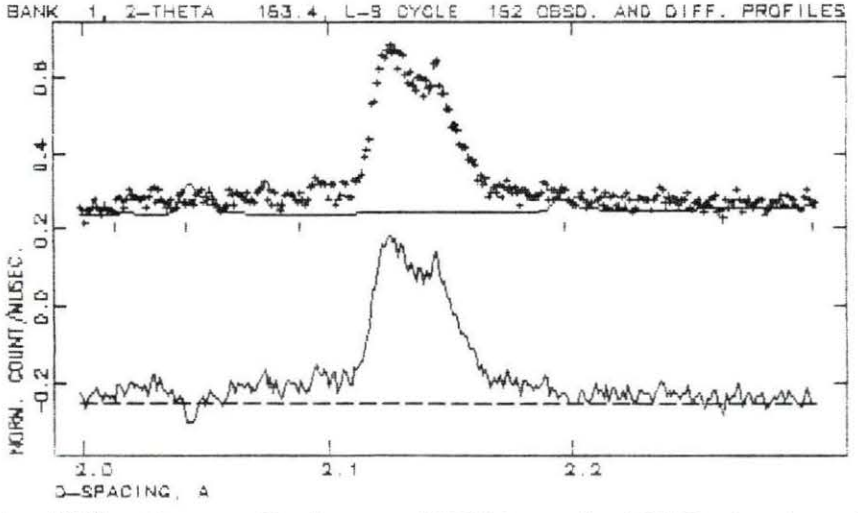

Figure 4.44: Diffraction profile for run 705706 on the HIPD showing the 2.0Å to 2.3Å region from the $+153^\circ$ detector bank ($P2_1/m$ space group)

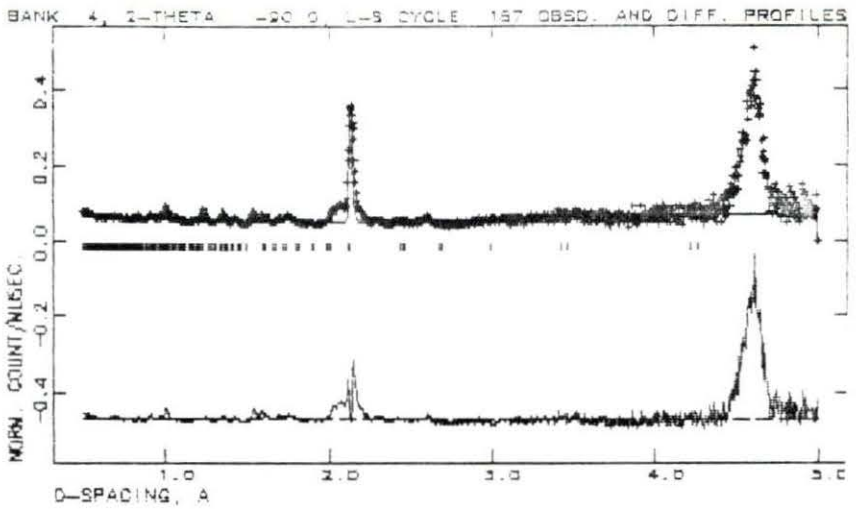

Figure 4.45: Diffraction profile for run 705706 on the HIPD showing the 0.5Å to 5.0Å region from the -90° detector bank ($R\bar{3}mr$ space group)

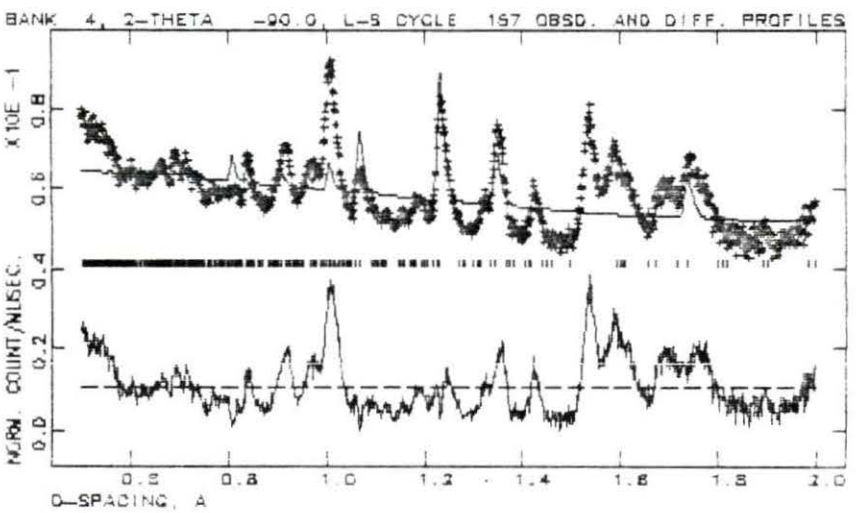

Figure 4.46: Diffraction profile for run 705706 on the HIPD showing the 0.5Å to 2.0Å region from the -90° detector bank ($R\bar{3}mr$ space group)

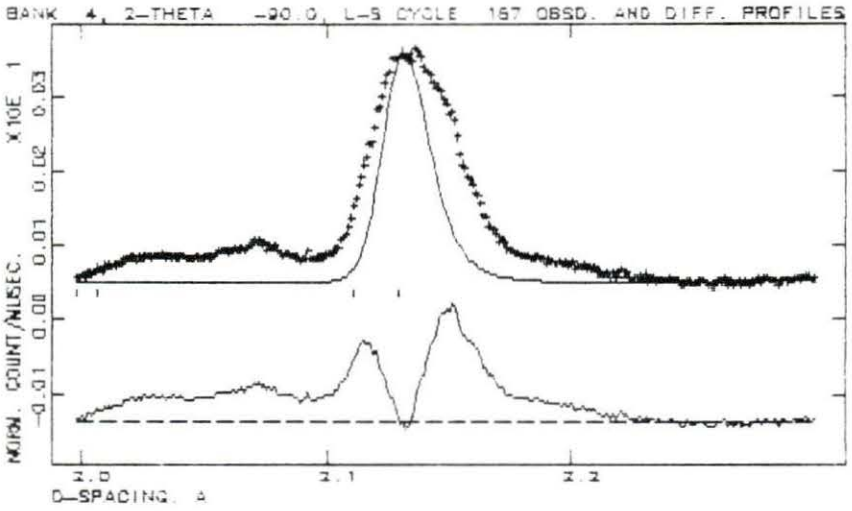

Figure 4.47: Diffraction profile for run 705706 on the HIPD showing the 2.0Å to 2.3Å region from the -90° detector bank ($R\bar{3}mr$ space group)

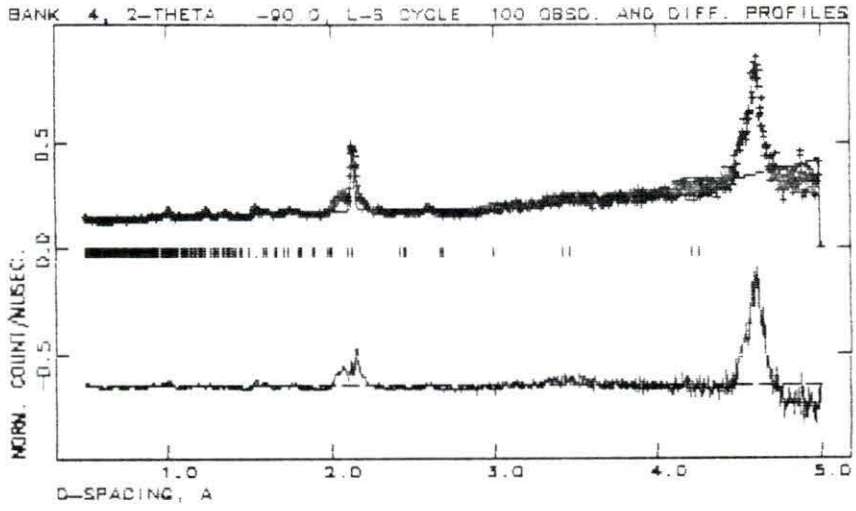

Figure 4.48: Diffraction profile for run 707708 on the HIPD showing the 0.5Å to 5.0Å region from the -90° detector bank ($R\bar{3}mr$ space group)

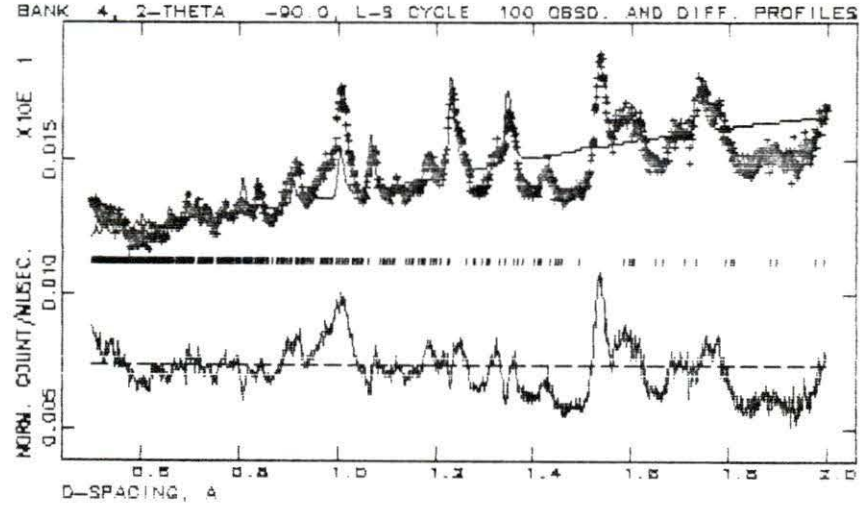

Figure 4.49: Diffraction profile for run 707708 on the HIPD showing the 0.5Å to 2.0Å region from the -90° detector bank ($R\bar{3}mr$ space group)

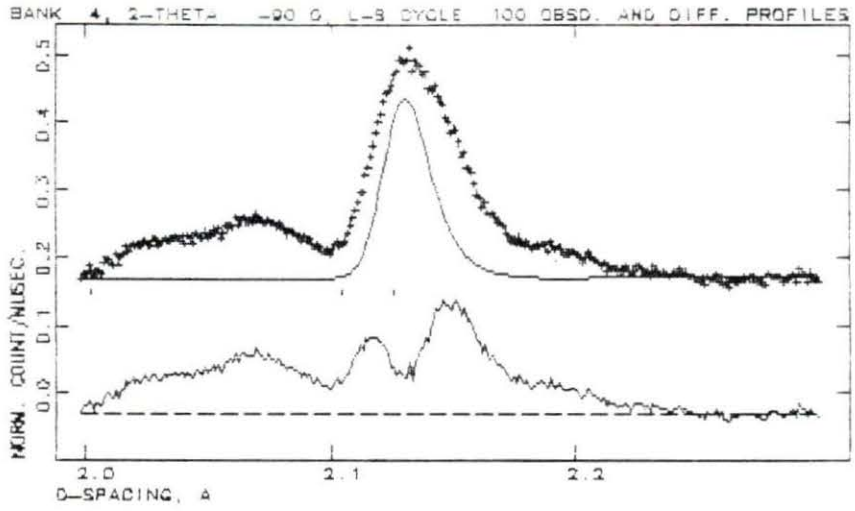

Figure 4.50: Diffraction profile for run 707708 on the HIPD showing the 2.0Å to 2.3Å region from the -90° detector bank ($R\bar{3}mr$ space group)

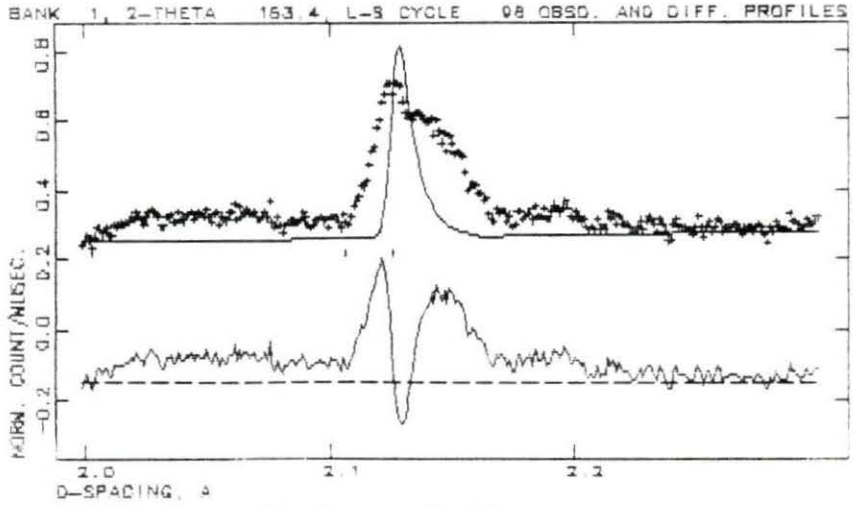

Figure 4.51: Diffraction profile for run 707708 on the HIPD showing the 2.0Å to 2.3Å region from the $+153^{\circ}$ detector bank ($R\bar{3}mr$ space group)

5. CONCLUSIONS

Several conclusion may be made from this work:

1. The strain-corrected electrical resistivity based on earlier work of Hsu [47] of nearly equiatomic nickel-titanium shows stress dependence on the low-temperature side of the anomalous resistivity peak that appears on cooling whereby the resistivity peak narrows with increasing tensile stress. In addition, the strain-corrected resistivity of single-phase martensitic NiTi was found to increase with increasing tensile stress.

2. The unit cell of the austenitic phase of NiTi was found to be described by the $Pm3m$ space group (B2 or CsCl structure) with $a = 3.023(3)$Å for the wire samples used in this study. This is in good agreement with the commonly accepted lattice parameter of 3.015Å (see, for example, Bührer *et al.* [20]). Differences in composition may explain the lattice parameter differences. In addition, the wires showed a large amount of preferred orientation with the $< 111 >$ direction along the wire axis.

3. For the yttrium-doped, NiTi sample, the space group of the martensite was determined to be $P2_1/m$ (monoclinic or distorted B19 structure) with the following lattice parameters: $a = 2.9036(8)$Å, $b = 4.116(1)$Å, $c = 4.663(1)$Å and $\beta = 97.836(2)^\circ$. Anisotropic thermal parameters were used to describe the thermal motion of the atoms. The martensite phase in the NiTi wires also seemed to show preferred orien-

tation, although the texture axis was not determined. This is in fairly good agreement with both x-ray and neutron diffraction work done by other researchers, particularly by Bührer *et al.* [20]. There was no success in applying the martensite structures proposed by Otsuka *et al.* [22] or by Golestaneh and Carpenter [39].

4. Upon cooling the wires to the high-temperature side of the anomalous resistivity peak (about 29°C), the 110 austenite reflection appeared to broaden. Upon further cooling to the low-temperature side of the anomalous resistivity peak (about 18°C), the 110 austenite reflection appeared to show early stages of splitting into two separate reflections, in agreement with work done by Ling and Kaplow [41]-[44]. This is considered to be due to the distortion of the austenite unit cell into a rhombohedral one. Furthermore, martensite peaks began to appear at about 18°C. For the two stress levels applied (1.9 and 4.5 MPa), no difference in the results was detected.

6. BIBLIOGRAPHY

[1] *Webster's New World Dictionary of the American Language*, Second College Edition, D. B. Guralnik, Editor-in-Chief (William Collins + World Publishing, Cleveland, 1978).

[2] Z. Nishiyama, *Martensitic Transformations* (Academic Press, New York, 1978).

[3] W. F. Smith, *Structure and Properties of Engineering Alloys* (McGraw-Hill, New York, 1981).

[4] K. Shimizu and T. Tadaki, "Shape Memory Effect: Mechanism," in *Shape Memory Alloys*, edited by H. Funakubo (Gordon and Breach, New York, 1987) pp. 1-60.

[5] R. J. Wasilewski, "Stress-Assisted Martensite Formation in TiNi," *Scripta Met.* **5**, 127-130 (1971).

[6] R. J. Wasilewski, "The Effects of Applied Stress on the Martensitic Transformation in TiNi," *Met. Trans.* **2**, 2973-2981 (1971).

[7] P. Ramon, "The Transformation Strain Dependence on Applied Stress in Equiatomic Nickel-Titanium Alloys of Powder Metallurgical Origin," Ph.D. Dissertation, Iowa State University, 1983.

[8] J. W. Christian, *The Theory of Transformations in Metals and Alloys* (Pergamon Press, Oxford, 1965).

[9] M. S. Wechsler, D. S. Lieberman and T. A. Read, "On the Theory of the Formation of Martensite," *J. of Metals* **197**, 1503-1515 (1953).

[10] D. S. Lieberman, M. S. Wechsler, and T. A. Read, "Cubic to Orthorhombic Diffusionless Phase Change–Experimental and Theoretical Studies of AuCd," *J. Appl. Phys.* **26**, No. 4, 473-484 (1955).

[11] F. E. Wang and W. J. Buehler, "Additional Unique Property Changes Observed during TiNi Transitions," *Appl. Phys. Lett.* **21**, No. 3, 105-106 (1972).

[12] L. M. Schetky, "Shape-Memory Alloys," *Sci. Am.* **241**, No. 5, 74-82 (1979).

[13] R. Banks, "Nitinol Heat Engines," in *Shape Memory Effects in Alloys*, edited by J. Perkins (Plenum Press, New York, 1975), pp. 537-545.

[14] J. Walker, "The Amateur Scientist: Wire That 'Remembers' its Shape," *Sci. Am.* **254**, No. 5, 124-127 (1986).

[15] M. S. Wechsler, "Shape Memory Alloys and Their Application to Automotive Systems," in *Proceedings of the Second Seminar and Exhibition on Innovation in Materials and Application in the Transportation Industry*, ATA-MAT 89, Vol. II. (Associazione Tecnica dell'Automobile, Turin, Italy, 1989) pp. 1-25.

[16] Y. Suzuki, "Application of Shape Memory Alloys," in *Shape Memory Alloys*, edited by H. Funakubo (Gordon and Breach, New York, 1987), pp. 176-225.

[17] M. S. Wechsler and S. T. Carey, Energy Beam Position Detector, U. S. patent pending.

[18] F. J. Wyant, "The Application of Low Temperature Heat Engines Using Shape Memory Alloys to Waste Heat Utilization in Electric Generating Power Plants," M. S. Thesis, Iowa State University, 1980.

[19] C. M. Wayman and K. Shimizu, "The Shape Memory ('Marmem') Effect in Alloys," *Metal Sci. J.* **6**, 175-183 (1972).

[20] W. Bührer, R. Gottardt and M. S. Wechsler, "The Influence of Applied Stress on the Martensitic Transformation in Ni-Ti," in *Proceedings of the International Conference on Martensitic Transformations*, ICOMAT-86 (The Japan Institute of Metals, Sendai, Japan, 1987).

[21] C. H. Hsu and M. S. Wechsler, " The Effect of Applied Stress on the Transformation Behavior of Ni-Ti," in *Proceedings of an International Conference on Solid-Solid Phase Transformations* (The Metallurgical Society of AIME, Warrendale, PA, 1982), pp. 1293-1297.

[22] K. Otsuka, T. Sawamura and K. Shimizu, "Crystal Structure and Internal Defects of Equiatomic TiNi Martensite," *Phys. Status Solidi (a)* **5**, 457-470 (1971).

[23] G. R. Purdy and J. G. Parr, "A Study of the Titanium-Nickel System between Ti_2Ni and TiNi," *Trans. of the Met. Soc. of AIME* **221**, 636-639 (1961).

[24] P. Duwez and J. L. Taylor, "The Structure of Intermediate Phases in Alloys of Titanium with Iron, Cobalt, and Nickel," *J. of Metals* **188**, 1173-1176 (1950).

[25] F. E. Wang, S. J. Pickart and H. A. Alperin, "Mechanism of the TiNi Martensitic Transformation and the Crystal Structures of TiNi-II and TiNi-III Phases," *J. Appl. Phys.* **43**, No. 1, 97-112 (1972).

[26] K. Chandra and G. R. Purdy, "Observations of Thin Crystals of TiNi in Pre-martensitic States," *J. Appl. Phys.* **39**, No. 5, 2176-2181 (1968).

[27] D. P. Dautovich and G. R. Purdy, "Phase Transformation in TiNi," *Canadian Met. Q.* **4**, No. 2, 129-143 (1965).

[28] T. V. Philip and P. A. Beck, "CsCl-Type Ordered Structures in Binary Alloys of Transition Alloys," *J. of Metals* **209**, 1269-1271 (1957).

[29] R. J. Wasilewski, S. R. Butler and J. E. Hanlon, "On the Martensitic Transformation in TiNi," *Metal Sci. J.* **1**, 104-110 (1967).

[30] K. M. Knowles and D. A. Smith, "The Crystallography of the Martensitic Transformation in Equiatomic Nickel-Titanium," *Acta Met.* **29**, 101-110 (1981).

[31] E. Goo and R. Sinclair, "The B2 to R Transformation in $Ti_{50}Ni_{47}Fe_3$ and $Ti_{49.5}Ni_{50.5}$ Alloys," *Acta Met.* **33**, No. 9, 1717-1723 (1985).

[32] R. F. Hehemann and G. D. Sandrock, "Relations between the Premartensitic Instability and the Martensite Structure in TiNi," *Scripta Met.* **5**, 801-806 (1971).

[33] G. M. Michal and R. Sinclair, "The Structure of TiNi Martensite," *Acta Crystallogr.* **B37**, 1803-1807 (1981).

[34] W. Bührer, R. Gotthardt, A. Kulik, O. Mercier and F. Staub, "Powder Neutron Diffraction Study of Nickel-Titanium Martensite," *J. Phys. F: Metal Physics* **13**, L77-L81 (1983).

[35] Y. Kudoh, M. Tokonami, S. Miyazaki and K. Otsuka, "Crystal Structure of the Martensite in Ti-49.2 at.% Ni Alloy Analyzed by the Single Crystal X-Ray Diffraction Method," *Acta Metall.* **33**, No. 11, 2049-2056 (1985).

[36] W. Bührer, R. Gottardt, A. Kulik and O. Mercier, "Neutron Diffraction Measurements in Equiatomic NiTi Alloys," *J. de Phys.* Colloque C4, Suppl. 12, **43**, C4-219 - C4-224 (1982).

[37] W. C. Hamilton, "On the Isotropic Temperature Factor Equivalent to a Given Anisotropic Temperature Factor," *Acta Crystallogr.* **12**, 609-613 (1959).

[38] T. Saburi, "Structure and Mechanical Behavior of Ti-Ni Shape Memory Alloys," in *Vol. 9, Shape Memory Materials*, edited by K. Otsuka and K. Shimizu (Materials Research Society, Pittsburgh, PA, 1989), pp. 77-91.

[39] A. A. Golestaneh and J. M. Carpenter, to be published in *Acta Metall.*

[40] H. Tietze, M. Müllner, P. Selgert and W. Assmus, "The Intermediate Phase of the Shape Memory Alloy NiTi," *J. Phys. F: Metal Physics* **15**, 263-271 (1985).

[41] H. C. Ling and R. Kaplow, "Phase Transitions and Shape Memory in NiTi," *Met. Trans. A* **11A**, 77-83 (1980).

[42] H. C. Ling and R. Kaplow, "Temperature-Controlled X-Ray Diffraction Stage for Simultaneous Monitoring of Structural and Dimensional Changes, with Specimen Straining Capability," *Rev. Sci. Instrum.* **51**, No. 10, 1335-1337 (1980).

[43] H. C. Ling and Kaplow, "Stress-Induced Shape Changes and Shape Memory in the R and Martensite Transformations in Equiatomic NiTi," *Met. Trans. A* **12A**, 2101-2111 (1981).

[44] H. C. Ling and R. Kaplow, "Macroscopic Length Changes during the B2=R and M—B2 Transitions in Equiatomic Ni-Ti Alloys," *Materials Sci. and Eng.* **51**, 193-201 (1981).

[45] K. Otsuka, T. Sawamura, K. Shimizu and C. M. Wayman, "Characteristics of the Martensitic Transformation in TiNi and the Memory Effect," *Met. Trans.* **2**, 2583-2588 (1971).

[46] S. Miyazaki and C. M. Wayman, "The R-Phase Transition and Associated Shape Memory Mechanism in Ti-Ni Single Crystals," *Acta Metall.* **36**, No. 1, 181-192 (1988).

[47] C. H. Hsu, "The Effect of Stress on the Transformation in Nickel-Titanium," Ph.D. Dissertation, Iowa State University, 1982.

[48] S. Miyazaki and K. Otsuka, "Deformation and Transition Behavior Associated with the R-Phase in Ti-Ni Alloys," *Met. Trans. A* **17A**, 53-63 (1986).

[49] D. Goldstein, L. Kabacoff and J. Tydings, "Effects of Stresses on the Phase Transformation of Nitinol," Naval Surface Weapons Center report NSWC TR 86-196, Silver Spring, MD (1986).

[50] C. M. Wayman, "Transformation, Self-Accommodation, Deformation and Shape Memory Behavior of NiTi Alloys," in *Vol. 9, Shape Memory Materials*, edited by K. Otsuka and K. Shimizu (Materials Research Society, Pittsburgh, PA, 1989), pp. 63-76.

[51] F. J. Di Salvo, Jr. and T. M. Rice, "Charge-Density Waves in Transition-Metal Compounds," *Physics Today* **32**, No. 4, 32-38 (1979).

[52] D. M. Goldstein, "Nitinol Strain Effects," *J. of Metals* **39**, No. 9, 23-27 (1987).

[53] M. S. Wechsler, personal communication, Departments of Nuclear Engineering and Materials Science and Engineering, Iowa State University, 1990.

[54] K. H. Lee, "Resistivity and Strain Behavior during Transformation Cycling in Nickel-Titanium," M. S. Thesis, Iowa State University, 1983.

[55] J. L. Murray, in *Binary Alloy Phase Diagrams, Vol. 2*, T. B. Massalski, Editor-in-Chief (American Society for Metals, Metals Park, OH, 1986).

[56] "Condensed Matter Research at LANSCE," edited by D. K. Hyer, Los Alamos National Laboratory publication LALP 90-7, January 1990.

[57] B. D. Cullity, *Elements of X-Ray Diffraction*, Second Edition (Addison-Wesley, Reading, MA, 1978).

[58] C. H. Hsu and M. S. Wechsler, "The Shape Memory Resistivity Behavior of Transformation-Fatigue-Cycled Nickel-Titanium Wires Near the Equiatomic Composition," Ames Laboratory report IS-4792, 1982.

[59] M. S. Wechsler, H. H. Baker, A. J. Bevolo, E. D. Gibson and F. C. Laabs, "Microstructure and Microchemistry of Equiatomic Nickel-Titanium," Ames Laboratory report IS-4797, 1982.

[60] A. C. Larson and R. B. Von Dreele, "Generalized Structure Analysis System," Los Alamos National Laboratory publication LAUR 86-748, 1988.

[61] H. M. Rietveld, "Line Profiles of Neutron Powder-Diffraction Peaks for Structure Refinement," *Acta Crystallogr.* **22**, 151-152 (1967).

[62] H. M. Rietveld, "A Profile Refinement Method for Nuclear and Magnetic Structures," *J. Appl. Crystallogr.* **2**, 65-71 (1969).

[63] W. I. F. David, "Powder Diffractometry," in *Neutron Scattering at a Pulsed Source*, edited by R. J. Newport, B. D. Rainford and R. Cywinski (Adam Hilger, Bristol, England, 1988), pp. 189-232.

[64] V. F. Sears, "Neutron Scattering Lengths and Cross Sections," in *Vol. 23, Part A Neutron Scattering*, edited by K. Sköld and D. L. Price (Academic Press, Orlando, FL, 1986) pp. 521-550.

[65] C. G. Windsor, *Pulsed Neutron Scattering* (Taylor and Francis, London, 1981).

[66] T. M. Sabine, R. B. Von Dreele and J.-E. Jørgensen, "Extinction in Time-of-Flight Neutron Powder Diffractometry," *Acta Crystallogr.* **A44**, 374-379 (1988).

[67] K. D. Rouse, M. J. Cooper and A. Chakera, "Absorption Corrections for Neutron Diffraction," *Acta Crystallogr.* **A26**, 682-691 (1970).

[68] A. W. Hewat, "Absorption Corrections for Neutron Diffraction," *Acta Crystallogr.* **A35**, 248 (1979).

[69] W. A. Dollase, "Correction of Intensities for Preferred Orientation in Powder Diffractometry: Application of the March Model," *J. Appl. Crystallogr.* **19**, 267-272 (1986).

[70] R. B. Von Dreele, J. D. Jorgensen and C. G. Windsor, "Rietveld Refinement with Spallation Neutron Powder Diffraction Data," *J. Appl. Crystallogr.* **15**, 581-589 (1982).

[71] R. B. Von Dreele, in a presentation at "The GSAS Workshop," Los Alamos National Laboratory, 1989.

[72] *Quantitative Texture Analysis* edited by H. J. Bunge and C. Esling (Deutsche Gesellschaft für Metallkunde, Clausthal, West Germany, 1982).

[73] G. E. Forsythe, M. A. Malcolm and C. B. Moler, *Computer Methods for Mathematical Computations* (Prentice-Hall, Englewood Cliffs, NJ, 1977).

7. ACKNOWLEDGEMENTS

There are many people who have contributed a great deal to the completion of this endeavor, and their work is greatly appreciated. First, I am indebted to my major professor, Dr. Monroe S. Wechsler. This project was initiated by him, and his dedication and attention to detail will always serve as a model for my own work in the future. I consider him to be a mentor and a friend. In addition, the work and patience of the other members of the Advisory Committee, Dr. Alan Goldman and Dr. Scott Chumbley, are appreciated. I would also like to express my gratitude to Mrs. Lorraine Wechsler for her kindness and friendship.

Second, a number of scientists and technicians at the Los Alamos National Laboratory were also invaluable. Dr. Joyce Goldstone, the scientist responsible for the NPD, taught me a great deal about spallation neutron sources, neutron diffraction and scientific experimentation in general. These experiments could not have been done without her capable assistance. Special thanks are due to Dr. Robert Brown for his help in the design and construction of the HIPD sample holder and of the temperature and resistance data acquisition system and for writing the HOTWIRE computer program. Also, thanks are owed to Dr. Robert Von Dreele, who taught me many of the subtleties of GSAS. In addition, the technical assistance of Mr. Thomas Ortiz and Mr. John Thomas are respectfully acknowledged.

Finally I would like to thank my family for their many years of support and encouragement. My parents, Dale and Doris Carey, have always encouraged me in all my efforts. Most importantly, my wife, Patsy Carey, needs to be thanked for putting her own life aside so that I could continue my education. Her love and support have truly made my contribution to this project possible. Lastly, I would like to acknowledge the two most important examples of twinning in my life–our twin daughters, Nicole Ellyse Carey and Megan Lindsay Carey who were born on April 24, 1990. While my involvement in this research project is coming to an end, my adventure with them is only beginning.

8. APPENDIX A: RESISTANCE AND TEMPERATURE DATA ACQUISITION PROGRAM

8.1 Description

A BASIC computer program, HOTWIRE, was written by R. D. Brown at the Los Alamos National Laboratory. The program is run on a Hewlett-Packard 85 Personal Computer. HOTWIRE gives instructions to a Hewlett-Packard Data Acquisition Controller to sample the output voltages of the thermocouples attached to the top and bottom of the NiTi sample wires and the voltage drops across a standard resistor and the NiTi wires. Provisions are also made for a third thermocouple which may be located at the middle of the wires during testing. The program then calculates the top and bottom thermocouple temperatures, and the electrical resistance of the wires. HOTWIRE also keeps track of the elapsed time between voltage samplings. All temperature, resistance and time data are written to a floppy disk. A plotting routine then allows graphs of resistance versus temperature, resistance versus time, and temperature versus time to be plotted.

8.2 HOTWIRE Computer Program

```
 10 ! ******PROGRAM HOTWIRE*************
 20 ! Calculates resistance
 30 ! Variable current through NiTi wire, reads dV
 40 ! Plots
 50 !
 60 ! Variables:
 70 !  Graphics on/off:G1=1/0
 80 !  time--T9 (sec)
 90 !  delay time (between readings)--09
100 !  Resistor value=R5=1.000
110 !  Resistance in ohms--01
120 !  T.C. measurements on slot#0, ch#5
130 !  # of thermocouples--N1
140 !  T(1)--temperature (C)
150 !  R3--reference vltg
160 !  R0-R2=params for temp calc
170 !  P0-P9=params for temp calc
180 ! ********************************
190 ! INITIALIZE
200 CLEAR
210 GOSUB 320
220 GOSUB 1560 ! Setup graph
230 ! Measurements
240 GOSUB 970
250 ! Store data
260 GOSUB 1240
270 ! Plot data
280 IF G1=1 THEN GOSUB 1830
290 WAIT D9
300 GOTO 230
310 END
320 ! ********************************
330 ! INITIALIZE
340 K1=0 ! Initial block #
350 ASSIGN# 2 TO "BLOCKS.NITI"
360 PRINT# 2,1 ; K1
```

```
370 N1=3 ! # of T.C.'s
380 D9=30*1000 ! Default delay time
390 ! Change delay time
400 ON KEY# 1,"DLY_TIM" GOSUB 810
410 G1=1 ! Graphics on (default)
420 ! Toggle graphics on/off
430 ON KEY# 2,"TGL_GR" GOSUB 1500
440 ON KEY# 3,"Rmnmx" GOSUB 870
450 ON KEY# 4,"EXIT" GOSUB 1920
460 KEY LABEL
470 ! Set up the printer
480 PRINTER IS 702,80 @ PRINT CHR$(27)&"154F"@ PRINT
    CHR$(27)&"11L"
490 WAIT 5000
500 !Set up the disk file
510 ! Stores 5 var's:
520 !   T9,01,T(1),T(2),V6
530 !  Create "DAT.NITI",3600,40
540 MASS STORAGE IS ":D700"
550 ! Setup 3421A:
560 ABORTIO 7 @ RESET 7 @ CLEAR 709
570 ! Params for temp conversion
580 R0=-.00000082
590 R1=.00003964
600 R2=.000000016
610 P0=-.051
620 P1=24850.3
630 P2=-382662
640 P3=99661057
650 P4=-10820624000
660 P5=603928550000
670 P6=-1.9109E13
680 P7=3.4782347E14
690 P8=-3.3991028E15
700 P9=1.3828514E16
710 R5=1
720 IMAGE K,SDD.DDD,K,DDD
730 IMAGE K,SDDD.D,K,SDDD.D
740 IMAGE K,SD.DDDD
750 ! SET UP THE GRAPH
```

```
760 X1=0 @ X9=100 ! Xmin,Xmax
770 T1=20 ! Xticks
780 Y1=1.35 @ Y9=1.6 ! Ymin, Ymax
790 T2=.05 ! Yticks
800 RETURN
810 ! ***********************************
820 !   Set delay time
830 CLEAR @ DISP "DELAY TIME NOW=";D9/1000
840 DISP "NEW DELAY TIME(sec)=";@ INPUT D9@ D9=D9*1000
850 DISP "DELAY TIME=";D9/1000
860 RETURN
870 ! ***********************************
880 ! CHANGE Rmin, Rmax
890 ALPHA
900 DISP "Rmin=";@ INPUT Y1
910 DISP "Rmax=";@ INPUT Y9
920 DISP "Rmin=";Y1
930 DISP "Rmax=";Y9
940 T2=(Y9-Y1)/5
950 GOSUB 1590
960 RETURN
970 ! ***********************************
980 !  MEASURMENTS
990 ! Time
1000 T9=TIME
1010 CLEAR 709
1020 ! NiTi RESISTANCE
1030 OUTPUT 709 ;"DCV 2"
1040 ENTER 709 ; V2 ! NiTi voltage drop
1050 OUTPUT 709 "DCV 6"
1060 ENTER 709 ; V6 ! Fixed resistor voltage drop
1070 IF V6<>0 THEN O1=V2*R5/V6 ELSE O1=0
1080 IF G1=0 THEN DISP "BLOCK=";K1
1090 IF G1=0 THEN DISP USING 740 ; "V-NiTi=";V2
1100 IF G1=0 THEN DISP USING 740 ; Vresis=";V6
1110 IF G1=0 THEN DISP USING 720 ; "RESIS=";O1
1120 ! N1 temperatures
1130 FOR I=1 TO N1
1140 OUTPUT 709 ;"DCV";I+2
1150 ENTER 709 ; V(I)
```

```
1160 NEXT I
1170 ! Read reference vltg
1180 OUTPUT 709 ;"REF03"
1190 ENTER 709 ; R3
1200 ! Convert to temps
1210 GOSUB 1390
1220 IF G1=0 THEN DISP USING 730 ; "Ttop=";T(1);"
     Tbtm=";T(2);"Tmid=";T(3) @  DISP
1230 RETURN
1240 ! ****************************
1250 ! STORE DATA
1260 ! K1=block counter
1270 ASSIGN# 2 TO "BLOCKS.NITI"
1280 READ# 2,1 ; K1@ K1=K1+1
1290 ! Store time,resis.,temps
1300 ASSIGN# 1 TO "DAT.NITI"
1310 PRINT# 1,K1
1320 PRINT# 1 ; T9,O1,T(1),T(2),T(3),V6
1330 ! T9=time, O1=NiTi resis, V6=Vresis, T(1)= Ttop, T(2)=Tbtm,
     T(3)=Tmid
1340 ASSIGN# 1 to *
1350 ! Store K1
1360 PRINT# 2,1 ; K1
1370 ASSIGN# 2 TO *
1380 RETURN
1390 ! ****************************
1400 ! CONVERT TO TEMPS
1410 !  Reference voltage
1420 V9=R0+R3(R1+R3*R2)
1430 ! Do all T.C.'s
1440 FOR I=1 TO N1
1450 V(I)=V(I)+V9
1460 T(I)=P0+V(I)*P1+V(I)^2*P2+V(I)^3*P3+V(I)^4*P4+V(I)^5*P5+
     V(I)^6*P6+V(I)^7*P7+V(I)^8*P8
1470 T(I)=T(I)+V(I)^9*P9
1480 NEXT I
1490 RETURN
1500 ! ****************************
1510 ! TOGGLE GRAPHICS
1520 IF G1=0 THEN DISP "GRAPHICS OFF" ELSE DISP "GRAPHICS ON"
```

```
1530 G1=INT(1-G1)
1540 IF G1=0 THEN DISP "GRAPHICS OFF" ELSE DISP "GRAPHICS ON"
1550 RETURN
1560 ! ****************************
1570 ! SET UP THE GRAPH
1580 CLEAR @ DISP "TITLE:";@ INPUT T1$
1590 GCLEAR @ GRAPH
1600 X5=X9-X1 @ Y5=Y9-Y1
1610 SCALE X1-.15*X5,X9+.15*X5,Y1-.15*Y5,Y9+.15*Y5
1620 ! Axes:
1630 ! Lower X-axis
1640 XAXIS Y1,T1,X1,X9
1650 FOR X=X1 TO X9 STEP T1
1660 MOVE X,Y1-.08*Y5
1670 LABEL VAL$(X)
1680 NEXT X
1690 ! Upper X-axis
1700 XAXIS Y9,T1,X1,X9
1710 ! Left Y-axis
1720 YAXIS X1,T2,Y1,Y9
1730 FOR Y=Y1 TO Y9 STEP T2
1740 MOVE X1-.15*X5,Y
1750 LABEL VAL$(Y)
1760 NEXT Y
1770 ! Right Y-axis
1780 YAXIS X9,T2,Y1,Y9
1790 ! Title
1800 MOVE X1,Y9+.05*Y5 @ LABEL T1$
1810 IF G1=0 THEN ALPHA
1820 RETURN
1830 ! ****************************
1840 ! PLOT POINTS
1850 PLOT T(1),O1 @ PENUP
1860 GCLEAR Y1-.09*Y5
1870 MOVE X1+.25*X5,Y1-.14*Y5
1880 O$=VAL$(O1) @ O$=O$[1,4]
1890 T$=VAL$(T(1)) @ T$=T$[1,4]
1900 LABEL "R="&O$&" Ttop="&T$
1910 RETURN
1920 ! ****************************
```

```
1930 ! Read from disk, plot vs. time
1940 ASSIGN# 1 TO "DAT.NITI"
1950 ASSIGN# 2 TO "BLOCKS.NITI"
1960 READ# 2,1 ; K9
1970 ! Plot resis vs. temp
1980 GOSUB 2540
1990 ! Plot resis vs. time
2000 GOSUB 2340
2010 ! Plot temp vs. time
2020 GOSUB 2060
2030 CLEAR @ BEEP @ DISP "DONE"
2040 END
2050 ! ****************************
2060 ! Temps vs. time
2070 ! Y-axis
2080 Y1=0 ! Ymin
2090 Y9=100 ! Ymax
2100 T2=20 ! Yticks
2110 ! Axes
2120 GOSUB 1590
2130 ! plot temp vs. time
2140 FOR K=1 TO K9
2150 READ# 1,K ; T9,01,T(1)
2160 T9=T9-T3
2170 PLOT T9,T(1) @ PENUP
2180 NEXT K
2190 COPY
2200 GOSUB 2890 ! Spaces
2210 RETURN
2220 ! ****************************
2230 ! Plot T3 vs time
2240 ! Axes
2250 GOSUB 1590
2260 FOR K=1 TO K9
2270 READ# 1,K ; T9,01,T(1),T(2),T(3)
2280 PLOT T9-T3,T(3) @ PENUP
2290 NEXT K
2300 COPY
2310 GOSUB 2890 ! Spaces
2320 RETURN
```

```
2330 ! ****************************
2340 ! Resistance vs. time
2350 ! Same Yaxis, change Xaxis
2360 ! Get min and max time from disk
2370 ASSIGN# 1 TO "DAT.NITI"
2380 ASSIGN# 2 TO "BLOCKS.NITI"
2390 READ# 1,1 ; T3 ! MIN TIME
2400 READ# 1,K9 ; T4 ! MAX TIME
2410 X9=T4-T3 @ X1=0
2420 T1=INT(X9/5)
2430 ! Axes
2440 GOSUB 1590
2450 ! Plot resis vs. time
2460 FOR K=1 TO K9
2470 READ# 1,K ; T9,O1
2480 PLOT T9-T3,O1 @ PENUP
2490 NEXT K
2500 COPY
2510 GOSUB 2890 ! Spaces
2520 RETURN
2530 ! ****************************
2540 ! Resis vs. temp(1)
2550 ! Same Yaxis and Xaxis
2560 ! Axes
2570 GOSUB 1590
2580 FOR K=1 TO K9
2590 READ# 1,K ; T9,O1,T(1)
2600 PLOT T(1),O1, @ PENUP
2610 NEXT K
2620 COPY
2630 GOSUB 2890 ! Spaces
2640 RETURN
2650 ! ****************************
2660 ! Resis vs. temp(2)
2670 ! No changes on X or Y axes
2680 ! Axes
2690 GOSUB 1560
2700 FOR K=1 TO K9
2710 READ# 1,K ; T9,O1,T(1),T(2)
2720 PLOT T(2),O1 @ PENUP
```

```
2730 NEXT K
2740 COPY
2750 GOSUB 2890 ! Spaces
2760 RETURN
2770 ! ****************************
2780 ! Resis vs. temp3
2790 ! No changes on X or Y
2800 ! Axes
2810 GOSUB 1560
2820 FOR K=1 TO K9
2830 READ# 1,K ; T9,O1,T(1),T(2),T(3)
2840 PLOT T(3),O1 @ PENUP
2850 NEXT K
2860 COPY
2870 GOSUB 2890 ! Space
2880 RETURN
2890 ! ****************************
2900 ! Leave spaces between graphs
2910 PRINTER IS 2
2920 FOR I=1 TO 5
2930 PRINT
2940 NEXT I
2950 PRINTER IS 702,80
2960 RETURN
```

9. APPENDIX B: CORRECTING NOMINAL RESISTIVITY DATA FOR A CHANGE IN FORM FACTOR USING STRAIN MEASUREMENTS

9.1 Resistivity Correction Factor

Consider a NiTi wire sample in the austenitic phase with length l_1 and cross-sectional area A_1. If the temperature of the sample is changed so the wire transforms to the martensitic phase, the sample will undergo changes in length and cross-sectional area to l_2 and A_2, respectively. Using the austenite lattice parameters found by refining the data in runs 526 and 704 and the martensite lattice parameters found by refining the data in run 266 (see Chapter 4), the following volume calculations can be made.

$$V_A = a^3 = 3.023^3 = 27.626\text{Å}^3 \tag{9.1}$$

$$V_M = abc\sin\beta = (2.9036)(4.116)(4.663)\sin 97.836^\circ = 55.208\text{Å}^3. \tag{9.2}$$

Since the austenite and martensite unit cells contain two and four atoms per unit cell, respectively, the volume per atom for each phase becomes:

$$\left[\frac{\text{volume}}{\text{atom}}\right]_A = \frac{27.626}{2} = 13.813\text{Å}^3/\text{atom} \tag{9.3}$$

$$\left[\frac{\text{volume}}{\text{atom}}\right]_M = \frac{55.208}{4} = 13.802\text{Å}^3/\text{atom} \tag{9.4}$$

The ratio of these two numbers is 0.9992 so the assumption of constant volume is quite reasonable.

It can be seen that if l_1 and A_1 are used to calculate the electrical resistivity from resistance measurements obtained after the wire has transformed to martensite, an incorrect value will result since the length and cross-sectional area are now l_2 and A_2, respectively. The uncorrected resistivity, ρ_u, and the corrected resistivity, ρ_c, are calculated from the measured electrical resistance, R, by

$$\rho_u = \frac{A_1}{l_1} R \tag{9.5}$$

and

$$\rho_c = \frac{A_2}{l_2} R \tag{9.6}$$

where $\frac{A_i}{l_i}$ is called the *form factor*. Setting Equation 9.5 equal to Equation 9.6 and solving for ρ_c,

$$\rho_c = \rho_u \frac{A_2 l_1}{A_1 l_2}. \tag{9.7}$$

If constant volume is assumed,

$$A_1 l_1 = A_2 l_2, \tag{9.8}$$

but l_1 and l_2 are related by the strain, ϵ,

$$\epsilon = \frac{l_2 - l_1}{l_1} \tag{9.9}$$

or

$$\frac{l_1}{l_2} = \frac{1}{1+\epsilon}. \tag{9.10}$$

Using Equation 9.10, Equation 9.8 now becomes

$$\frac{A_2}{A_1} = \frac{1}{1+\epsilon} \tag{9.11}$$

Finally, substituting Equation 9.10 and Equation 9.11 into Equation 9.7, the expression for the corrected resistivity is given as

$$\rho_C = \frac{\rho u}{(1+\epsilon)^2}. \tag{9.12}$$

The term, $\frac{1}{(1+\epsilon)^2}$ is called the *resistivity correction factor.*

9.2 Correcting Nominal Resistivity Curves

Figure 9.1 (same as Figure 1.5) shows the uncorrected resistivity and strain curves which were digitized using a 7470A Hewlett-Packard plotter and a program written by A. F. Rohach at Iowa State University. The results of this digitizing can be seen in Figures 9.2 and 9.3. It should be noted that the circled points in Figure 9.3 were interpolated instead of digitized and will be explained shortly.

Since it was nearly impossible to digitize two points–one from the resistivity curve and one form the strain curve–with exactly the same abscissa, it was necessary to interpolate between the raw data points. A FORTRAN program, CORRECT, was written which utilized a cubic spline subroutine [73] to interpolate between the digitized raw data. These results can be found in Figures 9.4 and 9.5. The interpolated points were calculated from -40°C to 100°C in one degree increments. Every third point is plotted on the interpolated graphs.

Where the graphs changed quickly, a high density of digitized points was desirable to allow the cubic polynomial to better interpolate the raw data. There was a limit to this, however, since the cubic spline subroutine required the raw data's abscissas to be increasing, and it was difficult to make the plotter's sight glass move in smaller increments than those used. For this reason, several points were inter-

polated before the cubic spline program was run. These points are circled on the raw data plots and were calculated by assuming a straight line connecting the two raw data points on either side of the interpolated region. CORRECT next took two data points, one interpolated strain value and one interpolated resistivity value at a particular temperature, and calculated a corrected resistivity using the resistivity correction factor. This corrected data may be seen in Figure 9.6.

Instabilities between 40°C and 60°C can be seen in the lower graph of Figure 9.6. This is due to the fact that the original plots in Figure 9.1 were not plotted at their true temperatures. Since both the original resistivity and strain graphs were made simultaneously, the plotting arms could not occupy exactly the same position on the graph paper. Therefore, one of the graphs was displaced by a few degrees in temperature with respect to the other graph. The problem, however, was that it was not known how many degrees or in what direction the displacement occurred.

By trying different temperature displacements, it was found that the best choice shifted the strain curves 1.5°C to the right with respect to the resistivity curves. For example, in Figures 9.4 and 9.5, 40°C on the resistivity curves corresponds to 38.5°C on the strain curves. Employing this shift, the corrected resistivity curves are shown in Figure 9.7.

In Figure 9.7 stress level 4 (56.1 MPa) still shows some discontinuities both on heating and cooling. They seem to be artifacts of the digitizing and interpolating steps since no amount of shifting of the strain curves gave a smoother plot than those seen in Figure 9.7. Since the original curves were continuous, it is assumed the corrected curves should also be continuous. Figure 9.8 shows the curves when these spurious points are omitted.

9.3 Correction for Possibly Miscalibrated Strain Data

The next question to be answered was whether the stress dependence seen on the plots was real, or whether this could be explained by an error in measurement of the strain values. This error, C_k, is termed the *strain error factor* and is thought of as being a constant which, when multiplied by the observed strain, yields the actual strain in the wires.

As can be seen from Figure 9.1, for two different applied stress, σ_i and σ_j, two different strains, ϵ_i and ϵ_j, result at a given temperature. Also, since resistivity shows stress dependence, there are two different resistivity values, ρ_i and ρ_j. Using Equation 9.12,

$$\rho c_i = \frac{\rho u_i}{(1+\epsilon_i)^2} \tag{9.13}$$

$$\rho c_j = \frac{\rho u_j}{(1+\epsilon_j)^2}. \tag{9.14}$$

If the two corrected resistivity plots coincide,

$$\rho c_i = \rho c_j \tag{9.15}$$

$$\frac{\rho u_i}{(1+\epsilon_i)^2} = \frac{\rho u_j}{(1+\epsilon_j)^2} \tag{9.16}$$

$$\frac{\rho u_i}{\rho u_j} = \frac{(1+\epsilon_i)^2}{(1+\epsilon_j)^2}. \tag{9.17}$$

Now, is there a constant, C_k, which, when multiplied by the strains, ϵ_i and ϵ_j, will make Equation 9.17 true? Equation 9.17 becomes

$$\frac{\rho u_i}{\rho u_j} = \frac{(1+\epsilon_i C_k)^2}{(1+\epsilon_j C_k)^2}. \tag{9.18}$$

Solving for C_k,

$$\frac{1+\epsilon_i C_k}{1+\epsilon_j C_k} = \sqrt{\frac{\rho u_i}{\rho u_j}} \tag{9.19}$$

$$1+\epsilon_i C_k = \sqrt{\frac{\rho u_i}{\rho u_j}} + \epsilon_j C_k \sqrt{\frac{\rho u_i}{\rho u_j}} \tag{9.20}$$

$$\epsilon_i C_k - \epsilon_j C_k \sqrt{\frac{\rho u_i}{\rho u_j}} = \sqrt{\frac{\rho u_i}{\rho u_j}} - 1 \tag{9.21}$$

$$C_k = \frac{\sqrt{\frac{\rho u_i}{\rho u_j}} - 1}{\epsilon_i - \epsilon_j \sqrt{\frac{\rho u_i}{\rho u_j}}}. \tag{9.22}$$

Since there are four different stress levels, there are six different combinations of i's and j's to give C_1 through C_6. Using the interpolated data for these six combinations at -40°C (Table 9.1) we can get approximate values of these C_k's which are summarized in Table 9.2. The average value of C_1 through C_6 is 1.91. If the observed strain had been multiplied by approximately 1.91, the plots on heating would nearly coincide, and the cooling curves would still show a stress dependence on the lower side of the resistivity peak (Figure 9.9). From this it can be concluded that the stress dependence seen in the resistivity plots is probably not due to any experimental errors since it seems very unlikely that the calibration of the instrumentation would have been off by nearly a factor of two.

Table 9.1: Interpolated resistivity and strain values at $-40^{\circ}C$

Curve Number	Resistivity, ρ_u $(\mu\Omega/cm)$	Strain, ϵ $(\Delta l/l)$
1	74.2506	0.029905
2	77.8405	0.045492
3	80.3960	0.054127
4	82.4058	0.060642

Table 9.2: Strain error factors for the six resistivity-strain combinations

i	j	k	C_k
1	2	1	1.606
1	3	2	1.763
1	4	3	1.836
2	3	4	2.063
2	4	5	2.089
3	4	6	2.126
			Average C_k = 1.91
			Standard Deviation in C_k = 0.211

9.4 CORRECT Computer Program

```
C
C   RESISTIVITY DEPENDS UPON THE FORM FACTOR OF THE SAMPLE.  SINCE
C   STRAIN CHANGES THIS FORM FACTOR, THE MEASURED RESISTIVITY MUST
C   BE CORRECTED FOR THIS CHANGE.
C   THIS PROGRAM WILL READ IN THE DIGITIZED GRAPHS OF RESISITIVITY
C   VERSUS TEMPERATURE AND OF STRAIN VERSUS TEMPERATURE.  BY USING
C   THE SUBROUTINE, SPLINE AND THE FUNCTION, SEVAL
C   (WRITTEN BY FORSYTHE, MALCOLM AND MOLER) THE GRAPHS WILL BE
C   INTERPOLATED BETWEEN THE DIGITIZED POINTS SO A CORRECTED
C   RESISTIVITY VERSUS TEMPERATURE GRAPH CAN BE CALCULATED.
C
      PROGRAM CORRECT
C   VARIABLES
C      X1(I):  UPPER GRAPH ABSCISSA (TEMPERATURE IN DEG C)
C      Y1(I):  UPPER GRAPH ORDINATE (RESISTIVITY IN MICRO-OHM-CM)
C      X2(I):  LOWER GRAPH ABSCISSA (TEMPERATURE IN DEG C)
C      Y2(I):  LOWER GRAPH ORDINATE (STRAIN IN %)
C      X(I),Y(I):      DATA ABSCISSAS AND ORDINATES USED IN SPLINE
C      B(I),C(I),D(I): SPLINE COEFFICIENTS
C      RESUN(I):       UNCORRECTED INTERPOLATED RESISTIVITY
C      STRAIN(I):      INTERPOLATED STRAIN
C      RESCOR(I):      CORRECTED RESISTIVITY
C      U:      ABSCISSA OF INTERPOLATED POINT
C      Y:      DUMMY VARIABLE
C      I:      DO LOOP INDEX
C      N:      NUMBER OF POINTS IN DATA SETS
C
      REAL X1(150),Y1(150),X2(150),Y2(150),B(150),C(150),D(150),
     & RESUN(150),STRAIN(150),RESCOR(150),U,L,X(150),Y(150)
      INTEGER I,N
      PRINT*,'ENTER N'
      READ*,N
C   READ IN DATA FILES WRITTEN BY DIGITIZING PROGRAM
C
      OPEN(10,FILE= 'X1.DAT',STATUS='UNKNOWN')
      OPEN(20,FILE= 'Y1.DAT',STATUS='UNKNOWN')
```

```
      OPEN(25,FILE= 'X2.DAT',STATUS='UNKNOWN')
      OPEN(30,FILE= 'Y2.DAT',STATUS='UNKNOWN')
      OPEN(40,FILE= 'RESCOR.DAT',STATUS='UNKNOWN')
      OPEN(50,FILE= 'RESUN.DAT',STATUS='UNKNOWN')
      OPEN(60,FILE= 'STRAIN.DAT',STATUS='UNKNOWN')
      DO 100 I=1,N
            READ(10,*) X1(I)
            READ(20,*) Y1(I)
            READ(25,*) X2(I)
            READ(30,*) Y2(I)
 100  CONTINUE
C   INTERPOLATE UPPER GRAPH
C
 200  DO 250 I=1,N
            X(I)= X1(I)
            Y(I)= Y1(I)
 250  CONTINUE
      CALL SPLINE(N,X,Y,B,C,D)
      DO 300 U= -40.,100.,1.
            RESUN(U)= SEVAL(N,U,X,Y,B,C,D)
            WRITE(50,45)U,RESUN(U)
 300  CONTINUE
C   INTERPOLATE LOWER GRAPH
C
      DO 350 I=1,N
            X(I)= X2(I)
            Y(I)= Y2(I)
 350  CONTINUE
      CALL SPLINE(N,X,Y,B,C,D)
      DO 400 U= -40.,100.,1.
            STRAIN(U)= SEVAL(N,U,X,Y,B,C,D)
            WRITE(60,45)U,STRAIN(U)
 400  CONTINUE
C   CORRECT RESISTIVITY FOR CHANGE IN FORM FACTOR
C
      DO 500 U= -40.,100.,1.
            STRAIN(U)= STRAIN(U)*0.01
            RESCOR(U)= RESUN(U)/((1. + STRAIN(U))**2)
            WRITE(40,45) U,RESCOR(U)
 500  CONTINUE
```

```
  45    FORMAT(5X,F5.1,5X,F8.4)
        STOP
        END
C
C****** SUBROUTINE SPLINE ****************************************
C
      SUBROUTINE SPLINE (N, X, Y, B, C, D)
      INTEGER N
      REAL X(N), Y(N), B(N), C(N), D(N)
C
C  THE COEFFICIENTS B(I), C(I), AND D(I), I=1,2,...,N ARE COMPUTED
C  FOR A CUBIC INTERPOLATING SPLINE
C
C  S(X) = Y(I) + B(I)*(X-X(I)) + C(I)*(X-X(I))**2 +
C         D(I)*(X-X(I))**3
C    FOR  X(I) .LE. X .LE. X(I+1)
C
C  INPUT..
C
C    N = THE NUMBER OF DATA POINTS OR KNOTS (N.GE.2)
C    X = THE ABSCISSAS OF THE KNOTS IN STRICTLY INCREASING ORDER
C    Y = THE ORDINATES OF THE KNOTS
C
C  OUTPUT..
C
C    B, C, D  = ARRAYS OF SPLINE COEFFICIENTS AS DEFINED ABOVE.
C
C  USING  P  TO DENOTE DIFFERENTIATION,
C
C    Y(I) = S(X(I))
C    B(I) = SP(X(I))
C    C(I) = SPP(X(I))/2
C    D(I) = SPPP(X(I))/6  (DERIVATIVE FROM THE RIGHT)
C
C  THE ACCOMPANYING FUNCTION SUBPROGRAM  SEVAL  CAN BE USED
C  TO EVALUATE THE SPLINE.
C
C
      INTEGER NM1, IB, I
      REAL T
```

```
C
      NM1 = N-1
      IF ( N .LT. 2 ) RETURN
      IF ( N .LT. 3 ) GO TO 50
C
C  SET UP TRIDIAGONAL SYSTEM
C
C  B = DIAGONAL, D = OFFDIAGONAL, C = RIGHT HAND SIDE.
C
      D(1) = X(2) - X(1)
      C(2) = (Y(2) - Y(1))/D(1)
      DO 10 I = 2, NM1
         D(I) = X(I+1) - X(I)
         B(I) = 2.*(D(I-1) + D(I))
         C(I+1) = (Y(I+1) - Y(I))/D(I)
         C(I) = C(I+1) - C(I)
   10 CONTINUE
C
C  END CONDITIONS.  THIRD DERIVATIVES AT  X(1)  AND  X(N)
C  OBTAINED FROM DIVIDED DIFFERENCES
C
      B(1) = -D(1)
      B(N) = -D(N-1)
      C(1) = 0.
      C(N) = 0.
      IF ( N .EQ. 3 ) GO TO 15
      C(1) = C(3)/(X(4)-X(2)) - C(2)/(X(3)-X(1))
      C(N) = C(N-1)/(X(N)-X(N-2)) - C(N-2)/(X(N-1)-X(N-3))
      C(1) = C(1)*D(1)**2/(X(4)-X(1))
      C(N) = -C(N)*D(N-1)**2/(X(N)-X(N-3))
C
C  FORWARD ELIMINATION
C
   15 DO 20 I = 2, N
         T = D(I-1)/B(I-1)
         B(I) = B(I) - T*D(I-1)
         C(I) = C(I) - T*C(I-1)
   20 CONTINUE
C
C  BACK SUBSTITUTION
```

```
C
      C(N) = C(N)/B(N)
      DO 30 IB = 1, NM1
         I = N-IB
         C(I) = (C(I) - D(I)*C(I+1))/B(I)
   30 CONTINUE
C
C  C(I) IS NOW THE SIGMA(I) OF THE TEXT
C
C  COMPUTE POLYNOMIAL COEFFICIENTS
C
      B(N) = (Y(N) - Y(NM1))/D(NM1) + D(NM1)*(C(NM1) + 2.*C(N))
      DO 40 I = 1, NM1
         B(I) = (Y(I+1) - Y(I))/D(I) - D(I)*(C(I+1) + 2.*C(I))
         D(I) = (C(I+1) - C(I))/D(I)
         C(I) = 3.*C(I)
   40 CONTINUE
      C(N) = 3.*C(N)
      D(N) = D(N-1)
      RETURN
C
   50 B(1) = (Y(2)-Y(1))/(X(2)-X(1))
      C(1) = 0.
      D(1) = 0.
      B(2) = B(1)
      C(2) = 0.
      D(2) = 0.
      RETURN
      END
C
C*** SEVAL ***********************************************************
C
        REAL FUNCTION SEVAL(N,U,X,Y,B,C,D)
        INTEGER N
        REAL U,X(N),Y(N),B(N),C(N),D(N)
C
C  THIS SUBROUTINE EVALUATES THE CUBIC SPLINE FUNCTION
C
C  SEVAL = Y(I) + B(I)*(U-X(I)) + C(I)*(U-X(I))**2 +
C          D(I)*(U-X(I))**3
```

```
C       WHERE X(I) .LT. U .LT. X(I+1), USING HORNER'S RULE
C
C  IF U .LT. X(1) THEN I = 1 IS USED.
C  IF U .GE. X(N) THEN I = N IS USED.
C
C  INPUT..
C
C       N = THE NUMBER OF DATA POINTS
C       U = THE ABSCISSA AT WHICH THE SPLINE IS TO BE EVALUATED
C       X,Y = THE ARRAYS OF DATA ABSCISSAS AND ORDINATES
C       B,C,D= ARRAYS OF SPLINE COEFFICIENTS COMPUTED BY SPLINE
C
C   IF U IS NOT IN THE SAME INTERVAL AS THE PREVIOUS CALL, THEN A
C   BINARY SERCH IS PERFORMED TO DETERMINE THE PROPER INTERVAL.
C
        INTEGER I,J,K
        REAL DX
        DATA I/1/
        IF ( I .GE. N ) I = 1
        IF ( U .LT. X(I) ) GO TO 10
        IF ( U .LE. X(I+1) ) GO TO 30
C
C  BINARY SEARCH
C
  10    I = 1
        J = N+1
  20    K= (I+J)/2
        IF ( U .LT. X(K) ) J = K
        IF ( U .GE. X(K) ) I = K
        IF ( J .GT. I+1 ) GO TO 20
C
C  EVALUATE SPLINE
C
  30    DX = U - X(I)
        SEVAL = Y(I) + DX*(B(I) + DX*(C(I) + DX*D(I)))
        RETURN
        END
```

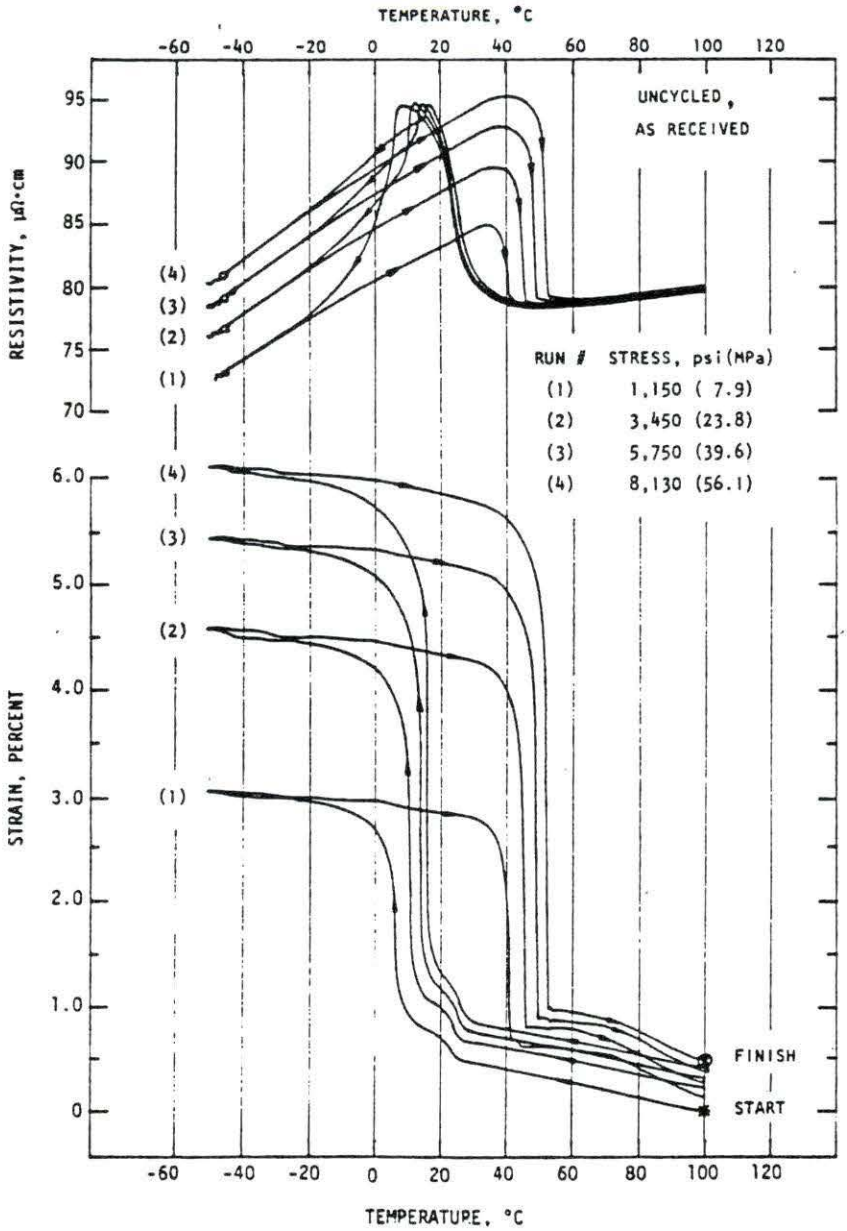

Figure 9.1: Nominal electrical resistivity and strain versus temperature for uncycled, as-received, NiTi wire

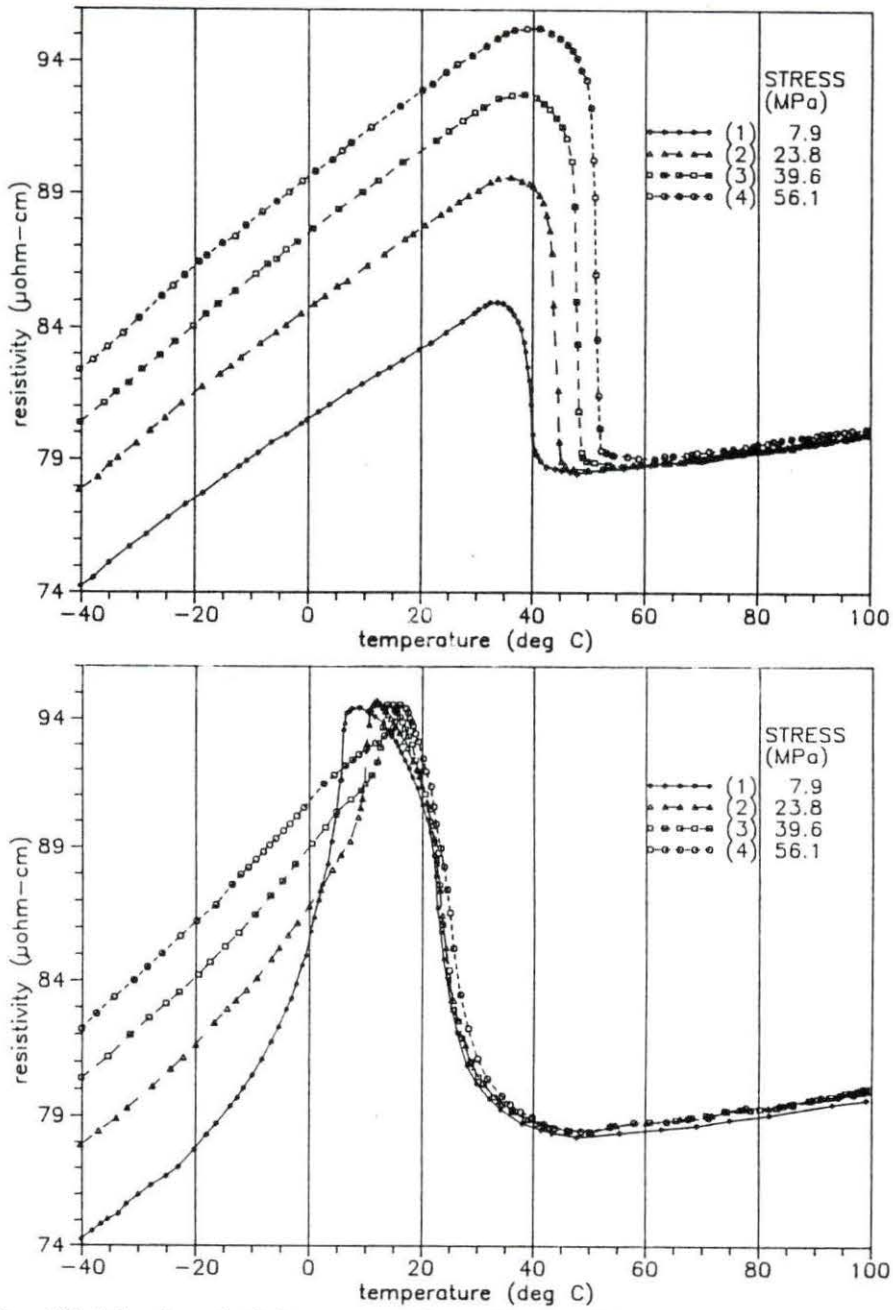

Figure 9.2: Digitized resistivity curves from Figure 9.1 upon heating (upper graph) and upon cooling (lower graph)

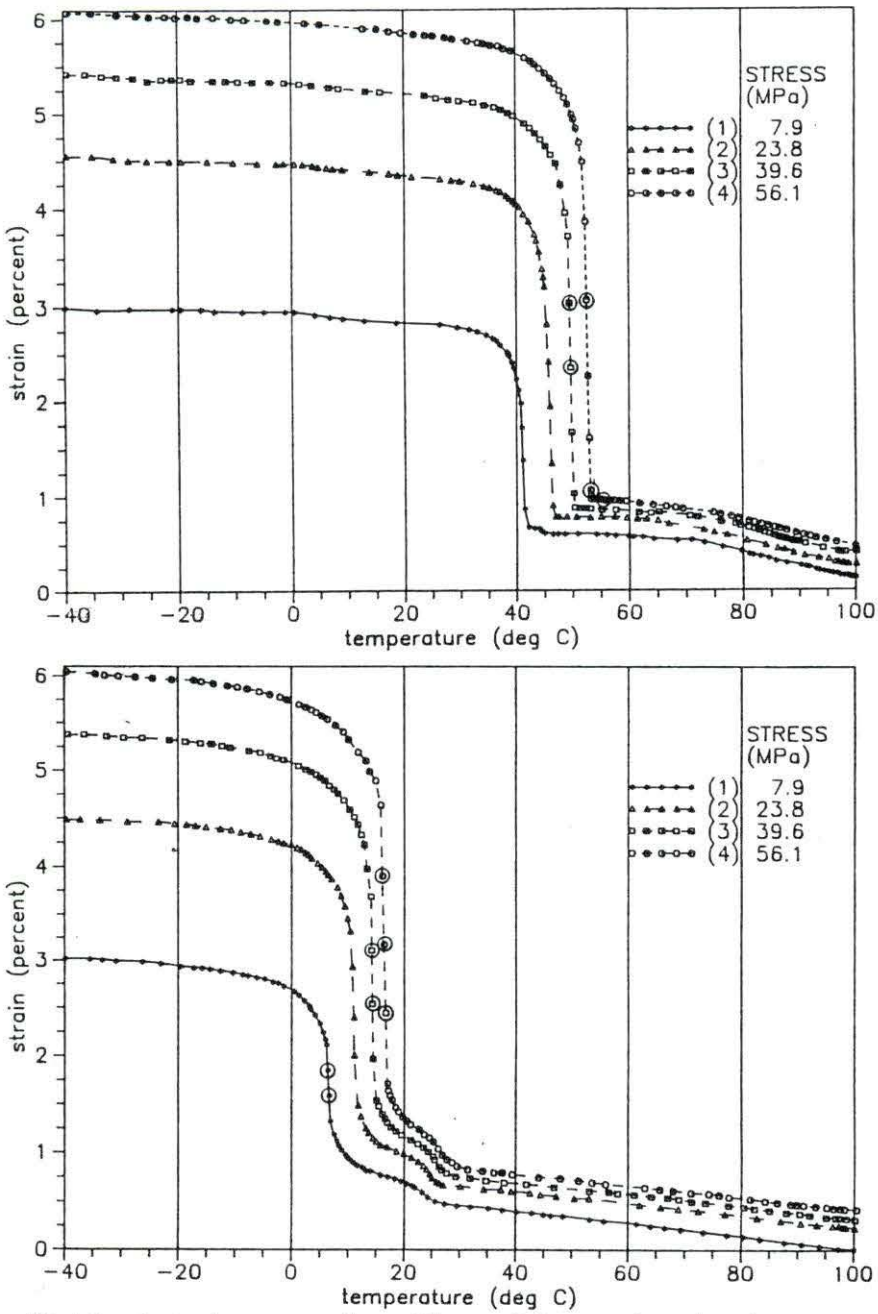

Figure 9.3: Digitized strain curves from Figure 9.1 upon heating (upper graph) and upon cooling (lower graph)

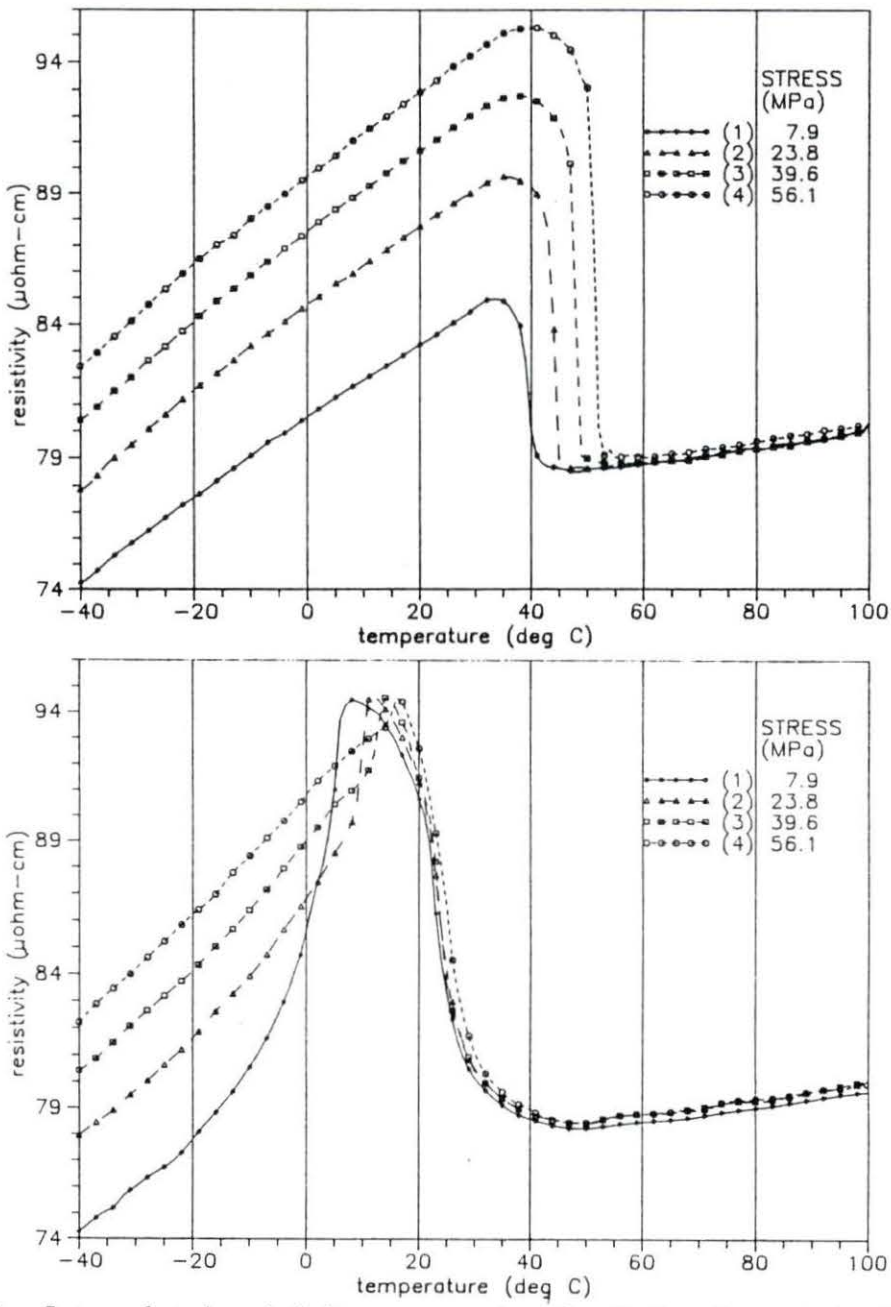

Figure 9.4: Interpolated resistivity curves using the digitized points in Figure 9.2 upon heating (upper graph) and upon cooling (lower graph)

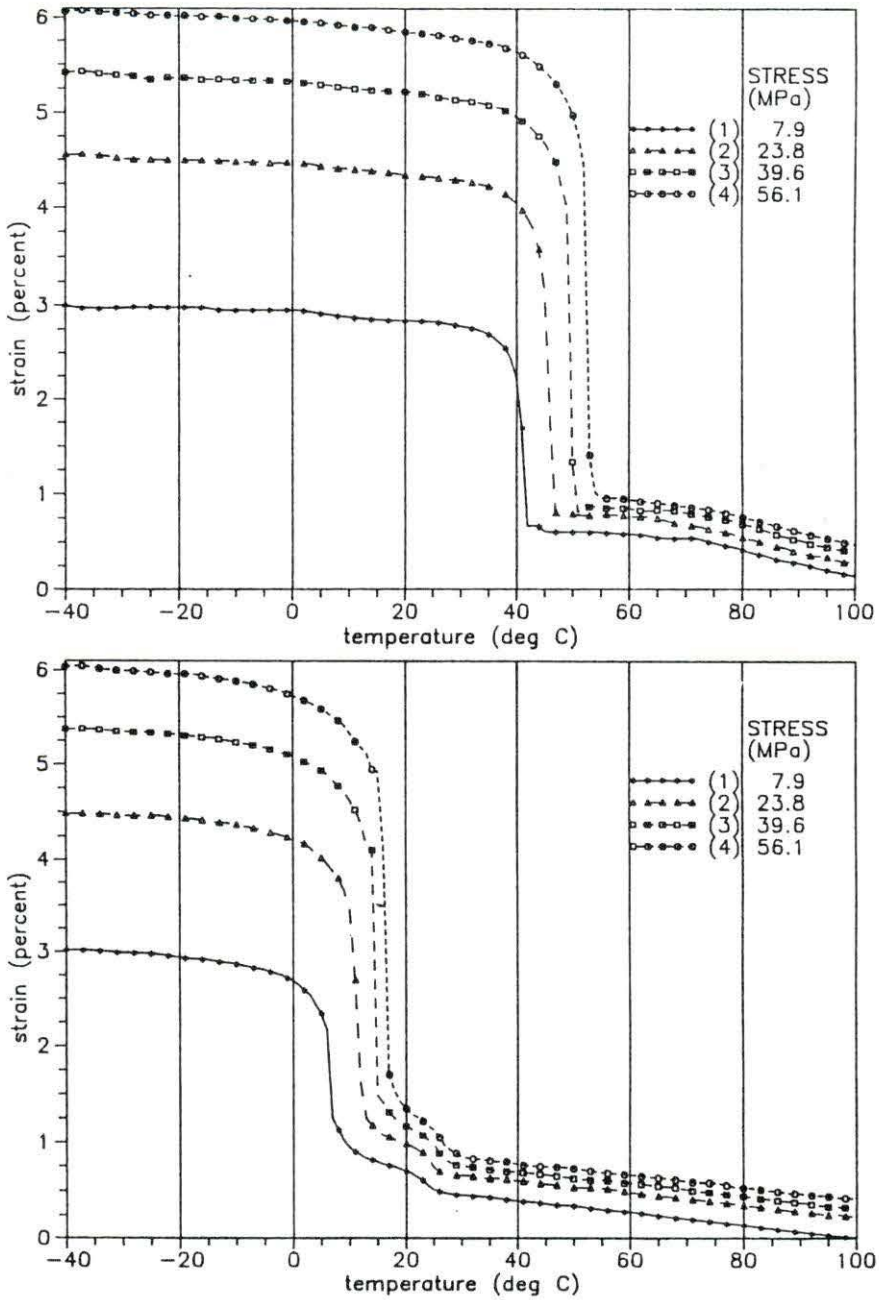

Figure 9.5: Interpolated strain curves using the digitized points in Figure 9.3 upon heating (upper graph) and upon cooling (lower graph)

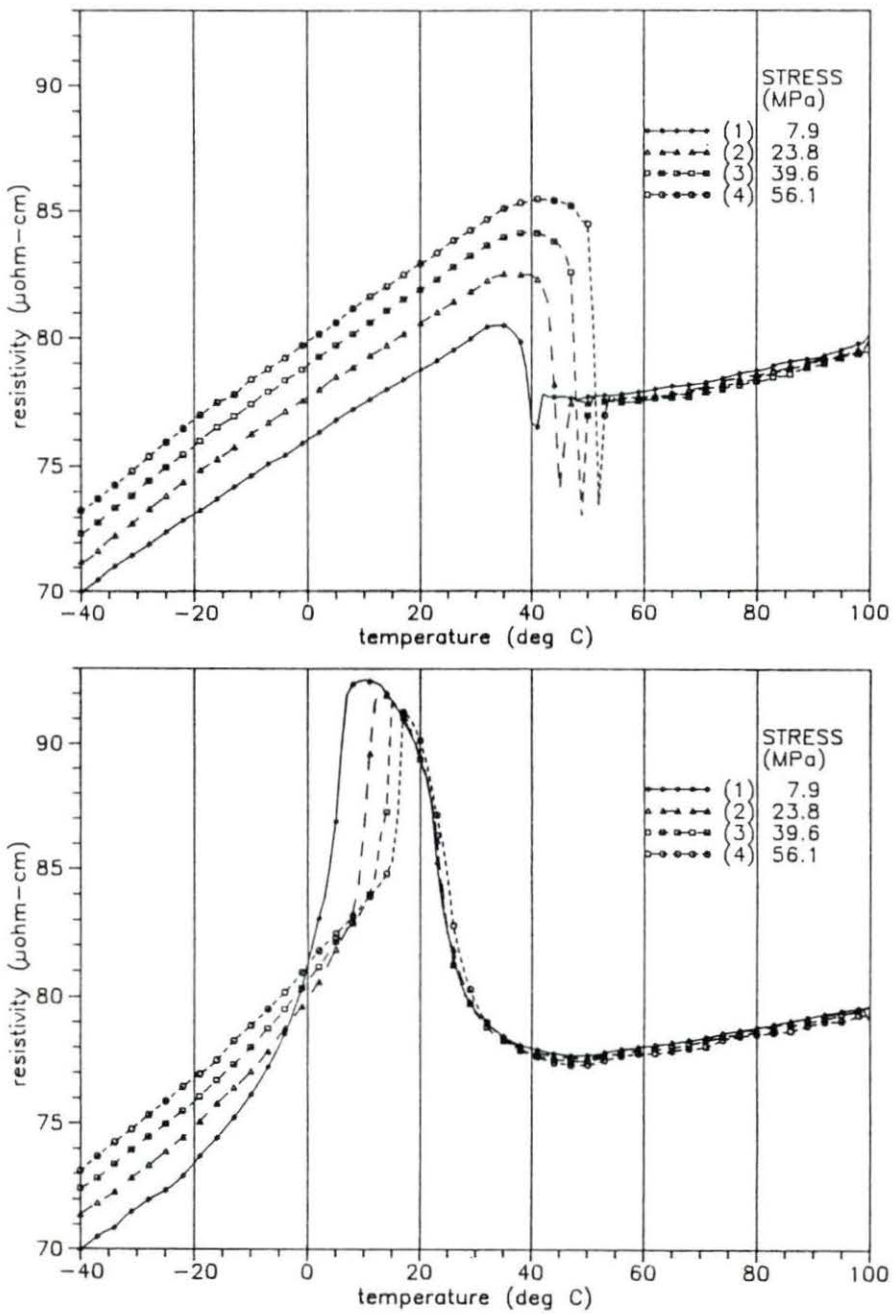

Figure 9.6: Corrected resistivity curves using the interpolated data in Figures 9.4 and 9.5 upon heating (upper graph) and upon cooling (lower graph)

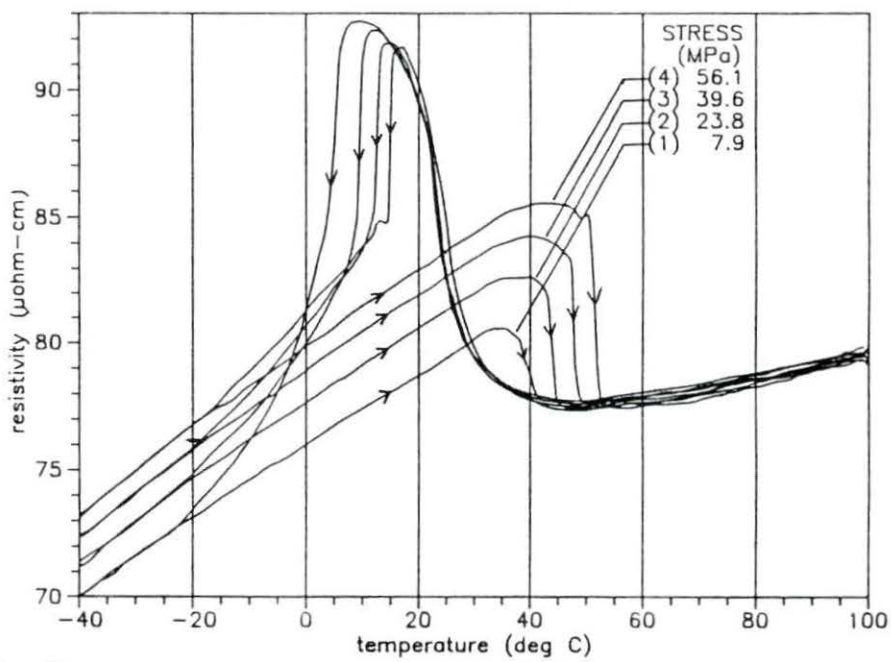

Figure 9.7: Corrected resistivity curves using the interpolated data from Figure 9.4 and 9.5 and shifting Figure 9.5 1.5°C to the right with respect to Figure 9.4

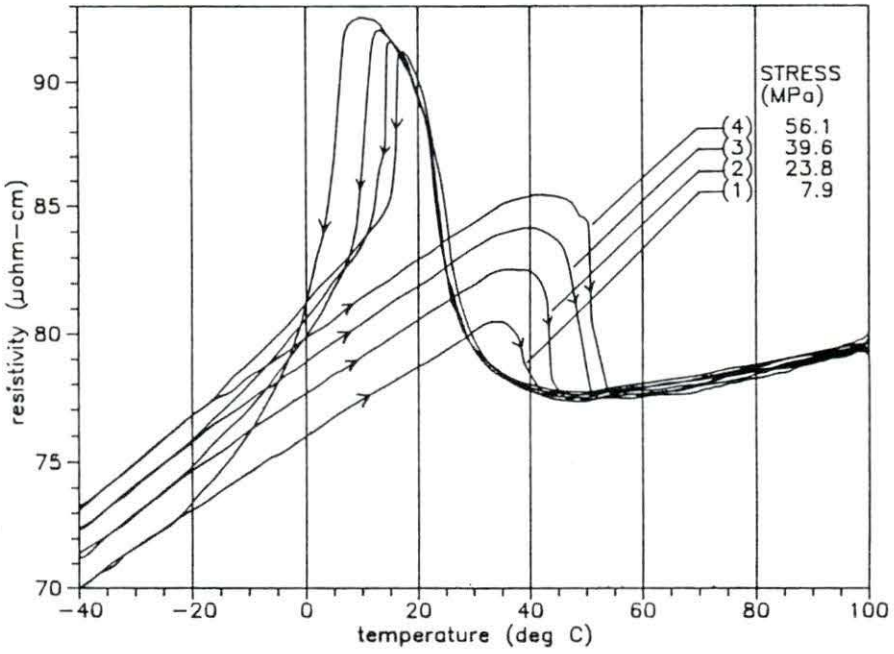

Figure 9.8: Figure 9.7 with spurious points in stress level 4 omitted

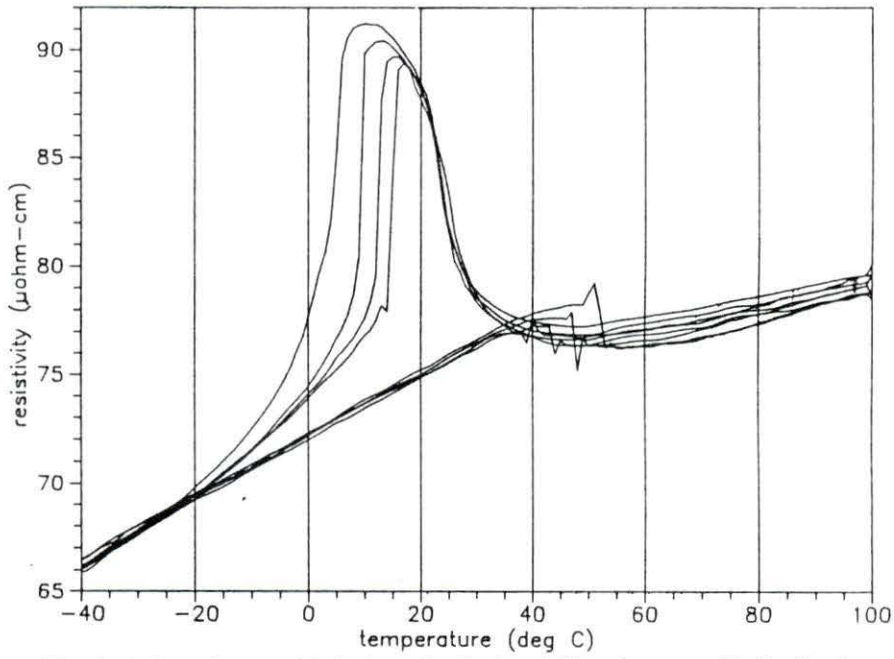

Figure 9.9: Resistivity data which has had the following applied: i) the resistivity correction factors, ii) the shift in temperature of the strain curves, and iii) the strain error factor equal to 1.91

10. APPENDIX C: ADDITIONAL DIFFRACTION PROFILES

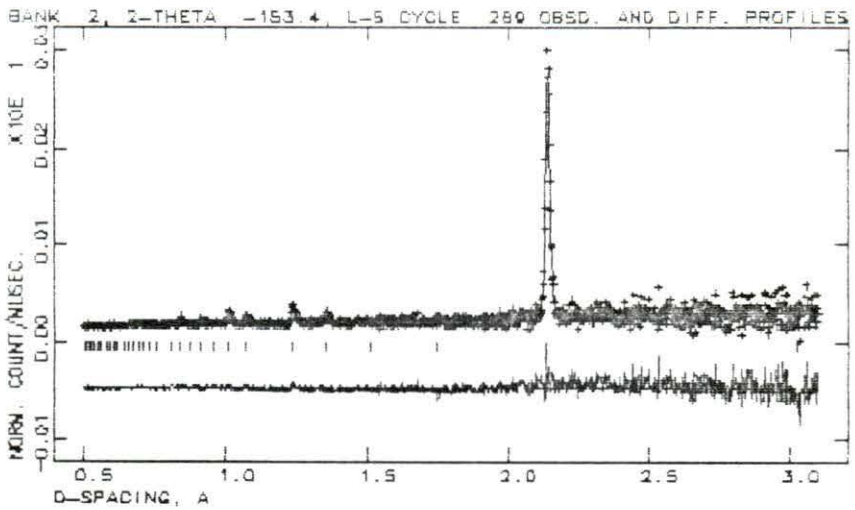

Figure 10.1: Diffraction profile for run 704 on the HIPD showing the 0.5Å to 3.1Å region from the -153° detector bank

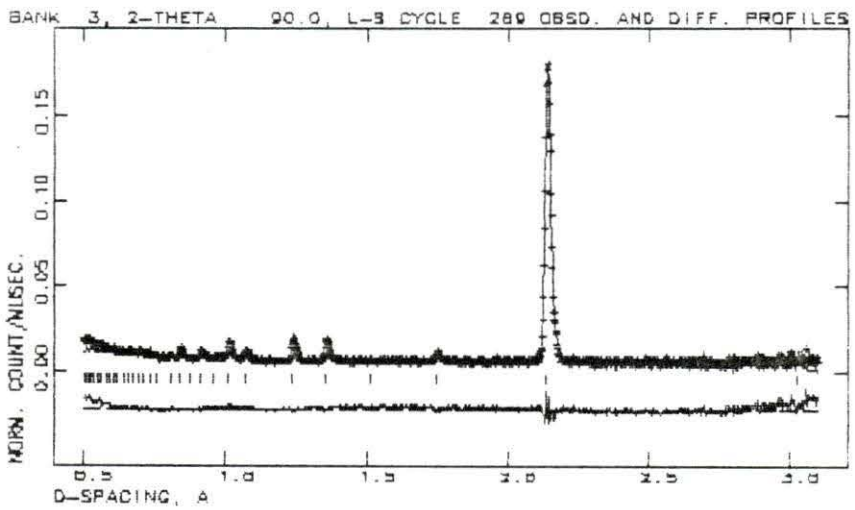

Figure 10.2: Diffraction profile for run 704 on the HIPD showing the 0.5Å to 3.1Å region from the $+90^{\circ}$ detector bank

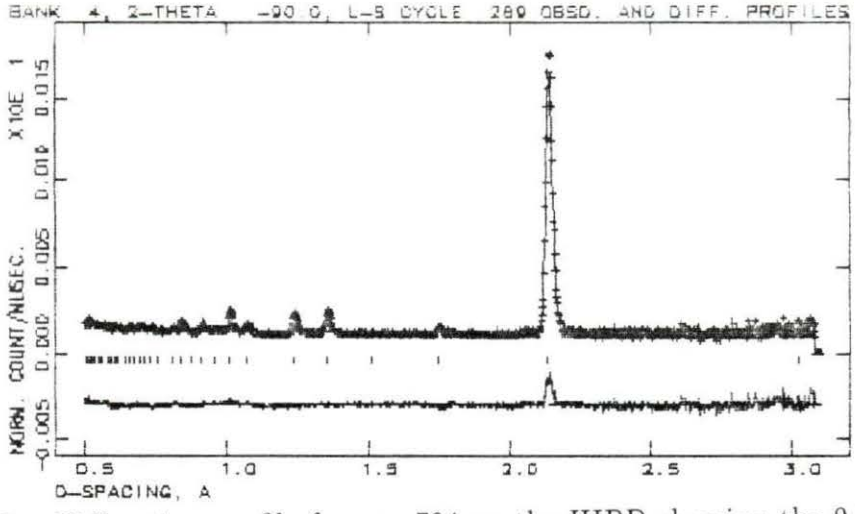

Figure 10.3: Diffraction profile for run 704 on the HIPD showing the 0.5Å to 3.1Å region from the -90° detector bank

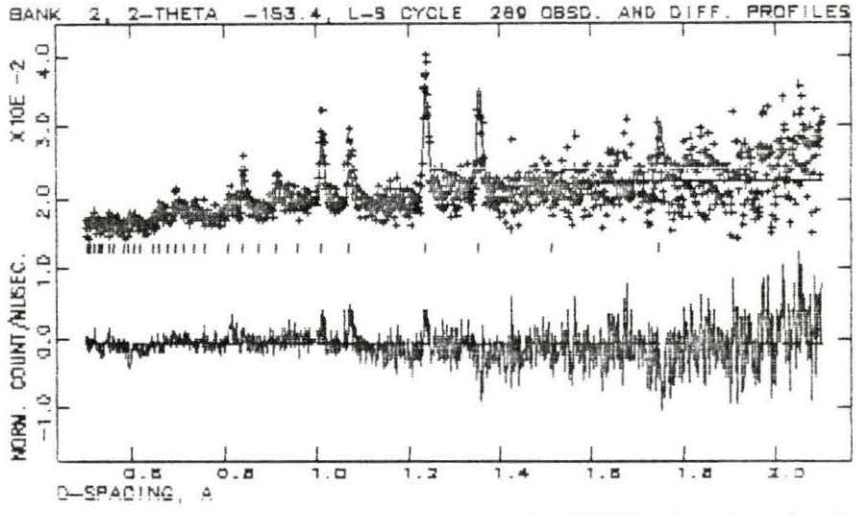

Figure 10.4: Diffraction profile for run 704 on the HIPD showing the 0.5Å to 2.1Å region from the -153° detector bank

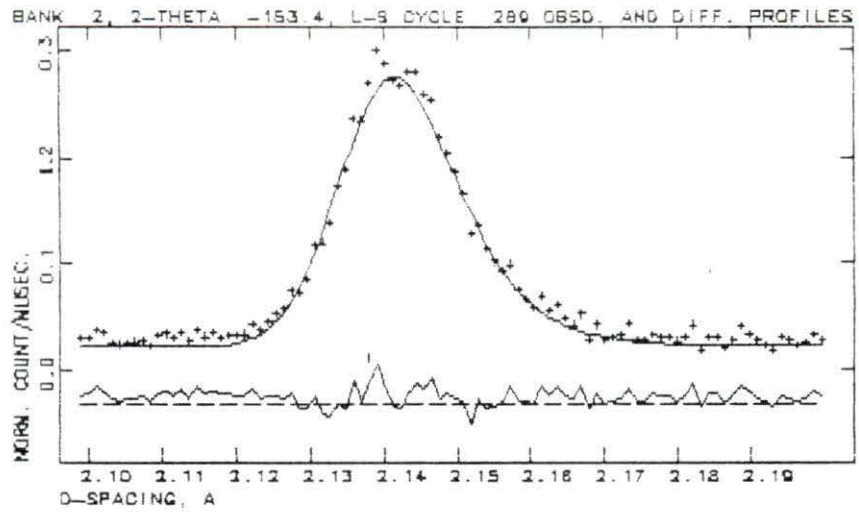

Figure 10.5: Diffraction profile for run 704 on the HIPD showing the 2.1Å to 2.2Å region from the -153° detector bank

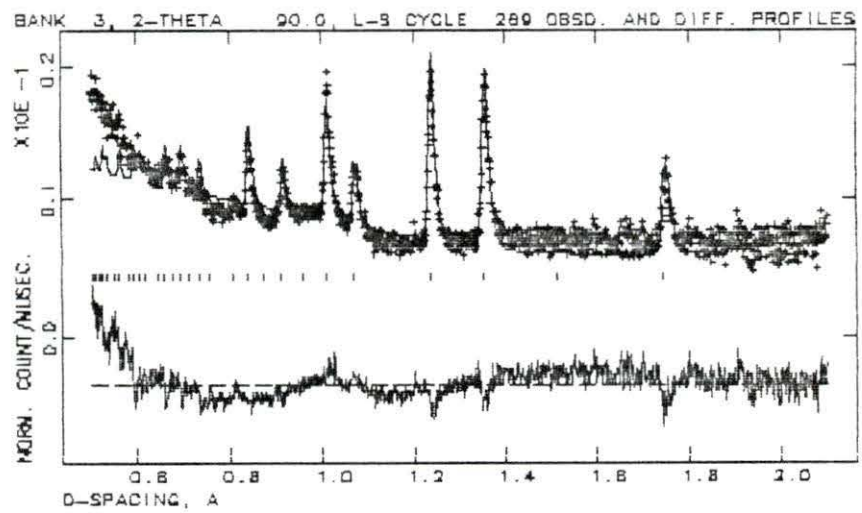

Figure 10.6: Diffraction profile for run 704 on the HIPD showing the 0.5Å to 2.1Å region from the $+90^{\circ}$ detector bank

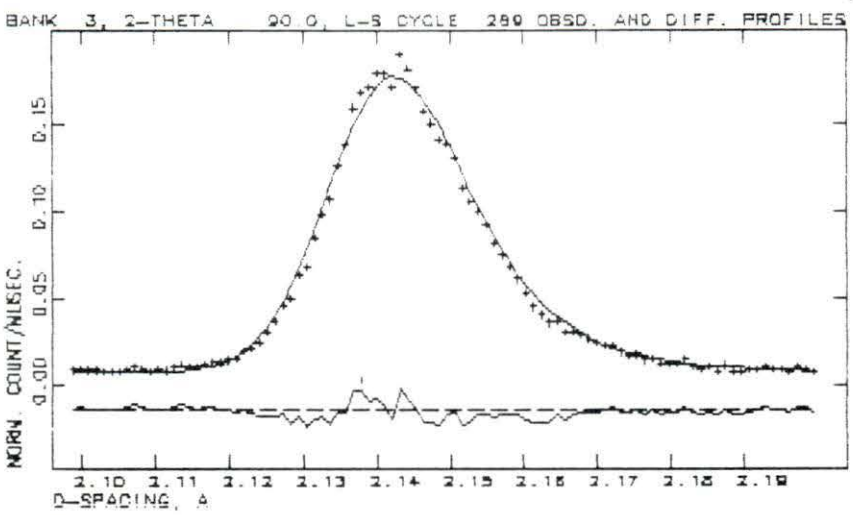

Figure 10.7: Diffraction profile for run 704 on the HIPD showing the 2.1Å to 2.2Å region from the $+90^{\circ}$ detector bank

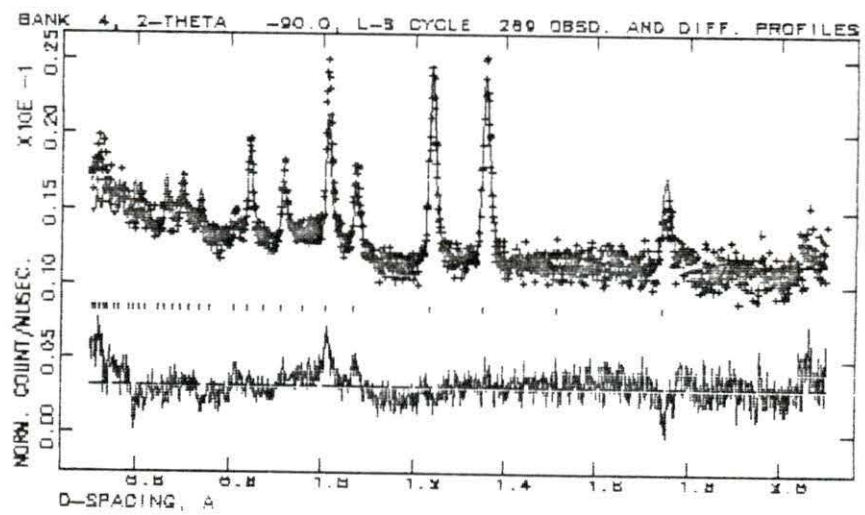

Figure 10.8: Diffraction profile for run 704 on the HIPD showing the 0.5Å to 2.1Å region from the -90° detector bank

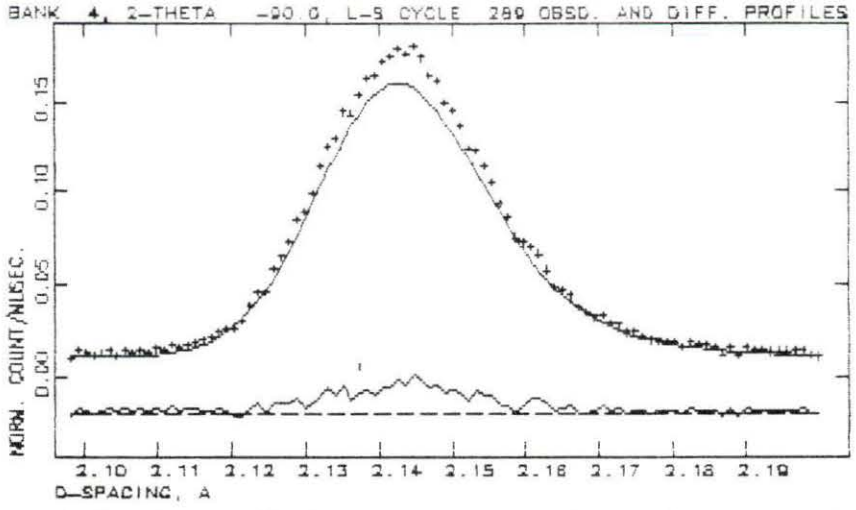

Figure 10.9: Diffraction profile for run 704 on the HIPD showing the 2.1Å to 2.2Å region from the -90° detector bank

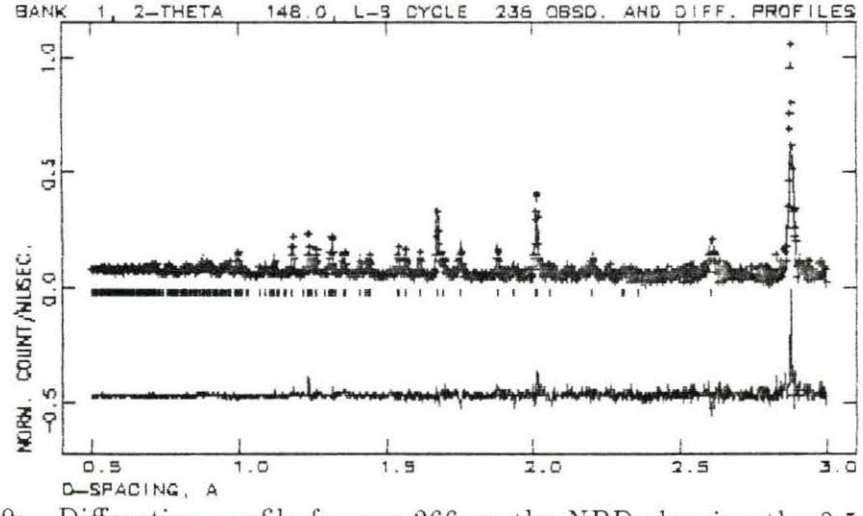

Figure 10.10: Diffraction profile for run 266 on the NPD showing the 0.5Å to 3.0Å region from the $+148^{\circ}$ detector bank

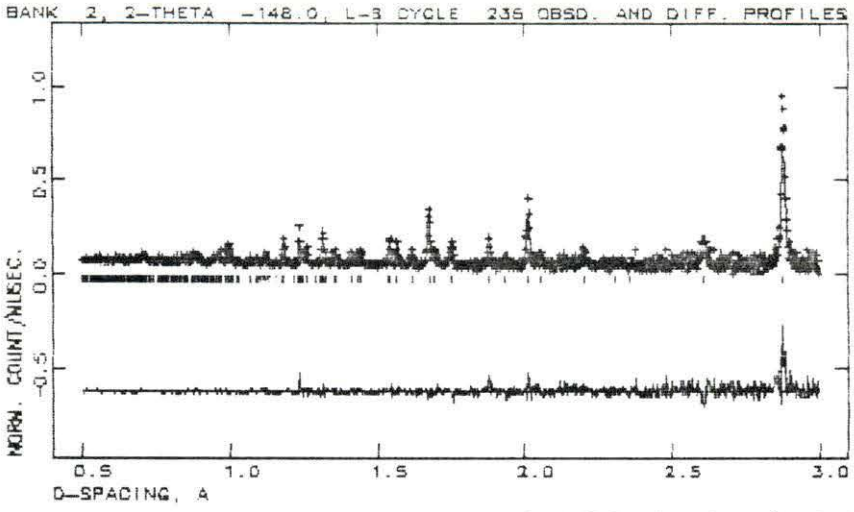

Figure 10.11: Diffraction profile for run 266 on the NPD showing the 0.5Å to 3.0Å region from the -148° detector bank

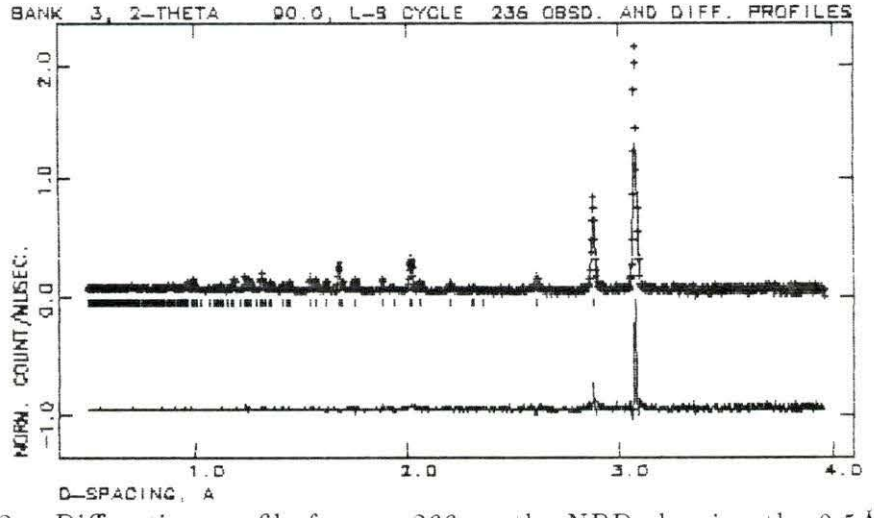

Figure 10.12: Diffraction profile for run 266 on the NPD showing the 0.5Å to 4.0Å region from the $+90^{\circ}$ detector bank

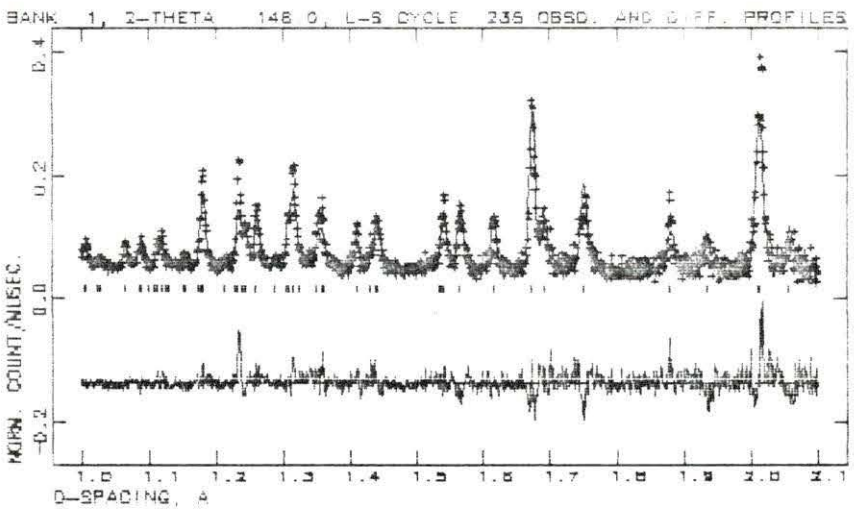

Figure 10.13: Diffraction profile for run 266 on the NPD showing the 1.0Å to 2.1Å region from the $+148^{\circ}$ detector bank

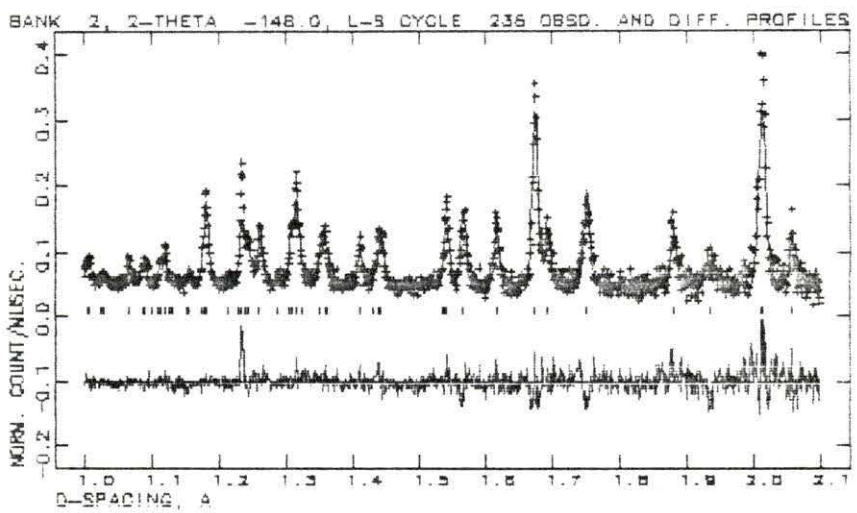

Figure 10.14: Diffraction profile for run 266 on the NPD showing the 1.0Å to 2.1Å region from the -148° detector bank

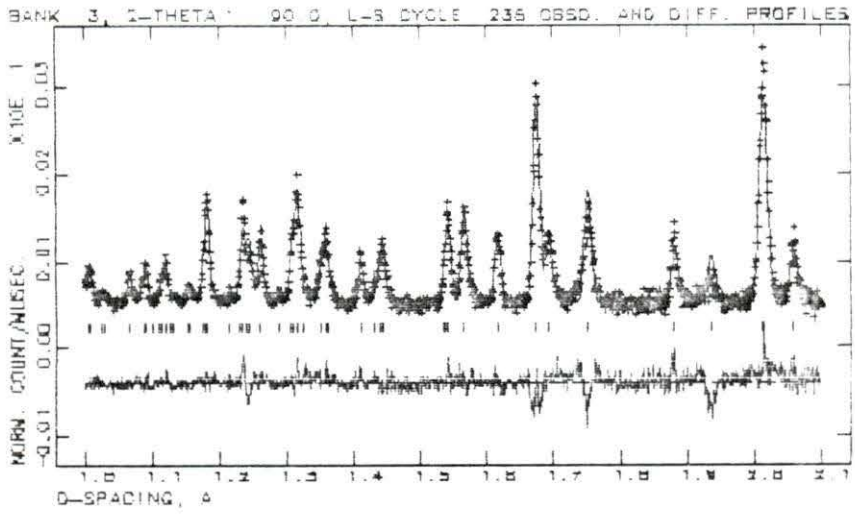

Figure 10.15: Diffraction profile for run 266 on the NPD showing the 1.0Å to 2.1Å region from the $+90^{\circ}$ detector bank

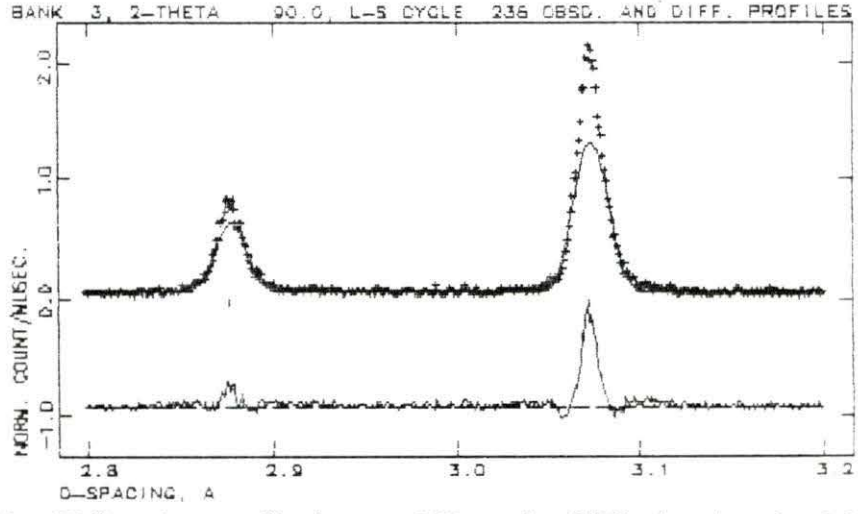

Figure 10.16: Diffraction profile for run 266 on the NPD showing the 2.8Å to 3.2Å region from the $+90^{\circ}$ detector bank

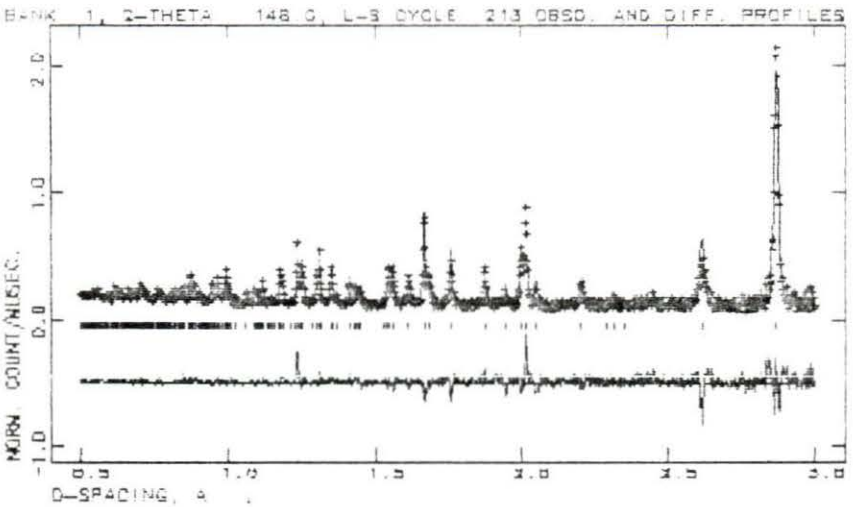

Figure 10.17: Diffraction profile for run 267 on the NPD showing the 0.5Å to 3.0Å region from the $+148^{\circ}$ detector bank

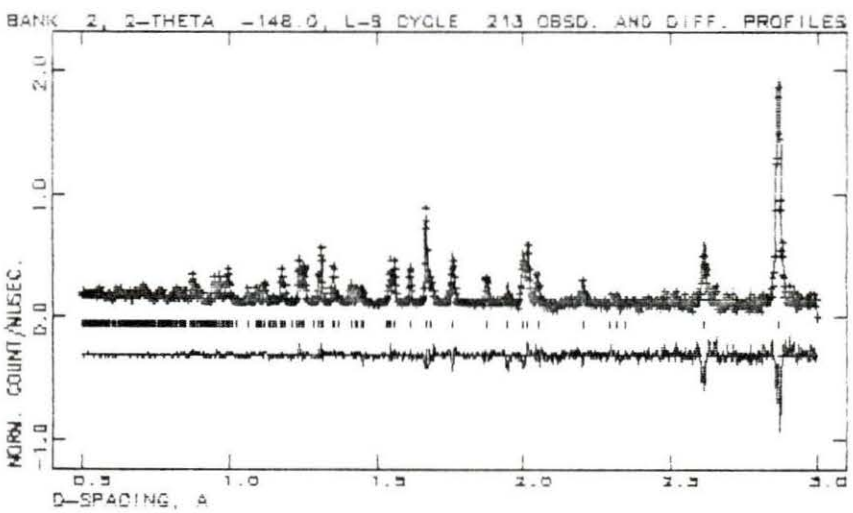

Figure 10.18: Diffraction profile for run 267 on the NPD showing the 0.5Å to 3.0Å region from the -148° detector bank

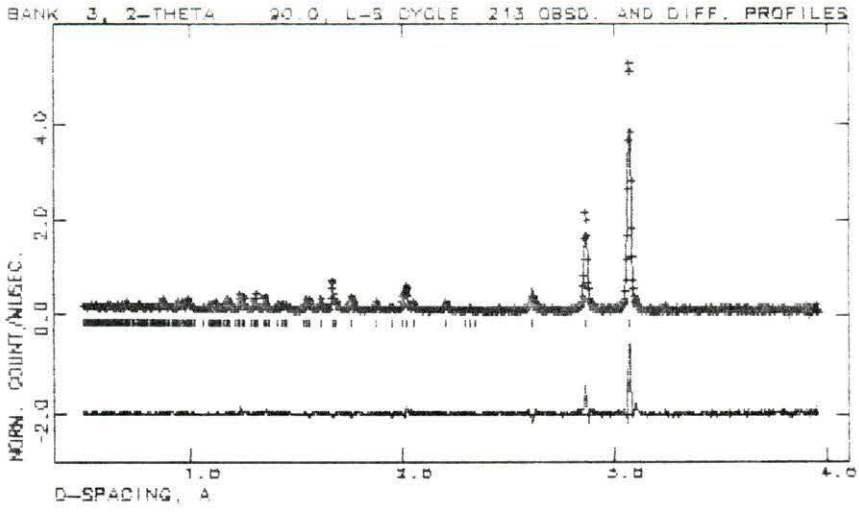

Figure 10.19: Diffraction profile for run 267 on the NPD showing the 0.5Å to 4.0Å region from the $+90^{\circ}$ detector bank

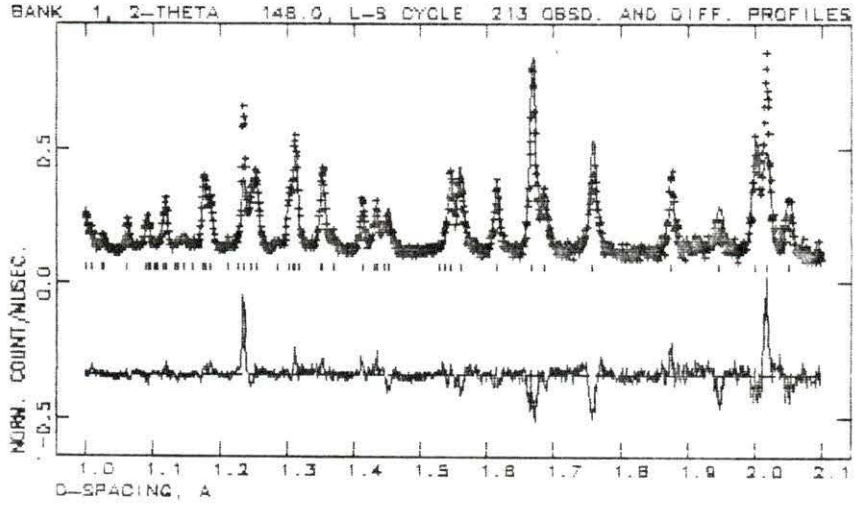

Figure 10.20: Diffraction profile for run 267 on the NPD showing the 1.0Å to 2.1Å region from the $+148^{\circ}$ detector bank

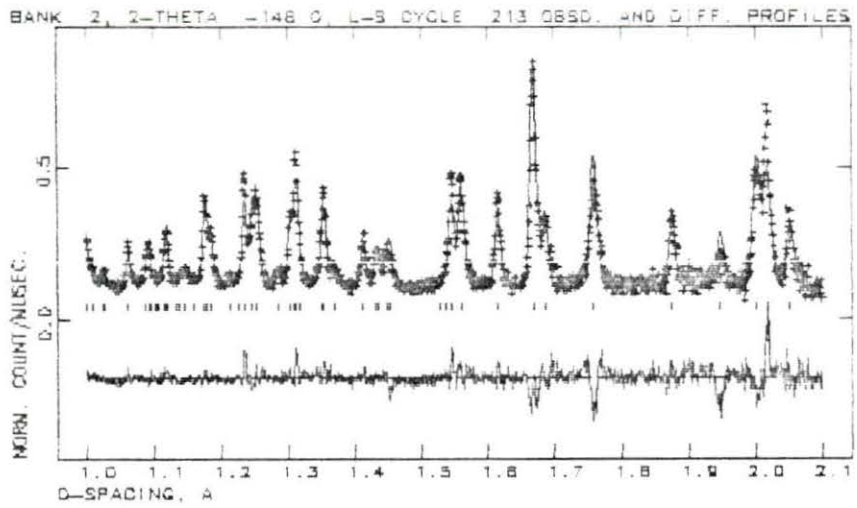

Figure 10.21: Diffraction profile for run 267 on the NPD showing the 1.0Å to 2.1Å region from the -148° detector bank

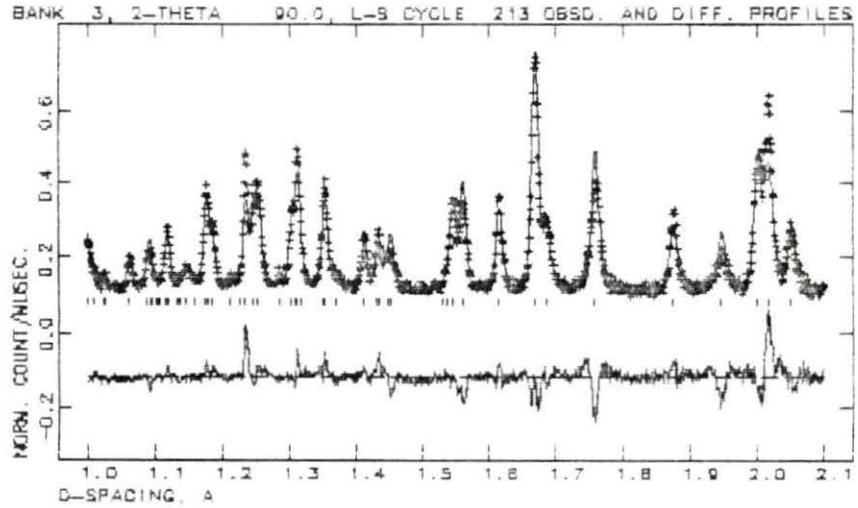

Figure 10.22: Diffraction profile for run 267 on the NPD showing the 1.0Å to 2.1Å region from the $+90^{\circ}$ detector bank

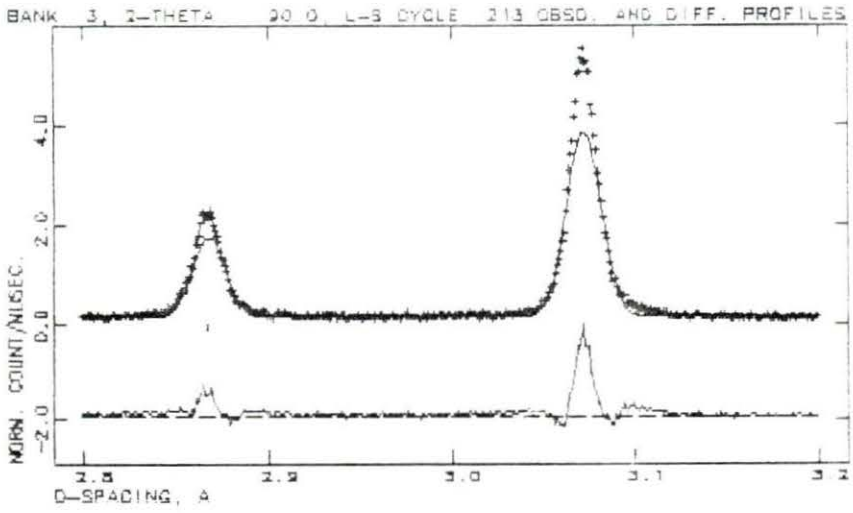

Figure 10.23: Diffraction profile for run 267 on the NPD showing the 2.8Å to 3.2Å region from the $+90^{\circ}$ detector bank

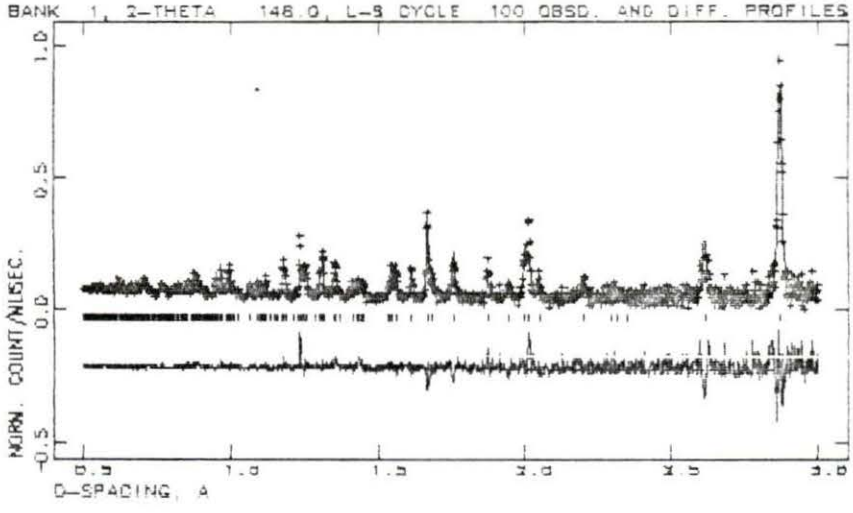

Figure 10.24: Diffraction profile for run 268 on the NPD showing the 0.5Å to 3.0Å region from the $+148^{\circ}$ detector bank

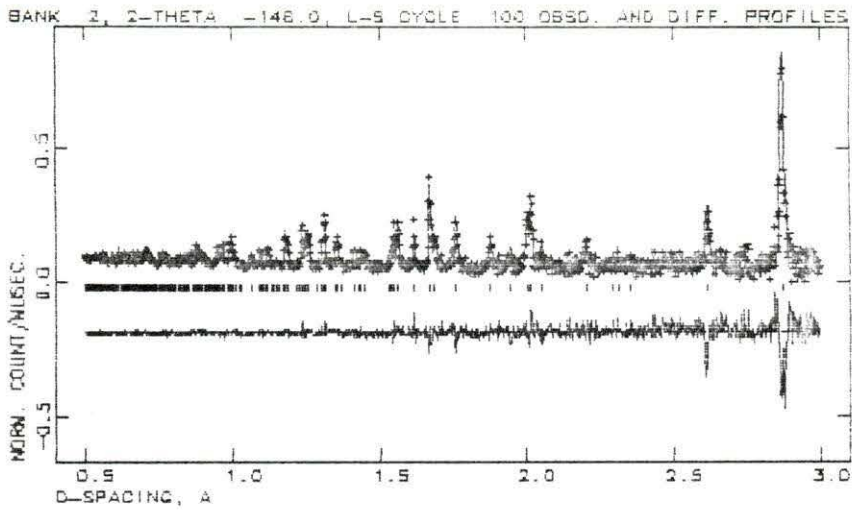

Figure 10.25: Diffraction profile for run 268 on the NPD showing the 0.5Å to 3.0Å region from the -148° detector bank

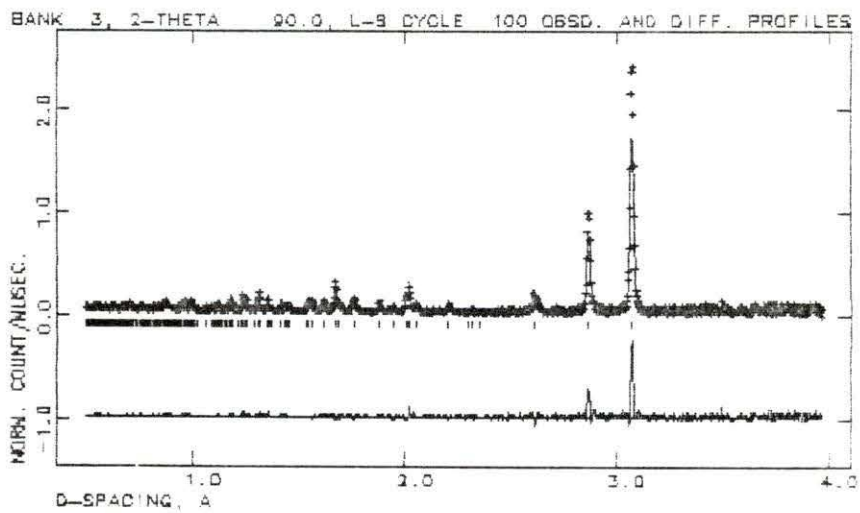

Figure 10.26: Diffraction profile for run 268 on the NPD showing the 0.5Å to 4.0Å region from the $+90^{\circ}$ detector bank

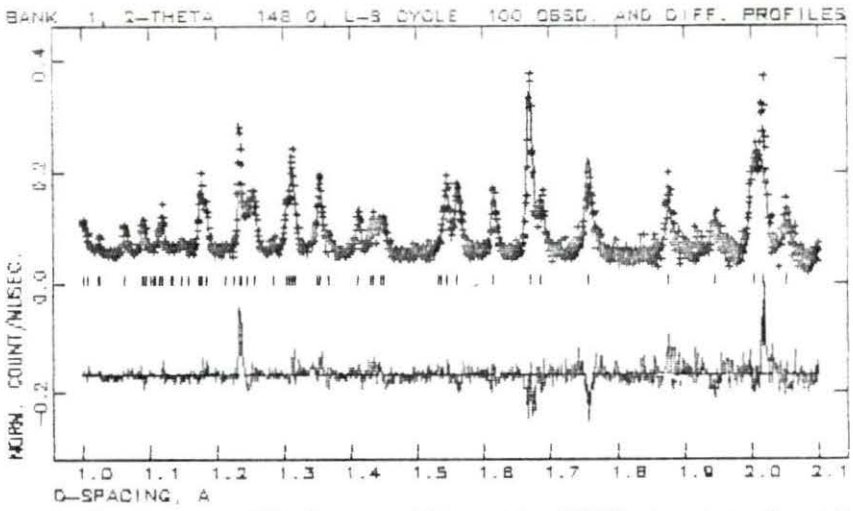

Figure 10.27: Diffraction profile for run 268 on the NPD showing the 1.0Å to 2.1Å region from the $+148^{\circ}$ detector bank

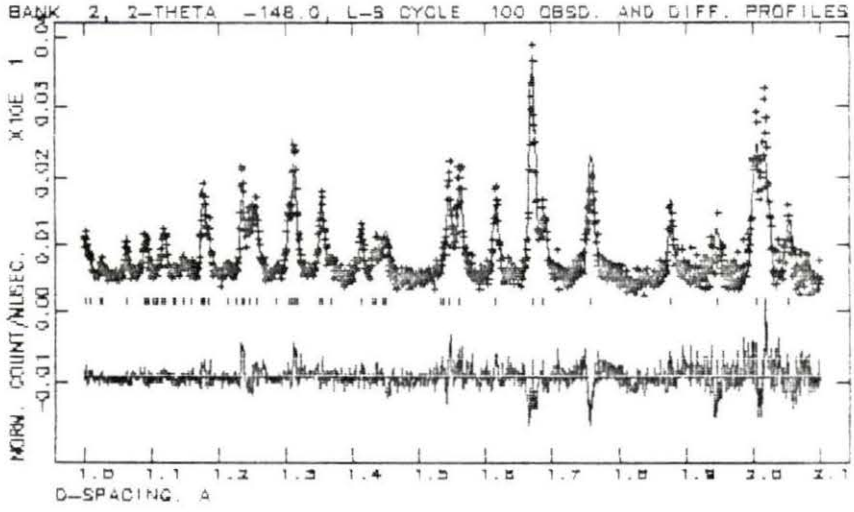

Figure 10.28: Diffraction profile for run 268 on the NPD showing the 1.0Å to 2.1Å region from the -148° detector bank

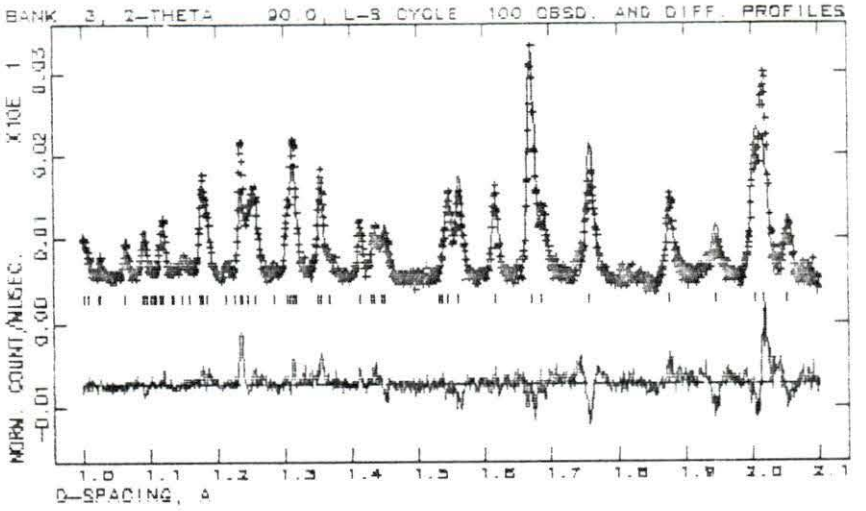

Figure 10.29: Diffraction profile for run 268 on the NPD showing the 1.0Å to 2.1Å region from the $+90^{\circ}$ detector bank

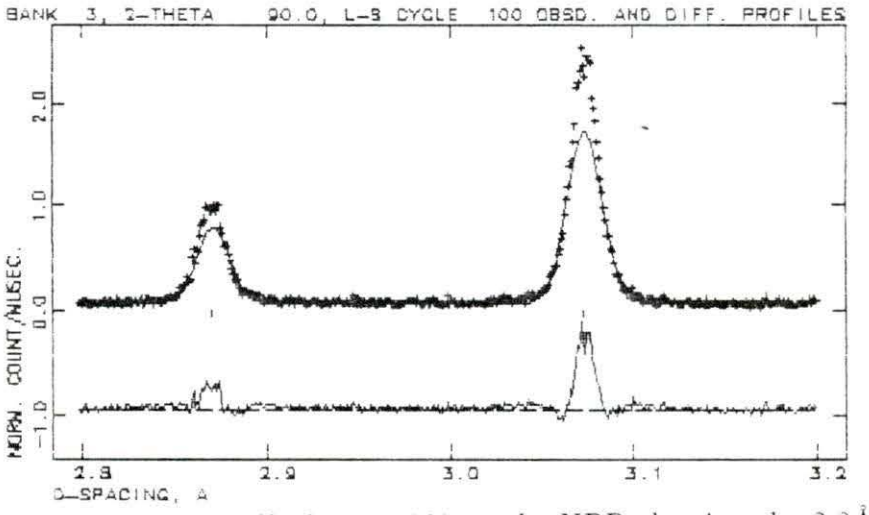

Figure 10.30: Diffraction profile for run 268 on the NPD showing the 2.8Å to 3.2Å region from the $+90^{\circ}$ detector bank

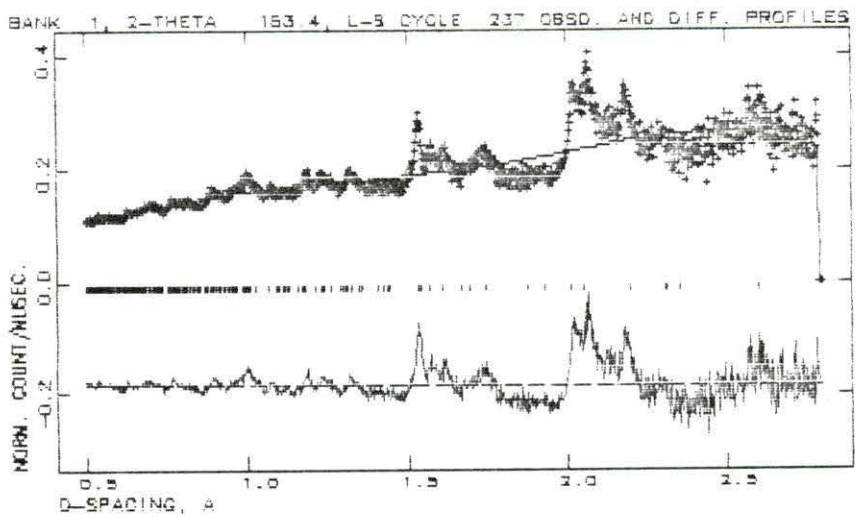

Figure 10.31: Diffraction profile for run 709 on the HIPD showing the 0.5Å to 2.8Å region from the $+153^{\circ}$ detector bank

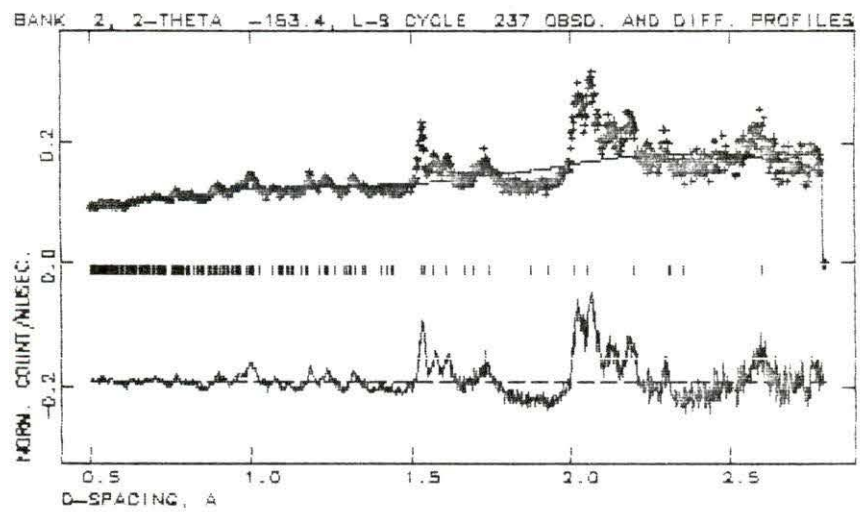

Figure 10.32: Diffraction profile for run 709 on the HIPD showing the 0.5Å to 2.8Å region from the -153° detector bank

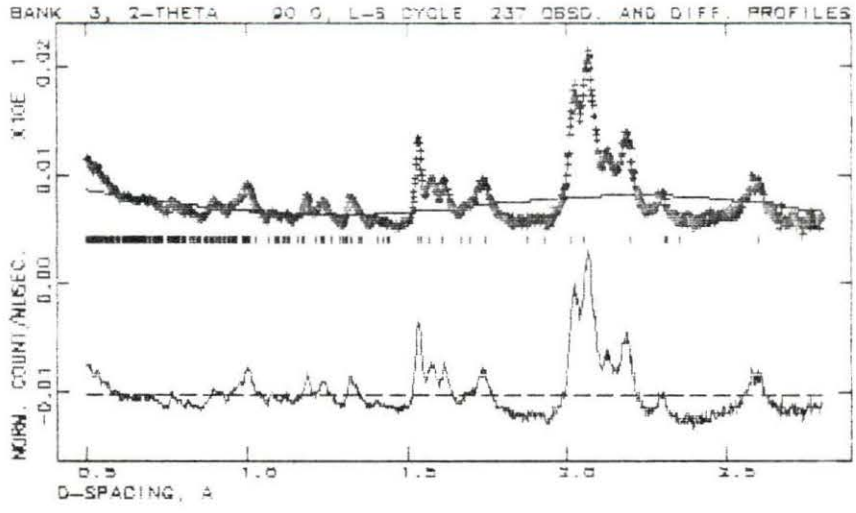

Figure 10.33: Diffraction profile for run 709 on the HIPD showing the 0.5Å to 2.8Å region from the $+90^{\circ}$ detector bank

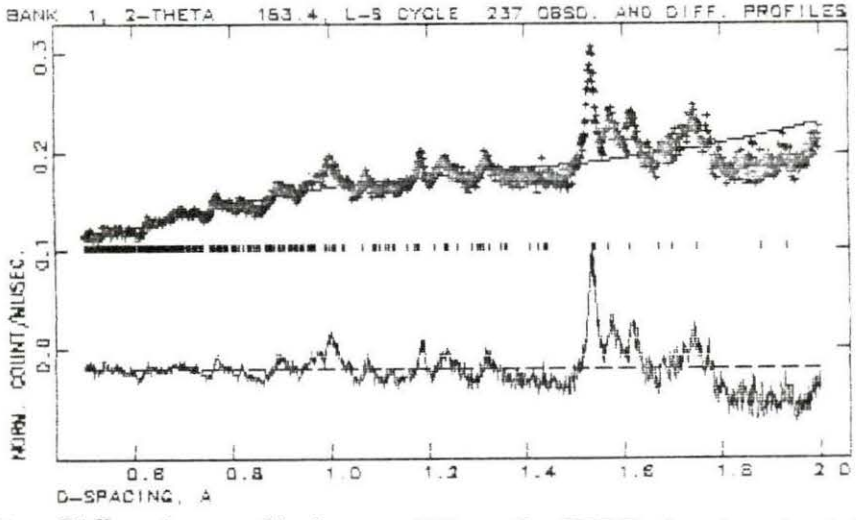

Figure 10.34: Diffraction profile for run 709 on the HIPD showing the 0.5Å to 2.0Å region from the $+153^{\circ}$ detector bank

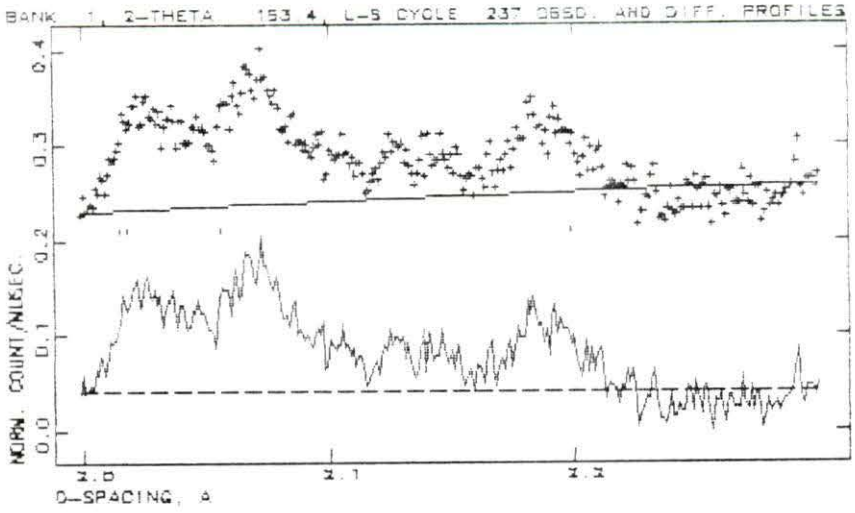

Figure 10.35: Diffraction profile for run 709 on the HIPD showing the 2.0Å to 2.3Å region from the $+153^{\circ}$ detector bank

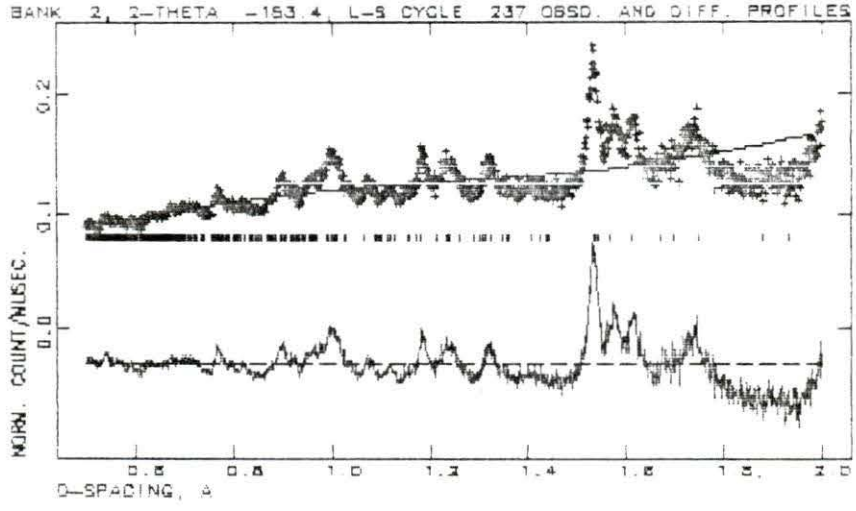

Figure 10.36: Diffraction profile for run 709 on the HIPD showing the 0.5Å to 2.0Å region from the -153° detector bank

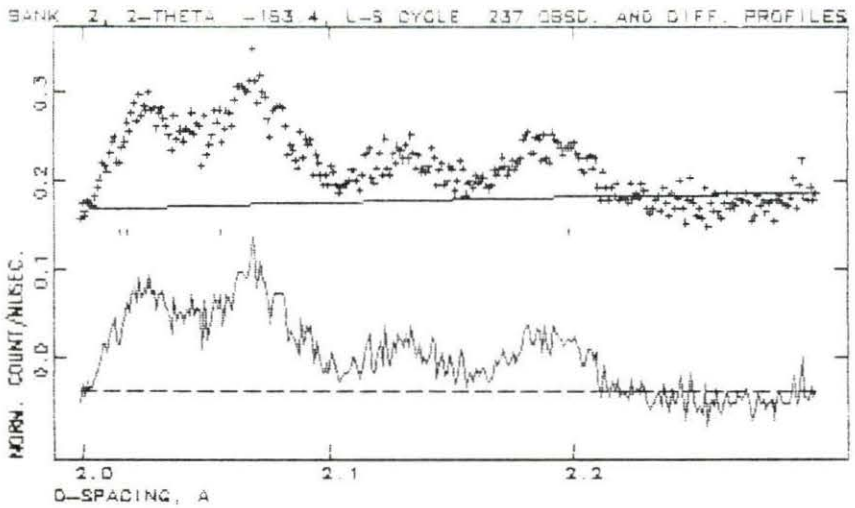

Figure 10.37: Diffraction profile for run 709 on the HIPD showing the 2.0Å to 2.3Å region from the -153° detector bank

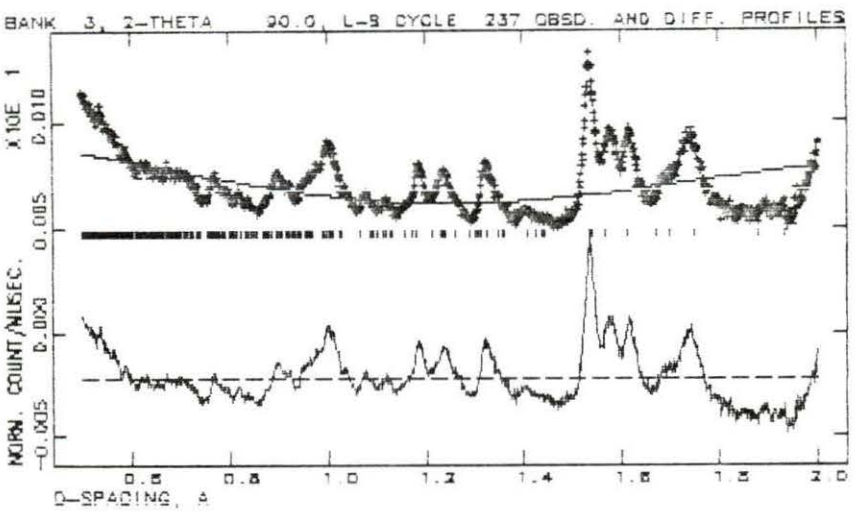

Figure 10.38: Diffraction profile for run 709 on the HIPD showing the 0.5Å to 2.0Å region from the $+90^{\circ}$ detector bank

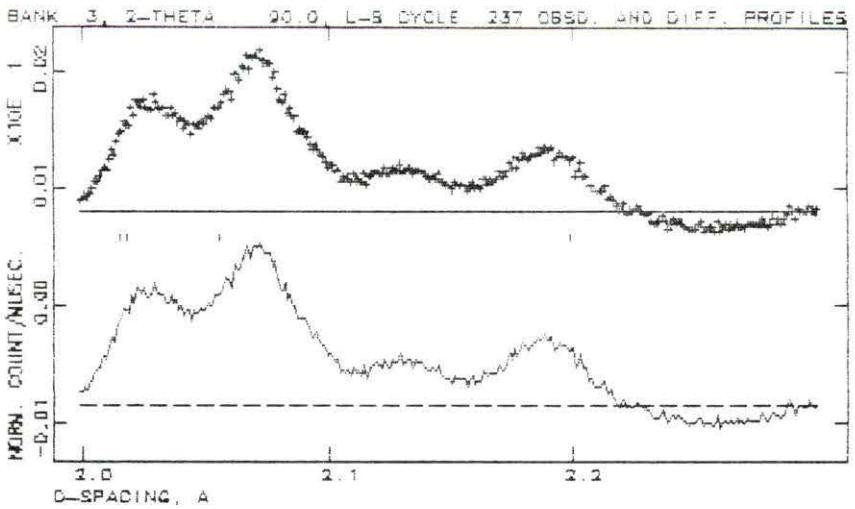

Figure 10.39: Diffraction profile for run 709 on the HIPD showing the 2.0Å to 2.3Å region from the $+90^{\circ}$ detector bank

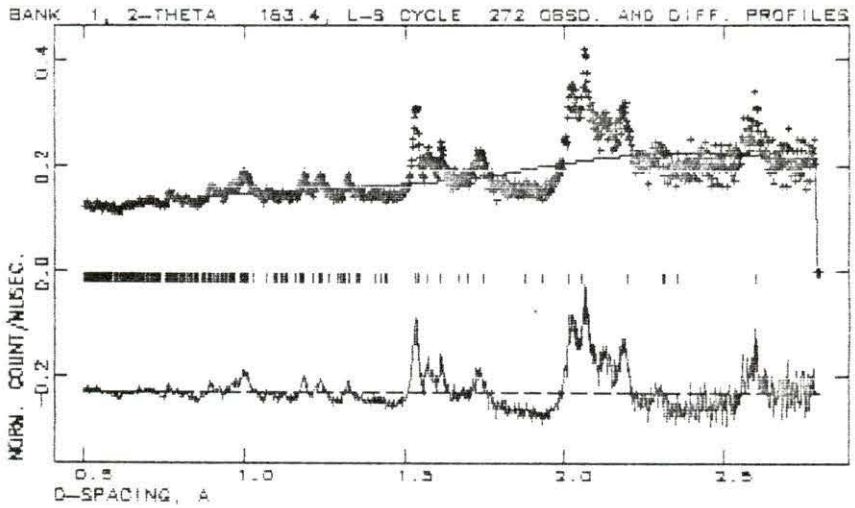

Figure 10.40: Diffraction profile for run 710 on the HIPD showing the 0.5Å to 2.8Å region from the $+153^{\circ}$ detector bank

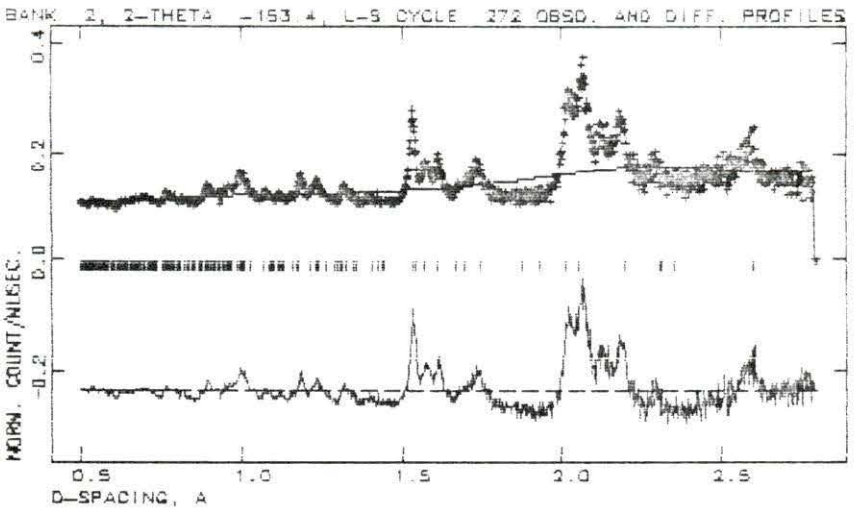

Figure 10.41: Diffraction profile for run 710 on the HIPD showing the 0.5Å to 2.8Å region from the -153° detector bank

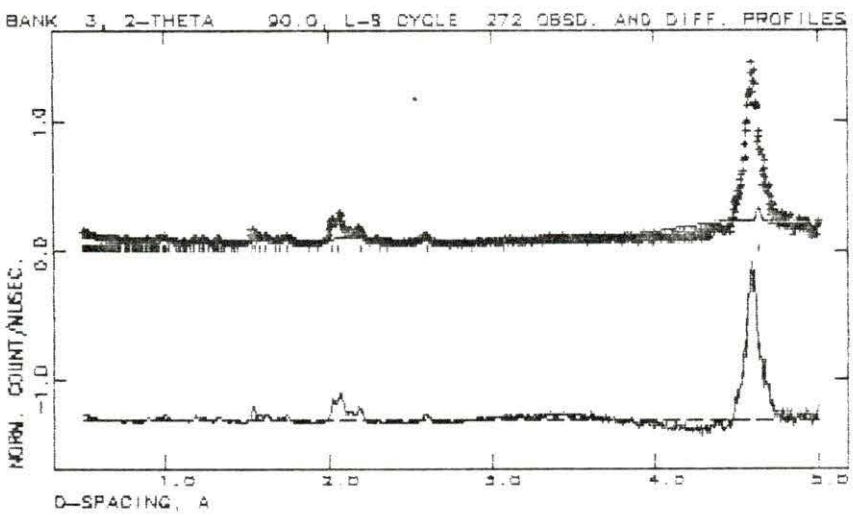

Figure 10.42: Diffraction profile for run 710 on the HIPD showing the 0.5Å to 5.0Å region from the $+90^{\circ}$ detector bank

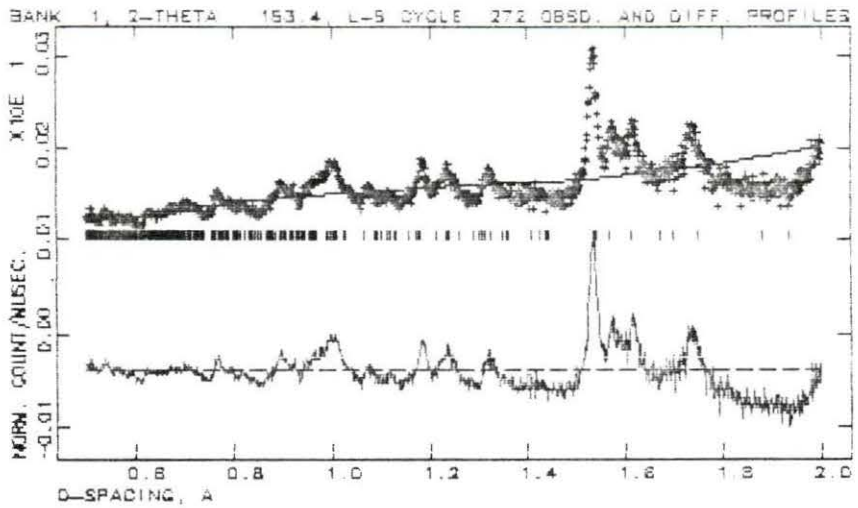

Figure 10.43: Diffraction profile for run 710 on the HIPD showing the 0.5Å to 2.0Å region from the $+153^{\circ}$ detector bank

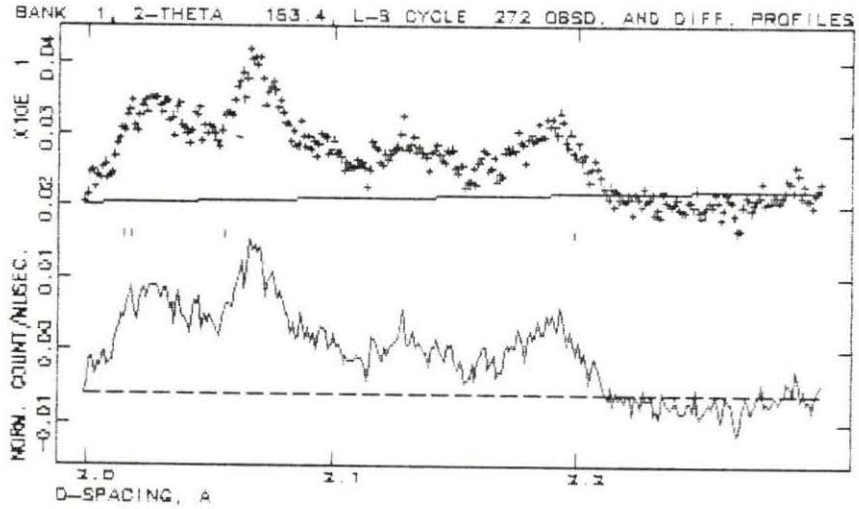

Figure 10.44: Diffraction profile for run 710 on the HIPD showing the 2.0Å to 2.3Å region from the $+153^{\circ}$ detector bank

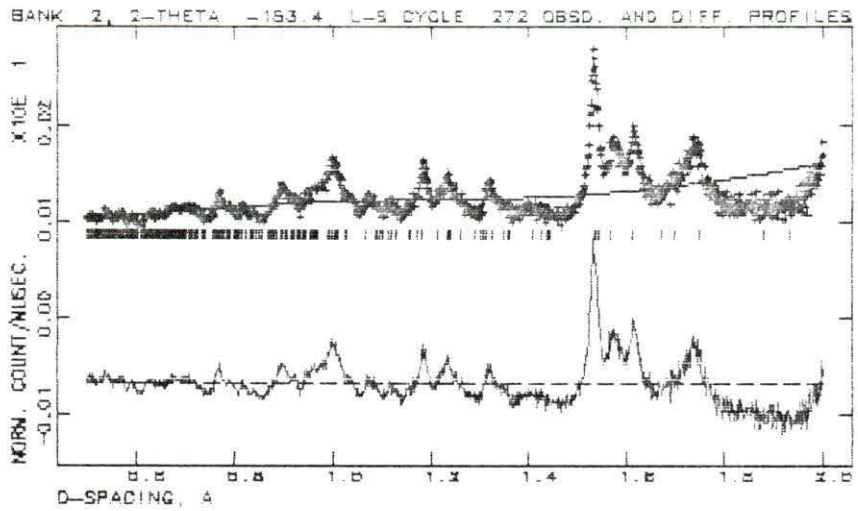

Figure 10.45: Diffraction profile for run 710 on the HIPD showing the 0.5Å to 2.0Å region from the -153° detector bank

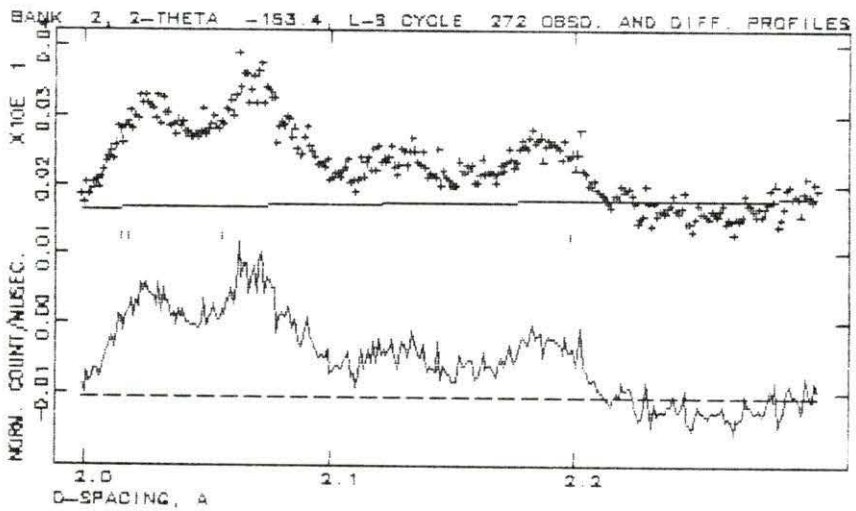

Figure 10.46: Diffraction profile for run 710 on the HIPD showing the 2.0Å to 2.3Å region from the -153° detector bank

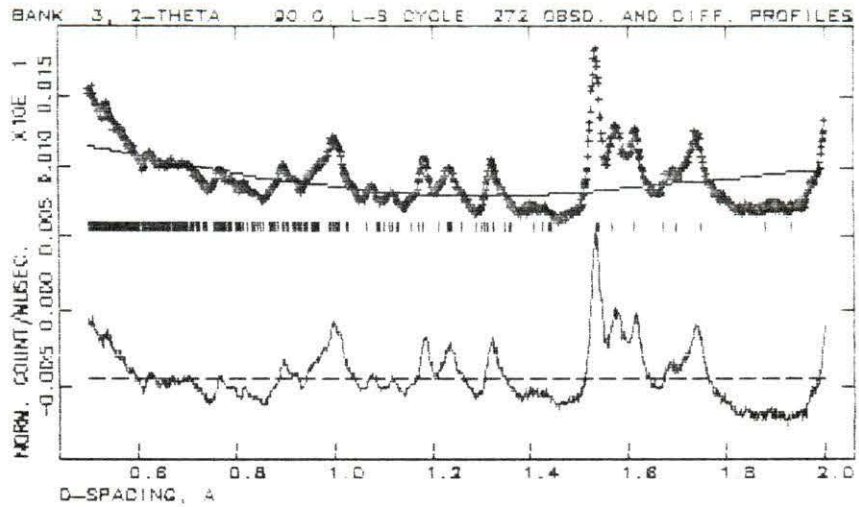

Figure 10.47: Diffraction profile for run 710 on the HIPD showing the 0.5Å to 2.0Å region from the $+90^{\circ}$ detector bank

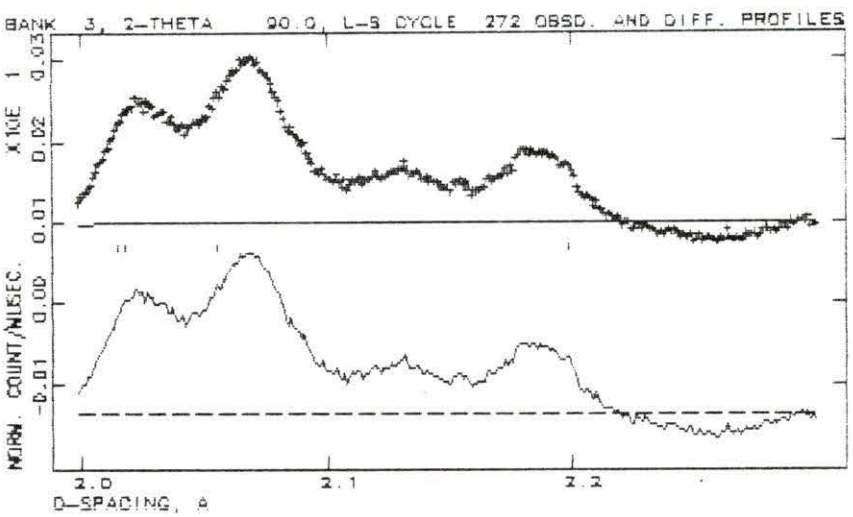

Figure 10.48: Diffraction profile for run 710 on the HIPD showing the 2.0Å to 2.3Å region from the $+90^{\circ}$ detector bank

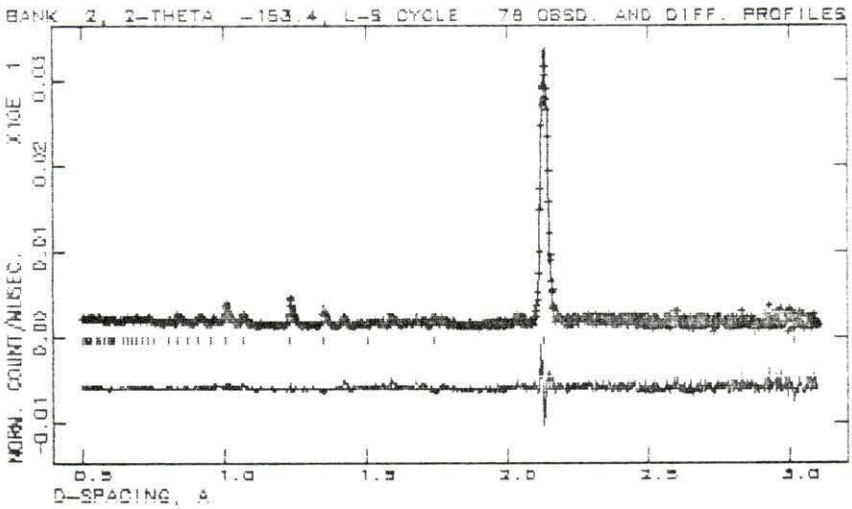

Figure 10.49: Diffraction profile for run 527530 on the HIPD showing the 0.5Å to 3.1Å region from the -153° detector bank ($Pm3m$ space group)

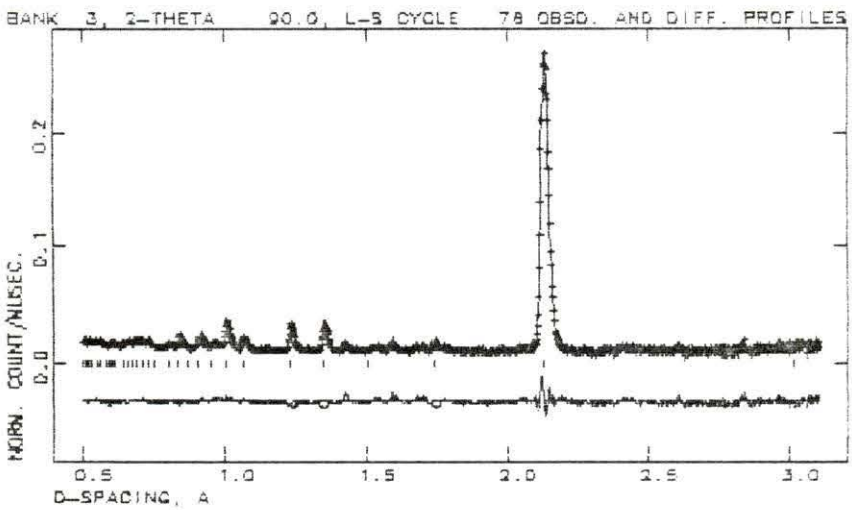

Figure 10.50: Diffraction profile for run 527530 on the HIPD showing the 0.5Å to 3.1Å region from the $+90^{\circ}$ detector bank ($Pm3m$ space group)

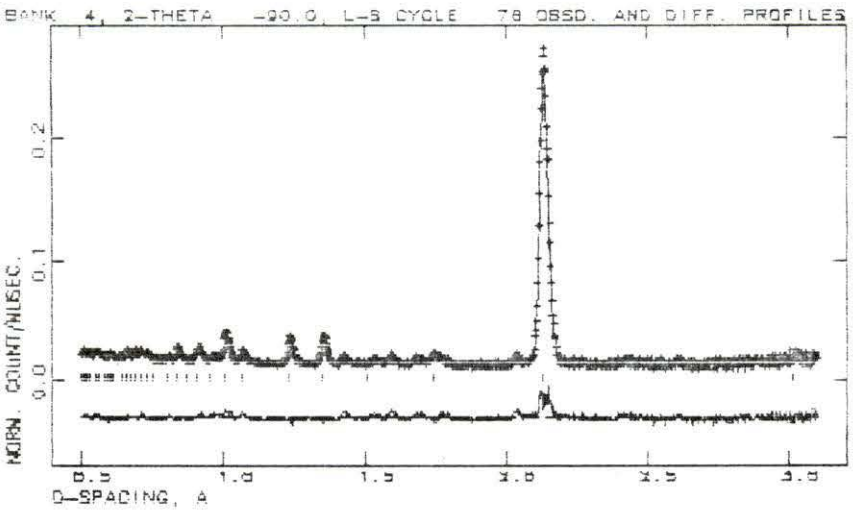

Figure 10.51: Diffraction profile for run 527530 on the HIPD showing the 0.5Å to 3.1Å region from the -90° detector bank ($Pm3m$ space group)

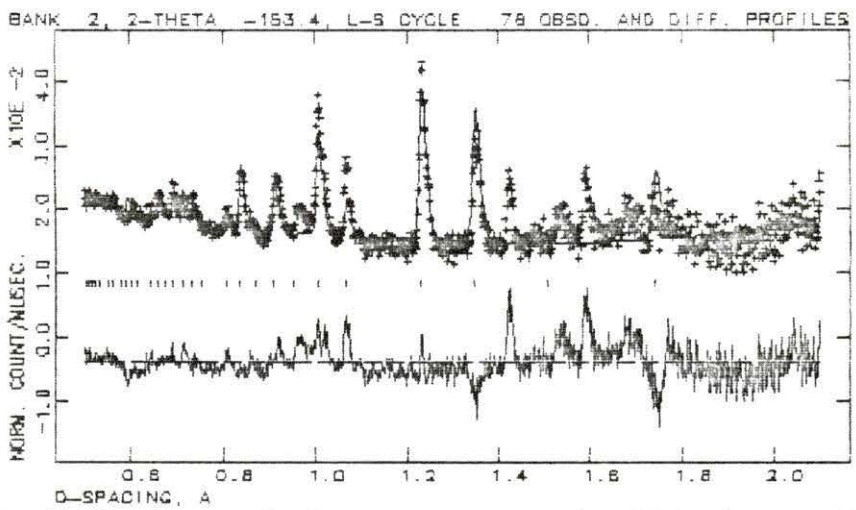

Figure 10.52: Diffraction profile for run 527530 on the HIPD showing the 0.5Å to 2.1Å region from the -153° detector bank ($Pm3m$ space group)

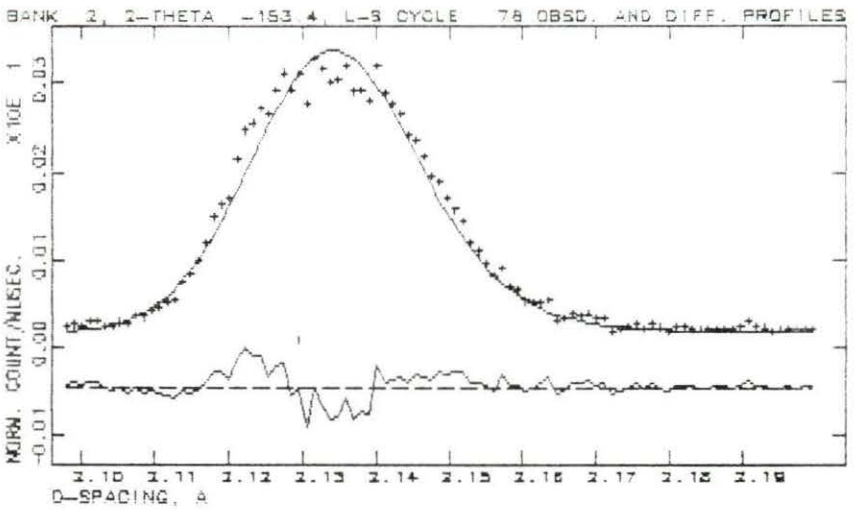

Figure 10.53: Diffraction profile for run 527530 on the HIPD showing the 2.1Å to 2.2Å region from the -153° detector bank ($Pm3m$ space group)

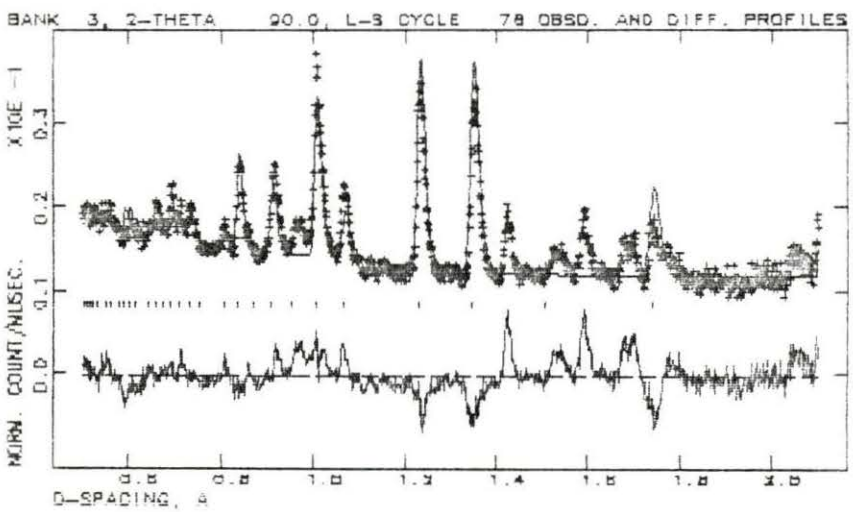

Figure 10.54: Diffraction profile for run 527530 on the HIPD showing the 0.5Å to 2.1Å region from the $+90^{\circ}$ detector bank ($Pm3m$ space group)

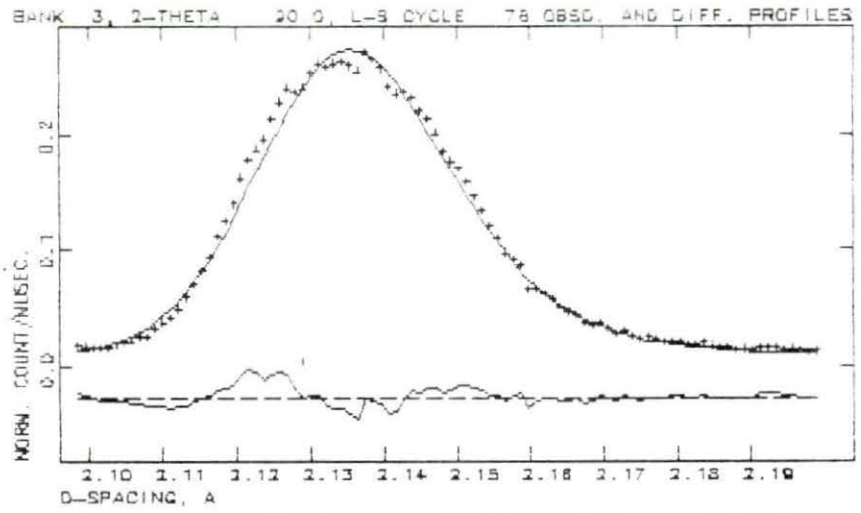

Figure 10.55: Diffraction profile for run 527530 on the HIPD showing the 2.1Å to 2.2Å region from the $+90^{\circ}$ detector bank ($Pm3m$ space group)

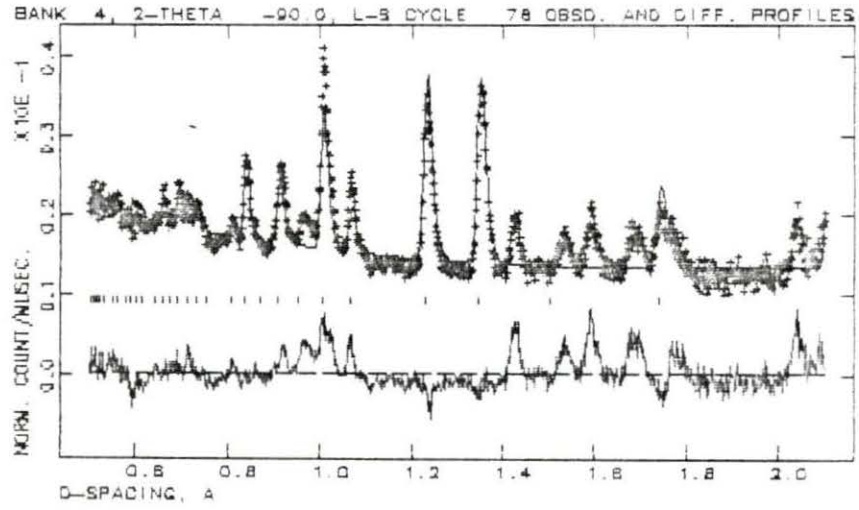

Figure 10.56: Diffraction profile for run 527530 on the HIPD showing the 0.5Å to 2.1Å region from the -90° detector bank ($Pm3m$ space group)

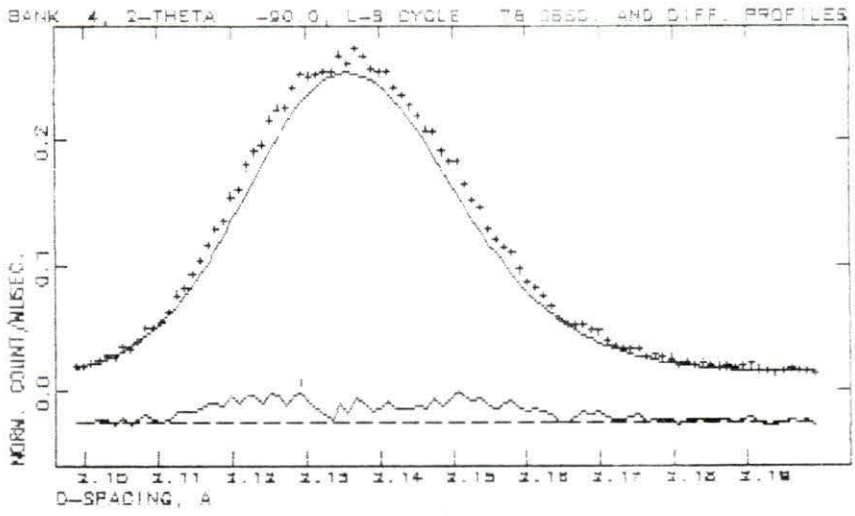

Figure 10.57: Diffraction profile for run 527530 on the HIPD showing the 2.1Å to 2.2Å region from the -90° detector bank ($Pm3m$ space group)

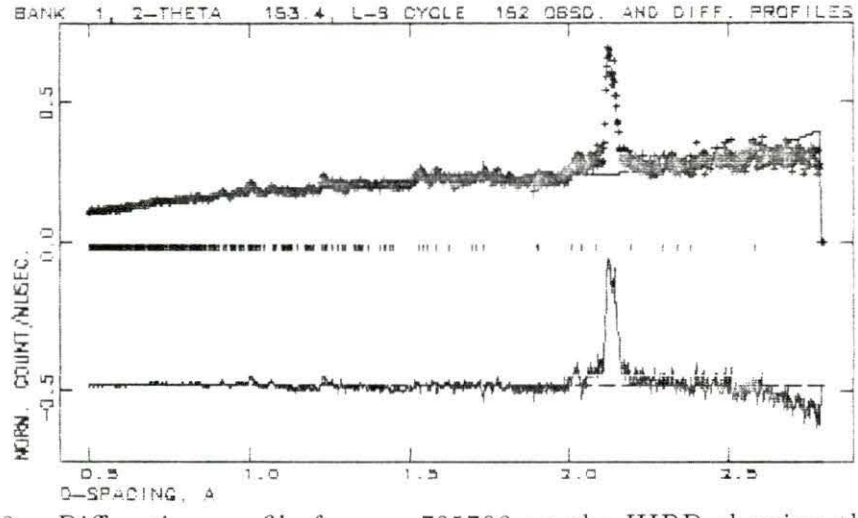

Figure 10.58: Diffraction profile for run 705706 on the HIPD showing the 0.5Å to 2.8Å region from the $+153^{\circ}$ detector bank using the $P2_1/m$ space group

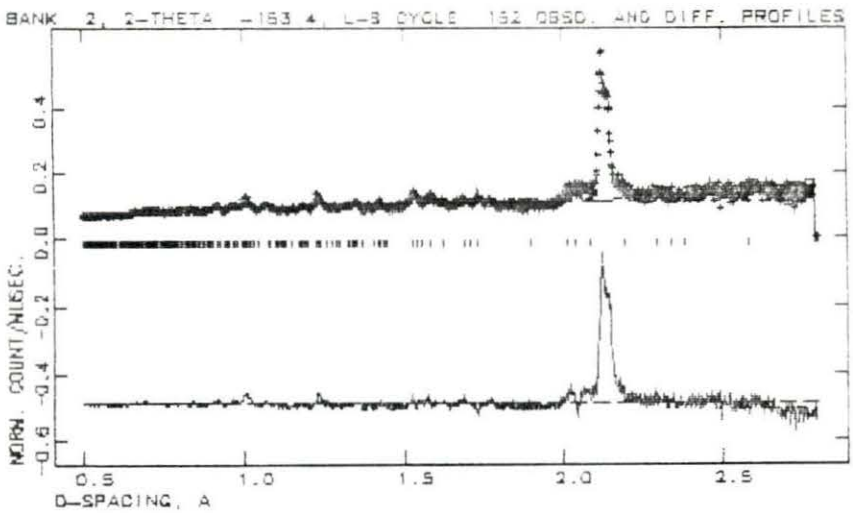

Figure 10.59: Diffraction profile for run 705706 on the HIPD showing the 0.5Å to 2.8Å region from the -153° detector bank using the $P2_1/m$ space group

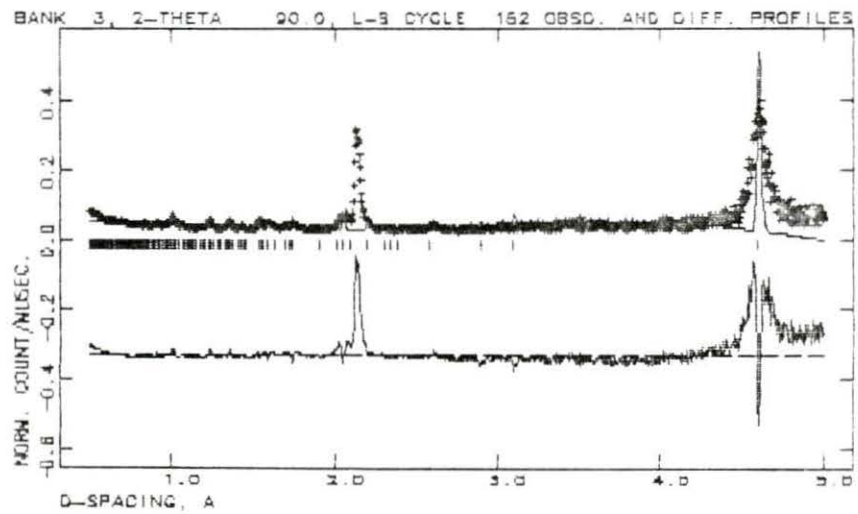

Figure 10.60: Diffraction profile for run 705706 on the HIPD showing the 0.5Å to 5.0Å region from the $+90^{\circ}$ detector bank using the $P2_1/m$ space group

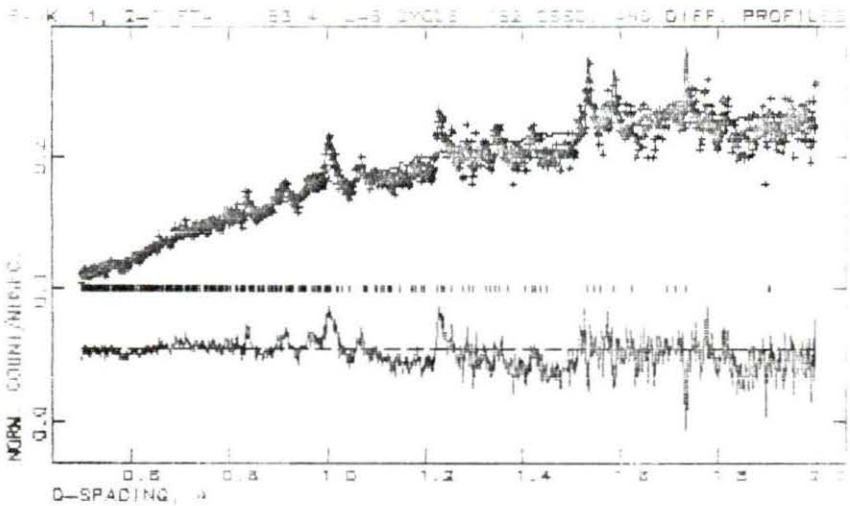

Figure 10.61: Diffraction profile for run 705706 on the HIPD showing the 0.5Å to 2.0Å region from the $+153^{\circ}$ detector bank using the $P2_1/m$ space group

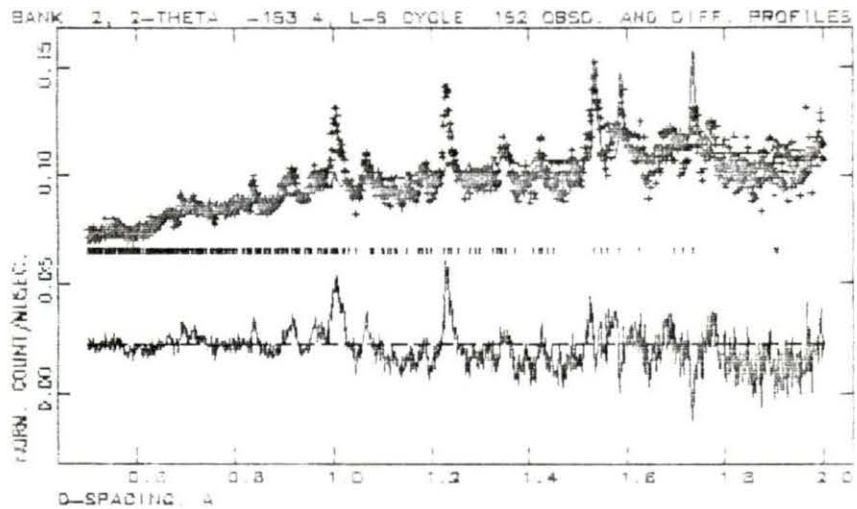

Figure 10.62: Diffraction profile for run 705706 on the HIPD showing the 0.5Å to 2.0Å region from the -153° detector bank using the $P2_1/m$ space group

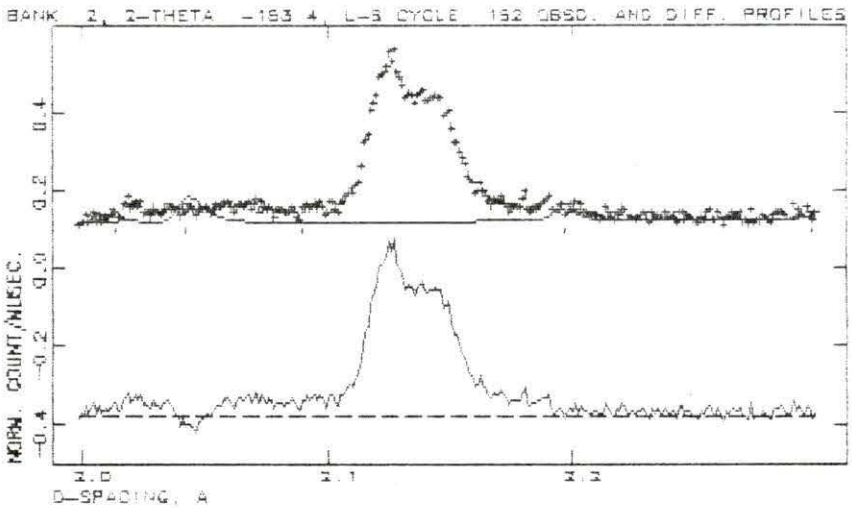

Figure 10.63: Diffraction profile for run 705706 on the HIPD showing the 2.0Å to 2.3Å region from the -153° detector bank using the $P2_1/m$ space group

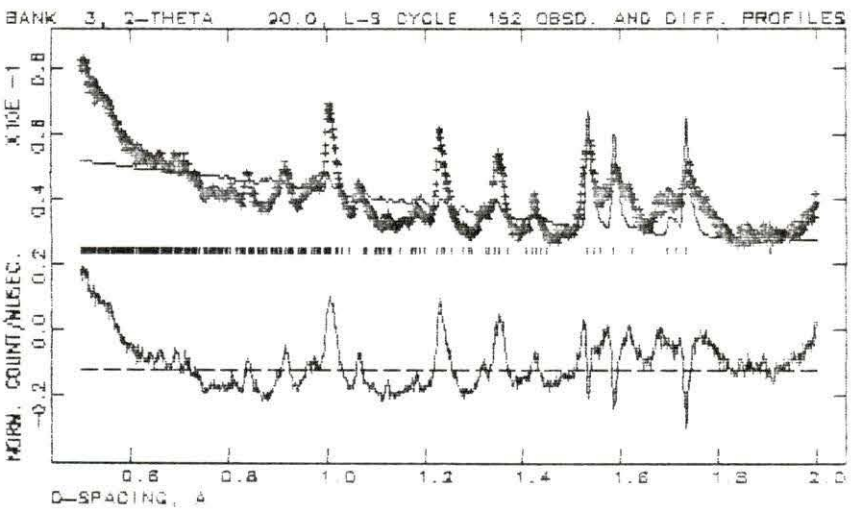

Figure 10.64: Diffraction profile for run 705706 on the HIPD showing the 0.5Å to 2.0Å region from the $+90^{\circ}$ detector bank using the $P2_1/m$ space group

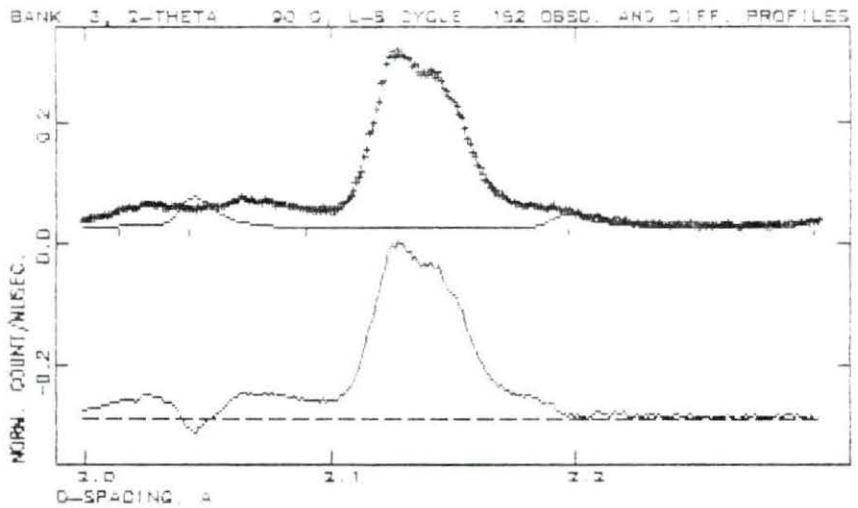

Figure 10.65: Diffraction profile for run 705706 on the HIPD showing the 2.0Å to 2.3Å region from the $+90^{\circ}$ detector bank using the $P2_1/m$ space group

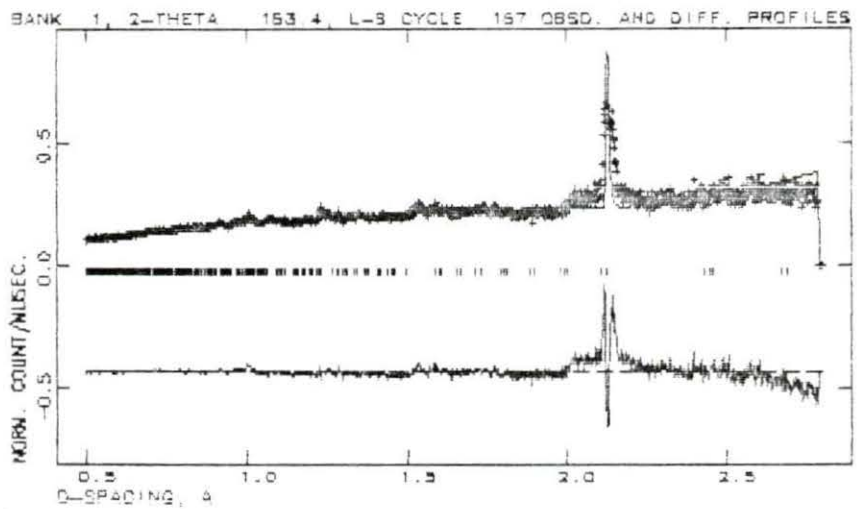

Figure 10.66: Diffraction profile for run 705706 on the HIPD showing the 0.5Å to 2.8Å region from the $+153^{\circ}$ detector bank using the $R\bar{3}mr$ space group

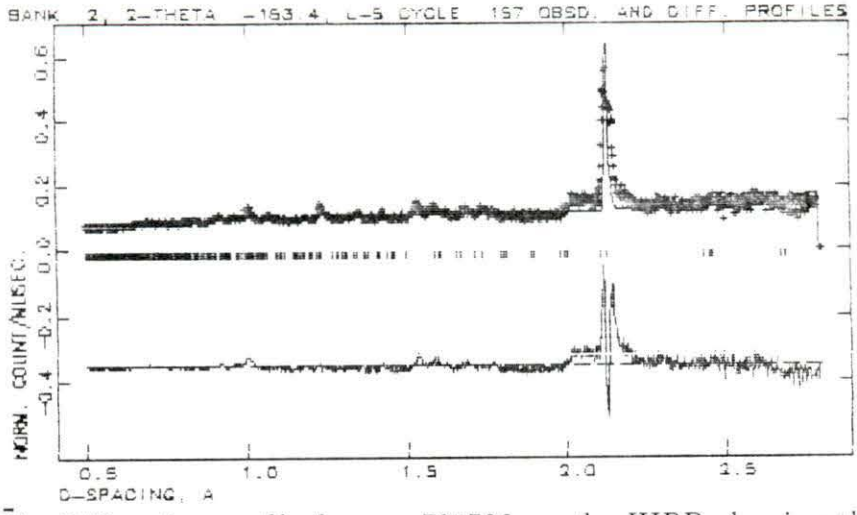

Figure 10.67: Diffraction profile for run 705706 on the HIPD showing the 0.5Å to 2.8Å region from the -153° detector bank using the $R\bar{3}mr$ space group

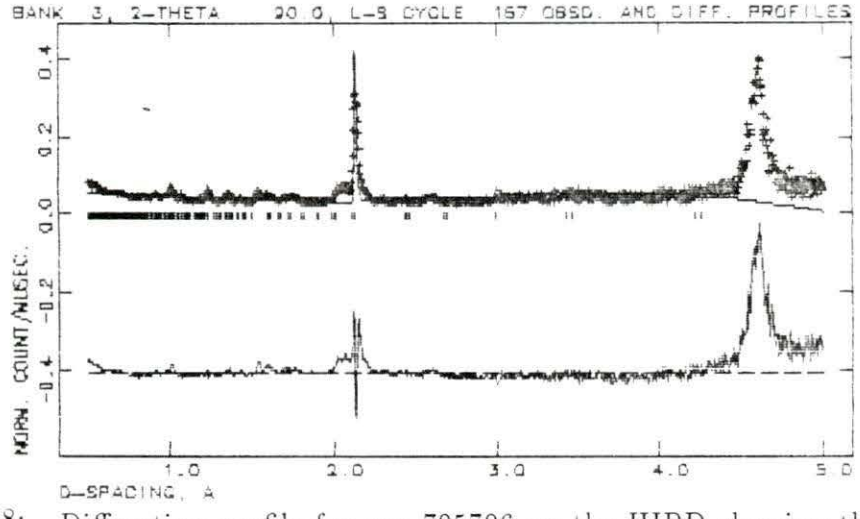

Figure 10.68: Diffraction profile for run 705706 on the HIPD showing the 0.5Å to 5.0Å region from the $+90^{\circ}$ detector bank using the $R\bar{3}mr$ space group

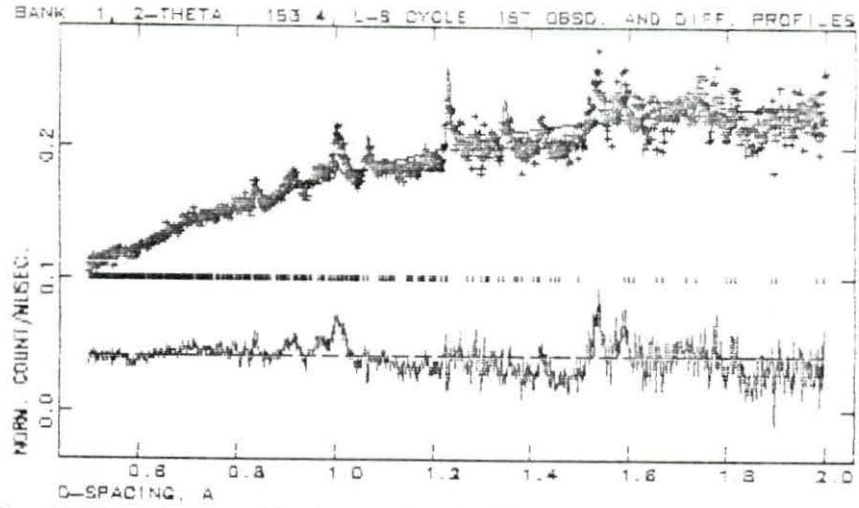

Figure 10.69: Diffraction profile for run 705706 on the HIPD showing the 0.5Å to 2.0Å region from the $+153^{\circ}$ detector bank using the $R\bar{3}mr$ space group

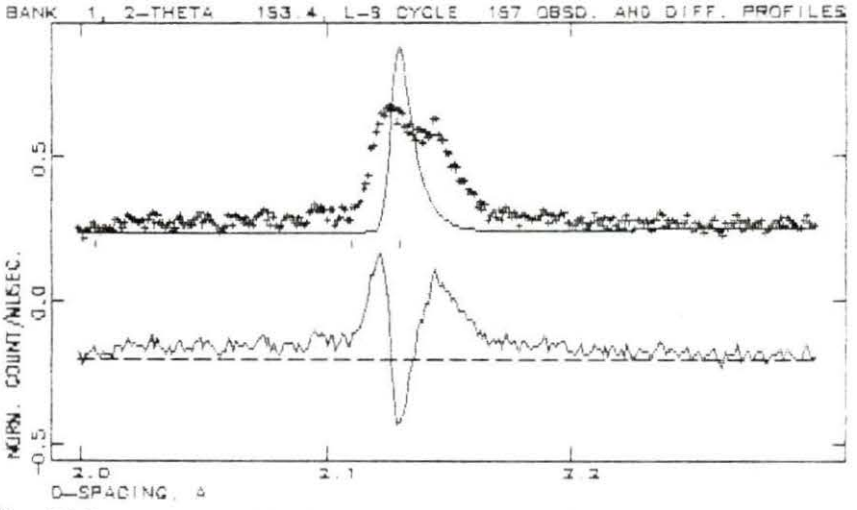

Figure 10.70: Diffraction profile for run 705706 on the HIPD showing the 2.0Å to 2.3Å region from the $+153^{\circ}$ detector bank using the $R\bar{3}mr$ space group

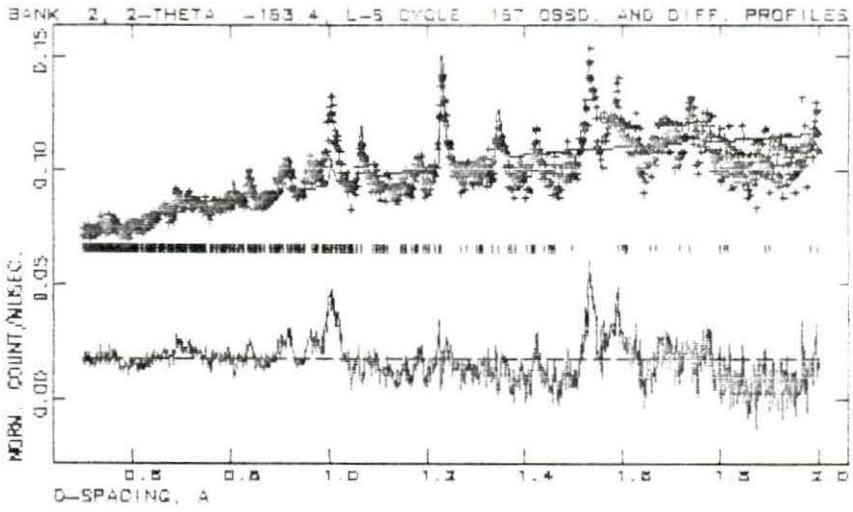

Figure 10.71: Diffraction profile for run 705706 on the HIPD showing the 0.5Å to 2.0Å region from the -153° detector bank using the $R\bar{3}mr$ space group

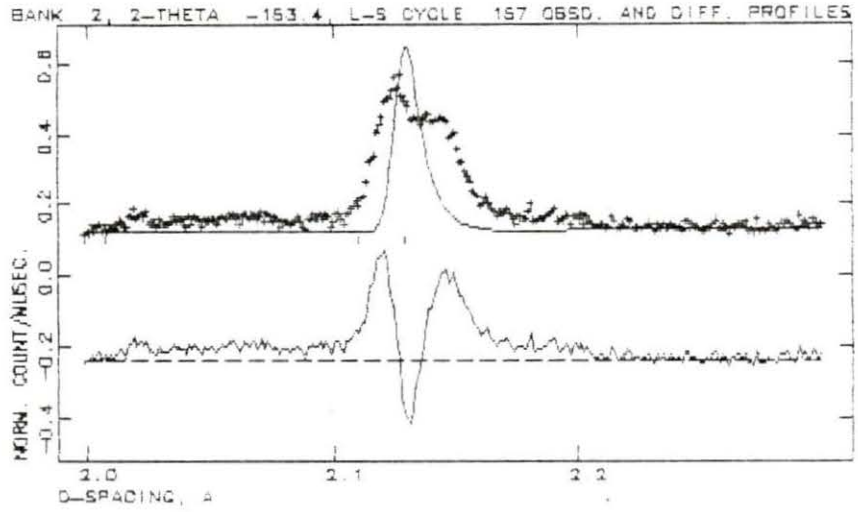

Figure 10.72: Diffraction profile for run 705706 on the HIPD showing the 2.0Å to 2.3Å region from the -153° detector bank using the $R\bar{3}mr$ space group

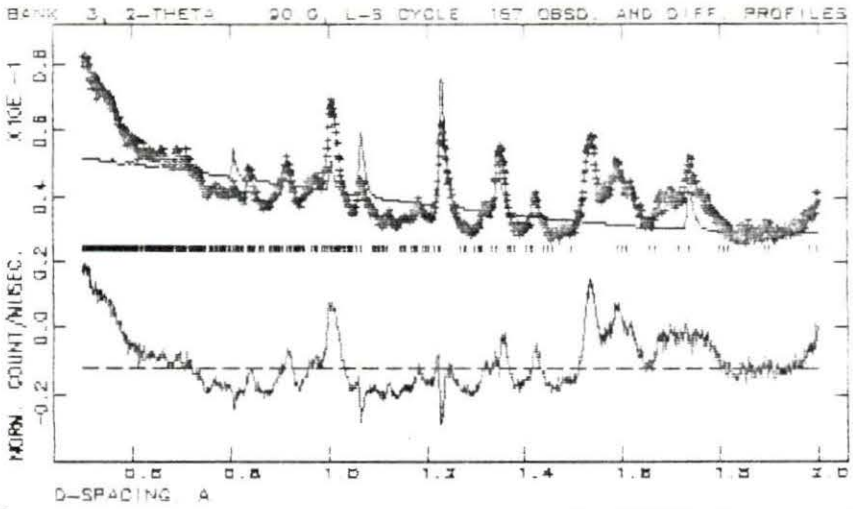

Figure 10.73: Diffraction profile for run 705706 on the HIPD showing the 0.5Å to 2.0Å region from the $+90^{\circ}$ detector bank using the $R\bar{3}mr$ space group

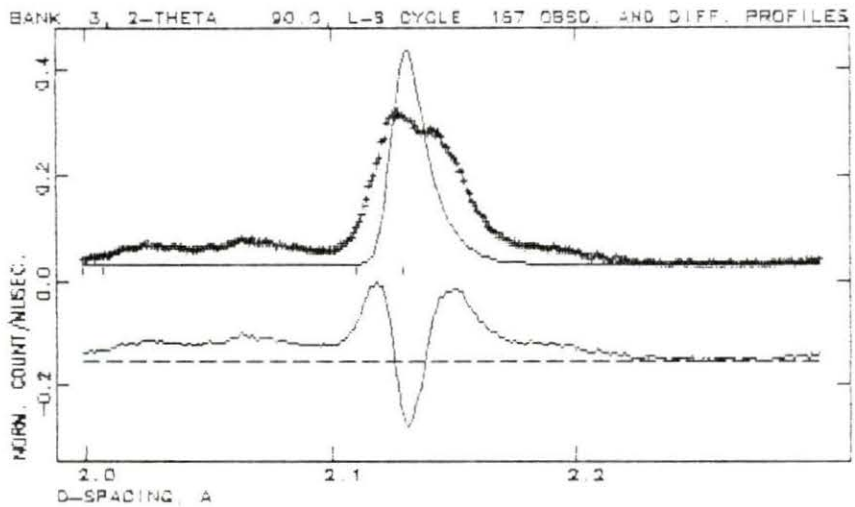

Figure 10.74: Diffraction profile for run 705706 on the HIPD showing the 2.0Å to 2.3Å region from the $+90^{\circ}$ detector bank using the $R\bar{3}mr$ space group

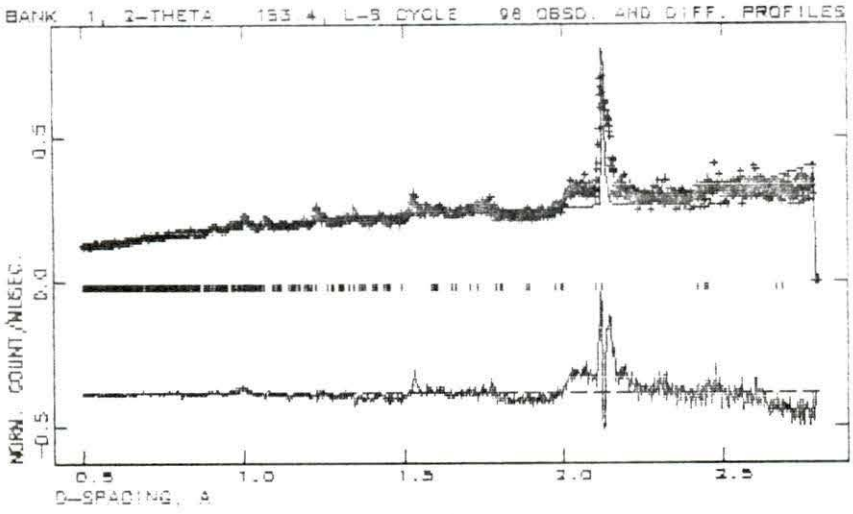

Figure 10.75: Diffraction profile for run 707708 on the HIPD showing the 0.5Å to 2.8Å region from the $+153^{\circ}$ detector bank using the $R\bar{3}mr$ space group

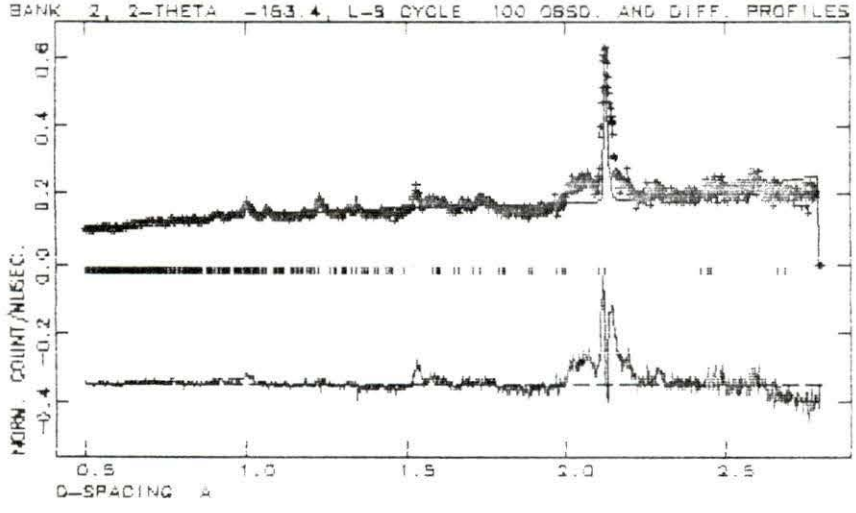

Figure 10.76: Diffraction profile for run 707708 on the HIPD showing the 0.5Å to 2.8Å region from the -153° detector bank using the $R\bar{3}mr$ space group

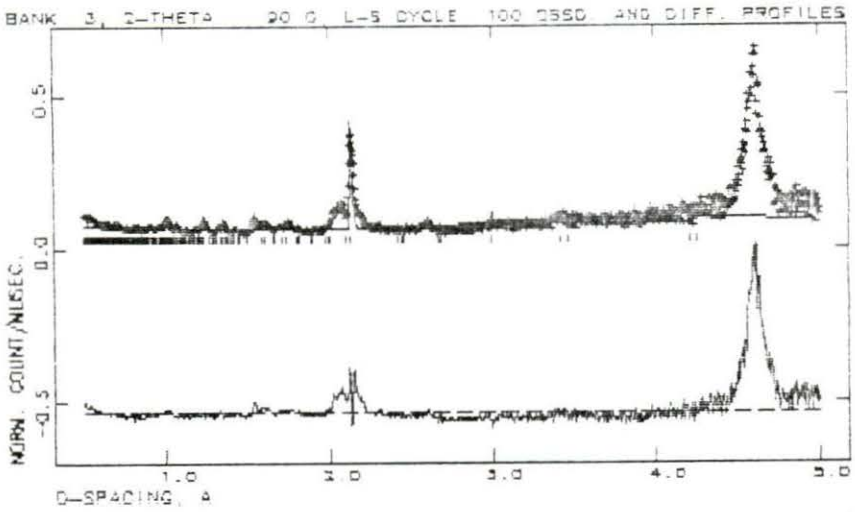

Figure 10.77: Diffraction profile for run 707708 on the HIPD showing the 0.5Å to 5.0Å region from the $+90^{\circ}$ detector bank using the $R\bar{3}mr$ space group

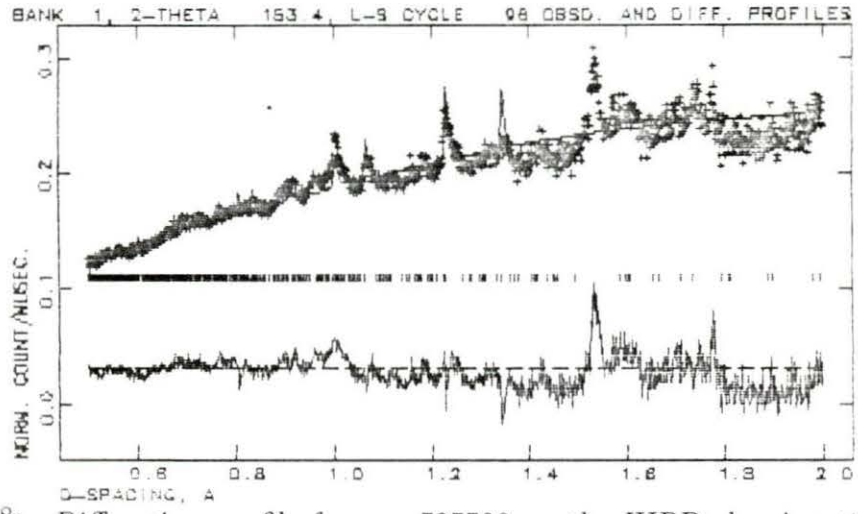

Figure 10.78: Diffraction profile for run 707708 on the HIPD showing the 0.5Å to 2.0Å region from the $+153^{\circ}$ detector bank using the $R\bar{3}mr$ space group

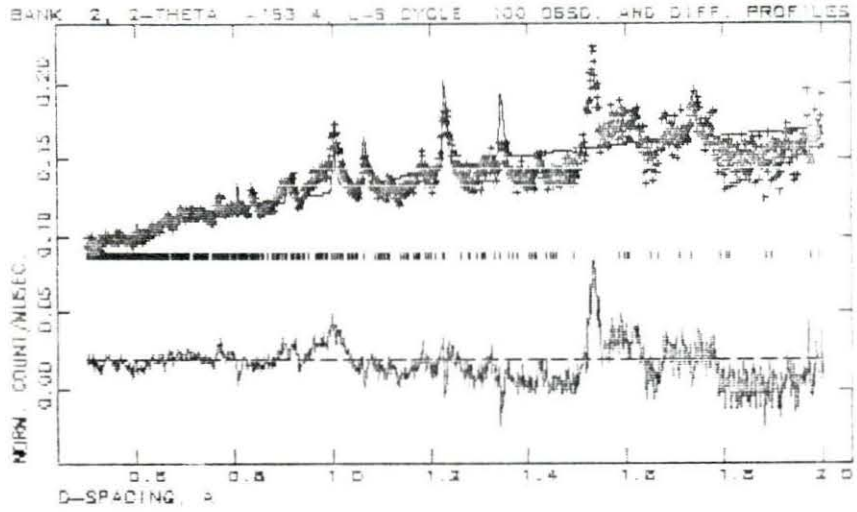

Figure 10.79: Diffraction profile for run 707708 on the HIPD showing the 0.5Å to 2.0Å region from the -153° detector bank using the $R\bar{3}mr$ space group

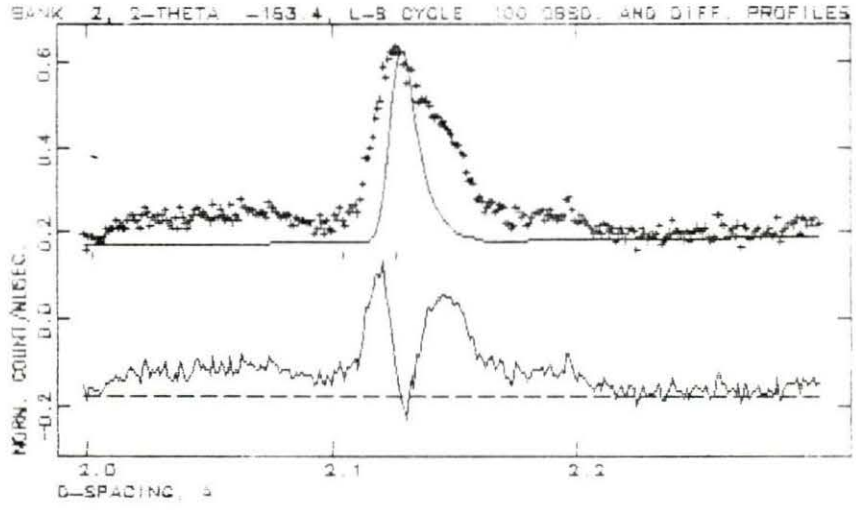

Figure 10.80: Diffraction profile for run 707708 on the HIPD showing the 2.0Å to 2.3Å region from the -153° detector bank using the $R\bar{3}mr$ space group

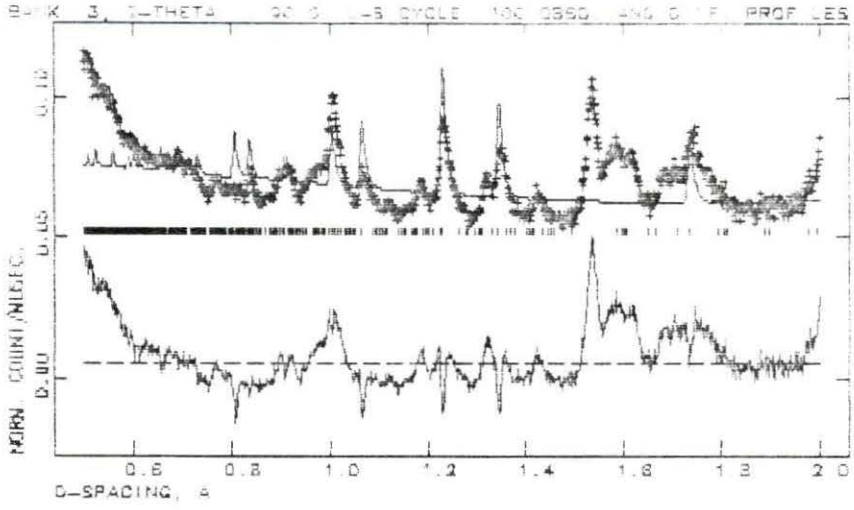

Figure 10.81: Diffraction profile for run 707708 on the HIPD showing the 0.5Å to 2.0Å region from the $+90^{\circ}$ detector bank using the $R\bar{3}mr$ space group

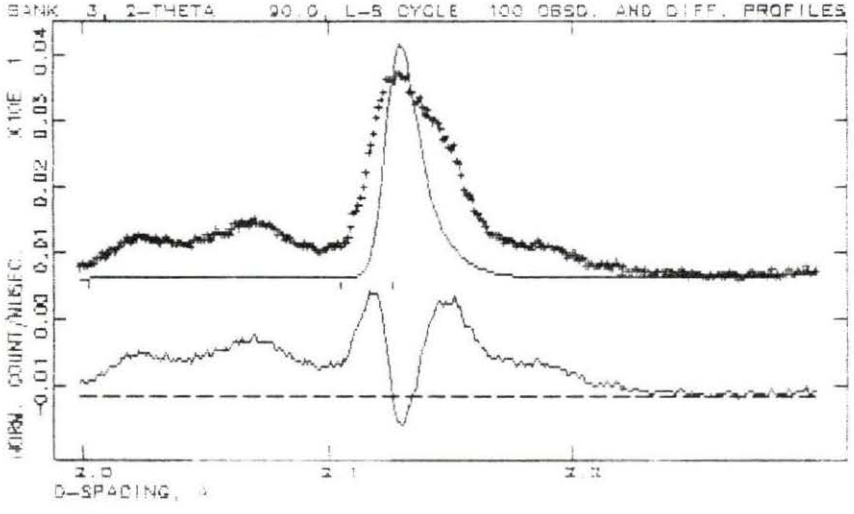

Figure 10.82: Diffraction profile for run 707708 on the HIPD showing the 2.0Å to 2.3Å region from the $+90^{\circ}$ detector bank using the $R\bar{3}mr$ space group